MECHANICAL SYSTEMS AT THE NANOSCALE

Mechanical systems at the nanoscale

Proefschrift

ter verkrijging van de graad van doctor
aan de Technische Universiteit Delft,
op gezag van de Rector Magnificus prof. dr. ir. J. T. Fokkema,
voorzitter van het College voor Promoties,
in het openbaar te verdedigen op dinsdag 1 december 2009 om 15.00 uur

door

Menno POOT

natuurkundig ingenieur
geboren te Maassluis.

Dit concept-proefschrift is goedgekeurd door de promotor:

Prof. dr. ir. H. S. J. van der Zant

Samenstelling promotiecommissie:

Rector Magnificus	voorzitter
Prof. dr. ir. H. S. J. van der Zant	Technische Universiteit Delft, promotor
Prof. dr. ir. L. P. Kouwenhoven	Technische Universiteit Delft
Prof. dr. ir. T. M. Klapwijk	Technische Universiteit Delft
Prof. dr. ir. J. E. Mooij	Technische Universiteit Delft
Dr. Ya. M. Blanter	Technische Universiteit Delft
Prof. dr. M. P. Blencowe	Dartmouth College, USA
Dr. E. M. Weig	Ludwig-Maximilians-Universität, Germany

Keywords: Nanomechanical devices, NEMS, QEMS, graphene, carbon nanotube, SQUID, backaction

Cover design: M. Poot

Front: Compliance profile of a nanodrum formed by a few-layer graphene sheet that is suspended over a circular hole.

Back: Scanning electron micrograph of a dc SQUID with a schematic overview of the measurement electronics. The device enables sensitive motion detection of an integrated micromechanical resonator.

Printed by: Gildeprint drukkerijen

Casimir PhD Series, Delft-Leiden, 2009-13

ISBN 978-90-8593-062-4

An electronic version of this dissertation is available at
`http://repository.tudelft.nl/`.

Contents

1

INTRODUCTION

Mechanics is probably the most well-known branch of physics as everyone encounters it in every-day life. It describes a wide range of effects: from the motion of galaxies and planets on a large scale, the vibrations of a bridge induced by traffic or wind, the stability of a riding bicycle to the trajectories of electrons in an old-fashioned television on a microscopic scale. In the early days of physics, mainly objects that could be seen or touched were studied, i.e. those on the human scale. The development of better and better telescopes and microscopes enabled the study of mechanical systems on both much larger and smaller length scales. Until the beginning of the twentieth century it was thought that the three laws of motion obtained by Newton described the dynamics of mechanical systems completely. The rapid developments in the early 1900s that led to the theory of special and general relativity and quantum mechanics showed that the laws of classical mechanics were not the whole truth.

Relativistic correction turns out to be important for objects with large masses or with velocities approaching the speed of light. It is therefore an important factor in astrophysics, where one studies the dynamics of heavy objects like galaxies and black holes or the bending of light by the curvature of space-time. Relativity is therefore most applicable to objects well beyond the human scale. When the masses and velocities of the objects involved are made smaller and smaller, the relativistic corrections eventually vanish and one obtains the classical laws of motion [1].

Quantum mechanics, on the other hand, is particularly well suited to describe the mechanics of objects at the other end of the length-scale range, i.e (sub)atomic objects. In the beginning of the twentieth century, quantum theory successfully explained the photoelectric effect, black-body radiation and the atomic emission spectra. Quantum mechanics is different from classical and relativistic mechanics in the sense that objects are no longer described by a definite position, but by a wavefunction. This wavefunction evolves deterministically according to the Schrödinger equation and its absolute value squared should be interpreted as the position probability-density function, the so-called Born rule [2]. To find the object at a particular location one has to *measure* its position. This process, however, inevitably disturbs the evolution of the wavefunction [3, 4].

Quantum mechanics does not only describe processes at the (sub)atomic scale successfully, but it also explains the microscopic origin of many macroscopic effects such as the electronic properties of solids, superfluidity and so on. Unlike in relativity where one can simply take the limit $m, v \to 0$, in quantum mechanics it is still not entirely clear how the transition from quantum mechanics to classical mechanics exactly happens [5, 6]. Although Ehrenfest's theorem implies that the expectation values of quantities obey Newton's second law [2], the classical laws of motion are not obtained by simply taking $\hbar \to 0$ [7].

Another issue that is still debated is how quantum mechanics should be interpreted [8]: as the truth, as a tool to calculate outcomes of an experiment or as an incomplete theory? These two issues are related and can be reformulated into the question "Can a macroscopic object be put in a quantum superposition?" This was first illustrated by Schrödinger in 1935 with the famous dead-or-alive cat *gedanken* experiment. Superpositions of small objects are readily observed, a good example are the singlet and triplet spin states in a molecule, but this becomes increasingly difficult for larger and larger systems mainly due to decoherence [9]. So far, superpositions have been created using the circulating current in superconducting quantum interference devices (SQUIDs) [10] and with fullerenes [11, 12].

Nanomechanical devices [13, 14] are interesting candidates to further increase the size of systems that can be put in a superposition [15]. These systems are the logical continuation of micromechanical devices that are made using integrated-circuit technology, but then on a much smaller, nanometer scale. Micro-electomechanical systems (MEMS) are currently widely used as, for example, accelerometers in airbags, pressure sensors or projectors. When scaling these devices down to the nanometer scale, their resonance frequencies increase and at the same time their mass decreases. From an application point of view this is interesting as this might enable single-atom mass-sensing, mechanical computing and efficient signal processing in the radio-frequency and microwave bands. From a scientific point of view these devices are interesting as they can be cooled to temperatures so low that the resonator is nearly always in its quantum-mechanical ground state. Moreover, the rapid progress in the development of position detectors have led to detectors that have sensitivities that are approaching the quantum limit on position detection [3].

In this Thesis, different types of micro- and nanomechanical devices are studied with the focus on their possible use for exploring the quantum regime for mechanical systems. In Chapter 2 the current state of the field is discussed and the relevant concepts are explained. Chapter 3 discusses how these nanomechanical systems are modelled using techniques from continuum mechanics. Chapters 4, 5 and 6 describe experiments on bottom-up fabricated carbon-based nanoelectromechanical systems (NEMS). These include few-layer graphene nanodrums (Ch. 4) and suspended carbon nanotubes (Ch. 5 and 6). Chapters 7 and 8 are devoted to the motion detection of, and backaction on, a top-down fabricated micromechanical resonator embedded in a dc SQUID.

REFERENCES

[1] S. Carroll, *Spacetime and Geometry: An Introduction to General Relativity* (Addison Wesley, 2004).

[2] D. J. Griffiths, *Introduction to Quantum Mechanics* (Prentice Hall, 1995).

[3] C. M. Caves, K. S. Thorne, R. W. P. Drever, V. D. Sandberg, and M. Zimmermann, *On the measurement of a weak classical force coupled to a quantum-mechanical oscillator. I. Issues of principle*, Rev. Mod. Phys. **52**, 341 (1980).

[4] V. B. Braginsky, Y. I. Vorontsov, and K. S. Thorne, *Quantum Nondemolition Measurements*, Science **209**, 547 (1980).

[5] S. L. Adler and A. Bassi, *Is Quantum Theory Exact?*, Science **325**, 275 (2009).

[6] J. Dunningham, A. Rau, and K. Burnett, *From Pedigree Cats to Fluffy-Bunnies*, Science **307**, 872 (2005).

[7] I. Katz, R. Lifshitz, A. Retzker, and R. Straub, *Classical to quantum transition of a driven nonlinear nanomechanical resonator*, New J. Phys. **10**, 125023 (20pp) (2008).

[8] A. J. Leggett, *The Quantum Measurement Problem*, Science **307**, 871 (2005).

[9] W. H. Zurek, *Decoherence, einselection, and the quantum origins of the classical*, Rev. Mod. Phys. **75**, 715 (2003).

[10] C. H. van der Wal, A. C. J. ter Haar, F. K. Wilhelm, R. N. Schouten, C. J. P. M. Harmans, T. P. Orlando, S. Lloyd, and J. E. Mooij, *Quantum Superposition of Macroscopic Persistent-Current States*, Science **290**, 773 (2000).

[11] M. Arndt, O. Nairz, J. Vos-Andreae, C. Keller, G. van der Zouw, and A. Zeilinger, *Wave-particle duality of C_{60} molecules*, Nature **401**, 680 (1999).

[12] L. Hackermüller, K. Hornberger, B. Brezger, A. Zeilinger, and M. Arndt, *Decoherence of matter waves by thermal emission of radiation*, Nature **427**, 711 (2004).

[13] A. Cleland, *Foundations of Nanomechanics* (Springer, 2003).

[14] K. L. Ekinci and M. L. Roukes, *Nanoelectromechanical systems*, Rev. Sci. Instrum. **76**, 061101 (pages 12) (2005).

[15] W. Marshall, C. Simon, R. Penrose, and D. Bouwmeester, *Towards Quantum Superpositions of a Mirror*, Phys. Rev. Lett. **91**, 130401 (2003).

2

QUANTUM *mechanics*

This chapter introduces the concepts related to mechanical systems in the quantum regime. These concepts will be useful when reading the forthcoming Chapters of this Thesis. The starting point is a brief review of the classical and quantum mechanical description of the harmonic oscillator. Then, Brownian motion and the effective resonator temperature are explained, and different cooling techniques are discussed. The quantum limit on position detection using continuous linear detectors is derived and it is shown that the physics of the position detector plays an important role.

Many of the abovementioned concepts and their implications became relevant in the 1970s when more and more sensitive gravitational wave detectors [1] were designed (see for example Refs. [2] and [3]), raising questions on the violations of the Heisenberg uncertainty principle [4–6]. Nowadays, these issues are important when measuring on micro- and nanomechanical devices with very sensitive detectors or at very low temperatures. Table 2.1 provides an overview of recent experiments with mechanical resonators that approach the quantum limit in position-detection sensitivity or that have a low resonator temperature. Different groups use different types of resonators: doubly clamped beams, singly clamped cantilevers, radial breathing modes of silica microtoroids, membranes, micromirrors and macroscopic bars. In general, two distinct methods for position detection are used: optical and electrical. Optical detectors typically use an interferometer in which light reflects back and forth between a mirror and the resonator. This will be explained in more detail in Sec. 2.3. Electrical readout often uses mesoscopic devices for a sensitive position detection. This includes single electron transistors (SETs), atomic and quantum point contacts (APCs and QPCs resp.), and superconducting quantum interference devices (SQUIDs). Also, the microwave equivalent of the optical interferometer, a superconducting stripline, is used.

This Chapter starts with a brief overview of the physics of the harmonic oscillator. Thermal and quantum noise are introduced in Sec. 2.2. To prepare a mechanical system in a quantum state, its thermal occupation should be low. Section 2.3 discusses the different cooling mechanisms that are used to cool the resonator below its environmental temperature. The position sensitivity of a linear detector is discussed in Section 2.4.

TABLE 2.1: Overview of recent experiments with micro- and nanomechanical resonators. Several types of resonators and detection methods are used by different groups in the field. The table shows the resonance frequency f_R, quality factor Q and the mass m of the resonator. From this, the zero-point motion u_0 is estimated. With the sensitivity $S^{1/2}_{u_n u_n}$, the resolution Δu_n is calculated. The experiments are done at a temperature T and in some of the experiments the resonator is cooled to a temperature T_R well below the environmental temperature. Also the final number of quanta n and the cooling factor T/T_R are indicated.

	Group	**Authors**	**Year**	**Resonator**	**Detector**
1	UCSB	Knobel & Cleland	2003	GaAs beam	SET
2	CalTech	Huang & Roukes	2003	Si beam	Magn. mot.
3	Schwab	LaHaye & Schwab	2004	SiN/Au beam	SET
4	LMU	Metzger & Karrai	2004	Si/Au cantilever	Optical
5	LKB Paris	Arcizet & Rousseau	2006	Si micromirror	Optical
6	Schwab	Naik & Schwab	2006	SiN/Al beam	SET
7	MPI-QO	Schliesser & Kippenberg	2006	Silica toroid	Optical
8	Vienna	Gigan & Zeilinger	2006	SiO_2/TiO_2 beam	Optical
9	LKB Paris	Arcizet & Heidmann	2006	Si micromirror	Optical
10	UCSB	Kleckner & Bouwmeester	2006	AFM cantilever	Optical
11	IBM	Poggio & Rugar	2007	Si cantilever	Optical
12	LMU	Favero & Karrai	2007	Si micromirror	Optical
13	NIST	Brown & Wineland	2007	Si cantilever	Capacitive
14	JILA	Flowers-Jacobs & Lehnert	2007	Gold beam	APC
15	CalTech	Li & Roukes	2007	SiC/Au cantilever	Piezoresist.
16	LKB Paris	Caniard & Heidmann	2007	micromirrors	Optical
17	LIGO	Corbitt & Mavalvala	2007	micromirror	Optical
18	Harris	Thompson & Harris	2008	SiN membrane	Optical
19	JILA	Regal & Lehnert	2008	Al beam	Stripline
20	Delft	Etaki, Poot & van der Zant	2008	AlGaSb beam	SQUID
21	MPI-QO	Schliesser & Kippenberg	2008	Silica toroid	Optical
22	Vienna	Groeblacher & Aspelmeyer	2008	Si cantilever	Optical
23	CalTech	Feng & Roukes	2008	SiC/Au beam	Optical
24	IBM	Poggio & Rugar	2008	Si cantilever	QPC
25	AURIGA	Vivante & Zendri	2008	Al bar	Capacitive
26	AURIGA	Vivante & Zendri	2008	Al bar	Capacitive
27	JILA	Teufel & Lehnert	2008	Al beam	Stripline
28	JILA	Teufel & Lehnert	2008	Al beam	Stripline
29	Alberta	Liu & Freeman	2008	Si cantilever	Optical
30	Vienna	Groeblacher & Aspelmeyer	2009	Si cantilever	Optical
31	MPI-QO	Schliesser & Kippenberg	2009	Silica toroid	Optical
32	MPI-QO	Anetsberger & Kippenberg	2009	SiN beam	Optical
33	JILA	Teufel & Lehnert	2009	Al beam	Stripline
34	Schwab	Rocheleau & Schwab	2009	SiN/Al beam	Stripline
35	Oregon	Park & Wang	2009	Silica sphere	Optical
36	LMU	Unterreithmeier & Kotthaus	2009	SiN beam	Optical
37	LMU	Unterreithmeier & Kotthaus	2009	SiN beam	Capacitive
38	Tang	Li & Tang	2009	Si cantilever	Optical
39	Painter	Eichenfeld & Painter	2009	Si ph. crystal	Optical
40	LIGO	LIGO Scientific	2009	Susp. mirror	Optical

Table continues on the next page.

TABLE 2.1: continued from the previous page.

	$\mathbf{f_R}$ (MHz)	**Q**	**m** (kg)	$\mathbf{u_0}$ (fm)	$\bar{\mathbf{S}}^{1/2}_{\mathbf{u_n u_n}}$ (fm/$\sqrt{\text{Hz}}$)	$\Delta\mathbf{u_n}$ (fm)	$\frac{\Delta \mathbf{u_n}}{\mathbf{u_0}}$
1	117.0	1700	$2.8 \cdot 10^{-15}$	5.05	2.0	658	130.21
2	$1.0 \cdot 10^{3}$	500	$3.4 \cdot 10^{-17}$	15.65			
3	19.7	35000	$9.7 \cdot 10^{-16}$	20.91	3.8	113	5.40
4	$7.3 \cdot 10^{-3}$	2000	$8.6 \cdot 10^{-12}$	11.54	$2.0 \cdot 10^{3}$	$4.8 \cdot 10^{3}$	
5	0.814	10000	$1.9 \cdot 10^{-7}$	$7.4 \cdot 10^{-3}$	$4.0 \cdot 10^{-4}$	$4.5 \cdot 10^{-3}$	0.62
6	21.9	120000	$6.8 \cdot 10^{-16}$	23.69	0.3	5.1	0.21
7	57.8	2890	$1.5 \cdot 10^{-11}$	0.10	$3.0 \cdot 10^{-3}$	0.53	5.42
8	0.278	9000	$9.0 \cdot 10^{-12}$	1.83			
9	0.8145	10000	$7.0 \cdot 10^{-11}$	0.38	$4.0 \cdot 10^{-4}$	$4.5 \cdot 10^{-3}$	0.011
10	$1.3 \cdot 10^{-3}$	137000	$2.4 \cdot 10^{-11}$	16.69	100.0	12	0.72
11	$3.8 \cdot 10^{-3}$	30000	$1.5 \cdot 10^{-13}$	121.07	1.0	0.45	0.0037
12	0.5466	1059	$1.1 \cdot 10^{-14}$	36.62	$1.0 \cdot 10^{3}$	$2.8 \cdot 10^{4}$	
13	$7.0 \cdot 10^{-3}$	20000	$1.0 \cdot 10^{-10}$	3.45			
14	43.1	5000	$2.3 \cdot 10^{-15}$	9.18	2.3	267	29.15
15	127.0	900	$5.0 \cdot 10^{-17}$	36.27	39.0	$1.8 \cdot 10^{4}$	
16	0.7105	16000	$6.4 \cdot 10^{-4}$	$1.4 \cdot 10^{-4}$	$2.7 \cdot 10^{-5}$	$2.3 \cdot 10^{-4}$	1.66
17	$1.7 \cdot 10^{-4}$	3200	$1.0 \cdot 10^{-3}$	$7.0 \cdot 10^{-3}$	0.2	0.058	8.34
18	0.134	1100000	$4.0 \cdot 10^{-11}$	1.25	0.54	0.24	0.19
19	0.237	2300	$2.0 \cdot 10^{-15}$	132.77	200.0	$2.5 \cdot 10^{3}$	19.16
20	2.0016	18000	$6.1 \cdot 10^{-13}$	2.62	10.0	132	50.52
21	74.0	57000	$1.0 \cdot 10^{-11}$	0.11	$1.0 \cdot 10^{-3}$	0.045	0.42
22	0.557	2000	$1.9 \cdot 10^{-10}$	0.28			
23	428.2	2500	$5.1 \cdot 10^{-17}$	19.56	1.64	851	43.49
24	$5.0 \cdot 10^{-3}$	2500	$2.0 \cdot 10^{-12}$	29.05	$1.0 \cdot 10^{3}$	$1.8 \cdot 10^{3}$	60.70
25	$8.7 \cdot 10^{-4}$	1200000	$1.1 \cdot 10^{3}$	$3.0 \cdot 10^{-6}$	$3.0 \cdot 10^{-5}$	$1.0 \cdot 10^{-6}$	0.34
26	$9.1 \cdot 10^{-4}$	880000	$1.1 \cdot 10^{3}$	$2.9 \cdot 10^{-6}$	$3.0 \cdot 10^{-5}$	$1.2 \cdot 10^{-6}$	0.42
27	1.525	300000	$6.2 \cdot 10^{-15}$	29.73	600.0	$1.7 \cdot 10^{3}$	57.03
28	1.525	10000	$6.2 \cdot 10^{-15}$	29.73	45.0	696	23.43
29	$1.0 \cdot 10^{3}$	18	$2.0 \cdot 10^{-17}$	20.04	$1.0 \cdot 10^{3}$	$9.5 \cdot 10^{6}$	
30	0.945	30000	$4.3 \cdot 10^{-11}$	0.45	$9.5 \cdot 10^{-3}$	0.067	0.15
31	65.0	2000	$7.0 \cdot 10^{-11}$	0.04	$1.5 \cdot 10^{-3}$	0.34	7.91
32	8.07	10000	$4.9 \cdot 10^{-15}$	14.54	0.64	23	1.57
33	1.04	160000	$1.1 \cdot 10^{-14}$	27.03	4.8	15	0.57
34	6.3	1000000	$2.1 \cdot 10^{-15}$	25.19	1.15	3.6	0.14
35	118.6	3400	$2.8 \cdot 10^{-11}$	0.05	0.26	61	
36	8.9	150000	$1.8 \cdot 10^{-15}$	22.84	700.0	$6.8 \cdot 10^{3}$	
37	8.9	150000	$1.8 \cdot 10^{-15}$	22.84	$2.0 \cdot 10^{4}$	$1.9 \cdot 10^{5}$	
38	13.86	4500	$4.5 \cdot 10^{-16}$	36.60	40.0	$2.8 \cdot 10^{3}$	76.01
39	8.2	150	$4.3 \cdot 10^{-14}$	4.87	0.04	12	2.41
40	$1.2 \cdot 10^{-4}$		$2.7 \cdot 10^{0}$	$1.6 \cdot 10^{-4}$	$1.0 \cdot 10^{-3}$		

Table continues on the next page.

TABLE 2.1: continued from the previous page.

	$\mathbf{f_R}$ (MHz)	**T** (K)	$\mathbf{T_R^{min}}$ (K)	$\bar{\mathbf{n}}$	**Cooling method**	**Factor**	**Ref.**
1	117.0	0.03	0.03	5.8			[7]
2	$1.0 \cdot 10^3$	4.2	4.2	95.2			[8]
3	19.7	0.035	0.056	64.6			[9]
4	$7.3 \cdot 10^{-3}$	295	18	$5.6 \cdot 10^7$	Photothermal	16.4	[10]
5	0.814	295	5	$1.4 \cdot 10^5$	Feedback	59.0	[11]
6	21.9	0.03	0.035	36.3	Backaction		[12]
7	57.8	300	11	4326.7	Sideband	27.3	[13]
8	0.278	295	10	$8.2 \cdot 10^5$	Sideband	29.5	[14]
9	0.8145	295	10	$2.8 \cdot 10^5$	Sideband	29.5	[15]
10	$1.3 \cdot 10^{-3}$	295	0.135	$2.5 \cdot 10^6$	Feedback	2185.2	[16]
11	$3.8 \cdot 10^{-3}$	2.2	0.0029	$1.7 \cdot 10^4$	Feedback	758.6	[17]
12	0.5466	300	175	$7.3 \cdot 10^6$	Photothermal	1.7	[18]
13	$7.0 \cdot 10^{-3}$	295	45	$1.5 \cdot 10^8$	Sideband	6.6	[19]
14	43.1	0.25	1	527.5			[20]
15	127.0	295	295	$5.3 \cdot 10^4$			[21]
16	0.7105	295	295	$9.4 \cdot 10^6$			[22]
17	$1.7 \cdot 10^{-4}$	295	0.8	$1.1 \cdot 10^8$	Sideband	368.8	[23]
18	0.134	294	0.0068	1153.7	Sideband	$4.32 \cdot 10^4$	[24]
19	0.237	0.04	0.017	1630.8	Sideband	2.4	[25]
20	2.0016	0.02	0.084	954.1			[26]
21	74.0	295	19.2	5900	Sideband	15.4	[27]
22	0.557	35	0.29	$1.2 \cdot 10^4$	Sideband	120.7	[28]
23	428.2	22	22	1168.1			[29]
24	$5.0 \cdot 10^{-3}$	4.2	4.2	$1.9 \cdot 10^7$			[30]
25	$8.7 \cdot 10^{-4}$	4.2	0.002	$5.3 \cdot 10^4$	Feedback	2100.0	[31]
26	$9.1 \cdot 10^{-4}$	4.2	$1.7 \cdot 10^{-4}$	4228.6	Feedback	$2.47 \cdot 10^4$	[31]
27	1.525	0.05	0.05	745.4			[32]
28	1.525	0.05	0.01	149.1	Sideband	5.0	[32]
29	$1.0 \cdot 10^3$	295	295	6448.8			[33]
30	0.945	5.3	0.0013	31.3	Sideband	4076.9	[34]
31	65.0	1.65	0.2	70	Sideband	8.3	[35]
32	8.07	300	300	$8.5 \cdot 10^5$			[36]
33	1.04	0.015	0.13	2841.8	Sideband		[37]
34	6.3	0.02	0.0011	3.8	Sideband	19.0	[38]
35	118.6	1.4	0.21	40.3	Sideband	6.7	[39]
36	8.9	295	295	$7.5 \cdot 10^5$			[40]
37	8.9	295	295	$7.5 \cdot 10^5$			[40]
38	13.86	295	295	$4.8 \cdot 10^5$			[41]
39	8.2	360	7.3	$2.0 \cdot 10^4$	Sideband	49.0	[42]
40	$1.2 \cdot 10^{-4}$	300	$1.4 \cdot 10^{-6}$	258.8	Feedback	$2.14 \cdot 10^8$	[43]

2.1 THE HARMONIC OSCILLATOR

The harmonic oscillator is probably the most extensively studied system in physics. Nearly everything that returns to its equilibrium position after being displaced, can be described by a harmonic oscillator. Examples range from the suspension of a car, traffic-induced vibrations of a bridge, and the voltage in an electrical LC network, to light in an optical cavity.

At first sight, the description of static and dynamic nanomechanical systems appears to be more complicated than that of a harmonic oscillator. However, when the displacement is small, the system has well-defined normal modes. Every deflection of the NEMS can be expanded in terms of these normal modes and the dynamics of the system is described by a set of uncoupled harmonic oscillators, as Chapter 3 will show. In most of the forthcoming Chapters, only one particular mode of the resonator is studied and its displacement is described by the position of a single harmonic oscillator. In this case, we make no distinction between the resonator (i.e. the entire nanomechanical system) and the mode that is studied.

THE CLASSICAL HARMONIC OSCILLATOR

In a harmonic oscillator, the potential energy depends quadratically on the displacement u from the equilibrium position:

$$V(u) = \frac{1}{2}k_R u^2, \tag{2.1}$$

where k_R is the spring constant. The parabolic shape of the potential results in a force that is proportional to the displacement. When damping and a driving force $F(t)$ are included, the equation of motion reads:

$$m\ddot{u} = -k_R u - m\gamma_R \dot{u} + F(t), \tag{2.2}$$

for a resonator with mass m and bandwidth γ_R. When the oscillator is displaced and released, it will oscillate at frequency ω_R with a slowly decreasing amplitude due to the damping. The quality factor $Q = \omega_R/\gamma_R$ indicates how many times the resonator moves back and forth before its energy has decreased by a factor e.

The harmonic oscillator responds linearly to an applied force; in other words, it is a linear system. Any linear system is characterized by its impulse response or Green's function [44]. For the harmonic oscillator, the impulse response $h_{HO}(t)$, is the solution to Eq. 2.2 with $F(t) = k_R\delta(t)$:

$$h_{HO}(t) = \sin(\omega_R t)e^{-\frac{\omega_R t}{2Q}}\Theta(t), \tag{2.3}$$

where $\delta(t)$ is the Dirac delta function and $\Theta(t)$ is the Heaviside stepfunction. The impulse response function[1] describes how the resonator reacts to a kick at time $t = 0$ and

[1]This is the Green's function for a high-Q resonator. For lower Q-values, the resonator oscillates at a slightly

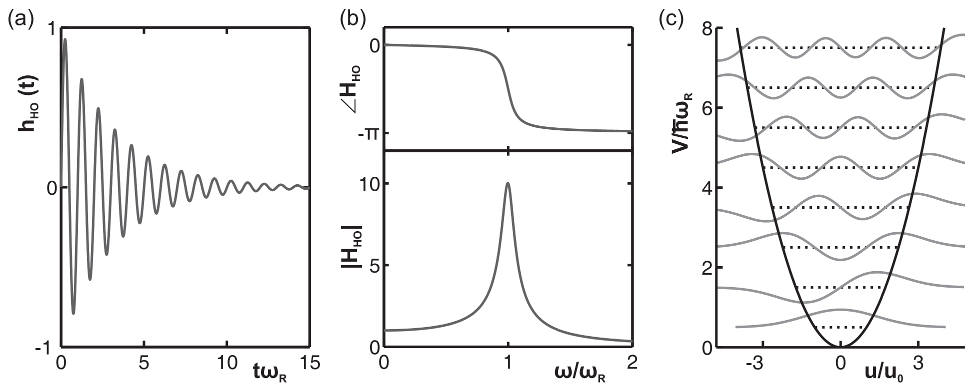

FIGURE 2.1: (a) The Green's function $h_{HO}(t)$ and (b) frequency response $H_{HO}(\omega)$ of a harmonic oscillator with $Q = 10$. (c) Eigenenergies E_n (dashed) and the corresponding wave functions $\psi_n(u)$ (solid) of the harmonic oscillator for $n = 0..7$.

is plotted in Fig. 2.1a. The time-evolution of the displacement for a force with arbitrary time-dependence $F(t)$ can be calculated directly from the impulse-response function:

$$u(t) = h_{HO}(t) \otimes F(t)/k_R. \tag{2.4}$$

In many experiments the oscillator is driven with a periodic force $F(t) = F_0 \cos(\omega t)$. After a short transient, the displacement oscillates in time with the same frequency as the driving force, but it can have a different phase. This is quantified by the transfer function $H_{HO}(\omega)$ that is obtained by taking the Fourier transformation[2] of the equation of motion, Eq. 2.2:

$$H_{HO}(\omega) = k_R \frac{u(\omega)}{F(\omega)} = \frac{\omega_R^2}{\omega_R^2 - \omega^2 + i\omega\omega_R/Q}. \tag{2.5}$$

The magnitude $|H_{HO}(\omega)|$ and phase $\angle H_{HO}(\omega)$ are plotted in Fig. 2.1b. When the driving frequency is far from the resonance frequency, the oscillator hardly moves and both $|H_{HO}|$ and $\angle H_{HO}$ are small. The amplitude grows when sweeping the frequency towards the natural frequency. Exactly on resonance, the amplitude has its maximum $|H_{HO}| = Q$. The phase response shows that at the resonance frequency, the displacement lags the driving

lower frequency $\omega_R' = \omega_R\sqrt{1-(1/2Q)^2}$ and the impulse response of an underdamped oscillator (i.e. one that has $Q > 1/2$) is: $h_{HO}(t) = \sin(\omega_R' t)\exp(-\omega_R t/2Q) \cdot [1-(2Q)^{-2}]^{-1/2}\Theta(t)$. An overdamped resonator returns to $u = 0$ without any oscillations and has a different impulse response. Throughout this Thesis it is assumed that $Q \gg 1$ so that $\omega_R' \approx \omega_R$ and h_{HO} is given by Eq. 2.3. Note, that Eq. 2.5 is valid for all (positive) values of Q.

[2] By convention [44], the Fourier transformation is defined as: $X(\omega) = \mathscr{F}[x(t)] = \int_{-\infty}^{+\infty} x(t)\exp(-i\omega t)\,\mathrm{d}t$ so that the inverse transformation is given by: $x(t) = \mathscr{F}^{-1}[X(\omega)] = \frac{1}{2\pi}\int_{-\infty}^{+\infty} X(\omega)\exp(+i\omega t)\,\mathrm{d}\omega$.

force by $-\pi/2$. When further increasing the driving frequency, the oscillator can no longer follow the driving force: the amplitude drops and the lag approaches $-\pi$. The motion is then 180^{o} out-of-phase with the applied force.

THE HARMONIC OSCILLATOR IN QUANTUM MECHANICS

In quantum mechanics the harmonic oscillator is described by the Hamiltonian $\hat{H} = \hat{p}^2/2m + \frac{1}{2}m\omega_R^2\hat{u}^2$ [4], as the classical displacement coordinate u and momentum $p = m\dot{u}$ have to be replaced by the *operators* $\hat{u}$ and $\hat{p} = -i\hbar\cdot\partial/\partial u$. The displacement is described by a wavefunction $\psi(u)$ that satisfies the time-independent Schrödinger equation:

$$\hat{H}\psi = -\frac{\hbar^2}{2m}\frac{\partial^2\psi}{\partial u^2} + \frac{1}{2}m\omega_R^2\hat{u}^2\psi = E\psi. \tag{2.6}$$

This equation is solved by introducing the creation and annihilation operators: $\hat{a}^\dagger = \sqrt{\frac{m}{2\hbar\omega_R}}\left(\omega_R\hat{u} - i\hat{p}\right)$ and $\hat{a} = \sqrt{\frac{m}{2\hbar\omega_R}}\left(\omega_R\hat{u} + i\hat{p}\right)$ respectively. The Hamiltonian then becomes $\hat{H} = \hbar\omega_R(\hat{n} + \frac{1}{2})$, where $\hat{n} = \hat{a}^\dagger\hat{a}$ is the number operator that counts the number of phonons in the oscillator. The eigenenergies are $E_n = \hbar\omega_R(n + \frac{1}{2})$, with eigenstates $|n\rangle$. The corresponding wave functions $\psi_n(u)$ are plotted in Fig. 2.1c. The lowest $(n = 0)$ eigenstate has a non-zero energy $E_0 = \frac{1}{2}\hbar\omega_R$, the so-called zero-point energy. Even when the oscillator relaxes completely, it still moves around the potential minimum at $u = 0$. The probability density of finding the resonator at position u, is given by $|\psi_0(u)|^2$ when the resonator is in the ground state. The zero-point motion u_0 is the standard deviation of this probability density:

$$u_0 \equiv \left(\int_{\infty}^{\infty} u^2|\psi_0(u)|^2\,\mathrm{d}u\right)^{1/2} = \langle 0|\,\hat{u}^2\,|0\rangle^{1/2} = \sqrt{\frac{\hbar}{2m\omega_R}}. \tag{2.7}$$

The zero-point motion is an important length scale that determines the effective resonator temperature and the quantum limit on continuous linear position measurement as the following Sections will show.

2.2 THERMAL AND QUANTUM NOISE

In the previous Section it was shown that a resonator always moves because it contains at least the zero-point energy. In practise, except at the lowest temperatures, the zero-point motion is overwhelmed by thermal noise. Thermal noise is generated by the environment of the resonator. As an example, consider a resonator in air. At room temperature, the air molecules have an average velocity of about 500 m/s. The molecules randomly hit the resonator and every collision gives the resonator a kick. These kicks occur independently of each other, so the resonator experiences a stochastic force $F_n(t)$ that is white and that has a Gaussian distribution. Other thermal noise sources are phonons in the substrate that couple to the resonator via the clamping points, fluctuating amounts of charge on

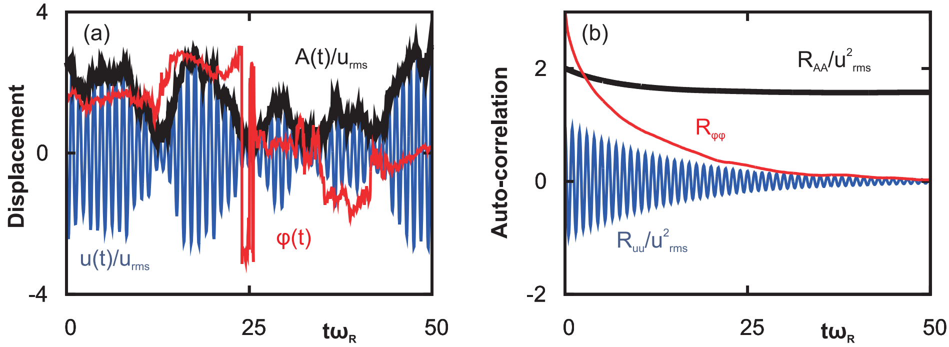

FIGURE 2.2: (a) Simulated time-trace of the displacement (blue), amplitude (black) and phase (red) of a resonator that is driven by Gaussian white noise for $Q = 50$. The phase φ is in radians and both the displacement u and amplitude A are normalized by the root-mean-square displacement u_{rms}. The corresponding autocorrelation functions are shown in (b).

nearby impurities and so on. The force noise can be described by an autocorrelation function $R_{F_nF_n}(t) = \mathbb{E}[F_n(t')F_n(t'+t)]$ or by its power spectral density[3] (PSD) $\overline{S}_{F_nF_n}(\omega)$ [45]. For white noise, the latter is independent of frequency and $F_n(t)$ has an infinite variance. For a given $F_n(t)$ the realized displacement is easily found using the Green's function, i.e. with Eq. 2.4. Figure 2.2a shows a simulated time-trace of this so-called Brownian motion. The resonator oscillates back and forth with frequency ω_R and its phase and amplitude vary on a much longer timescale. The displacement can be written as $u(t) = A(t)\cos[\omega_R t + \varphi(t)]$ (see Supplement) and the time-traces of the amplitude A and phase φ are plotted in Fig. 2.2a as well. Figure 2.2b shows the calculated autocorrelation functions of the displacement, amplitude and phase. The displacement autocorrelation $R_{uu}(t)$ displays oscillations with period $2\pi/\omega_R$, whereas R_{AA} and $R_{\varphi\varphi}$ do not contain these rapid oscillations. All three functions fall off at timescales $\sim Q/\omega_R$. Note, that $R_{AA}(t)$ does not go to zero for long times as $A(t)$ is always positive and is therefore always correlated with the current amplitude.

The displacement PSD is proportional to the force noise PSD, which is given by [45]:

$$\overline{S}_{uu}(\omega) = k_R^{-2}|H_{HO}(\omega)|^2\overline{S}_{F_nF_n}. \tag{2.8}$$

This can be used to find the variance of the displacement. When $\overline{S}_{F_nF_n}$ is white in the

[3] In this Thesis, the engineering convention for the single-sided power spectral density, $\overline{S}_{XX}(\omega) = S_{XX}(\omega) + S_{XX}(-\omega)$, is used. Here, $S_{XX}(\omega) = \mathscr{F}[R_{XX}]$ is the double-sided PSD and R_{XX} is its autocorrelation function. The variance of X is given by $\langle X^2\rangle = R_{XX}(0) = (2\pi)^{-1}\cdot\int_{-\infty}^{\infty} S_{XX}(\omega)\,\mathrm{d}\omega = (2\pi)^{-1}\cdot\int_0^{\infty}\overline{S}_{XX}(\omega)\,\mathrm{d}\omega$.

bandwidth of the resonator, which is typically assumed, this gives:

$$\langle u^2 \rangle = \frac{1}{2\pi}\int_0^\infty \overline{S}_{uu}(\omega)\,\mathrm{d}\omega = \frac{\pi}{2}\frac{Q\omega_R}{k_R^2}\overline{S}_{F_nF_n}. \tag{2.9}$$

The force noise PSD is related to the temperature and in equilibrium, the resonator temperature equals the environmental temperature. The equipartition theorem [46] relates the variance of the displacement to the equilibrium temperature:

$$\frac{1}{2}k_R\langle u^2\rangle = \frac{1}{2}m\langle \dot{u}^2\rangle = \frac{1}{2}k_\mathrm{B}T. \tag{2.10}$$

The thermal energy $k_\mathrm{B}T$ is shared equally between the potential energy and the kinetic energy. By combining Eqs. 2.9 and 2.10, a relation between the force noise PSD and the properties of the resonator is found:

$$\overline{S}_{F_nF_n}(\omega) = 4k_\mathrm{B}Tm\omega_R/Q. \tag{2.11}$$

This so-called fluctuation-dissipation theorem shows that on one hand the force noise PSD can directly be obtained from the resonator properties and temperature, without knowing its microscopic origin. And, on the other hand, that the force noise determines the dissipation (i.e. quality factor) of the resonator.

In equilibrium, the temperature of the resonator is proportional to the variance of its Brownian motion as indicated by Eq. 2.10. However, out of equilibrium the force noise is no longer given by Eq. 2.11, and the resonator temperature can be different from T. The effective resonator temperature T_R is defined as:

$$T_R \equiv \frac{k_R\langle u^2\rangle}{k_\mathrm{B}} = \frac{k_R}{2\pi k_\mathrm{B}}\int_0^\infty \overline{S}_{uu}(\omega)\,\mathrm{d}\omega = \frac{k_R}{2\pi k_\mathrm{B}}\int_0^\infty |H_R|^2\overline{S}_{FF}(\omega)\,\mathrm{d}\omega, \tag{2.12}$$

which yields $T_R = T$ in equilibrium. When the force noise is larger than that of Eq. 2.11, the effective resonator temperature is higher than the environmental temperature. When $\langle u^2\rangle$ is smaller than its equilibrium value, $T_R < T$.

When the resonator is cooled to very low temperatures where $k_\mathrm{B}T \sim \hbar\omega_R$, the classical description breaks down as the quantized energy-level structure (Fig. 2.1c) becomes important. Semi-classically, the thermal and quantum effects are combined when the the force noise of Eq. 2.11 is replaced by the Callen and Welton equation [47]:

$$\overline{S}_{F_nF_n}(\omega) = \frac{4m\omega}{Q}\cdot\frac{1}{2}\hbar\omega\coth\left(\frac{\hbar\omega}{2k_\mathrm{B}T}\right), \tag{2.13}$$

so that for $Q \gg 1$:

$$\langle u^2\rangle = u_0^2\cdot\coth\left(\frac{\hbar\omega_R}{2k_\mathrm{B}T}\right) \quad\Leftrightarrow\quad T = \frac{\hbar\omega_R/2}{k_\mathrm{B}}\ln^{-1}\left(\frac{\langle u^2\rangle + u_0^2}{\langle u^2\rangle - u_0^2}\right)^{1/2}. \tag{2.14}$$

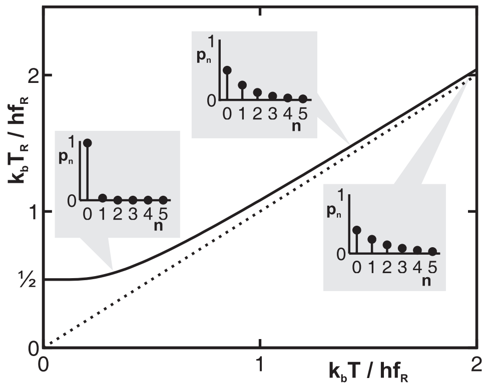

FIGURE 2.3: The resonator temperature T_R plotted against the environmental temperature T. At low temperatures the resonator temperature saturates at the zero-point energy: $T_R = \frac{1}{2}\hbar\omega_R/k_\mathrm{B}$ and at high temperatures $T_R = T$ (dashed line). The insets show the occupation probability P_n of the energy levels at $k_\mathrm{B}T/\hbar\omega_R =$ 0.3, $1/\ln 2 \approx 1.44$ and 2.0.

This yields $T_R = T$ for high temperatures ($k_\mathrm{B}T \gg \hbar\omega_R$) and $T_R = \frac{1}{2}\hbar\omega_R/k_\mathrm{B}$ at zero temperature. Note, that sometimes Eq. 2.14 is used as the definition of T_R instead of Eq. 2.12.

In thermal equilibrium, the energy levels of a harmonic oscillator have occupation probabilities that are given by:

$$P_n = \left(e^{-\frac{\hbar\omega_R}{k_\mathrm{B}T}}\right)^n \left(1 - e^{-\frac{\hbar\omega_R}{k_\mathrm{B}T}}\right). \tag{2.15}$$

The average thermal occupation is $\overline{n} = \sum_{n=0}^{\infty} nP_n = [\exp(\hbar\omega_R/k_\mathrm{B}T)-1]^{-1}$ [46], which equals $k_\mathrm{B}T_R/\hbar\omega_R - \frac{1}{2}$. Figure 2.3 shows the resonator temperature and the occupation probabilities for different temperatures T. For $k_\mathrm{B}T = \ln(2)\hbar\omega_R$ the resonator is in the ground state exactly half of the time. At any non-zero temperature, there is always a finite probability to find the resonator in an excited state. With the statement that "the resonator is cooled to its ground state" one actually means $\overline{n} \lesssim 1$.

2.3 COOLING

To prepare a nanomechanical system in the ground state, the thermal occupation of its normal modes should be minimal. The most direct approach is to mount an ultra-high frequency ($f_R > 1\,\mathrm{GHz}$) resonator in a dilution refrigerator ($T < 50\,\mathrm{mK}$) so that $\overline{n} = [\exp(hf_R/k_\mathrm{B}T) - 1]^{-1} \leq 1$. Such a resonator will, however, have a very small zero-point motion and the readout of tiny high-frequency signals at millikelvin temperatures is difficult. An alternative approach is to do the experiments with lower-frequency resonators and/or at higher temperatures. The thermal occupation is then higher than one and cooling techniques such as active feedback cooling or sideband cooling have to be used to

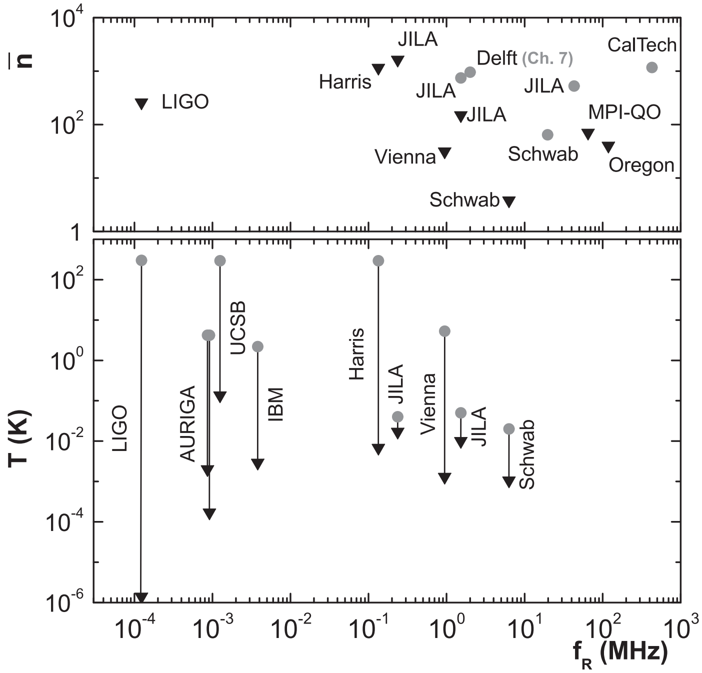

FIGURE 2.4: Overview of mechanical resonators with low temperature or occupation, compiled from Table 2.1. The top panel shows the experiments with the lowest occupation numbers. These are reached using conventional cooling (gray) and active feedback and sideband cooling (black). The bottom axis is located at $\bar{n} = 1$. When the thermal occupation is below this value, the resonator is cooled to the ground state. The bottom panel shows the starting temperature T (gray) and the final temperature T_R^{min} (black) achieved by groups that have actively cooled their resonator below 100 mK.

reduce the temperature of the resonator T_R well below the environmental temperature T. Figure 2.4 shows how recent experiments (Table 2.1) are approaching the limit $n \leq 1$ over a range of frequencies that spans seven orders of magnitude.

ACTIVE FEEDBACK COOLING

When the position of the resonator is measured and fed back to the resonator, the Brownian motion of the resonator can be amplified or suppressed. In the latter case, the resonator is cooled. Actually, the lowest resonator temperature, $T_R = 1.4\,\mu$K, has been obtained using this method (see Table 2.1) [43]. Figure 2.5a shows a schematic of the process. The resonator, with frequency $\omega_0/2\pi$ and Q-factor Q_0, is driven by the thermal force noise $F_n(t)$ and its displacement $u(t)$ is measured. The detector adds noise to the signal, the so-called imprecision noise $u_n(t)$. The apparent position is thus the sum of the physical displacement and the detector noise: $v = u + u_n$. The information contained in v is used

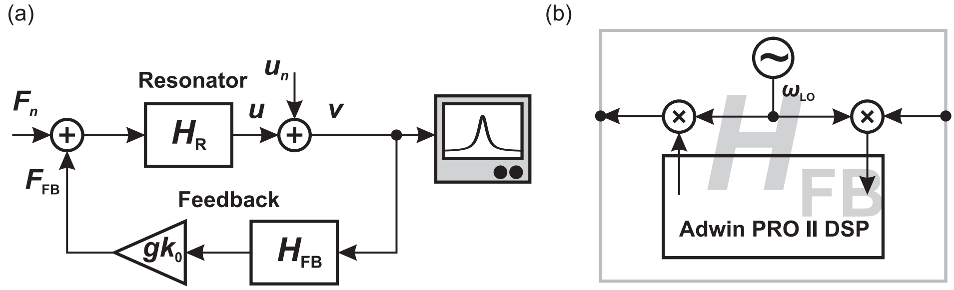

FIGURE 2.5: (a) In the active feedback cooling scheme the resonator displacement u is measured. The detector adds imprecision noise u_n and sum of this noise and the physical displacement is measured using a spectrum analyzer. This signal is also fed back to the resonator to attenuate the Brownian motion. In the feedback loop a filter with response H_{FB} and a variable gain $g \cdot k_0$ are included. The resulting feedback force F_{FB} adds up with the thermal force noise F_n. The resonator's response to the applied forces is determined by its transfer function $H_R = H_{HO}/k_0$. (b) Our implementation of the feedback uses mixing with a frequency ω_{LO} and a fast, programmable digital signal processer (DSP).

to apply a force F_{FB} that damps the resonator motion[4]. The relation between the feedback force and the apparent position is described by the linear system[5] or filter H_{FB}. The output of the filter is multiplied by a selectable gain[6] g and converted to a force using the spring constant k_0. This forms a closed-loop system [44, 50] with the following equations of motion:

$$m\ddot{u}(t) + m\omega_0\dot{u}(t)/Q_0 + m\omega_0^2 u(t) = F_n(t) + F_{FB}(t), \tag{2.16}$$

$$F_{FB}(t) = m\omega_0^2 g \cdot h_{FB}(t) \otimes [u(t) + u_n(t)]. \tag{2.17}$$

The feedback changes the resonator response from H_R to the closed-loop transfer function H'_R, given by:

$$H_R'^{-1} = H_R^{-1} - gk_0 H_{FB}, \quad \text{or} \quad H'_R = \frac{k_0^{-1}}{1 - \left(\frac{\omega}{\omega_0}\right)^2 + \frac{i}{Q_0}\frac{\omega}{\omega_0} - gH_{FB}}. \tag{2.18}$$

[4] In principle, also the backaction force noise of the detector (see the next Section) has to be included [31, 48]. This term was, however, so far never important in the active feedback cooling experiments [16, 17, 31, 43, 49].
[5] For a phase-insensitive feedback, the feedback system must be linear and time-invariant. On the other hand, to obtain a phase-sensitive state (for example a squeezed state), the system cannot be time-invariant.
[6] The gain g and filter H_{FB} are defined such that $|H_{FB}(\omega_0)| = 1$.

Using this result, the PSDs of the physical and observed displacement are obtained:

$$\overline{S}_{uu}(\omega) = \frac{\overline{S}_{F_nF_n}/(m\omega_0^2)^2 + g^2|H_{FB}|^2\overline{S}_{u_nu_n}}{\left|1-\left(\frac{\omega}{\omega_0}\right)^2+\frac{i}{Q_0}\frac{\omega}{\omega_0}-gH_{FB}(\omega)\right|^2}, \tag{2.19}$$

$$\overline{S}_{vv}(\omega) = \frac{\overline{S}_{F_nF_n}/(m\omega_0^2)^2 + \left|1-\left(\frac{\omega}{\omega_0}\right)^2+\frac{i}{Q_0}\frac{\omega}{\omega_0}\right|^2\overline{S}_{u_nu_n}}{\left|1-\left(\frac{\omega}{\omega_0}\right)^2+\frac{i}{Q_0}\frac{\omega}{\omega_0}-gH_{FB}(\omega)\right|^2}. \tag{2.20}$$

The resonator displacement PSD $\overline{S}_{uu}$ shows that the resonator indeed responds to the force noise with H_R' instead of H_R. The force noise still contains the original contribution $S_{F_nF_n}$, but now it also has a contribution due to the imprecision noise that is fed back to the resonator. The apparent position PSD is not simply the sum of $\overline{S}_{uu}$ and $\overline{S}_{u_nu_n}$ because the feedback creates correlations between the imprecision noise $u_n(t)$ and the actual resonator position $u(t)$.

Different implementations of the feedback filter H_{FB} are possible, each with their advantages and drawbacks. In any case, the real part of H_{FB} changes the resonance frequency, whereas the imaginary part changes the damping. The PSDs of the true and apparent resonator displacement are plotted in Fig. 2.6 for two feedback schemes that are widely used:

- Velocity-proportional feedback with $h_{FB}(t) = -\omega_0^{-1}\cdot\partial/\partial t,\ H_{FB} = -i\omega/\omega_0$. The transfer function is imaginary and the damping rate has been changed from ω_0/Q_0 to $\omega_0/Q_0\cdot(1+gQ_0)$. At low gains $\overline{S}_{uu}$ is lowered and the resonator is cooled. This is sketched in Fig. 2.6a. When the gain is increased further, the tails of $\overline{S}_{uu}$ start to rise as the detector noise is fed back into the resonator, but the total area under $\overline{S}_{uu}$, i.e. $\langle u^2\rangle$, still decreases. Above a certain value $g = g_{\min}$, too much detector noise is fed back to the resonator and the resonator temperature starts to increase. The minimum resonator temperature in the limit $g \gg Q_0^{-1}$ is [17]:

$$T_{R,\min} = \sqrt{\frac{m\omega_0^3 T}{k_B Q_0}\overline{S}_{u_nu_n}} = \frac{2T}{\sqrt{\mathrm{SNR}}},\ \text{where SNR} = \frac{\overline{S}_{uu}(\omega_0)_{g=0}}{\overline{S}_{u_nu_n}}. \tag{2.21}$$

  The lowest resonator temperature is thus limited by the signal-to-noise ratio (SNR) of the original thermal noise peak and the detector noise floor. The lowest T_R is obtained at $g_{\min} = \sqrt{\mathrm{SNR}}/Q_0$.

- Displacement-proportional feedback with $h_{FB}(t) = -\delta(t),\ H_{FB} = -1$. In this case, the transfer function is real, which changes the resonance frequency to $\omega_0\cdot(1+g)^{1/2}$. From Fig. 2.6b it is clear that for the parameters used ($Q_0 = 100, k_0^2\overline{S}_{u_nu_n}/\overline{S}_{F_nF_n} = 10^2$) only heating instead of cooling is achieved with proportional feedback. The

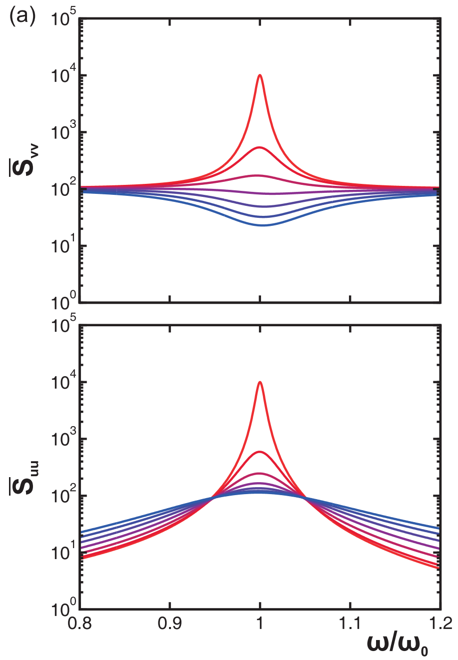

FIGURE 2.6: Feedback cooling of a resonator with $Q_0 = 100$ using velocity-proportional (a) and displacement-proportional (b) feedback. The top panels show the PSD of the observed displacement $\overline{S}_{vv}$ and the bottom panels show the physical displacement PSD, $\overline{S}_{uu}$. The gain is stepped from $g = 0$ (red) to $g = 0.2$ (blue). These plots are calculated with $\overline{S}_{u_n u_n} = 10^2$ and all PSDs are scaled by $\overline{S}_{F_n F_n}/(m\omega_0^2)^2$.

difference with velocity-proportional feedback is that the gain should be Q_0 times larger to cool the resonator by the same factor. This also feeds back much more detector noise to the resonator. In the language of the last part of this Section, the resonator is coupled to a hotter bath instead of to a colder one.

The resonator temperature as a function of gain is plotted in Fig. 2.7 for both cases. This shows that with a lower detector noise floor, proportional feedback can indeed cool the resonator, but that it is still less efficient than velocity-proportional feedback. Finally, note that the peak due to the Brownian motion in S_{vv} becomes distorted by the feedback as is clearly visible in the top panels of Fig. 2.6. S_{vv} can even become smaller than $\overline{S}_{u_n u_n}$ due to the abovementioned correlations between u_n and u.

So far, active feedback cooling experiments were done on resonators in the kHz range, where one can simply measure the position, differentiate and feed the resulting signal back to the resonator. However, when the frequencies are higher, delays in the feedback circuit start to play a role. The force is then applied when the resonator has al-

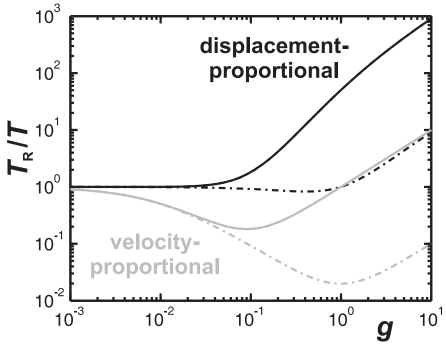

FIGURE 2.7: Resonator temperature for velocity-proportional (gray) or displacement-proportional (black) feedback vs feedback gain g for a resonator with $Q_0 = 100$. The solid lines are for $k_0^2\overline{S}_{u_n u_n}/\overline{S}_{F_n F_n} = 10^2$ and the dash-dotted lines for $k_0^2\overline{S}_{u_n u_n}/\overline{S}_{F_n F_n} = 1$. The original signal-to-noise ratios were 10^2 and 10^4 respectively.

ready advanced and a purely velocity-proportional feedback will have a displacement-proportional component, degrading the cooling performance. The effect of a delay is even more dramatic when it equals half the resonator period, so that the Brownian motion is actually amplified instead of attenuated. Furthermore, the bandwidth (or sampling speed in the case of a digital filter) of H_{FB} should be at least a few times ω_R, which makes its design challenging for $\omega_R \gtrsim 1\,\mathrm{MHz}$. Our approach, shown in Fig. 2.5b, is different: first we multiply (mix) the signal $v(t)$ with a local oscillator $\cos(\omega_{LO}t)$ to down-mix the high-frequency signal at $\omega = \omega_R$ to $\omega = \omega_R - \omega_{LO}$. Then the signal at the difference frequency is read in with a digital signal processor (DSP), which estimates the complex amplitude A_c of the displacement (see Supplement). This is done using the discrete-time version of $\hat{A}_c(t) \equiv \gamma_F \int_{-\infty}^{t} v(t')\exp(-i\omega_F t')\exp(-\gamma_F[t-t']/2)\,\mathrm{d}t'$, where ω_F is the filter frequency and γ_F is the filter width. The estimated complex displacement $\hat{A}_c$ is multiplied by $\exp(i\omega_F t)$ to generate the signal at ω_F and subsequently by $\exp(-i\theta)$ to phase-shift the response. Then the real part is negated, multiplied by the gain g and put out using a digital-to-analog converter[7]. Finally, the second mixer mixes the signal with the same local oscillator and up-converts the feedback signal from $\omega = \omega_R - \omega_{LO}$ back to[8] $\omega = \omega_R$.

We call this feedback filter the "Fourier filter" as it measures the components in the

[7]Note that the estimation $\hat{A}_c(t)$ is not time invariant, whereas the final output is. This is because the complex amplitude is again multiplied by $\exp(-i\omega_F t)$. See also footnote 5.

[8]This also generates a signal at $\omega = 2\omega_{LO} - \omega_R = \omega_R - 2\omega_F$ when $\omega_{LO} < \omega_R$, or at $\omega = \omega_R + 2\omega_F$ when $\omega_{LO} > \omega_R$. In other words, a copy of the Fourier transform of the signal is mirrored in ω_{LO}. When the resonator response vanishes at this mirrored frequency (i.e. when $|\omega_R - \omega_{LO}| \ll \gamma_R$), the presence of the mixers does not change the system's response. This is assumed throughout the rest of this Section.

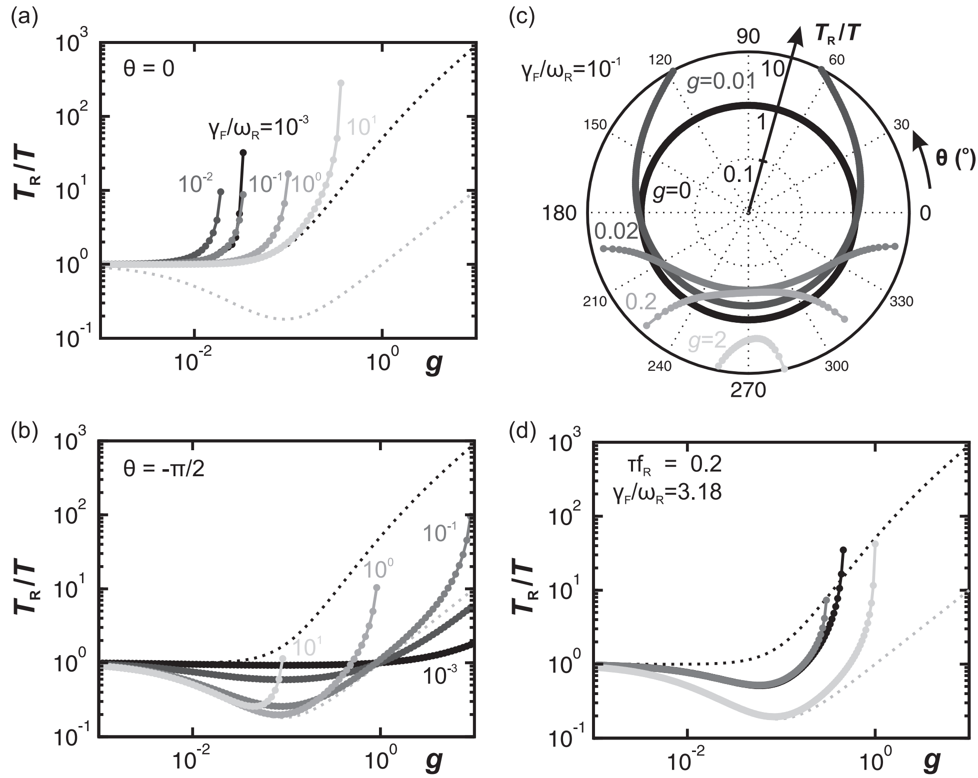

FIGURE 2.8: The calculated resonator temperature when using the Fourier filter. (a) and (b) show the dependence of T_R on the feedback gain for different values of the filter width γ_F for $\theta = 0$ (a) and $\theta = -\pi/2$ respectively. The dotted lines show the displacement- and velocity-proportional curves of Fig. 2.7 for comparison. (c) Polar plot of the resonator temperature (on the radial axis) when the phase θ is varied for $\gamma_F = 0.1 \cdot \omega_R$. (d) The effect of a delay τ on T_R for the velocity-proportional (black) and Fourier filter with (light gray) and without (dark gray) delay compensation for $\theta = -\pi/2$. For all simulations shown in this Figure, $Q_0 = 100$, $k_0^2 \overline{S}_{u_n u_n} / \overline{S}_{F_n F_n} = 10^2$ and $\omega_F = \omega_R$ have been used.

Fourier spectrum in a band γ_F around $\omega = \omega_F$. Its response function is given by:

$$h_{FB}(t) = -\gamma_F \cos\left((\omega_F + \omega_{LO})t - \theta\right) e^{-\gamma_F t/2} \Theta(t), \tag{2.22}$$

$$\begin{aligned} H_{FB}(\omega) &= -\gamma_F \cdot \frac{(\gamma_F/2 + i\omega)\cos\theta + (\omega_F + \omega_{LO})\sin\theta}{\left((\omega_F + \omega_{LO})^2 + (\gamma_F/2)^2\right) - \omega^2 + i\omega\gamma_F} \\ &\approx \gamma_F \frac{-i\omega\cos\theta - (\omega_F + \omega_{LO})\sin\theta}{(\omega_F + \omega_{LO})^2 - \omega^2 + i\omega\gamma_F} \text{ for } \gamma_F \ll \omega_F + \omega_{LO}. \end{aligned} \tag{2.23}$$

A closer look at the filter's frequency response shows that the denominator of H_{FB} is equal to that of a harmonic oscillator response. The numerator represents a displacement-proportional feedback for $\theta = 0$ and a velocity-proportional feedback for $\theta = -\pi/2$. The resonator temperature that is obtained using this filter is shown in Fig. 2.8a to c. For $\theta = 0$, the resonator temperature closely follows the curve for displacement-proportional feedback up to a point where the closed-loop system becomes unstable. The same is true for $\theta = -\pi/2$, which follows the velocity-proportional curve. The lowest resonator temperature in Fig. 2.8b is reached when the filter width $\gamma_F \approx 0.98\omega_F$. The phase dependence of T_R is shown in the polar plot of Fig. 2.8c. For $g = 0$, there no feedback and the datapoints lie on the unit circle $T_R = T$ (black). When the gain is increased (dark gray), the circle deforms and cooling is achieved for θ around $-\pi/2$ because the curve lies inside the unit circle where $T_R < T$. At the opposite side ($\theta \sim +\pi/2$), the resonator temperature diverges when $g \geq 1/Q_0$ and the θ-range where this happens increases with increasing gain (lighter shades of gray).

So far, the Fourier filter appears to be slightly less effective than velocity-proportional feedback, but this changes when delays are taken into account. A delay τ multiplies H_{FB} by a factor $\exp(-i\omega\tau)$, resulting in a frequency-dependent phase shift. Its overall effect can be cancelled by adding $-\omega_R\tau$ to θ, giving the filter the same real and imaginary components at $\omega = \omega_R$ as in the case of zero delay. Note, however, that the phase still changes with frequency. If it changes too much over the width of the resonance peak, then the cooling is affected. One thus needs $\omega_R/Q\tau \ll \pi$, which is equivalent to the statement that the delay should be much smaller than the phase-correlation time. The effect of a small delay on the resonator temperature is shown in Fig. 2.8d. All filters become unstable at at high gains where the resonator temperature diverges. The difference between the velocity-proportional and the Fourier filter without delay compensation is small. For both filters the minimum of the curves in Fig. 2.8d has shifted upwards, so the lowest achievable resonator temperature has degraded by the presence of the delay. However, when using the Fourier filter with delay compensation ($\theta \to \theta - \omega_R\tau$), the filter is stable for larger gains as shown in Fig. 2.8d and reaches approximately the same minimal temperature as the velocity-proportional filter did for $\tau = 0$. Further analysis and an experimental realization have to show how good this implementation of the feedback filter is.

SIDEBAND COOLING

Another commonly used cooling technique is sideband cooling [51–53]. In this technique the resonator is embedded in an optical [13–15, 23, 24, 27, 28, 34, 35, 39, 42] or microwave cavity [19, 25, 32, 38]. Figure 2.9a shows a schematic drawing of an optical cavity where the right mirror is the mechanical resonator. Both mirrors have a low transmission so that a photon is reflected many times before it can go out through the left mirror, and then to the detector. Such a cavity has many different eigenmodes, but here we focus on a single one with its resonance frequency denoted by ω_c. In analogy with the Q-factor and linewidth γ_R of a mechanical resonator, the cavity has a finesse $\mathscr{F}$ and linewidth κ. A laser sends light with frequency ω_d into the cavity. Because the resonance frequency of the

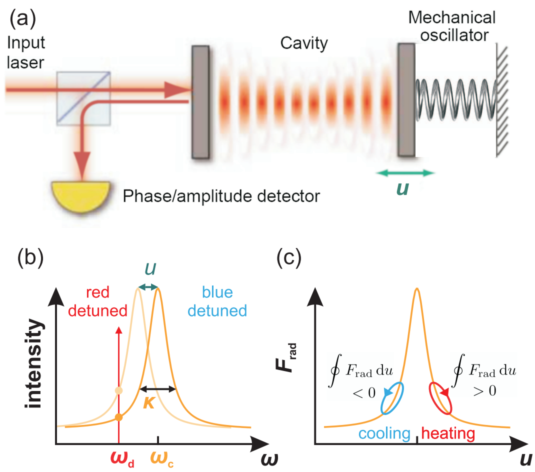

FIGURE 2.9: (a) schematic overview of an optical cavity. The cavity is driven via an input laser with frequency ω_d. The left mirror is fixed, but the right mirror is a mechanical resonator that can move. The resonator displacement u determines the length of the cavity and thus the cavity resonance frequency ω_c. A part of the circulating power is transmitted by the left mirror to a detector. The linewidth of the cavity is κ. Adapted from Ref. [51] (b) When the cavity is driven on its resonance, the intensity inside the cavity is largest, a detuning reduces the intensity. A displacement of the resonator shifts the cavity resonance (light orange) and changes the intensity of the light inside the cavity (orange and light orange dots). (c) The displacement dependence of the radiation pressure F_{rad}. When the resonator oscillates, the force reacts with a delay due to a finite value of κ as indicated by the ellipsoidal trajectories.

cavity, is determined by the cavity length, a displacement of the resonator changes ω_c. As illustrated in Fig. 2.9b this leads to a change in the intensity (and phase) of the light in the cavity, which results in a change in the detector output. Optical cavities used this way are very sensitive position detectors for two reasons: first, it enhances the intensity of the light by a factor $\mathscr{F}$ and secondly it makes the intensity depend strongly on the position [52].

Each photon in the cavity carries a momentum $\hbar\omega_d/c$ whose direction is reversed when it reflects off the mirror. The resonator thus experiences a kick every time a photon reflects. The average force exerted on the resonator is proportional to the number of photons present in the cavity, n_c. This so-called photon pressure F_{rad} depends on the driving and resonance frequency of the cavity. Therefore, it also depends on the displacement of the resonator. This is illustrated in Fig. 2.9c. A small change in change in u leads to proportional change in radiation pressure. This thus changes the effective spring constant of the resonator to $k_R = k_0 - \partial F_{\text{rad}}/\partial u$; the so-called "optical spring" [23, 54, 55]. Similar to displacement-proportional feedback this can cool the resonator [23, 43]. A much stronger cooling effect is, however, the fact that the number of photons does not respond immediately to a change in displacement, but that they can only slowly leak out of the cavity at a rate $\sim \kappa$. This causes a delay in the response of the radiation pressure as indicated by the ellipsoids in Fig. 2.9c. In the case of red-detuned driving ($\omega_d < \omega_c$) work is done by the resonator so that it looses energy, whereas for blue-detuned driving ($\omega_d > \omega_c$) the resonator gains energy. This increased damping for red detuning cools the resonator effectively, as the backaction temperature associated with the detector is very low [53, 56, 57]. This process is called "dynamical backaction" and the cooling mechanism is called "sideband cooling" because the cavity is driven off-resonance, i.e. on a sideband[9].

The ultimate limit on resonator temperature that can be reached with sideband-cooling has been studied using the radiation-pressure Hamiltonian in the rotating-wave approximation [56, 57]:

$$\hat{H} = \hbar\Delta\hat{c}^\dagger\hat{c} + \hbar\omega_0\hat{a}^\dagger\hat{a} + \hbar\omega_0 G\hat{c}^\dagger\hat{c}(\hat{a}^\dagger + \hat{a}). \tag{2.24}$$

Here, $G = u_0\omega_0^{-1}\partial\omega_c/\partial u$ is the coupling constant and $\hat{c}^\dagger$ ($\hat{c}$) is the creation (annihilation) operator for a cavity photon (from (to) a photon with frequency ω_d). $\Delta = \omega_d - \omega_c$ is the detuning of the laser light with respect to the cavity resonance frequency. The idea is that a phonon, together with a red-detuned driving photon can excite a photon in the cavity because this up-converts the driving photon to a frequency closer to the cavity resonance. This removal of phonons cools the resonator. The opposite process is also possible: a cavity photon can emit a phonon and a lower-frequency photon, thereby heating the resonator. The rate of these two processes depends on the density-of-states of the cavity at $\omega_d + \omega_0$ and $\omega_d - \omega_0$. If the detuning is at exactly at the mechanical frequency $\Delta = -\omega_0$ and the cavity linewidth is small, the lowest temperatures are obtained. In the good-cavity limit ($\omega_m \gtrsim \kappa$) the lowest resonator occupation is $\bar{n}_{\min} = (\kappa/4\omega_0)^2 \ll 1$ [52, 56, 57], enabling cooling to the ground state. Although the good-cavity limit (also called the resolved-sideband regime) has been reached in recent experiments, ground-state cooling has not yet been demonstrated, due to the fact that the driving cannot be increased to sufficiently high powers. The final temperature is in principle independent of the power in the cavity, but the cooling power increases with it [53]. The cooling power should be large enough to remove the heat coming from the environment to reach the ground state. Table 2.1 and Fig. 2.4 show the final thermal occupation numbers that have been reached up to now. The lowest occupation factor $\bar{n} = 3.8$ has been achieved by sideband cooling using a superconducting stripline [38].

GENERAL CONSIDERATION

Finally, also other cooling mechanisms like bolometric (photothermal) [10, 18, 59] and backaction cooling [12] (see the next Section) are used, as shown in Table 2.1. In general, cooling is the reduction of the Brownian motion of the resonator and, as implied by Eq. 2.12, this is done by modifying the resonator's response function, one way or the other. Cooling can be done by increasing the effective spring constant and/or by increasing the damping. This is, however, not the picture that comes to mind when one talks about cooling. Cooling is done by placing the object in contact with something that is colder. The

[9] A recent proposal uses a displacement-dependent cavity damping instead of the usual displacement-dependent cavity frequency [58].

final temperature of the resonator is then the weighted sum of the original temperature and the temperature of the cold object T_c, with the heat conductance to the environment, κ_0, and to the the cold object, κ_c, as weights. The resonator temperature is thus:

$$T_R = \frac{\kappa_0 T + \kappa_c T_c}{\kappa_0 + \kappa_c}. \tag{2.25}$$

The fluctuation-dissipation theorem (cf. Eq. 2.11) shows that force noise in the environment causes damping of the resonator. When the resonator is coupled to something else as well, it experiences more force noise and hence also more damping. Its effective temperature thus depends on the exact balance between these contributions.

To measure the displacement, the resonator is coupled to a detector. The damping rate of the resonator $\gamma_R = \omega_R/Q$ is increased from its original value $\gamma_0 = \omega_0/Q_0$ to $\gamma_R = \gamma_0 + \gamma_{BA}$. The origin of γ_0 is the coupling to the environment, whereas γ_{BA} is induced by the detector. With these couplings to the two baths, the resonator temperature becomes [12, 32, 60]:

$$T_R = \frac{\gamma_0 T + \gamma_{BA} T_{BA}}{\gamma_0 + \gamma_{BA}}. \tag{2.26}$$

When he resonator is strongly coupled to the detector, its effective temperature is $T_R = T_{BA}$, the so-called backaction temperature of the detector. Eq. 2.12 shows that it is determined by the force noise exerted on the resonator:
$T_{BA} = S_{F_{BA,n}F_{BA,n}}/4k_\mathrm{B} m\gamma_{BA}$.

The additional damping is associated with a velocity-proportional force on the resonator. Such a force can be applied using active feedback or exerted by the detector when it does not respond instantaneously to the resonator displacement. Whether this delay is due to photons in an interferometer that slowly leak away, due to heat capacity [10, 18, 59], or due to a true velocity-dependent detector response is irrelevant. In any of these cases, the resonator is cooled (for $T_{BA} < T$) or heated (for $T_{BA} > T$) when it is coupled to the detector. In the case of active feedback cooling the backaction temperature is determined by the position noise u_n that is fed back to the resonator.

2.4 QUANTUM LIMITS ON POSITION DETECTION

Since the discovery of the Heisenberg uncertainty principle in 1927 it is known that quantum mechanics imposes limitations on the uncertainty with which quantities can be measured. This was first discovered for single measurements of conjugate variables, such as the position u and momentum p of a particle, or the components σ_x,σ_y and σ_z of a spin-1/2 particle. When the system is initially in a superposition of the eigenstates of the operator corresponding to the quantity that is measured, a strong measurement then gives one of the eigenvalues as the outcome. The probability for measuring a value m_i is given by $|c_i|^2$ when $|\psi\rangle = \sum_i c_i |m_i\rangle$ was the expansion of the original state in the basis of eigenstates of the operator $\hat{m}$, with $\hat{m}|m_i\rangle = m_i|m_i\rangle$. At the same time, the wavefunction collapses into the state corresponding to the measured value m_i: $|\psi\rangle \to |m_i\rangle$.

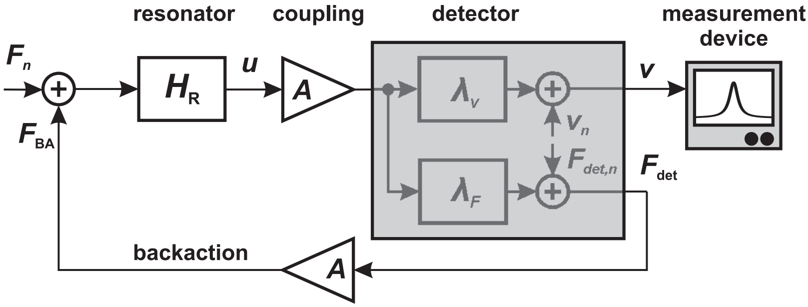

FIGURE 2.10: The detector is coupled (via A) to the resonator. Its output $v(t)$ depends linearly on $u(t)$ with a response function λ_v but also contains detector noise v_n. The detector exerts a backaction force $F_{BA} = AF_{det}$ on the resonator that contains a stochastic part $F_{BA,n}$ and a linear response to $u(t)$. Both contributions add up with the thermal or quantum force noise F_n. The resonator displacement u is obtained via the transfer function $H_R = H_{HO}/k_0$.

To find the probability of a certain outcome of a measurement of a different quantity n, the state $|m_i\rangle$ has to be expanded in the basis $|n_i\rangle$. The uncertainties in m and n satisfy: $\Delta m \cdot \Delta n \geq \left|[\hat{m}, \hat{n}]/2i\right|$, where $[\hat{m}, \hat{n}] = \hat{m}\hat{n} - \hat{n}\hat{m}$ is the commutator of $\hat{m}$ and $\hat{n}$. For $\hat{m} = \hat{u}$ and $\hat{n} = \hat{p}$, this yield the Heisenberg uncertainty principle for position and momentum: $\Delta u \cdot \Delta p \geq \hbar/2$. Note that quantum mechanics does not forbid to determine the position with arbitrary accuracy in a single measurement.

The measurements described in this Thesis are, however, not single, strong measurements, but weak continuous measurements instead. First continuous (linear) detectors are introduced and then the quantum limits on position detection are explored. The analysis presented in this Section is based on the work by Clerk and co-workers [61, 62].

CONTINUOUS LINEAR DETECTORS

A continuous linear position detector gives an output that depends linearly on the current and past position of the resonator. The output signal of the detector[10] is related to the displacement by:

$$v(t) = A\lambda_v(t) \otimes u(t) + v_n(t). \tag{2.27}$$

Here, λ_v is the responsivity of the detector, v_n is the detector noise and A is a dimensionless coupling strength. In the case of an optical interferometer, v represents the number of photons arriving at the photon counter whereas in our dc SQUID detector (Ch. 7 and Ch. 8) it is the (change in the average) SQUID voltage.

The detector does not only add noise to the measured signal, it also exerts a force $F_{BA}(t)$ on the resonator. This is the so-called backaction force. Backaction, in its most

[10] Continuous linear detectors are usually (implicitly) assumed to be time-invariant [63]. Unless stated otherwise, this is also assumed in this Thesis. Examples where the linear detector is not time-invariant are frequency-converting, stroboscopic and quadrature measurements [5, 6, 63, 64].

general definition, is the influence of a measurement or detector on an object. The back-action force has three different contributions:

- A deterministic force that is independent of the displacement. This changes the equilibrium position of the resonator. Without loss of generality it can thus be set to zero.
- A force that responds linearly to the displacement: $F_{BA,u} = A\lambda_F(t) \otimes Au(t)$. This changes the effective resonator response from H_R to H'_R, where $H'^{-1}_R = H^{-1}_R + A^2\lambda_F(\omega)$. Note the similarity with the active feedback scheme that was discussed in the previous Section. Backaction can thus also lead to cooling [12].
- A stochastic force $F_{BA,n} \equiv AF_{det,n}$ that is caused by the fluctuations in the detector, $F_{det,n}$. This force noise and the imprecision noise v_n can be correlated, i.e. $\overline{S}_{F_{det,n}v_n} \neq 0$.

This process of action and backaction is shown schematically in Fig. 2.10: The resonator position is coupled to the input of the detector, which adds imprecision noise v_n and exerts force noise on the resonator. For small coupling A, the statistical properties of $F_{det,n}$ and v_n are independent of the resonator displacement [61, 62].

To find the sensitivity of the detector, v_n is referred back to the input using the known response function λ_v and gain A. This yields the equivalent input noise PSD: $\overline{S}_{u_n u_n} = \overline{S}_{v_n v_n}/|A\lambda_v|^2$. This power spectral density is an important parameter that characterizes the detector. Using optimal-control and estimation theory, the best estimate $\hat{u}$ for the resonator displacement in the absence of the detector, u_i, is found. The resolution of the detector is $\Delta u = \left(\mathbb{E}[u_i^2 - \hat{u}^2]\right)^{1/2}$, as explained in detail in the Supplement to this Chapter. The resolution is plotted in Fig. 2.11a as a function of the coupling strength A. With a low coupling (top panel of Fig. 2.11b) Δu is large (i.e. the detector has a low resolution) because of the large equivalent input noise (dashed line) of the detector. An increase of the coupling reduces Δu because $\overline{S}_{u_n u_n}$ is proportional to A^{-2}. The resolution becomes better with increasing A up to the point where the optimal value $A = A_{\text{opt}}$ is reached (middle panel). A further increase of A makes the backaction noise dominant, driving the resonator significantly (dotted line in the bottom panel) above the original displacement u_i.

THE HAUS-CAVES DERIVATION OF THE QUANTUM LIMIT

The system analysis of the linear detector discussed above is valid for any – quantum limited or not – linear detector. An elegant way of deriving the quantum limit of a continuous linear position detector was given by Haus & Mullen [65] and was extended by Caves [63]. They consider the situation where the input and output signal of the detector are carried by single bosonic modes, $\hat{a}_u$ and $\hat{a}_v$ respectively. When the "photon number gain" of the detector is G, one might think that the modes are related to each other by $\hat{a}_v = \sqrt{G}\hat{a}_u$. This is, however, not valid as $[\hat{a}_v, \hat{a}_v^\dagger] = G \neq 1$ [62, 63] and the actual relation is $\hat{a}_v = \sqrt{G}\hat{a}_u + \hat{v}_n$.

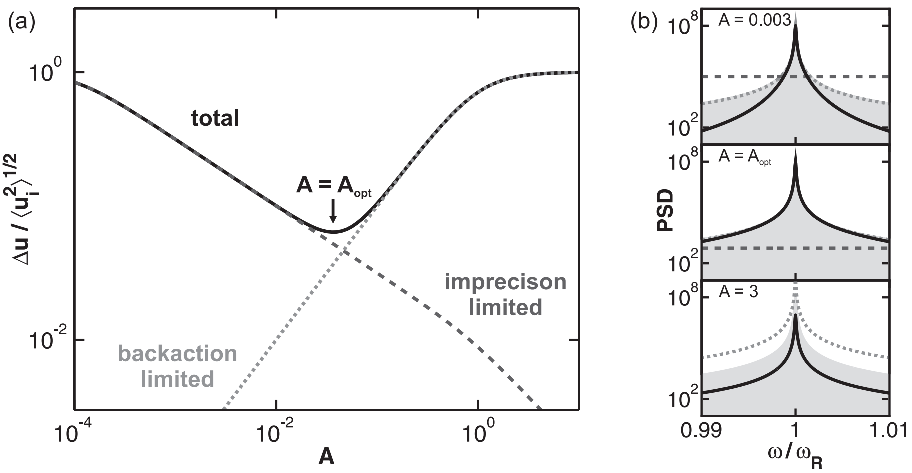

FIGURE 2.11: (a) The position resolution of the detector in units of the amplitude of the Brownian motion for different coupling strengths A. The solid line is the total resolution; the dotted line is the contribution of the backaction force noise (Eq. 2.35) and the dashed line the contribution of the imprecision noise (Eq. 2.36). The total resolution is optimized at $A = A_{\text{opt}} \approx 0.0355$. The panels in (b) show the power spectral densities of the original displacement ($\overline{S}_{u_i u_i}$, filled gray), the realized displacement ($\overline{S}_{uu}$, dotted), the equivalent input noise ($\overline{S}_{u_n u_n}$, dashed) and the estimated signal ($\overline{S}_{\hat{u}\hat{u}}$, solid line) at a small coupling (top), the optimal coupling (middle) and at high coupling (bottom). The resolution and PSDs have been calculated for $Q_0 = 10^4$, $\lambda_v = 1$, $\lambda_F = 0$, $\overline{S}_{v_n v_n} \cdot k_0^2 = \overline{S}_{F_{det,n} F_{det,n}} = \overline{S}_{F_n F_n}$ and $\overline{S}_{F_{det,n} v_n} = 0$.

Here, $\hat{v}_n$ represents the noise added by the amplifier. This operator has a vanishing expectation value ($\langle \hat{v}_n \rangle = 0$) and is uncorrelated with the input signal ($[\hat{a}_v, \hat{v}_n] = [\hat{a}_v^\dagger, \hat{v}_n] = 0$). This yields $[\hat{v}_n, \hat{v}_n^\dagger] = 1 - G$ for the commutator and, more importantly, $\Delta v^2 = G u_0^2 + \frac{1}{2}|G-1|$ for the resolution. The first term is the amplified zero-point motion of the signal (i.e. the resonator motion) and the second one is the noise added by the amplifier. In the limit of large gain ($G \gg 1$), the equivalent input noise of the detector is $\Delta u_{eq}^2 \equiv \Delta v^2/G - u_0 = \frac{1}{2}$. This means that a quantum-limited detector adds half a vibrational quantum of noise to the signal.

As pointed out in Ref. [62] most practical detectors cannot easily be coupled to a single bosonic mode that caries the information of the resonator to the detector, because there is also a mode that travels from the detector towards the resonator. Therefore, the linear-system analysis at the beginning of this Section used to further explore the quantum limits on continuous linear position detection.

A QUANTUM-LIMITED DETECTOR

In the previous discussion, no constraints were enforced on the detector noises $F_{det,n}$ and v_n. When both noise contributions could be made small enough, the resolution would be arbitrarily good. This is unfortunately not possible. It can be shown that the power spectral densities must satisfy[11]:

$$\overline{S}_{v_n v_n}(\omega)\cdot\overline{S}_{F_{det,n}F_{det,n}}(\omega)-\left|\overline{S}_{F_{det,n}v_n}(\omega)\right|^2\geq|\hbar\lambda_v(\omega)|^2, \tag{2.28}$$

or, equivalently, this can be referred to the input:

$$\overline{S}_{u_n u_n}(\omega)\cdot\overline{S}_{F_{BA,n}F_{BA,n}}(\omega)-\left|\overline{S}_{F_{BA,n}u_n}(\omega)\right|^2\geq\hbar^2. \tag{2.29}$$

These constraints enforce the quantum limit of the linear detector and should be considered as the continuous-detector equivalent of the Heisenberg uncertainty principle: Accurately measuring the position results in a lot of force noise and vice versa.

The analysis of Clerk *et al.* continues by finding the gain where the total added noise at the input, i.e. $\overline{S}_{u_n u_n}(\omega)+|H_R'|^2\overline{S}_{F_{BA,n}F_{BA,n}}(\omega)$, is minimized. As they already point out, this is not entirely correct because at every frequency a different optimal gain is required. Usually, only the optimal gain at $\omega=\omega_0$ is used and then the magnitude of the signal and detector noise are equal at that frequency. In that case, the imprecision noise and the backaction-induced displacement provide exactly half of the total added noise [9, 37, 62]. However, by minimizing the total *resolution*, the true optimal gain is found. Figure 2.12 shows this process. The resolution is optimized at $A=0.87$ and reaches a value of 0.81 times the zero-point motion. All three methods (the Haus-Caves derivation, the total added noise at the input, and the optimal estimator) indicate that the detector adds about the same amount of noise as the zero-point fluctuations of the resonator itself.

Now that the quantum limit is explored theoretically, it is time to see how far the currently-used detectors are away from this limit. Figure 2.13a shows the resolution Δu_n due to the imprecision noise $\overline{S}_{u_n u_n}$ of the experiments listed in Table 2.1. (For the exact definition of Δu_n, see Eq. 2.37 in the Supplement.) In some experiments, the imprecision noise is so low that the resolution Δu_n drops well below the zero-point motion. This most clearly demonstrated with the relatively low-frequency resonators that are read-out optically [11, 15, 17, 31, 34]. At room temperature, the thermal occupation is so high in these experiments that the heating due to the backaction noise is not visible. Other experiments with $\Delta u_n < u_0$ are done at low temperature, where the thermal occupation of the resonator is lower [12, 37, 38] and an increase in resonator temperature due to backaction is seen [12]. The experiments done by Teufel and coworkers (lines 27, 28 and 33 in Table 2.1) also illustrate an important point. When cooling the resonator, in this case using sideband cooling [32], the quality factor decreases. The resolution then becomes worse when the sensitivity stays the same because the resonator bandwidth increases. The opposite occurs when the damping of the resonator is reduced: the resolution is improved, but the resonator temperature increases significantly [37]. So far, no experiment has achieved a low occupation number $\bar{n}$ and a near quantum-limited position detector *at the same time*.

[11] Here, it is assumed that the measurement of $v(t)$ does not result in an additional force noise on the resonator and that the detector has a large power gain. For more details, see Ref. [62].

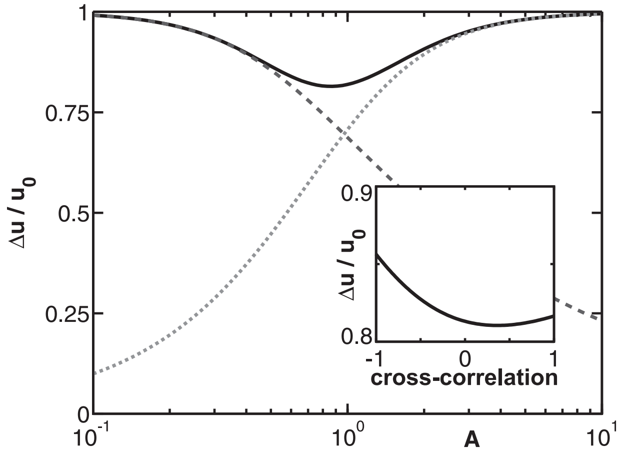

FIGURE 2.12: The quantum limit for a continuous linear position detector. The resolution of the detector in units of the zero-point motion is plotted for different coupling strengths A. The solid line is the total resolution; the dotted and dashed line are the contribution of backaction and imprecision noise. The inset shows that the total resolution depends on the cross-correlation coefficient $S_{F_{BA,n}u_{BA,n}}/(S_{F_{BA,n}F_{BA,n}} \cdot S_{u_n u_n})^{1/2}$. The main panel is calculated with an optimal cross-correlation of 0.36. For all values of A the total added noise is slightly less than u_0

2.5 BOTTOM-UP VS TOP-DOWN NEMS

The micro- and nanomechanical devices listed in Table 2.1 are made using so-called top-down fabrication techniques. Nanoscale structures are made by etching parts of a larger structure, for example a thin film on a substrate, or by depositing material (evaporating, sputtering) on a resist mask that is subsequently removed in a lift-off process. In both cases, patterning of resist is needed, which is done using optical or electron-beam lithography. State-of-the-art top-down fabricated devices have thicknesses and widths of less than 100 nanometer.

A different approach is to use the small structures that nature gives us, to build or assemble devices. Good examples are inorganic nanowires[12], carbon nanotubes and few-layer graphene. The last two are examples of carbon-based materials. Their structure and mechanical properties will be discussed in depth in Ch. 3. Using bottom-up materials, mechanical devices with true nanometer dimensions are made.

Table 2.2 shows the properties of the mechanical resonators that have been made so far using bottom-up fabricated devices. Their frequencies are high: by choosing the right device geometry resonances in the UHF band (300 MHz - 3 GHz) are readily made, as Table 2.2 shows. When comparing the quality factors and zero-point motion of these devices, it

[12] Sometimes "nanowire" is also used for top-down fabricated devices. Here, this term is used exclusively for grown wires.

TABLE 2.2: Overview of recent experiments with bottom-up resonators. Several types of resonators are used: carbon nanotubes (CNT), nanowires (NW), single-layer graphene (SLG), and few-layer graphene (FLG) or graphene oxide (FLGO) sheets. The table shows the resonance frequency f_R and quality factors at room and cryogenic temperature (Q_{RT} and Q_{cryo} resp.). T_{min} is the lowest temperature at which the resonator is measured. m is the mass of the resonator and ℓ is its length. From these data, the zero-point motion u_0 is calculated.

Type	$\mathbf{f_R}$ (MHz)	$\mathbf{Q_{RT}}$	$\mathbf{Q_{cryo}}$	$\mathbf{T_{min}}$ (K)	ℓ (μm)	**m** (kg)	$\mathbf{u_0}$ (pm)	**Ref.**
CNT	55	80		300	1.75	$7.4\cdot10^{-21}$	4.52	[66]
CNT	60	100		300	1.25	$1.0\cdot10^{-20}$	3.66	Ch. 5
CNT	350	440		300	0.5	$5.3\cdot10^{-20}$	0.67	[67]
CNT	3120	8		300	0.77	$5.8\cdot10^{-20}$	0.22	[68]
CNT	154	20		300	0.265	$1.1\cdot10^{-19}$	0.69	[68]
CNT	573	20		300	0.193	$4.0\cdot10^{-22}$	6.03	[68]
CNT	167	200	2000	5	0.9	$1.4\cdot10^{-21}$	6.03	[69]
CNT	328.5	1000		300	0.205	$1.6\cdot10^{-21}$	4.01	[70]
CNT	230		200	6	0.45	$4.8\cdot10^{-22}$	8.73	[71]
CNT	0.9	3		300	12.6	$4.1\cdot10^{-16}$	0.15	[72]
CNT	62	50		300	2.05	$2.2\cdot10^{-17}$	0.08	[73]
CNT	360		120000	0.02	0.8	$5.3\cdot10^{-21}$	2.09	Ch. 6
CNT	50	40	600	4	1	$1.3\cdot10^{-21}$	11.41	[74]
Pt NW	105.3		8500	4	1.3	$4.0\cdot10^{-17}$	0.045	[75]
GaN NW	2.235	2800		300	5.5	$1.9\cdot10^{-16}$	0.141	[76]
Si NW	1.842	4200		300	5.2	$2.4\cdot10^{-17}$	0.437	[77]
Si NW	1.842	2000	10000	77	11.2	$4.6\cdot10^{-16}$	0.099	[77]
SnO_2 NW	59	2200		300	2.5	$2.2\cdot10^{-16}$	0.025	[78]
SLG	70.5	78		300	1.1	$1.4\cdot10^{-18}$	0.287	[79]
FLG	32	64		300	2.8	$2.7\cdot10^{-17}$	0.098	[80]
FLG	160	25		300	4.75	$4.5\cdot10^{-16}$	0.011	[81]
FLGO	57.6	3000		300	2.75	$7.8\cdot10^{-17}$	0.043	[82]
FLG	8.36	97		300	8	$3.5\cdot10^{-17}$	0.169	[83]
SLG	130	125	14000	5	3	$2.2\cdot10^{-18}$	0.169	[84]

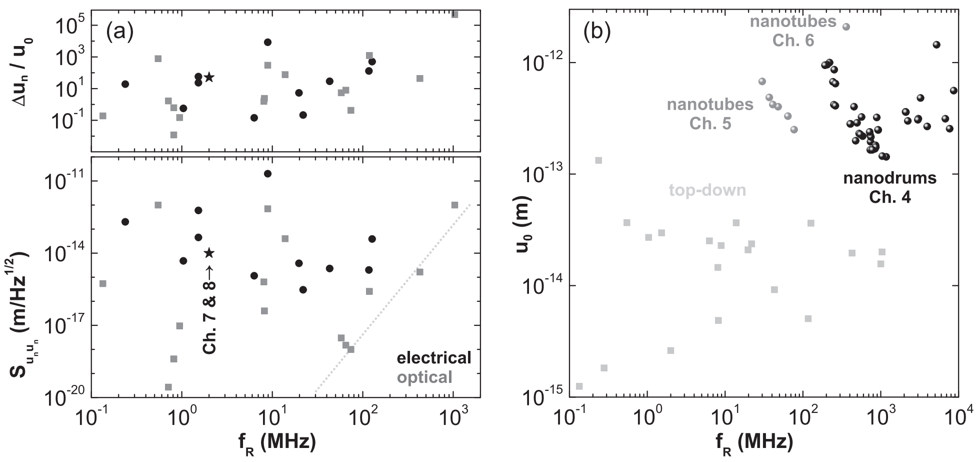

FIGURE 2.13: (a) Sensitivity and resolution of the experiments that are listed in Table 2.1. Experiments with optical (electrical) detection are shown in gray (black). The dc SQUID position detector used in Chs. 7 and 8 is indicated with a star. The dotted line shows that an increase of the resonance frequency is often accompanied by an increase in the sensitivity. (b) Comparison of the resonance frequency and zero-point motion of top-down (Table 2.1) and the bottom-up devices that are studied in the forthcoming Chapters. The resonance frequencies and zero-point motion are much larger for the bottom-up devices.

is clear that the performance of nanowires is more or less comparable to top-down fabricated devices. This is because their thickness is of the order of 10-100 nm, about the size of the smallest top-down fabricated devices. Therefore, we will focus on carbon nanotubes and graphene resonators in the rest of this Section.

Due to their low mass m and high strength (Sec. 3.4) the frequencies of carbon-based resonators are high, enabling ground state cooling using standard cryogenic techniques. Furthermore their zero-point motion u_0 is large. Note that in Table 2.1 u_0 was given in fm, whereas in Table 2.2 it is in pm. Figure 2.13 illustrates this point more clearly.

A major drawback of making smaller resonators to increase their frequency, is that the quality factor decreases [85]. Top-down devices have surfaces with many defects due to the fabrication process. This provides an easy channel for dissipation, resulting in a low Q-factor. The decrease in Q-factor with device dimension is therefore often attributed to the increase in surface-to-volume ratio. Bottom-up devices are expected not to suffer from this, as their surface can be defect-free. Until recently, this was, however, never observed. The quality factors shown in Table 2.2 are in general disappointingly low. Only recently, we obtained ultra-high quality factor carbon nanotube resonators as shown in Ch. 6. The last hurdle for observing quantum effects in carbon-based NEMS is the fact that the position detectors for these devices are not yet so sophisticated as those for the larger top-down structures. The sensitivity is therefore not as high as one wishes.

SUPPLEMENT

COMPLEX GREEN'S FUNCTION AND DISPLACEMENT

The complex displacement is defined as $u_c(t) \equiv A_c \exp(i\omega_R t)$ with the requirement that $\mathrm{Re}[u_c(t)] = u(t)$. A convenient way of implementing this, is using the complex extension of the resonator Green's function, Eq. 2.3:

$$u_c(t) = h_c(t) \otimes F(t)/k_R, \qquad h_c(t) = -ie^{i\omega_R t} \cdot e^{-\frac{\omega_R t}{2Q}} \Theta(t), \tag{2.30}$$

so that $\mathrm{Re}[h_c] = h_{HO}$. The amplitude and phase of the resonator displacement are in this case given by the modulus and argument of the complex amplitude: $A(t) = |A_c|$ and $\varphi(t) = \angle A_c$ respectively. Note that A and φ are not uniquely defined, but that this particular choice corresponds to the usual notion of the amplitude and phase.

OPTIMAL FILTERING OF $v(t)$

In the presence of both position and force noise, one wants to reconstruct the resonator motion in the absence of the detector, $u_i(t) = h_R(t) \otimes F_n(t)$, as good as possible from the measured time trace $v(t)$. This is done by finding the estimator $\hat{u} = g(t) \otimes v(t)$ that minimizes the resolution squared: $\Delta u^2 = \mathbb{E}[(u_i - \hat{u})^2]$. Using the autocorrelation functions and converting these into noise PSDs using the Wiener-Khinchin theorem [45, 62] the resolution is written as:

$$\Delta u^2 = R_{u_i u_i}(0) - 2R_{u_i \hat{u}}(0) + R_{\hat{u}\hat{u}}(0) = \frac{1}{2\pi} \int_{-\infty}^{\infty} \left[S_{u_i u_i}(\omega) - 2G(\omega) S_{u_i v}(\omega) + |G(\omega)|^2 S_{vv} \right] \mathrm{d}\omega. \tag{2.31}$$

Minimizing this, yields the optimal filter $G_{\mathrm{opt}} = S_{v u_i}/S_{vv}$ [45], where:

$$S_{v u_i} = S^*_{u_i v} = A H_R (H'_R)^* \lambda^*_v S_{F_n F_n}, \tag{2.32}$$

$$\begin{aligned} S_{vv} = S^*_{vv} &= A^2 |H'_R|^2 |\lambda_v|^2 \left(S_{F_n F_n} + A^2 S_{F_{det,n} F_{det,n}} \right) \\ &+ S_{v_n v_n} + 2A^2 \mathrm{Re}\left[\lambda_v (H'_R)^* S_{F_{det,n} v_n} \right], \end{aligned} \tag{2.33}$$

so that the squared resolution is:

$$\Delta u^2 = \frac{1}{2\pi} \int_0^{\infty} \left[S_{u_i u_i}(\omega) - |G_{\mathrm{opt}}(\omega)|^2 S_{vv} \right] \mathrm{d}\omega. \tag{2.34}$$

Depending on the properties of the detector and the coupling A, two important cases can be distinguished:

- The detector exerts backaction force noise, but the displacement noise is negligible: $S_{v_n v_n} = 0$. In this case the integral in Eq. 2.34 is easily solved and one finds:

  $$\Delta u^2_{BA} = \langle u_i^2 \rangle \cdot \left(1 + \frac{S_{F_n F_n}}{A^2 S_{F_{det,n} F_{det,n}}} \right)^{-1} = \langle u_i^2 \rangle \cdot \left(1 + \frac{S_{F_n F_n}}{S_{F_{BA,n} F_{BA,n}}} \right)^{-1}. \tag{2.35}$$

  The resolution thus improves with coupling A as this determines the backaction force noise. This increase goes approximately as A^2.

- The detector adds displacement imprecision noise and the backaction noise is very small, i.e. $S_{F_{det,n}F_{det,n}} = 0$. In this case Eq. 2.34 reduces to:

$$\Delta u_{imp}^2 = \langle u_i^2 \rangle \cdot J(x, Q_0), \text{ with } x^4 = k_0^2 \frac{S_{v_n v_n}/A^2|\lambda_v|^2}{S_{F_n F_n}} = k_0^2 \frac{S_{u_n u_n}}{S_{F_n F_n}} = \frac{Q_0^2}{\text{SNR}}, \tag{2.36}$$

under the assumption that the detector noise PSD referred to the detector input $S_{u_n u_n} = S_{v_n v_n}/A^2|\lambda|^2$ is white. $J(x, Q_0)$ is a complicated function that tends to 1 for $x \gg Q^{1/2} \gg 1$, i.e. when the signal to noise ratio is well below unity. When $x \to 0$ the function $J(x, Q_0)$ goes to zero as $x^3/Q_0\sqrt{2}$. The resolution improves with increasing coupling as the resonator signal is amplified more and more with respect to the noise floor $S_{v_n v_n}$.

For practical purposes it is convenient to use a slightly different definition of the resolution [9] that is independent of the signal-to-noise ratio:

$$\Delta u_n^2 = S_{u_n u_n} \frac{\pi}{2} \frac{f_R}{Q}. \tag{2.37}$$

This definition is based on the fact that one can measure the position during a time $\sim Q/f_R$ before the resonator has forgotten its initial amplitude and phase (see also Fig. 2.2). Note, that this definition does not take the effect of backaction noise into account.

REFERENCES

[1] K. S. Thorne, *Gravitational-wave research: Current status and future prospects*, Rev. Mod. Phys. **52**, 285 (1980).

[2] H. Billing, K. Maischberger, A. Rudiger, R. Schilling, L. Schnupp, and W. Winkler, *An argon laser interferometer for the detection of gravitational radiation*, J. Phys. E **12**, 1043 (1979).

[3] J. Weber, *Advances in gravitational radiation detection*, Gen. Rel. and Grav. **3**, 59 (1972).

[4] D. J. Griffiths, *Introduction to Quantum Mechanics* (Prentice Hall, 1995).

[5] V. B. Braginsky and F. Y. Khalili, *Quantum measurement* (Nature Publishing Group, 1992).

[6] C. M. Caves, K. S. Thorne, R. W. P. Drever, V. D. Sandberg, and M. Zimmermann, *On the measurement of a weak classical force coupled to a quantum-mechanical oscillator. I. Issues of principle*, Rev. Mod. Phys. **52**, 341 (1980).

[7] R. G. Knobel and A. N. Cleland, *Nanometre-scale displacement sensing using a single electron transistor*, Nature **424**, 291 (2003).

[8] X. M. H. Huang, C. A. Zorman, M. Mehregany, and M. L. Roukes, *Nanoelectromechanical systems: Nanodevice motion at microwave frequencies*, Nature **421**, 496 (2003).

[9] M. D. LaHaye, O. Buu, B. Camarota, and K. C. Schwab, *Approaching the Quantum Limit of a Nanomechanical Resonator*, Science **304**, 74 (2004).

[10] C. Metzger Höhberger and K. Karrai, *Cavity cooling of a microlever*, Nature **432**, 1002 (2004).

[11] O. Arcizet, P.-F. Cohadon, T. Briant, M. Pinard, A. Heidmann, J.-M. Mackowski, C. Michel, L. Pinard, O. Français, and L. Rousseau, *High-Sensitivity Optical Monitoring of a Micromechanical Resonator with a Quantum-Limited Optomechanical Sensor*, Phys. Rev. Lett. **97**, 133601 (pages 4) (2006).

[12] A. Naik, O. Buu, M. D. LaHaye, A. D. Armour, A. A. Clerk, M. P. Blencowe, and K. C. Schwab, *Cooling a nanomechanical resonator with quantum back-action*, Nature **443**, 193 (2006).

[13] A. Schliesser, P. Del'Haye, N. Nooshi, K. J. Vahala, and T. J. Kippenberg, *Radiation Pressure Cooling of a Micromechanical Oscillator Using Dynamical Backaction*, Phys. Rev. Lett. **97**, 243905 (pages 4) (2006).

[14] S. Gigan, H. R. Bohm, M. Paternostro, F. Blaser, G. Langer, J. B. Hertzberg, K. C. Schwab, D. Bauerle, M. Aspelmeyer, and A. Zeilinger, *Self-cooling of a micromirror by radiation pressure*, Nature **444**, 67 (2006).

[15] O. Arcizet, P.-F. Cohadon, T. Briant, M. Pinard, and A. Heidmann, *Radiation-pressure cooling and optomechanical instability of a micromirror*, Nature **444**, 71 (2006).

[16] D. Kleckner and D. Bouwmeester, *Sub-kelvin optical cooling of a micromechanical resonator*, Nature **444**, 75 (2006).

[17] M. Poggio, C. L. Degen, H. J. Mamin, and D. Rugar, *Feedback Cooling of a Cantilever's Fundamental Mode below 5 mK*, Phys. Rev. Lett. **99**, 017201 (pages 4) (2007).

[18] I. Favero, C. Metzger, S. Camerer, D. König, H. Lorenz, J. P. Kotthaus, and K. Karrai, *Optical cooling of a micromirror of wavelength size*, Appl. Phys. Lett. **90**, 104101 (pages 3) (2007).

[19] K. R. Brown, J. Britton, R. J. Epstein, J. Chiaverini, D. Leibfried, and D. J. Wineland, *Passive Cooling of a Micromechanical Oscillator with a Resonant Electric Circuit*, Phys. Rev. Lett. **99**, 137205 (pages 4) (2007).

[20] N. E. Flowers-Jacobs, D. R. Schmidt, and K. W. Lehnert, *Intrinsic Noise Properties of Atomic Point Contact Displacement Detectors*, Phys. Rev. Lett. **98**, 096804 (pages 4) (2007).

[21] M. Li, X. H.Tang, and M. L. Roukes, *Ultra-sensitive NEMS-based cantilevers for sensing, scanned probe and very high-frequency applications*, Nat Nano **2**, 114 (2007).

[22] T. Caniard, P. Verlot, T. Briant, P.-F. Cohadon, and A. Heidmann, *Observation of Back-Action Noise Cancellation in Interferometric and Weak Force Measurements*, Physical Review Letters **99**, 110801 (pages 4) (2007).

[23] T. Corbitt, Y. Chen, E. Innerhofer, H. Müller-Ebhardt, D. Ottaway, H. Rehbein, D. Sigg, S. Whitcomb, C. Wipf, and N. Mavalvala, *An All-Optical Trap for a Gram-Scale Mirror*, Phys. Rev. Lett. **98**, 150802 (pages 4) (2007).

[24] J. D. Thompson, B. M. Zwickl, A. M. Jayich, F. Marquardt, S. M. Girvin, and J. G. E. Harris, *Strong dispersive coupling of a high-finesse cavity to a micromechanical membrane*, Nature **452**, 72 (2008).

[25] C. A. Regal, J. D. Teufel, and K. W. Lehnert, *Measuring nanomechanical motion with a microwave cavity interferometer*, Nat Phys **4**, 555 (2008).

[26] S. Etaki, M. Poot, I. Mahboob, K. Onomitsu, H. Yamaguchi, and H. S. J. van der Zant, *Motion detection of a micromechanical resonator embedded in a d.c. SQUID*, Nat Phys **4**, 785 (2008).

[27] A. Schliesser, R. Riviere, G. Anetsberger, O. Arcizet, and T. Kippenberg, *Resolved-sideband cooling of a micromechanical oscillator*, Nat Phys **4**, 415 (2008).

[28] S. Gröblacher, S. Gigan, H. R. Böhm, A. Zeilinger, and M. Aspelmeyer, *Radiation-pressure self-cooling of a micromirror in a cryogenic environment*, EPL **81**, 54003 (2008).

[29] X. L. Feng, C. J. White, A. Hajimiri, and M. L. Roukes, *A self-sustaining ultrahigh-frequency nanoelectromechanical oscillator*, Nat Nano **3**, 342 (2008).

[30] M. Poggio, M. P. Jura, C. L. Degen, M. A. Topinka, H. J. Mamin, D. Goldhaber-Gordon, and D. Rugar, *An off-board quantum point contact as a sensitive detector of cantilever motion*, Nat Phys **4**, 635 (2008).

[31] A. Vinante, M. Bignotto, M. Bonaldi, M. Cerdonio, L. Conti, P. Falferi, N. Liguori, S. Longo, R. Mezzena, A. Ortolan, et al., *Feedback Cooling of the Normal Modes of a Massive Electromechanical System to Submillikelvin Temperature*, Phys. Rev. Lett. **101**, 033601 (pages 4) (2008).

[32] J. D. Teufel, J. W. Harlow, C. A. Regal, and K. W. Lehnert, *Dynamical Backaction of Microwave Fields on a Nanomechanical Oscillator*, Phys. Rev. Lett. **101**, 197203 (pages 4) (2008).

[33] N. Liu, F. Giesen, M. Belov, J. Losby, J. Moroz, E. A. Fraser, G. McKinnon, J. T. Clement, V. Sauer, K. W. Hiebert, et al., *Time-domain control of ultrahigh-frequency nanomechanical systems*, Nat Nano **3**, 715 (2008).

[34] S. Gröblacher, J. B. Hertzberg, M. R. Vanner, G. D. Cole, S. Gigan, K. C. Schwab, and M. Aspelmeyer, *Demonstration of an ultracold micro-optomechanical oscillator in a cryogenic cavity*, Nat Phys **5**, 485 (2009).

[35] A. Schliesser, O. Arcizet, R. Riviere, G. Anetsberger, and T. J. Kippenberg, *Resolved-sideband cooling and position measurement of a micromechanical oscillator close to the Heisenberg uncertainty limit*, Nat Phys **5**, 509 (2009).

[36] G. Anetsberger, O. Arcizet, Q. P. Unterreithmeier, E. M. Weig, J. P. Kotthaus, and T. J. Kippenberg, *Near-field cavity optomechanics with nanomechanical oscillators*, arXiv:0904.4051 (2009).

[37] J. D. Teufel, T. Donner, M. A. Castellanos-Beltran, J. W. Harlow, and K. W. Lehnert, *Nanomechanical motion measured with precision beyond the standard quantum limit*, arXiv:0906.1212 (2009).

[38] T. Rocheleau, T. Ndukum, C. Macklin, J. B. Hertzberg, A. A. Clerk, and K. C. Schwab, *Preparation and Detection of a Mechanical Resonator Near the Ground State of Motion*, arXiv:0907.3313v1 (2009).

[39] Y.-S. Park and H. Wang, *Resolved-sideband and cryogenic cooling of an optomechanical resonator*, Nat Phys **5**, 489 (2009).

[40] Q. P. Unterreithmeier, E. M. Weig, and J. P. Kotthaus, *Universal transduction scheme for nanomechanical systems based on dielectric forces*, Nature **458**, 1001 (2009).

[41] M. Li, W. H. P. Pernice, and X. H. Tang, *Broadband all-photonic transduction of nanocantilevers*, Nat Nano **4**, 377 (2009).

[42] M. Eichenfield, R. Camacho, J. Chan, K. J. Vahala, and O. Painter, *A picogram- and nanometre-scale photonic-crystal optomechanical cavity*, Nature **459**, 550 (2009).

[43] B. Abbott *et al.*, *Observation of a kilogram-scale oscillator near its quantum ground state*, New J. Phys. **11**, 073032 (2009).

[44] A. V. Oppenheim, A. S. Willsky, and S. Hamid, *Signals and Systems*, Prentice Hall signal processing series (Prentice Hall, 1997), 2nd ed.

[45] K. S. S. . A. M. Breipohl, *Random Signals: Detection, Estimation and Data Analysis* (John Wiley and Sons, 1988).

[46] C. Kittel and H. Kroemer, *Thermal Physics* (W. H. Freeman, 2000).

[47] H. B. Callen and T. A. Welton, *Irreversibility and Generalized Noise*, Phys. Rev. **83**, 34 (1951).

[48] S. Mancini, D. Vitali, and P. Tombesi, *Optomechanical Cooling of a Macroscopic Oscillator by Homodyne Feedback*, Phys. Rev. Lett. **80**, 688 (1998).

[49] P. F. Cohadon, A. Heidmann, and M. Pinard, *Cooling of a Mirror by Radiation Pressure*, Phys. Rev. Lett. **83**, 3174 (1999).

[50] J. L. Garbini, K. J. Bruland, W. M. Dougherty, and J. A. Sidles, *Optimal control of force microscope cantilevers. I. Controller design*, J. Appl. Phys. **80**, 1951 (1996).

[51] T. J. Kippenberg and K. J. Vahala, *Cavity optomechanics: Back-action at the mesoscale*, Science **321**, 1172 (2008).

[52] F. Marquardt and S. M. Girvin, *Optomechanics*, Physics **2**, 40 (2009).

[53] J. D. Teufel, C. A. Regal, and K. W. Lehnert, *Prospects for cooling nanomechanical motion by coupling to a superconducting microwave resonator*, New J. Phys **10**, 095002 (11pp) (2008).

[54] A. Buonanno and Y. Chen, *Signal recycled laser-interferometer gravitational-wave detectors as optical springs*, Phys. Rev. D **65**, 042001 (2002).

[55] T. Corbitt, D. Ottaway, E. Innerhofer, J. Pelc, and N. Mavalvala, *Measurement of radiation-pressure-induced optomechanical dynamics in a suspended Fabry-Perot cavity*, Phys. Rev. A **74**, 021802 (pages 4) (2006).

[56] I. Wilson-Rae, N. Nooshi, W. Zwerger, and T. J. Kippenberg, *Theory of Ground State Cooling of a Mechanical Oscillator Using Dynamical Backaction*, Phys. Rev. Lett. **99**, 093901 (pages 4) (2007).

[57] F. Marquardt, J. P. Chen, A. A. Clerk, and S. M. Girvin, *Quantum Theory of Cavity-Assisted Sideband Cooling of Mechanical Motion*, Phys. Rev. Lett. **99**, 093902 (pages 4) (2007).

[58] F. Elste, S. M. Girvin, and A. A. Clerk, *Quantum Noise Interference and Backaction Cooling in Cavity Nanomechanics*, Phys. Rev. Lett. **102**, 207209 (pages 4) (2009).

[59] G. Jourdan, F. Comin, and J. Chevrier, *Mechanical Mode Dependence of Bolometric Backaction in an Atomic Force Microscopy Microlever*, Phys. Rev. Lett. **101**, 133904 (pages 4) (2008).

[60] A. A. Clerk and S. Bennett, *Quantum nanoelectromechanics with electrons, quasi-particles and Cooper pairs: effective bath descriptions and strong feedback effects*, New J. Phys. **7**, 238 (2005).

[61] A. A. Clerk, *Quantum-limited position detection and amplification: A linear response perspective*, Phys. Rev. B **70**, 245306 (2004).

[62] A. A. Clerk, M. H. Devoret, S. M. Girvin, F. Marquardt, and S. R. J., *Introduction to Quantum Noise, Measurement and Amplification*, arXiv:0810.4729v1 pp. 1–102 (2008).

[63] C. M. Caves, *Quantum limits on noise in linear amplifiers*, Phys. Rev. D **26**, 1817 (1982).

[64] V. B. Braginsky, Y. I. Vorontsov, and K. S. Thorne, *Quantum Nondemolition Measurements*, Science **209**, 547 (1980).

[65] H. A. Haus and J. A. Mullen, *Quantum Noise in Linear Amplifiers*, Phys. Rev. **128**, 2407 (1962).

[66] V. Sazonova, Y. Yaish, H. Üstünel, D. Roundy, T. A. Arias, and P. L. McEuen, *A tunable carbon nanotube electromechanical oscillator*, Nature **431**, 284 (2004).

[67] K. Jensen, J. Weldon, H. Garcia, and A. Zettl, *Nanotube Radio*, Nano Lett. **7**, 3508 (2007).

[68] D. Garcia-Sanchez, A. S. Paulo, M. J. Esplandiu, F. Perez-Murano, L. Forró, A. Aguasca, and A. Bachtold, *Mechanical Detection of Carbon Nanotube Resonator Vibrations*, Phys. Rev. Lett. **99**, 085501 (pages 4) (2007).

[69] B. Lassagne, D. Garcia-Sanchez, A. Aguasca, and A. Bachtold, *Ultrasensitive Mass Sensing with a Nanotube Electromechanical Resonator*, Nano Lett. **8**, 3735 (2008).

[70] K. Jensen, K. Kim, and A. Zettl, *An atomic-resolution nanomechanical mass sensor*, Nat Nano **3**, 533 (2008).

[71] H.-Y. Chiu, P. Hung, H. W. C. Postma, and M. Bockrath, *Atomic-Scale Mass Sensing Using Carbon Nanotube Resonators*, Nano Lett. **8**, 4342 (2008).

[72] L. B. Biedermann, R. C. Tung, A. Raman, and R. G. Reifenberger, *Flexural vibration spectra of carbon nanotubes measured using laser Doppler vibrometry*, Nanotechnology **20**, 035702 (2009).

[73] A. Eriksson, S. Lee, A. A. Sourab, A. Isacsson, R. Kaunisto, J. M. Kinaret, and E. E. B. Campbell, *Direct Transmission Detection of Tunable Mechanical Resonance in an Individual Carbon Nanofiber Relay*, Nano Lett. **8**, 1224 (2008).

[74] B. Lassagne, Y. Tarakanov, J. Kinaret, D. Garcia-Sanchez, and A. Bachtold, *Coupling Mechanics to Charge Transport in Carbon Nanotube Mechanical Resonators*, Science **325**, 1107 (2009).

[75] A. Husain, J. Hone, H. W. C. Postma, X. M. H. Huang, T. Drake, M. Barbic, A. Scherer, and M. L. Roukes, *Nanowire-based very-high-frequency electromechanical resonator*, Appl. Phys. Lett. **83**, 1240 (2003).

[76] C.-Y. Nam, P. Jaroenapibal, D. Tham, D. E. Luzzi, S. Evoy, and J. E. Fischer, *Diameter-Dependent Electromechanical Properties of GaN Nanowires*, Nano Lett. **6**, 153 (2006).

[77] M. Belov, N. J. Quitoriano, S. Sharma, W. K. Hiebert, T. I. Kamins, and S. Evoy, *Mechanical resonance of clamped silicon nanowires measured by optical interferometry*, J. Appl. Phys. **103**, 074304 (pages 7) (2008).

[78] W. Y. Fung, E. N. Dattoli, and W. Lu, *Radio frequency nanowire resonators and in situ frequency tuning*, Appl. Phys. Lett. **94**, 203104 (pages 3) (2009).

[79] J. S. Bunch, A. M. van der Zande, S. S. Verbridge, I. W. Frank, D. M. Tanenbaum, J. M. Parpia, H. G. Craighead, and P. L. McEuen, *Electromechanical resonators from graphene sheets*, Science **315**, 490 (2007).

[80] D. Garcia-Sanchez, A. M. van der Zande, A. S. Paulo, B. Lassagne, P. L. McEuen, and A. Bachtold, *Imaging Mechanical Vibrations in Suspended Graphene Sheets*, Nano Letters **8**, 1399 (2008).

[81] J. S. Bunch, S. S. Verbridge, J. S. Alden, A. M. van der Zande, J. M. Parpia, H. G. Craighead, and P. L. McEuen, *Impermeable Atomic Membranes from Graphene Sheets*, Nano Lett. **8**, 2458 (2008).

[82] J. T. Robinson, M. Zalalutdinov, J. W. Baldwin, E. S. Snow, Z. Wei, P. Sheehan, and B. H. Houston, *Wafer-scale Reduced Graphene Oxide Films for Nanomechanical Devices*, Nano Letters **8**, 3441 (2008).

[83] S. Shivaraman, R. A. Barton, X. Yu, J. Alden, L. Herman, M. Chandrashekhar, J. Park, P. L. McEuen, J. M. Parpia, H. G. Craighead, et al., *Free-Standing Epitaxial Graphene*, Nano Letters **9**, 3100 (2009).

[84] C. Chen, S. Rosenblatt, K. I. Bolotin, W. Kalb, P. Kim, I. Kymissis, H. L. Stormer, T. F. Heinz, and J. Hone, *Performance of monolayer graphene nanomechanical resonators with electrical readout*, Nat Nano **advance online publication**, (2009).

[85] K. L. Ekinci and M. L. Roukes, *Nanoelectromechanical systems*, Rev. Sci. Instrum. **76**, 061101 (pages 12) (2005).

3

NANOMECHANICS

In this Chapter, the framework of continuum mechanics is used to study mechanical devices at the nanoscale. From the general theories of elasticity, the governing equations for the flexural vibrations of beams and suspended plates are obtained. The relation between stress and strain for an isotropic material and for the highly anisotropic carbon-based materials are given. The results obtained in this Chapter, are illustrated by analyzing the mechanics of the nanomechanical devices that are discussed in the forthcoming Chapters.

3.1 CONTINUUM MECHANICS

The dynamics of mechanical objects is usually much more complicated than the simple one-dimensional harmonic oscillator described in Ch. 2. In principle, the dynamics of all particles (i.e. atoms and electrons) which make up the oscillator should be taken into account. However, Chapters 4 and 5 will demonstrate that even for nanometer-sized objects continuum mechanics is, with some modifications, still applicable. This means the dynamics of the individual particles is irrelevant when one talks about deflections and deformations; the microscopic details only determine the properties and values of macroscopic quantities like the Young's modulus or the Poisson ratio.

The basis of continuum mechanics lies in the relations between strain and stress in a material. The strain tells how the material is deformed with respect to its relaxed state. After the deformation of the material, the part that was originally at position $\mathbf{x}$ is displaced by $\mathbf{u}$ to its new location $\mathbf{x}+\mathbf{u}$. The strain describes how much an infinitesimal line segment

Parts of this Chapter have been published in Phys. Stat. Sol. (b) **244**, 4252–4256 (2007) and in Nat. Phys. **4**, 785–788 (2008) is elongated by the deformation $\mathbf{u}(x, y, z)$ and is given by[1] [1]:

$$\gamma_{ij} = \frac{1}{2}\left(\frac{\partial u_i}{\partial x_j} + \frac{\partial u_j}{\partial x_i} + \frac{\partial u_m}{\partial x_i}\frac{\partial u_m}{\partial x_j}\right). \tag{3.1}$$

The diagonal elements (i.e. $i = j$) of the first two terms are the normal strains, whereas the off-diagonal elements ($i \neq j$) are the shear strains. The last, non-linear term is only relevant when the deformations are large and can usually safely be neglected [2]. Note that the strain is symmetric under a reversal of the indices $\gamma_{ij} = \gamma_{ji}$.

To deform a material external forces have to be applied. This gives rise to forces inside the material. When the material is thought of a as composed of small elements, each element feels the force exerted on its faces by the neighboring elements. Its magnitude and direction depend not only on the location in the material but also on the *orientation* of the element (see Fig. 3.1a). The force $\delta\mathbf{F}$ on a small area δA of the element is given by:

$$\delta F_i = \sigma_{ij} n_j \delta A, \tag{3.2}$$

where $\mathbf{n}$ is the vector perpendicular to the surface and σ is the stress tensor. Now consider an element of the material with mass m and volume V. When it is moving with a speed $\mathbf{v} = \dot{\mathbf{u}}$ its momentum $\mathbf{p}$ is:

$$\mathbf{p} = \int_m \mathbf{v}\,\mathrm{d}m = \int_V \rho\mathbf{v}\,\mathrm{d}V, \tag{3.3}$$

where ρ is the mass density. The rate of change of momentum equals the sum of the forces working on the element. These forces include stress σ at the surface and body forces $\mathbf{F_b}$:

$$\frac{\mathrm{d}\mathbf{p}}{\mathrm{d}t} = \int_V \mathbf{F_b}\,\mathrm{d}V + \int_{\delta V} \sigma\,\mathrm{d}A. \tag{3.4}$$

Using the Green-Gauss theorem, the integral over the boundary δV of the element can be converted into an integral over the volume: $\int_{\delta V} \sigma\,\mathrm{d}A = \int_V \partial\sigma_{ij}/\partial x_i \hat{\mathbf{x}}_i\,\mathrm{d}V$. Eq. 3.4 should hold for *any* element because so far nothing has been specified about the shape or size of the element. This then yields Cauchy's first law of motion [1]:

$$\rho\ddot{u}_j = \frac{\partial\sigma_{ij}}{\partial x_i} + F_j. \tag{3.5}$$

A similar analysis for the angular momentum yields Cauchy's second law of motion: $\sigma_{ij} = \sigma_{ji}$. With these equations (and boundary conditions) the stress distribution can be calculated for a given applied force profile $\mathbf{F_b}(x, y, z)$.

[1] In this Thesis, the so-called Einstein notation [1] for the elements of vectors and tensors is employed. When indices appear on one side of an equal sign only, one sums over them, without explicitly writing the summation sign. For example, $x_i = R_{ij}x_j$ reads as $x_i = \sum_{j=1}^{3} R_{ij}x_j$. The index runs over the three rectangular coordinates (x, y, z), where $x_1 = x$, $x_2 = y$ and $x_3 = z$. Finally, the symbols $\hat{\mathbf{x}}_i$ ($\hat{\mathbf{x}}$, $\hat{\mathbf{y}}$ and $\hat{\mathbf{z}}$) denote the unit vectors in the fixed rectangular coordinate system (which form a basis) so that a vector $\mathbf{r}$ can be expressed as: $\mathbf{r} = r_i\hat{\mathbf{x}}_\mathbf{i}$

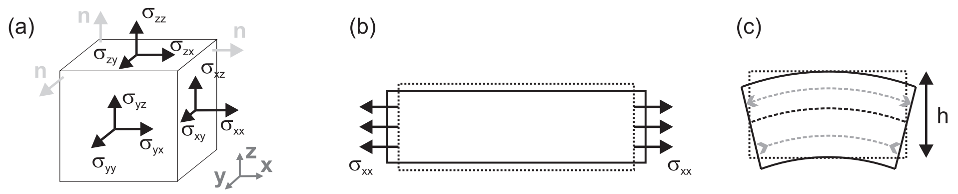

FIGURE 3.1: (a) Visualization of the stress tensor on a cubic element. The force per unit area is the inner product of the stress tensor and the normal vector of the surface **n** (b) Deformation of a plate under plane stress. The original plate (dotted) is deformed by the stress σ_{xx}. (c) Bending of a plate with thickness h. The top part of the plate is extended, whereas the bottom is compressed. The black dashed line indicates the neutral plane.

The strain tensor describes the deformation of the material, whereas the stress tensor gives the forces acting inside the material. These two quantities are of course related to each other. When the deformations are not too large, the stress and strain tensor are related linearly by the elasticity tensor **E**:

$$\sigma_{ij} = E_{ijkl}\gamma_{kl} \tag{3.6}$$

The properties of the stress and strain tensor imply that $E_{ijkl} = E_{jikl} = E_{ijlk} = E_{klij}$, so **E** has at most 21 independent elements out of a total of $3 \times 3 \times 3 \times 3 = 81$ elements. This makes it possible to express Eq. 3.6, containing the fourth rank tensor **E**, in a convenient matrix representation:

$$\begin{bmatrix} \sigma_{xx} \\ \sigma_{yy} \\ \sigma_{zz} \\ \sigma_{xz} \\ \sigma_{yz} \\ \sigma_{xy} \end{bmatrix} = \begin{bmatrix} E_{xxxx} & E_{xxyy} & E_{xxzz} & E_{xxxz} & E_{xxyz} & E_{xxxy} \\ E_{xxyy} & E_{yyyy} & E_{yyzz} & E_{yyxz} & E_{yyyz} & E_{yyyx} \\ E_{xxzz} & E_{yyzz} & E_{zzzz} & E_{zzzx} & E_{zzzy} & E_{zzxy} \\ E_{xxxz} & E_{yyxz} & E_{zzzx} & E_{xzzx} & E_{xzzy} & E_{yxxz} \\ E_{xxyz} & E_{yyyz} & E_{zzzy} & E_{xzzy} & E_{yxxz} & E_{xyyz} \\ E_{xxxy} & E_{yyyx} & E_{zzxy} & E_{yxxz} & E_{xyyz} & E_{xyyx} \end{bmatrix} \begin{bmatrix} \gamma_{xx} \\ \gamma_{yy} \\ \gamma_{zz} \\ 2\gamma_{xz} \\ 2\gamma_{yz} \\ 2\gamma_{xy} \end{bmatrix}, \tag{3.7}$$

or in short hand notation: $[\sigma] = [E][\gamma]$. The inverse of the elasticity tensor is called the compliance tensor **C**, which expresses the strain in terms of the stress:

$$\gamma_{ij} = C_{ijkl}\sigma_{kl}, \text{ or } [\gamma] = [C][\sigma]. \tag{3.8}$$

The number of independent elements of **E** is further reduced when the (crystal structure of the) material has symmetries [2–4]. The most drastic example is an isotropic material, which looks the same in all directions. In this case, only two independent parameters remain: the Young's modulus E and Poisson's ratio ν. The compliance matrix is in this case given by:

$$[C] = \begin{bmatrix} 1/E & -\nu/E & -\nu/E & 0 & 0 & 0 \\ -\nu/E & 1/E & -\nu/E & 0 & 0 & 0 \\ -\nu/E & -\nu/E & 1/E & 0 & 0 & 0 \\ 0 & 0 & 0 & 1/G & 0 & 0 \\ 0 & 0 & 0 & 0 & 1/G & 0 \\ 0 & 0 & 0 & 0 & 0 & 1/G \end{bmatrix}, \tag{3.9}$$

where $G = E/(2+2\nu)$ is the shear modulus. By inverting $[C]$, the elasticity matrix is obtained:

$$[E] = \frac{1}{(1+\nu)(1-2\nu^2)} \begin{bmatrix} E(1-\nu) & E\nu & E\nu & 0 & 0 & 0 \\ E\nu & E(1-\nu) & E\nu & 0 & 0 & 0 \\ E\nu & E\nu & E(1-\nu) & 0 & 0 & 0 \\ 0 & 0 & 0 & G & 0 & 0 \\ 0 & 0 & 0 & 0 & G & 0 \\ 0 & 0 & 0 & 0 & 0 & G \end{bmatrix}. \tag{3.10}$$

When a plane stress σ_{xx} is applied, a material will be stretched in the x-direction, as illustrated in Fig. 3.1b. The resulting strain $\gamma_{xx} = \sigma_{xx}/E$ induces a stress in the y- and z-directions, which are nulled by a negative strain (i.e. contraction) in these directions which is ν times smaller than the strain in the x-direction. This follows directly from the structure of the compliance matrix. Using the elasticity matrix (Eq. 3.10), the stresses due to a plane strain can be calculated [1].

For non-isotropic materials, the Young's modulus and Poisson's ratio depend on the direction of the applied stress and are defined as: $E_i = 1/C_{iiii}$ and $\nu_{ij} = -C_{iijj}/C_{iiii}$ $(i \neq j)$ [5]. The Young's modulus and Poisson's ratio of materials that are frequently used for nanomechanical devices are indicated in Table 3.1.

3.2 ENERGY, BENDING RIGIDITY AND TENSION

In the previous Section the relation between the stress and strain in a material was given. Here, we focus on the energy needed to deform the material. From this, the equations of motion are derived. The potential energy stored in the nanomechanical device depends on the strain field. For small deformations, the potential energy U depends quadratically on the strain and it should also be invariant under coordinate transformations [1], leading to

$$U = \int_V U' \, \mathrm{d}V; \qquad U' = \frac{1}{2} E_{ijkl}\gamma_{ij}\gamma_{kl}, \tag{3.11}$$

so that $\sigma_{ij} = \partial U'/\partial\gamma_{ij}$. For an isotropic material this reduces to [4]:

$$U' = \frac{1}{2}\frac{E}{1+\nu}\left(\gamma_{ij}^2 + \frac{\nu}{1-2\nu}\gamma_{kk}^2\right), \tag{3.12}$$

TABLE 3.1: Mechanical properties of materials that are used in nanomechanical devices. Most materials have a density ρ around $3 \cdot 10^3\,\mathrm{kg/m^3}$ and a Young's modulus of the order of $10^2\,\mathrm{GPa}$. The carbon-based materials graphite and diamond are slightly lighter, but much stiffer. Compiled from Refs. [2] and [6].

Material	$\rho(10^3\,\mathrm{kg/m^3})$	E(Gpa)	ν
Silicon	2.33	130.2	0.28
Si_3N_4	3.10	357	0.25
SiC	3.17	166.4	0.40
SiO_2 (crystaline)	2.65	85.0	0.09
SiO_2 (amorphous)	2.20	~ 80	0.17
Diamond	3.51	992.2	0.14
Graphite (in-plane)	2.20	920	0.052
Graphite (out-of-plane)	2.20	33	0.076
Aluminum	2.70	63.1	0.36
Gold	19.30	43.0	0.46
Platinum	21.50	136.3	0.42
Niobium	8.57	151.5	0.35
GaAs	5.32	85.3	0.31
InAs	5.68	51.4	0.35

When a torque is applied to a beam or plate it bends, as illustrated in Fig. 3.1c. The top part which was at $z = h/2$ is extended whereas the bottom part of the beam, originally at $z = -h/2$, is compressed. There is a plane through the beam where the longitudinal strain is zero, the so-called neutral plane. The vertical displacement of this plane is indicated by $u(x, y)$. For small deflections, the neutral plane lies midway through the plate [4], i.e. at $z = 0$. First the entire displacement profile $u_i(x_j)$ is expressed in terms of $u(x, y)$ to find the equations of motion for $u(x, y)$, following the analysis by Landau and Lifshitz [4]. The radius of curvature R_c of the neutral plane in the bent plate is $R_c = \partial^2 u/\partial x^2$. The bending energy is proportional to R_c^{-2}.

Although Eq. 3.11 is valid for any mechanical system that is in the linear regime, but it is not straightforward to analyze a system this way. Therefore, we focus on plates and beams, simple geometries where the equation of motion can be obtained without too much effort.

PLATES

A plate is a thin object that has a large length and width. The perpendicular stress components at the faces of the plate vanish (except at the clamping points): $\sigma_{ij} n_j$. For a thin plate, the normal vector n_j at the top and bottom face point in the z-direction to first order in u or R_c^{-1}. The condition for vanishing stress thus becomes: $\sigma_{xz} = \sigma_{yz} = \sigma_{zz} = 0$ at the faces. Because the plate is assumed to be thin, this does not only hold at the faces, but also inside the material. For an isotropic material, characterized by its Young's modulus E and

Poisson ratio ν, the displacement and strain fields are:

$$\begin{aligned} u_x &= -z\cdot\partial u/\partial x, & \gamma_{xx} &= -z\cdot\partial^2 u/\partial x^2 \\ u_y &= -z\cdot\partial u/\partial y, & \gamma_{yy} &= -z\cdot\partial^2 u/\partial y^2 \\ u_z &= u, & \gamma_{zz} &= z\nu/(1-\nu)\cdot\nabla^2 u \\ \gamma_{xz} = \gamma_{yz} &= 0, & \gamma_{xy} &= -z\cdot\partial^2 u/\partial x\partial y. \end{aligned} \tag{3.13}$$

Inserting this into Eq. 3.12 and carrying out the integration over z in Eq. 3.11, yields the energy needed to bend the plate:

$$U_B = \frac{Eh^3}{24(1-\nu^2)}\iint\left[\left(\frac{\partial^2 u}{\partial x^2}+\frac{\partial^2 u}{\partial y^2}\right)^2 + 2(1-\nu)\left(\left\{\frac{\partial^2 u}{\partial x\partial y}\right\}^2 - \frac{\partial^2 u}{\partial x^2}\frac{\partial^2 u}{\partial y^2}\right)\right]\mathrm{d}x\,\mathrm{d}y. \tag{3.14}$$

Moreover, the displacement and strain averaged over the thickness h, $\overline{u}_i(x,y)$ and $\overline{\gamma}_{ij}(x,y)$ respectively, are all zero to first order in u, except $\overline{u}_z = u(x,y)$, as the contributions above and below the neutral plane cancel each other.

It is also possible that the plate is not only bent, but that it is also under a longitudinal tension $\mathbf{T}$, which is positive for tensile stress and negative for compressive stress. It is clear that when the plate is bent, i.e. when $\partial^2 u/\partial x^2 \neq 0$, that the longitudinal tension will result in a restoring force in the z-direction. The tension results in a strain field $\overline{\gamma}_{\alpha\beta} = \frac{1}{2}(\partial\overline{u}_\alpha/\partial x_\beta + \partial\overline{u}_\alpha/\partial x_\beta + \partial\overline{u}/\partial x_\alpha\cdot\partial\overline{u}/\partial x_\beta)$, where the Greek indices run over the x and y coordinate only. The stretching energy is in this case:

$$U_T = \frac{1}{2}\iint \gamma_{\alpha\beta}T_{\alpha\beta}\,\mathrm{d}x\,\mathrm{d}y, \text{ where } T_{\alpha\beta} = h\overline{\sigma}_{\alpha\beta}. \tag{3.15}$$

The equation of motion for the vertical deflection of the plate is obtained when the variation of the total potential energy $U = U_B + U_T + U_F$ is considered for an arbitrary variation in the displacement $u \to u+\delta u$. Here, $U_F = -\iint Fu\,\mathrm{d}x\,\mathrm{d}y$ includes the effect of an external force F (per unit area) in the z-direction. Combining this yields the equation of motion:

$$\rho h\frac{\partial^2 u}{\partial t^2} + \left(D\nabla^4 - \frac{\partial}{\partial x_\alpha}T_{\alpha\beta}\frac{\partial}{\partial x_\beta}\right)u(x,y) = F(x,y), \tag{3.16}$$

where ρ is the mass density of the material[2]. $D = Eh^3/12(1-\nu^2)$ is the so-called bending rigidity of the plate that quantifies how much energy it costs to bend a unit area of the plate. The tension satisfies $\partial T_{\alpha\beta}/\partial x_\beta = 0$, making the system of equations non-linear. For small deformations, however, the tension is not caused by the bending of the plate, but instead by clamping. The tension is then independent of u and Eq. 3.16 becomes linear.

[2]Note that in principle the first term should read $\rho h\partial^2 u/\partial t^2 + \rho h^3\partial/\partial t^2(\partial^2 u/\partial x^2 + \partial^2 u/\partial x^2)/12)$ as the material is also moving in the x and y direction. These corrections are, however, negligible when $h/\ell \ll 1$.

FIGURE 3.2: The distance between the clamping points ℓ differs from the length of the free beam ℓ_0 and tension is induced. If the tension is large enough, it is energetically favorable for the beam to displace, releasing strain energy at the cost of bending energy. This is called buckling. Due to the displacement $u(x)$ the length of the beam is extended to $L(t)$.

BEAMS

Many nanomechanical devices have a width that is much smaller then their length. This means that these devices are not plates, but doubly clamped beams or cantilevers as Table 2.1 indicated. For a beam, the normal components of the stress on the side faces should also vanish, i.e. $\sigma_{yy} = \sigma_{xy} = 0$ at $y = \pm w/2$. The derivation of the equation of motion then proceeds as in the case of a plate, but now the integration over y can also be done directly. This yields the Euler-Bernoulli beam equation with tension:

$$\rho A \frac{\partial^2 u}{\partial t^2} + D \frac{\partial^4 u}{\partial x^4} - T \frac{\partial^2 u}{\partial x^2} = F, \tag{3.17}$$

where the cross-sectional area A equals wh for a rectangular beam. The bending rigidity $D = Eh^3 w/12(1-\nu^2)$ can be written as the product of the Young's modulus and the second moment of inertia $D = EI/(1-\nu^2)$, where the small correction $(1-\nu^2)$ is often omitted [2]. Thus for a rectangular beam the second moment of inertia is $I = h^3 w/12$, whereas for a (solid) cylinder with radius r it is $I = \pi r^4/4$ [2]. Note that the units of the bending rigidity, tension and external force are different from the case of a plate due to the integration over the y-coordinate. D is given in Nm^2 instead of $\mathrm{Nm}(=\mathrm{J})$ and T is in N instead of N/m. Finally, the external force is given per unit length instead of per unit area. From the context it should be clear what the meaning of the different symbols is.

3.3 BUCKLED BEAMS

For the SQUID experiments described in Chapter 7, a rectangular beam is used that is buckled. To calibrate the dc SQUID position detector using the temperature dependence of the resonator's Brownian motion, the relation between the displacement u and the change in magnetic flux has to be calculated. This requires a full description of the flexural bending modes of the buckled beam. The analysis presented in this Section also allows the calculation of the resonance frequency, which is in excellent agreement with the experimental results in Ch. 7.

The starting point is the Euler-Bernoulli beam equation (Eq. 3.17) without an external force, i.e. $F = 0$. The boundary conditions of a doubly-clamped beam are $u(x=0) = u(x =$

$\ell) = 0$ and $\partial u/\partial x(x=0) = \partial u/\partial x(x=\ell) = 0$ [2]. The beam is under a tension T that is compressive (negative) for a buckled beam. The tension has two contributions: first the beam can be compressed or elongated by the fact that it is clamped. Figure 3.2a shows that the length of the free beam (ℓ_0) and that of the clamped beam (ℓ) can be different. This is the so-called residual tension, $T_0 = EA\gamma_0$, with $\gamma_0 = (\ell - \ell_0)/\ell_0$. In the case of the SQUID experiments this effect is due to the lattice mismatch between the beam and the substrate. The second contribution comes from the stretching of the beam when it is displaced vertically. The resulting length of the beam is denoted by L. Combining both effects gives:

$$T \approx T_0 + \frac{EA}{2\ell}\int_0^\ell \left(\frac{\partial u}{\partial x}\right)^2 \mathrm{d}x. \tag{3.18}$$

The total deflection u is the sum of a static (u_{dc}) and oscillating part (u_{ac}). To find the eigenmodes of the beam, u_{ac} is taken infinitesimal, so that the beam equation is separated into:

$$D\frac{\partial^4 u_{\mathrm{dc}}}{\partial x^4} - T_{\mathrm{dc}}\frac{\partial^2 u_{\mathrm{dc}}}{\partial x^2} = 0, \tag{3.19}$$

$$\rho A\frac{\partial u_{\mathrm{ac}}^2}{\partial t^2} + D\frac{\partial^4 u_{\mathrm{ac}}}{\partial x^4} - T_{\mathrm{dc}}\frac{\partial^2 u_{\mathrm{ac}}}{\partial x^2} = T_{\mathrm{ac}}\frac{\partial^2 u_{\mathrm{dc}}}{\partial x^2}, \tag{3.20}$$

with:

$$T_{\mathrm{dc}} = T_0 + \frac{EA}{2\ell}\int_0^\ell \left(\frac{\partial u_{\mathrm{dc}}}{\partial x}\right)^2 \mathrm{d}x, \tag{3.21}$$

$$T_{\mathrm{ac}} = \frac{EA}{\ell}\int_0^\ell \frac{\partial u_{\mathrm{dc}}}{\partial x}\frac{\partial u_{\mathrm{ac}}}{\partial x}\mathrm{d}x. \tag{3.22}$$

Eq. 3.19 only has a non-trivial solution $u_{\mathrm{dc}} = u_{\max}[1-\cos(2\pi n x/\ell)]/2$ when $T_{\mathrm{dc}} = n^2 T_c$, where $T_c = -4\pi^2 D/L^2$ is the critical tension at which the beam buckles and n is an integer. When an initially unstrained beam is compressed slightly, work is done and the energy stored in U_T increases. When the compressive residual tension T_0 is made more negative than T_c, it becomes energetically favorable for the beam to convert a part of U_T into the bending energy U_B. The beam buckles to a displacement that keeps the tension exactly at T_c (for n=1). The value of the displacement depends on the residual tension that caused it: $u_{\max} = 2\ell/\pi([T_c - T_0]/EA)^{1/2}$.

The eigenfrequencies of buckled beams were calculated by Nayfeh *et al.* [7]. Following this analysis, the homogeneous solution to Eq. 3.20 is written as:

$$u_{\mathrm{ac}}^{(h)} = c_1\sin(k_+ x/\ell) + c_2\cos(k_+ x/\ell) + c_3\sinh(k_- x/\ell) + c_4\cosh(k_- x/\ell), \tag{3.23}$$

with:

$$k_\pm = \left(\pm 2\pi^2 + \sqrt{(2\pi^2)^2 + \frac{m\omega^2\ell^3}{D}}\right)^{1/2}. \tag{3.24}$$

A particular solution is:

$$u_{\mathrm{ac}}^{(p)} = c_5 \cos(2\pi x/\ell). \tag{3.25}$$

The boundary conditions provide four equations for the five coefficients c_i. A fifth equation is obtained when the entire solution $u_{\mathrm{ac}} = u_{\mathrm{ac}}^{(h)} + u_{\mathrm{ac}}^{(p)}$ is inserted into Eqs. 3.20 and 3.22 as the right hand side of Eq. 3.20 depends on u_{ac} itself. These conditions can be written as:

$$\begin{bmatrix} 0 & 1 & 0 & 1 & 1 \\ k_+ & 0 & k_- & 0 & 0 \\ \sin k_+ & \cos k_+ & \sinh k_- & \cosh k_- & 1 \\ k_+ \cos k_+ & -k_+ \sin k_+ & k_- \cosh k_- & k_- \sinh k_- & 0 \\ \frac{k_+ \cos k_+ - k_+}{k_+^2 - 4\pi^2} & -\frac{k_+ \sin k_+}{k_+^2 - 4\pi^2} & -\frac{k_- \cosh k_- - k_-}{k_-^2 - 4\pi^2} & -\frac{k_- \sinh k_-}{k_-^2 - 4\pi^2} & \frac{\omega^2 m \ell^4}{4\pi^4 E A u_{\max}^2} - \frac{1}{2} \end{bmatrix} \times$$

$$\begin{bmatrix} c_1 \\ c_2 \\ c_3 \\ c_4 \\ c_5 \end{bmatrix} = \begin{bmatrix} 0 \\ 0 \\ 0 \\ 0 \\ 0 \end{bmatrix}. \tag{3.26}$$

This equation has the trivial solution $c_i = 0$ for every value of ω, but at the eigenfrequencies a solution exists with some of the coefficients c_i non-zero. This only occurs when the matrix in Eq. 3.26 is not invertible, i.e. at the frequencies $\omega = \omega_n$ where its determinant is zero. The eigenfrequencies and modes are calculated for the beam used in Ch. 7 which has a length $\ell = 50\,\mu$m, a bending rigidity $D = 3.20 \cdot 10^{-15}$ J and a buckling displacement $u_{\max} = 1.5\,\mu$m. Figure 3.3 shows that the frequency of the fundamental mode increases with increasing buckling. The second mode has an eigenfrequency $\omega_2/2\pi = 1.44$ MHz and is independent of $u_{\max}$, as the mode is anti-symmetric around the node, giving $T_{\mathrm{ac}} = 0$. When $u_{\max}$ is increased to $0.92\,\mu$m, the two lowest modes cross and the fundamental mode is higher in frequency than the second mode.[3] Thus, when the length of the beam, bending rigidity and the buckling displacement are known, the eigenfrequencies and modeshapes of a buckled beam can be calculated.

3.4 CARBON-BASED NEMS

Carbon exists in many different forms, ranging from amorphous coal to crystalline graphite and diamond. Diamond has a face-centered cubic structure as shown in Fig. 3.4a and is one of the hardest materials known. Its Young's modulus (Table 3.1) is extremely high: about 1 TPa. Graphite has a very different crystal structure: it consists of stacked planes of carbon atoms in a hexagonal arrangement (Fig. 3.4b). Its Young's modulus for in-plane

[3] We classify the modes by their shape and not by the ordering of eigenfrequencies. The fundamental mode is the mode without a node.

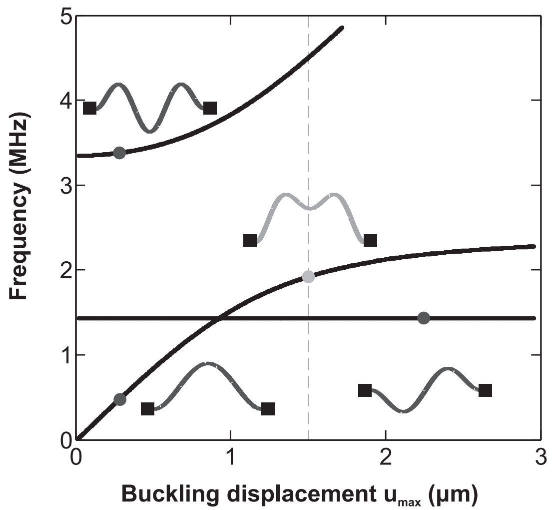

FIGURE 3.3: The calculated eigenfrequencies of the beam used in Ch. 7. The mode shapes at the position of the dots are shown. At a buckling of $u_{max} = 1.5\,\mu$m (dashed line), the fundamental flexural mode (inset) has an eigenfrequency of 1.93 MHz.

stress is nearly as high as that of diamond, but it is much lower for out-of-plane stress as Table 3.1 indicates. This difference is caused by the nature of the bonds holding the carbon atoms together. Atoms in one of the planes are covalently bonded to each other, whereas different planes are held together by the much weaker van der Waals force.

Graphite and diamond were already known for millennia, but in the last decades novel allotropes of carbon were discovered. First, in 1985 C_{60} molecules, called buckyballs, were discovered [8]. Then in the early 1990s carbon nanotubes were discovered [9]. These consist of cylinders of hexagonally ordered carbon atoms; similar to what one would get if one would take a single layer of graphite and role it up into a cylinder. Figure 3.4 shows the structure of these four different carbon allotropes. In 2004 another allotrope called "graphene" was discovered [10, 11]. This is a single layer of graphite, which is, unlike a nanotube, flat. This material is usually deposited onto a substrate using mechanical exfoliation and sheets of mm-size have been reported [12]. Although truly two-dimensional structures are not energetically stable [13], graphene can exist due to fact that it contains ripples that stabilize its atomically thin structure [14–17].

Although nanomechanical devices have been made out of diamond using top-down fabrication techniques [18, 19], the focus in this Thesis is on bottom-up fabricated carbon-based NEMS made from few-layer graphene or suspended carbon nanotubes. First, the basic structure of graphene and graphite are studied and then it is discussed how these

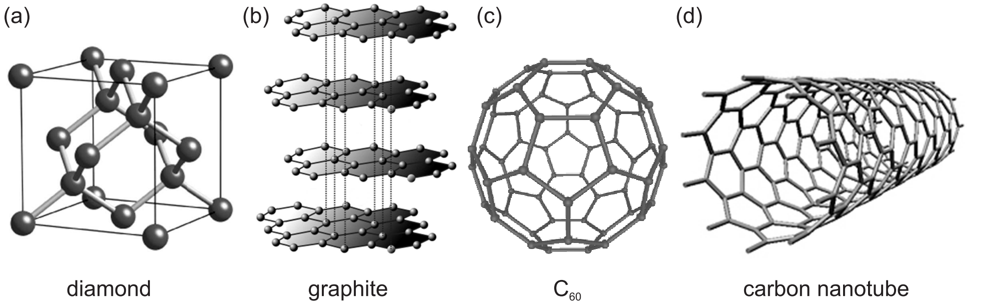

FIGURE 3.4: The structure of the different allotropes of carbon. (a) Diamond has two intertwined face-centered cubic lattices. (b) Graphite consists of stacked planes of hexagonally ordered carbon atoms. A single plane is called a "graphene sheet". (c) A C_{60} buckyball molecule. (d) A single-walled carbon nanotube, which can be viewed as a graphene sheet that has been rolled up and sewn together.
Image (a) adapted from H. Tsuya: JPSJ Online-News and Comments [Apr. 10, 2006]. Images (b) and (c) were taken from wikipedia.org. Image (d) courtesy of Maria Foldvari: `http://www.pharmacy.uwaterloo.ca/research/foldvari/about/index.html`

results can be used to understand the mechanical properties of nanotubes and of very thin graphite structures.

The unit cell of graphene consists of a hexagon with a carbon atom on each corner and has its sides have a length $d_{cc} = 0.14\,\text{nm}$, as illustrated in Fig. 3.5a. Each of these six carbon atoms lies in three different unit cells; a single unit cell thus contains two carbon atoms. The unit cell has an area of $5.22\cdot10^{-20}\,\text{m}^2$ so the two-dimensional mass density is $\rho_{2d} = 6.8\cdot10^{-7}\,\text{kg/m}^2$. From this number the mass of a single-walled carbon nanotube (SWNT) can be calculated. A SWNT with radius r has a mass per unit length of $2\pi r\rho_{2d}$. In most nanotube growth procedures, not just SWNTs are produced, but also multi-walled nanotubes (MWNTs) and ropes. MWNTs consist of SWNTs wrapped around each other and ropes are bundles of nanotubes that lie against each other. These structures have a larger mass per unit length then a SWNT with the same radius. In principle, their mass can be found by counting the number of carbon atoms that it contains, but often only their outer dimensions can be measured and the inner structure remains unknown. Fortunately, to a good approximation, the linear mass density is given by ρA, with $A = \pi r^2$ and $\rho = 1.35\cdot10^3\,\text{kg/m}^3$ for the different types of carbon nanotube structures.

In graphite the graphene layers are stacked on top of each other (see Fig. 3.4b and 3.5b) with an inter-layer spacing $c = 0.335\,\text{nm}$. The planes are not located exactly above each other but every other layer is shifted by half the unit cell, or equivalently, it is rotated by 60^o around an axis through one of the carbon atoms. Three of the six atoms are on top of the atoms in the other layer and the other three are located at the center of the hexagon

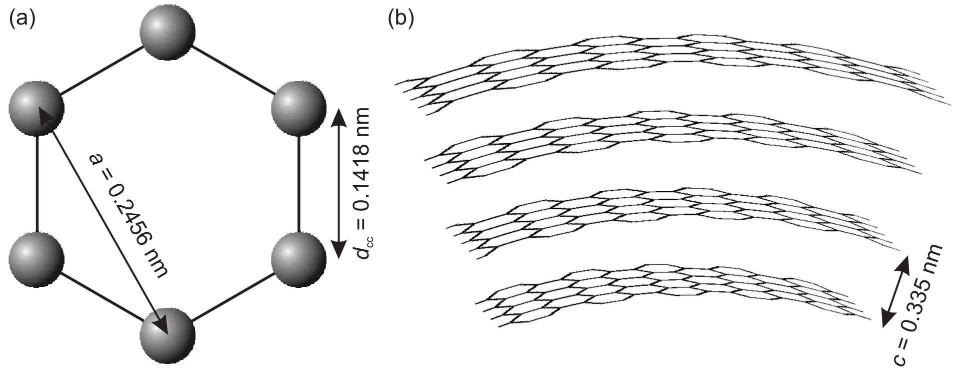

FIGURE 3.5: (a) The unit cell of graphene with the dimensions indicated. a is the length of the two translation vectors $\mathbf{a}_{1,2} = \frac{1}{2}a[\pm 1, \sqrt{3}, 0]$, and d_{cc} is the distance between two carbon atoms. The area of the unit cell is $\frac{1}{2}\sqrt{3}a^2 = 5.22 \cdot 10^{-20}\,\mathrm{m}^2$. (b) Bending of a few-layer graphene sheet. The distance between the graphene layers is $c = 0.335\,\mathrm{nm}$.

below them. The elasticity tensor of graphite is represented by[4] [3]:

$$[E] = \begin{bmatrix} 1.16 & 0.29 & 0.11 & 0 & 0 & 0 \\ 0.29 & 1.16 & 0.11 & 0 & 0 & 0 \\ 0.11 & 0.11 & 0.05 & 0 & 0 & 0 \\ 0 & 0 & 0 & 0.002 & & 0 \\ 0 & 0 & 0 & 0 & 0.002 & 0 \\ 0 & 0 & 0 & 0 & 0 & 0.44 \end{bmatrix} \mathrm{TPa}. \tag{3.27}$$

The hexagonal lattices formed by the carbon atoms have a six-fold rotational symmetry, which ensures that the elastic properties are the same when looking in any direction along the planes, i.e. they are isotropic in those directions [3, 4]. On the other hand, the mechanical properties for deformations perpendicular to the planes are quite different. It is therefore convenient to introduce the in- and out-of-plane Young's modulus, $E_{\Box}$ and $E_{\perp}$ respectively, and the corresponding Poisson's ratios $\nu_{\Box}$ and $\nu_{\perp}$. They are defined such that

[4]The values of the elastic constants depend on the quality of the graphite samples. Therefore, slightly different values can be found in the literature. Compare, for example, the data in Refs. [20] and [21] with the values in Ref. [3]

the compliance matrix is given by[5]:

$$[C] = \begin{bmatrix} 1/E_{\square} & -\nu_{\square}/E_{\square} & -\nu_{\perp}/E_{\perp} & 0 & 0 & 0 \\ -\nu_{\square}/E_{\square} & 1/E_{\square} & -\nu_{\perp}/E_{\perp} & 0 & 0 & 0 \\ -\nu_{\perp}/E_{\perp} & -\nu_{\perp}/E_{\perp} & 1/E_{\perp} & 0 & 0 & 0 \\ 0 & 0 & 0 & 1/G_{\square} & 0 & 0 \\ 0 & 0 & 0 & 0 & 1/G_{\square} & 0 \\ 0 & 0 & 0 & 0 & 0 & 1/G_{\perp} \end{bmatrix}, \tag{3.28}$$

where $E_{\square} = 0.92\,\mathrm{TPa}$, $E_{\perp} = 33\,\mathrm{GPa}$, $G_{\square} = 1.8\,\mathrm{GPa}$, $G_{\perp} = 0.44\,\mathrm{TPa}$, $\nu_{\square} = 0.052$ and $\nu_{\perp} = 0.076$.

The bending rigidity for an anisotropic material depends on the direction of bending. Therefore, for graphite the analysis in Sec. 3.2 has to be generalized. The rigidity for bending along the sheets (see Fig. 3.5b) is calculated using the compliance tensor in Eq. 3.28:

$$D = E_{\square} h^3 / 12(1 - \nu_{\square}^2), \tag{3.29}$$

which only contains the in-plane elastic constants. When the number of graphene layers becomes small, corrections to Eq. 3.29 have to be made. Consider the situation in Fig. 3.5b where a few-layer graphene sheet is bent with a radius of curvature R_c. In the continuum case, the bending energy is given by $U_B/\ell W \equiv \frac{1}{2} D/R_c^2 = \frac{1}{2}\int_{-h/2}^{h/2} E_{\square}(z/R_c)^2\,\mathrm{d}z$, when taking $\nu = 0$ for simplicity. In the case of a small number of layers N, the continuum approximation in the z-direction is no longer valid and the stress is located only at the position of the sheets $z_i = c(i - [N+1]/2)$. The integral over z is replaced by a sum and the bending rigidity becomes:

$$D_N = \frac{E_{\square} h^3}{12(1-\nu_{\square}^2)} \frac{N-1}{N}, \tag{3.30}$$

where the thickness is set by the number of layers $h = Nc$. For a single layer the bending rigidity vanishes according to Eq. 3.30. However, molecular dynamics simulations have shown that a single layer of graphene still has a finite bending rigidity: of the order of one eV [16, 22, 23] (compare this to the value for a double layer calculated with Eq. 3.30: $D_2 = 54\,\mathrm{eV}$). The rigidity of a single layer comes from the fact that electrons in the delocalized π-orbitals, located below and above the sheet, repel each other when the sheet is bent [23]. Moreover, molecular dynamics simulations also show that nanotube devices [24] and graphene membranes [25–27] are accurately described by continuum mechanics, taking the modifications of the bending rigidity into account.

3.5 SUSPENDED CARBON NANOTUBES

In Chapters 5 and 6 the flexural bending mode vibrations of suspended nanotubes are studied. An AFM image of a typical device is shown in Fig. 3.6a. A nanotube is connected

[5] Note that this definition is slightly different from the conventional definition of the Poisson's ratio in an anisotropic material where $\nu_{xz} = -C_{xxzz}/C_{xxxx}$ and $\nu_{zx} = -C_{xxzz}/C_{zzzz}$ [5].

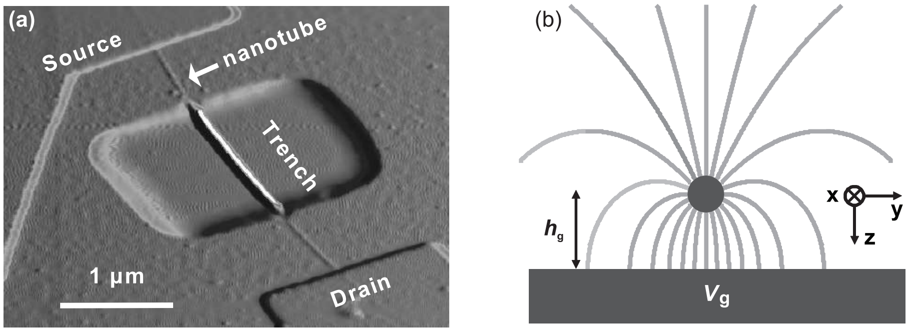

FIGURE 3.6: (a) an AFM image of a suspended nanotube device connected to the source and drain electrode. The tube is suspended above the trench only. This device has a length $\ell = 1.25\,\mu$m and the radius of the tube is: $r = 1.4$ nm. (b) Field lines of the electrostatic potential induced by the gate electrode. When the distance between the tube and the gate h changes, the gate capacitance C_g changes.

to source and drain electrodes, enabling transport measurements. The tube is suspended above a gate electrode at a distance h_g, which can be used to drive the resonator [28]. One of the key features of these thin resonators is that their frequency is electrically tunable over a large range with a static gate voltage.

In the experiments described in Chapters 5 and 6, suspended nanotubes that bridge a length of the order of one micrometer are used. This is long enough for the continuum approximation to be valid as shown in Ref. [24]. The bending mode vibrations are therefore accurately described by the Euler-Bernoulli beam equation [29, 30] with tension included, i.e. Eq. 3.17. The electrostatic force per unit length $F(x,t)$ depends on the capacitance between the nanotube and the gate electrode C_g and the voltage V_g between them. The capacitance depends on the distance between the gate and the tube $h_\mathrm{g} - u(x)$. This implies that the potential energy[6] $U_F = -C_\mathrm{g} V_\mathrm{g}^2/2$ is displacement dependent, which results in a force F on the tube. Under the assumption that the effect of the source and drain electrodes is negligible, the tube is basically an infinitely long grounded cylinder, suspended above a conducting plate at an electrostatic potential $\phi(z=0) = V_\mathrm{g}$. The potential profile for $u = 0$ is given by [32]:

$$\phi(y,z) = V_\mathrm{g} - V_g \frac{1}{\operatorname{arccosh}(h_\mathrm{g}/r)} \ln\left(\frac{\left[z + \sqrt{h_\mathrm{g}^2 - r^2}\right]^2 + y^2}{\left[z - \sqrt{h_\mathrm{g}^2 - r^2}\right]^2 + y^2} \right). \tag{3.31}$$

The field lines associated with this potential are shown in Fig. 3.6b. The deflection of the nanotube is included account by replacing h_g with $h_\mathrm{g} - u$. After dividing the locally

[6]This is the potential energy for the tube, in contrast to the energy stored in the capacitor: $+C_\mathrm{g} V_\mathrm{g}^2/2$. The difference in the sign is because the voltage source performs work when the capacitance changes [31], which should also be taken into account.

induced charge by the gate voltage, the capacitance per unit length $c_g(x)$ is obtained[7]:

$$c_g(x) = \frac{2\pi\epsilon_0}{\operatorname{arccosh}\big([h_\mathrm{g} - u(x)]/r\big)} \approx \frac{2\pi\epsilon_0}{\operatorname{arccosh}\big(h_\mathrm{g}/r\big)} + \frac{2\pi\epsilon_0}{\sqrt{h_\mathrm{g}^2 - r^2}\,\operatorname{arccosh}^2\big(h_\mathrm{g}/r\big)} u(x). \quad (3.32)$$

The last approximation is allowed because the displacement u is much smaller than h_g. This in contrast to top-down fabricated devices, where higher order terms can be important and electrostatic softening of the spring constant might occur [34]. The electrostatic potential energy is written as: $U_F = -\int_0^\ell c_g(x) V_\mathrm{g}^2/2\,\mathrm{d}x$ which equals by definition $U_F = -\int_0^\ell F u\,\mathrm{d}x$, so that the force per unit length F equals:

$$F(t) = \frac{1}{2}\frac{\partial c_g}{\partial u} V_\mathrm{g}^2(t) = \frac{\pi\epsilon_0 V_\mathrm{g}^2(t)}{\sqrt{h_\mathrm{g}^2 - r^2}\,\operatorname{arccosh}^2\big(h_\mathrm{g}/r\big)}. \quad (3.33)$$

The gate voltage consists of two parts: a static part V_g^dc and a time-dependent part $V_\mathrm{g}^\mathrm{ac}\cos(\omega t)$ to drive the nanotube at frequency $f = \omega/2\pi$. The experimental condition $V_\mathrm{g}^\mathrm{ac} \ll V_\mathrm{g}^\mathrm{dc}$ ensures that terms proportional to $(V_\mathrm{g}^\mathrm{ac})^2$ are negligible. The force is then the sum of a static and driving contribution: $F = F_\mathrm{dc} + F_\mathrm{ac}\cos(\omega t)$, with $F_\mathrm{dc} = \pi\epsilon_0/(h_\mathrm{g}^2 - r^2)^{1/2}\operatorname{arccosh}^2\big(h_\mathrm{g}/r\big)\cdot(V_\mathrm{g}^\mathrm{dc})^2$ and $F_\mathrm{ac}(t) = \pi\epsilon_0/(h_\mathrm{g}^2 - r^2)^{1/2}\operatorname{arccosh}^2\big(h_\mathrm{g}/r\big)\cdot 2V_\mathrm{g}^\mathrm{dc}V_\mathrm{g}^\mathrm{ac}(t)$.

When the amplitude of the oscillation u_ac is small compared to the larger of the tube's radius and the static displacement, terms proportional to u_ac^2 are negligible and the tube is in the linear regime[8]. Similar to the analysis presented in the previous section the equation of motion (Cf. Eq. 3.17) can be separated in this case:

$$D\frac{\partial^4 u_\mathrm{dc}}{\partial x^4} - T_\mathrm{dc}\frac{\partial^2 u_\mathrm{dc}}{\partial x^2} = F_\mathrm{dc}, \quad (3.34)$$

$$-\omega^2\rho A u_\mathrm{ac} + i\omega\eta u_\mathrm{ac} + D\frac{\partial^4 u_\mathrm{ac}}{\partial x^4} - T_\mathrm{dc}\frac{\partial^2 u_\mathrm{ac}}{\partial x^2} - T_\mathrm{ac}\frac{\partial^2 u_\mathrm{dc}}{\partial x^2} = F_\mathrm{ac}. \quad (3.35)$$

The driving force excites oscillations of the tube that can be tuned with the dc tension, which is calculated using the equation for the static displacement.

TENSION

Similar to the case of the buckled beam, the tension has two contributions. The first one is due to the clamping: The length of the suspended part of the tube is not necessarily equal to the length when it would not be clamped. The tube could be strained during the

[7] This expression might appear different from those in Refs [29] and [33], but note that $\operatorname{arccosh}(x) = \ln(x + \sqrt{x^2 - 1}) \approx \ln(2x)$ for $x \gg 1$.

[8] This refers to the dynamical behavior. The static displacement is actually nonlinear when the tube is in the strong bending limit [29].

growth process or lay slightly curved on the substrate before suspending it. This is the residual tension, T_0. The second contribution is the displacement-induced tension: The gate electrode pulls the nanotube towards it, thereby elongating the tube. Moreover, an oscillating nanotube experiences a time-dependent variation in its length. Both effects are included in Eq. 3.18. As it contains the static displacement, it has to be solved self-consistently [29, 33] with Eq. 3.34 to find the static displacement. The resulting tension is then inserted into Eq. 3.35 to find the eigenfrequencies ω_n and the response function $u_{\mathrm{ac}}(x,\omega)$.

SCALING AND STATIC DISPLACEMENT

To analyze the system of equations 3.34, 3.35 and 3.18, it is useful to take a closer look at their scaling behavior [33]. In this section, we use the convention that primed variables indicate scaled (dimensionless) variables. An obvious way to normalize the coordinate x is to divide it by the tube length: $x' = x/\ell$, so that the equation for the static displacement Eq. 3.34 becomes:

$$\frac{\partial^4 u_{\mathrm{dc}}}{\partial x'^4} - \frac{\ell^2 T_{\mathrm{dc}}}{D}\frac{\partial^2 u_{\mathrm{dc}}}{\partial x'^2} = \frac{\ell^4 F_{\mathrm{dc}}}{D} \equiv l_{\mathrm{dc}}. \tag{3.36}$$

On the right hand side, a natural length scale for the static displacement, l_{dc}, appears. However, scaling the displacement with l_{dc} is not handy because l_{dc} equals zero at zero gate voltage. Therefore u_{dc} (and u_{ac}) are scaled by the radius of the tube: $u'_{\mathrm{dc}} = u_{\mathrm{dc}}/r$. Moreover, the tension has become dimensionless, resulting in an equation for the static displacement where the number of parameters has been reduced from 5 to 2:

$$\frac{\partial^4 u'_{\mathrm{dc}}}{\partial x'^4} - T'_{\mathrm{dc}}\frac{\partial^2 u'_{\mathrm{dc}}}{\partial x'^2} = l'_{\mathrm{dc}}, \tag{3.37}$$

where

$$T'_{\mathrm{dc}} = \frac{\ell^2 T_{\mathrm{dc}}}{D} = T'_0 + \frac{Ar^2}{2I}\int_0^1 \left(\frac{\partial u'_{\mathrm{dc}}}{\partial x'}\right)^2 \mathrm{d}x' \quad \text{and} \quad l'_{\mathrm{dc}} = l_{\mathrm{dc}}/r. \tag{3.38}$$

The definition of T'_{dc} with the ℓ^2 dependence shows that tension becomes more and more important when the length of the device increases. Note, that for a cylindrical resonator $Ar^2/2I = 2$ so that the strain in the nanotube is $\gamma = (r/2\ell)^2 T'_{\mathrm{dc}}$. The solution[9] to Eq. 3.37 is [35, 36]:

$$u'_{\mathrm{dc}}(x') = \frac{l'_{\mathrm{dc}}}{2k^2}\left(\frac{\sinh(k)(\cosh(kx')-1)}{k\cosh(k)-k} - \frac{\sinh(kx')}{k} - x'(x'-1)\right), \tag{3.39}$$

with $k = T'^{1/2}_{\mathrm{dc}}$. Figure 3.7a shows the dc displacement profiles for different values of the static tension. In the case where the bending rigidity dominates (top panel) the profile is rounded at the edge, whereas for high tension (lower panel) the profile is much sharper.

[9] In this section a finite static force is assumed. For the case $\ell_{\mathrm{dc}} = 0$ with $T_0 < T_c$ see the previous Section.

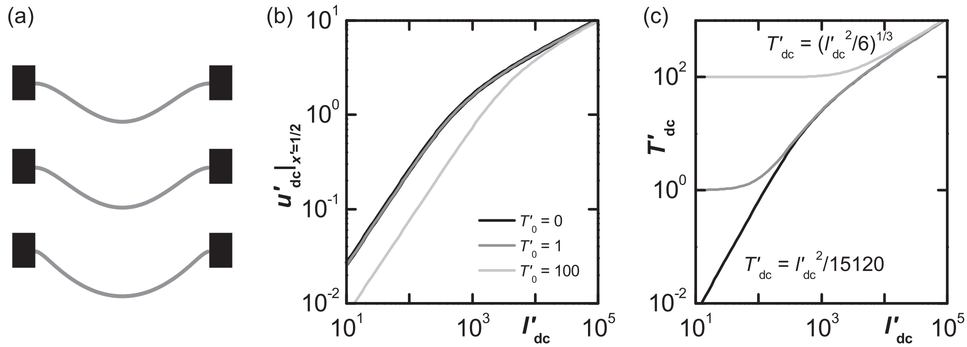

FIGURE 3.7: (a) static displacement profiles for $T'_{dc} = 0$ (top), $T'_{dc} = 50$ (middle) and $T'_{dc} = 10^3$ (bottom). (b) the calculated static displacement at the center of the nanotube and the corresponding tension (c) for various value of the residual tension T'_0. The limits for the tension for small and large static forces are indicated.

The tension and center deflection are calculated by solving Eq. 3.39 self-consistently with 3.38 and are plotted in Fig. 3.7b and c. Two different slopes can be distinguished in the double-logarithmic plot of Fig. 3.7b. These correspond to the weak and strong bending regime of the nanotube [29]. The two regimes cross at $T'^*_{dc} = 6\sqrt{70} \approx 50.2$, $l^*_{dc'} = 36 \cdot 70^{3/4} \approx 871$. The gate voltage at which $l'_{dc} = l^*_{dc'}$ is called the cross-over voltage, V^*_g. Finally, the static spring constant can be defined as the force required to deflect the center of the nanotube by a given amount:

$$k_{dc} \equiv \left(\frac{\partial u_{dc}(\ell/2)}{\partial \ell F_{dc}}\right)^{-1} = \frac{D}{\ell^3}\left(\frac{\mathrm{d}u'_{dc}}{\mathrm{d}l'_{dc}}\right)^{-1} = \frac{D}{\ell^3}\left(\frac{\partial u'_{dc}}{\partial l'_{dc}} + \frac{\partial u'_{dc}}{\partial T'_{dc}}\frac{\partial T'_{dc}}{\partial l'_{dc}}\right)^{-1}. \tag{3.40}$$

The first term gives the linear response on the applied force; the second term is important in the strong bending regime.

EIGENFREQUENCIES

A similar scaling analysis can be applied to Eq. 3.35. One immediately finds the length scale $l_{ac} = \ell^4 F_{ac}/D$ for the ac force and $T'_{ac} = T_{ac}\ell^2/EI$. Furthermore, $\Omega = (D/\rho A)^{1/2}/\ell^2$ is the characteristic frequency scale for the bending mode vibrations. With $t' = t\Omega$ and $\omega' = \omega/\Omega$, the dynamic equation becomes[10]:

$$-\omega'^2 u'_{ac} + i\omega'\eta' u'_{ac} + \frac{\partial^4 u'_{ac}}{\partial x'^4} - T'_{dc}\frac{\partial^2 u'_{ac}}{\partial x'^2} - T'_{ac}\frac{\partial^2 u'_{dc}}{\partial x'^2} = l'_{ac}, \tag{3.41}$$

where similar to the static tension

$$T'_{ac} = \frac{\ell^2 T_{ac}}{D} = 4\int_0^1 \frac{\partial u'_{ac}}{\partial x'}\frac{\partial u'_{dc}}{\partial x'}\,\mathrm{d}x'. \tag{3.42}$$

[10] $\eta' = \eta\ell^4\Omega/D$, so that when $\eta \equiv m\omega_R/Q\ell$ the dimensionless damping parameter becomes: $\eta' = \omega'_R/Q$.

Now consider the eigenfunctions $\xi_n(x')$ of the operator $\mathscr{L}$ that contains the spatial part of Eq. 3.41:

$$\mathscr{L}\xi_n(x') = \left(\frac{\partial^4}{\partial x'^4} - T'_{\mathrm{dc}}\frac{\partial^2}{\partial x'^2}\right)\xi_n - T'_{\mathrm{ac}}[\xi_n]\frac{\partial^2 u'_{\mathrm{dc}}}{\partial x'^2} = \omega_n'^2(T_{\mathrm{dc}}, u_{\mathrm{dc}})\cdot\xi_n(x'). \tag{3.43}$$

The eigenfunctions $\xi_n(x')$ are orthonormalized:

$$\int_0^1 \xi_m(x')\xi_n(x')\,\mathrm{d}x' = \delta_{m,n}. \tag{3.44}$$

The displacement is expanded [11] in the basis formed by the eigenfunctions ξ_n [38, 39]:

$$u_{\mathrm{ac}}(x) = \sum_n u_{\mathrm{ac}}^{(n)}\cdot\xi_n(x). \tag{3.45}$$

Inserting this into 3.41 and taking the inner product with ξ_n yields the displacement of mode n, $u_{\mathrm{ac}}^{(n)}$:

$$\left(\omega_n'^2 - \omega'^2 + i\omega'\eta'\right)u_{\mathrm{ac}}^{(n)} = l_{\mathrm{ac}}a_n; \qquad a_n = \int_0^1 \xi_n(x')\,\mathrm{d}x'. \tag{3.46}$$

So, as anticipated in Ch. 2, the frequency response of each mode is equal to the response function of a damped driven harmonic oscillator. Note that with these definitions, the mass and spring constant appearing in the zero-point motion (Eq. 2.7) and the equipartition theorem (Eq. 2.10) are equal to the total mass m and $k_R = m\omega_n^2$ respectively. There is no need at all to introduce an effective mass. Anti-symmetric modes have a vanishing value of a_n and are usually not visible in nanomechanical experiments as in most cases both the driving and detection mechanisms couple to the average displacement of the resonator. Different detectors or driving forces might couple differently to the displacement profile and could detect these modes. An example of this is a nanotube resonator coupled to a local gate instead of a back gate.

The eigenfunctions of $\mathscr{L}$ are found using an analysis similar to the one presented the previous Section. The homogeneous solution (i.e. the solution with the ac tension term equal to zero) to Eq. 3.43 is:

$$\xi_n^{(h)} = c_1\sin(k_+x') + c_2\cos(k_+x') + c_3\sinh(k_-x') + c_4\cosh(k_-x'), \tag{3.47}$$

where the definition of $k_\pm$, Eq. 3.24, is generalized to:

$$k_\pm = \left(\mp T'_{\mathrm{dc}}/2 + \sqrt{(T'_{\mathrm{dc}}/2)^2 + \omega'^2}\right)^{1/2}, \tag{3.48}$$

[11] The operator $\mathscr{L}$ is Hermitian when working on functions that satisfy the boundary conditions. This vector space is thus spanned by the orthogonal eigenfunctions of $\mathscr{L}$ for any (fixed) value of T'_{dc} [37]. Note, that the operator itself depends on the the static tension and displacement: $\mathscr{L} = \mathscr{L}(T'_{\mathrm{dc}}, u'_{\mathrm{dc}})$.

as the static tension is no longer exactly at the critical value $T_{\text{dc}} = T_c$. A particular solution to Eq. 3.43 is:

$$\xi_n^{(p)} = c_5 \left(\frac{1}{2k} \frac{\sinh(k)\cosh(kx')}{\cosh(k)-1} - \frac{\sinh(kx')}{2k} - \frac{1}{k^2} \right) = \frac{c_5}{l'_{\text{dc}}} \frac{\partial^2 u'_{\text{dc}}}{\partial x'^2}. \tag{3.49}$$

Again, the boundary conditions provide four equations for the five coefficients c_i and the fifth equation is obtained when the entire solution $\xi_n(x') = \xi_n^{(h)}(x') + \xi^{(p)}(x')$ is inserted into Eqs. 3.42 and 3.43 yielding:

$$\begin{bmatrix} 0 & 1 & 0 & 1 & \mu \\ k_+ & 0 & k_- & 0 & -1/2 \\ \sin k_+ & \cos k_+ & \sinh k_- & \cosh k_- & \mu \\ k_+ \cos k_+ & -k_+ \sin k_+ & k_- \cosh k_- & k_- \sinh k_- & 1/2 \\ \mathscr{D}[\sin k_+ x'] & \mathscr{D}[\cos k_+ x')] & \mathscr{D}[\sinh k_- x'] & \mathscr{D}[\cosh k_- x')] & \mathscr{D}[\xi^{(p)}/c_5] - \omega'^2/l_{\text{dc}}.^2 \end{bmatrix} \times$$

$$\begin{bmatrix} c_1 \\ c_2 \\ c_3 \\ c_4 \\ c_5 \end{bmatrix} = \begin{bmatrix} 0 \\ 0 \\ 0 \\ 0 \\ 0 \end{bmatrix}, \tag{3.50}$$

where $\mu = \sinh(k)/(2k\cosh(k) - 2k) - 1/k^2$ is the displacement of the particular solution at the boundaries: $\mu = \xi^{(p)}(0)/c_5 = \xi^{(p)}(1)/c_5$ and $\mathscr{D}[f(x')] = 4\int_0^1 f(x') \cdot \partial^2(u'_{\text{dc}}/l'_{\text{dc}})/\partial x'^2 \, \mathrm{d}x'$. The analytical solutions of the $\mathscr{D}[f]$ are given in Ref. [36].

In the absence of tension, the resonance frequency of the first bending mode is [2]: $f_0 \approx 22.4 \cdot \Omega/2\pi$, and the other eigenfrequencies are given in Table 3.2. Note that these frequencies do not have a harmonic spectrum. If, on the other hand, a large residual tension is present and the static deflection is small ($T'_{\text{dc}} \approx T'_0 \gg 1$) the resonance frequency is that of a string under tension:

$$f_{T_0,n} = \frac{n+1}{2\ell} \sqrt{\frac{T_{\text{dc}}}{\rho A}}, \tag{3.51}$$

where the higher modes are harmonics of the fundamental one. This well-known "guitar string" behavior changes when the tension is induced by the gate. In this case ($T'_{\text{dc}} \gg T'_0, 1$) the nanotube behaves more like a rubber band that is under tension due to its own weight. The ac tension has to be included and the resonance frequencies are:

$$f_{T_{\text{dc}},n} = \frac{n+1}{2\ell} \sqrt{\frac{T_{\text{dc}}}{\rho A}} \cdot \left(1 + \frac{6a_n^2}{\pi^2 (n+1)^2}\right)^{1/2}. \tag{3.52}$$

For odd modes $a_n = 0$ and the resonance frequencies equal that of a string under tension (Eq. 3.51), but for even modes the frequencies are different. Table 3.2 indicates that the ac tension only changes the first few modes significantly.

TABLE 3.2: Eigenfrequencies and other parameters for the first 10 flexural eigenmodes in limit of pure bending and pure tension. a_n indicates the average displacement of the mode per unit deflection and $\langle \xi'_n | \xi'_n \rangle = \int_0^1 (\partial \xi_n / \partial x')^2 \, \mathrm{d}x'$.

Mode	**Bending**				**Tension**		
n	$f_n/(\Omega/2\pi)$	f_n/f_0	a_n	$\langle \xi'_n \| \xi'_n \rangle$	$f_{T_{dc},n}/f_{T_0,0}$	a_n	$\langle \xi'_n \| \xi'_n \rangle$
0	22.4	1.00	0.83	12.3	1.22	0.90	9.9
1	61.7	2.76	0	46.1	2.00	0	39.5
2	120.9	5.40	0.36	98.9	3.01	0.30	88.8
3	199.9	8.93	0	171.6	4.00	0	157.9
4	298.6	13.34	0.23	264.0	5.00	0.18	246.7
5	417.0	18.64	0	376.2	6.00	0	355.3
6	555.2	24.81	0.17	508.0	7.00	0.13	483.6
7	713.1	31.87	0	659.7	8.00	0	631.7
8	890.7	39.81	0.13	831.0	9.00	0.10	799.4
9	1 088.1	48.63	0	1022.2	10.00	0	987.0

Nanotubes can be in any of the three limits discussed above (i.e. bending only, strong residual tension and strong deflection-induced tension), depending on the residual tension and gate voltage. To find the entire tuning-curve $f_R(V_g^{dc})$, one first has to solve Eqs. 3.37 and 3.38 to obtain the static tension and dc displacement. This is then inserted into Eq. 3.50 to find the resonance frequencies. Figure 3.8a shows the calculated eigenfrequencies, plotted against the static pulling force for different residual tensions. The higher the residual tension is, the higher the resonance frequencies are at low values of l'_{dc}. The value $T'_0 = -39.4 \approx T_c$ indicates that the nanotube is close to buckling; this is visible by the nearly vanishing resonance frequency of the first mode at low l'_{dc}. When the static force is increased, all resonance frequencies increase and the differences due to the different residual tensions become smaller.

To relate the dimensionless quantities in this Section to the physical ones, the dimensions of the suspended nanotubes are needed. Table 3.3 shows the estimated sizes and the calculated values of several parameters for different nanotube devices. Tubes A and B are used in the mixing experiments discussed in Ch. 5 and Tube C is the device studied in Ch. 6. Finally, the parameters for a nanotube with a resonance frequency of 1 GHz are given. Such a nanotube resonator can be cooled to the ground state, by using a dilution refrigerator, making the use of other cooling techniques (Sec. 2.3) unnecessary. However, the current associated with the motion in the mixing experiments of Ch. 5 is proportional to the average displacement amplitude; it is thus proportional to the length scale l_{ac} that determines the amplitude. As a consequence, the mechanical signal drops rapidly

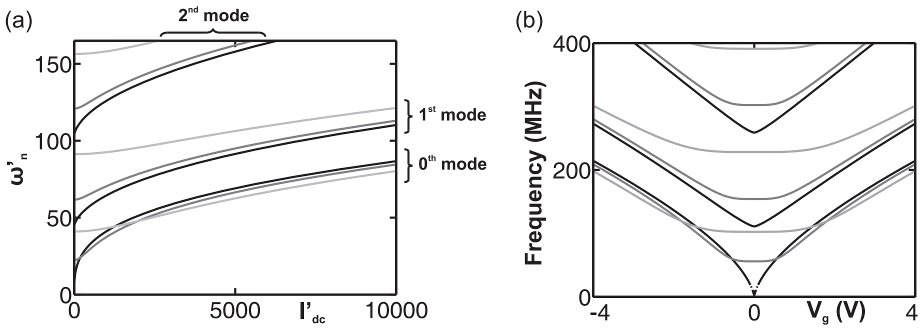

FIGURE 3.8: (a) Calculated eigenfrequencies ω'_n of the first three flexural modes ($n = 0, 1, 2$) of a suspended carbon nanotube as a function of the static pulling force l'_{dc}. The different shades of gray correspond to different residual tensions $T'_0 = -39.4$ (black), $T'_0 = 0$ (gray) and $T'_0 = +100$ (light gray). (b) The data plotted in (a) is converted to real frequencies and static gate voltage using the parameters for Tube A (See Table 3.3). The residual tensions are $T_0 = -91,\ 0,\ +230$ pN for the black, gray and light gray curves respectively.

with decreasing length, making the measurement of single-walled carbon nanotubes with $f_0 > 1$ GHz (corresponding to a device length $\ell <\sim 0.2\,\mu$m, see Table 3.3) challenging as the signal is about $100\times$ smaller compared to a $f_0 = 100$ MHz device with $\ell \approx 0.6\,\mu$m. The latter tube can also operate a 1 GHz frequency by tuning it with a gate-induced tension of $T'_{\mathrm{dc}} = 5 \cdot 10^3$. In this case the signal decreases too, but our model shows that it is only by a factor of 10. A tension of $T'_{\mathrm{dc}} = 5 \cdot 10^3$ corresponds to a strain of about 0.2%, which is larger than the values that we reach in our experiment, but are still smaller than the strains at which single-walled carbon nanotubes break [40–42].

3.6 NANODRUMS

In Chapter 4 nanomechanical measurements on suspended few-layer graphene sheets are discussed. This Section focusses on the modelling of these so-called nanodrums. In the experiments, an atomic force microscope tip is used to apply a force F_{tip} to the flake as illustrated in Fig. 3.9a. The point (x_0, y_0) where the force is applied can be varied and the resulting deflection of the nanodrum is measured. The restoring force that opposes the applied force has several contributions[12]: First of all there is the bending rigidity of the flake D. Secondly, tension may be present in the flake. Finally, there can be a pressure difference ΔP between the environment and the inside of the nanodrum that can be applied externally [43] or induced by the deflection of the flake, i.e. $\Delta P = \Delta P[u]$. Including

[12]The indentation of the flake is not included in this analysis as it requires the shape of the tip to be (accurately) known. This contribution adds up linearly to the total compliance of the flake and is determined experimentally from the compliance at the supported part of the flake.

TABLE 3.3: Data for four different tubes. The values of the parameters are calculated from the nanotube radius r, length ℓ and distance to the gate electrode h_g. The resonance frequency f_R, tension T_{dc} and static displacement $u_{dc}(\ell/2)$ are evaluated for a gate voltage $V_g^{dc} = 4\,\mathrm{V}$ and zero residual tension. m, f_0 and D are the mass, resonance frequency of the nanotube without tension and the bending rigidity respectively. Furthermore, the static and dynamic spring constants are k_{dc} and k_R, C_g is the capacitance to the gate and u_0 the zero-point motion.

	Tube A	Tube B	Tube C	1 GHz	
ℓ	1.25	1.15	0.80	0.23	μm
r	1.4	1.6	1.5	1.0	nm
h_g	500	500	230	500	nm
m	7.5	7.9	5.15	0.99	10^{-21} kg
D	3.6	6.18	4.77	0.94	10^{-24} Nm^2
f_0	56.0	81	152	1000	MHz
f_R	210.9	218	392	1007	MHz
k_R	13.2	14.8	31.2	39.4	10^{-3} N/m
u_0	2.3	2.21	2.04	2.91	pm
C_g	10.58	9.94	7.77	1.85	aF
$\partial C_g/\partial u$	3.22	3.09	5.90	0.54	zF/nm
$F_{dc}\ell$	26	25	47.22	4.29	pN
l_{dc}	$1.4\cdot10^4$	$6.1\cdot10^3$	$5.1\cdot10^3$	55	μm
$u_{dc}(\ell/2)$	6.2	4.9	4.35	0.14	nm
k_{dc}	10.5	11.9	25.2	30.2	10^{-3} N/m
T_{dc}	0.46	0.43	0.62	0.0036	nN
T'_{dc}	199	92	83	0.20	
V_g^*	1.2	1.9	2.0	16	V
l'_{dc}	$9.9\cdot10^3$	$3.8\cdot10^3$	$3.4\cdot10^3$	55	

all these terms in Eq. 3.16 of Sec. 3.2 yields [4, 25, 44]:

$$\left(D\nabla^4 - \frac{\partial}{\partial x_\alpha}T_{\alpha\beta}\frac{\partial}{\partial x_\beta}\right)u(x,y;x_0,y_0) = F_{\rm tip}\delta(x-x_0,y-y_0)+\Delta P, \tag{3.53}$$

where the ∇-operator and the partial derivatives $\partial/\partial x_i$ are working in the xy-plane only, as the z-dependence is absorbed in the bending rigidity (see Sec. 3.2) and the tension $T_{\alpha\beta} = \int_0^h \sigma_{\alpha\beta}\,\mathrm{d}z$. This equation is difficult to solve in its most general form, but fortunately some simplifications can be made. The tension tensor can have both normal and shear components. It is, however, always possible to find two orthogonal directions where the shear components are zero [1]. For uniform tension these directions are independent of position, so without loss of generality the x and y-axis are taken along the principle directions of the tension. As shown in Chapter 4, no difference in tension in the x and y direction is observed, i.e. $\Delta T = (T_{xx} - T_{yy})/2$ must be small so that $T_{\alpha\beta} \approx T\delta_{ij}$. Then, when omitting the pressure term for the moment, Eq. 3.53 is greatly simplified. In polar coordinates[13] it reads:

$$\left(D\nabla^4 - T\nabla^2\right)u(r,\theta;r_0,\theta_0) = \frac{F_{\text{tip}}}{r}\delta(r-r_0,\theta-\theta_0). \tag{3.54}$$

The flake with radius R is clamped at the edge of the circular hole so the boundary conditions are $u(R) = 0$ and $\mathrm{d}u/\mathrm{d}r|_{r=R} = 0$. Furthermore, the deflection at the center is finite ($u(0) < \infty$) and smooth ($\mathrm{d}u/\mathrm{d}r|_{r=0} = 0$). The solution is written as:

$$u(r,\theta;r_0,\theta_0) = \sum_{m=0}^{\infty} R_m(r;r_0)\cos(m\theta - m\theta_0). \tag{3.55}$$

Inserting this into Eq. 3.54 yields for the radial coefficients:

$$\begin{aligned} R_0(r;r_0) = \quad & A_0 I_0(\lambda r/R) + B_0 K_0(\lambda r/R) + \\ & C_0 \ln(r/R) + D_0 + R_0^{(p)}(r;r_0), \end{aligned} \tag{3.56}$$

$$\begin{aligned} R_m(r;r_0) = \quad & A_m I_m(\lambda r/R) + B_m K_m(\lambda r/R) + \\ & C_m(r/R)^{-m} + D_m(r/R)^m + R_m^{(p)}(r;r_0) \quad (m > 0), \end{aligned} \tag{3.57}$$

where I_m and K_m are the Bessel functions of the first and second kind respectively, and $\lambda = \sqrt{TR^2/D}$ is a dimensionless parameter that indicates the importance of the tension in comparison with the bending rigidity of the flake. The set of coefficients $\{A_m, B_m, C_m, D_m\}$ are calculated analytically; for the particular solutions $R_m^{(p)}$ only an integral solution was found. Figure 3.9b shows the deflection profiles calculated where the force is applied at different distances r_0 from the center. The deflection of the flake is clearly reduced when the AFM tip is moved away from center of the nanodrum. This indicates that its local compliance $k_f^{-1}(r_0,\theta_0) = \partial u(r_0,\theta_0;r_0,\theta_0/\partial F_{\text{tip}}$ decreases. As the tension is assumed to be isotropic, k_f^{-1} is independent of θ_0 and its radial profile contains all the information. This profile is shown in Fig. 3.9c for different values of the tension. For small tension ($\lambda = 0$), the profile is rounded at the edge of the hole, whereas for large tension ($\lambda \to \infty$) the compliance profile becomes much shaper[14] at the edge and diverges at the center for a point force. In practice the tip has a finite radius of curvature which prevents that the spring constant of the flake $k_f(r_0 = 0)$ vanishes.

When a finite pressure difference ΔP is applied, the total displacement is the sum of the contribution due to applied force F_{tip} and the one due to ΔP because Eq. 3.54 is linear.

---

[13] $\nabla^2 = \frac{\partial^2}{\partial x^2} + \frac{\partial^2}{\partial y^2} = \frac{\partial^2}{\partial r^2} + \frac{1}{r}\frac{\partial}{\partial r} + \frac{1}{r^2}\frac{\partial^2}{\partial\theta^2}$ and
$\nabla^4 = \frac{\partial^4}{\partial x^4} + \frac{\partial^4}{\partial y^4} = \frac{\partial^4}{\partial r^4} + \frac{2}{r}\frac{\partial^3}{\partial r^3} - \frac{1}{r^2}\frac{\partial^2}{\partial r^2} + \frac{1}{r^3}\frac{\partial}{\partial r} + \frac{4}{r^4}\frac{\partial^2}{\partial\theta^2} + \frac{1}{r^4}\frac{\partial^4}{\partial\theta^4} + \frac{2}{r^2}\frac{\partial^4}{\partial r^2\partial\theta^2} - \frac{2}{r^3}\frac{\partial^3}{\partial r\partial\theta^2}$.

[14] In the limit $\lambda \to \infty$, the ∇^4 term in Eq. 3.54 vanishes and only a second order differential equation remains. Therefore, the boundary conditions $\mathrm{d}u/\mathrm{d}r|_{r=0,R} = 0$ are discarded.

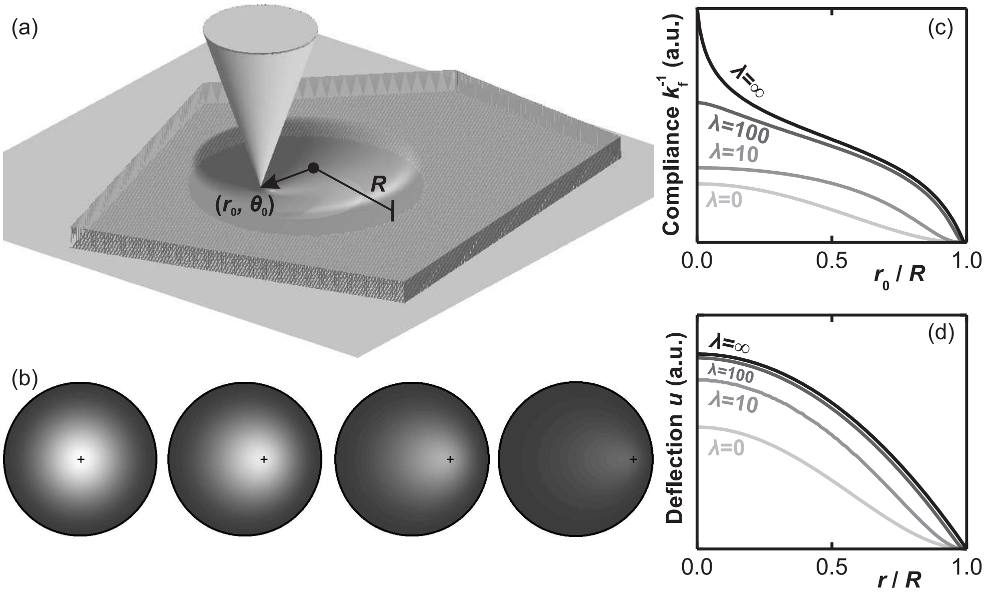

FIGURE 3.9: (a) Schematic overview of the nanodrum. A few-layer graphene flake is suspended over a circular hole with radius R. A force is applied at the point (r_0, θ_0) using an AFM tip. This results in a deflection of the nanodrum (b) Colormaps of the calculated deflection profile (Eq. 3.54) of a nanodrum with vanishing tension. The force is applied at the location of the cross and the color scale is identical in all four panels: white corresponds to a large deflection and dark gray to no deflection. (c) The calculated radial compliance profile for different values of the tension, with $\lambda^2 = TR^2/D$. (d) A difference in hydrostatic pressure between the top and bottom side of the drum results in the plotted deflection profiles.

The displacement profile due to the pressure difference is:

$$u_p(r) = \frac{\Delta P R^4}{D} \frac{\lambda (r/R)^2 I_1(\lambda) + 2I_0(\lambda) - 2I_0(\lambda r/R)}{4\lambda^3 I_1(\lambda)}. \tag{3.58}$$

These profiles are plotted in Fig. 3.9d. Similar to the compliance profiles, one can see that when tension is dominant the profile reaches the edge at an angle, whereas for a stiffer plate the profile is much more rounded.

When the tension in the x and y-direction is not equal, an additional term[15] $-\Delta T(\partial^2/\partial x^2 - \partial^2/\partial y^2)$ appears on the left hand side of Eq. 3.54. The first order correction $\Delta u(r,\theta; r_0, \theta_0)$ to the original displacement profile $u(r,\theta; r_0,\theta_0)$ satisfies

$$\left(D\nabla^4 - T\nabla^2\right)\Delta u(r,\theta; r_0,\theta_0) = \Delta T \left(\frac{\partial^2}{\partial x^2} - \frac{\partial^2}{\partial y^2}\right) u(r,\theta; r_0,\theta_0) \equiv \Delta T \Phi(r,\theta; r_0,\theta_0). \tag{3.59}$$

[15]In polar coordinates $\frac{\partial^2}{\partial x^2} - \frac{\partial^2}{\partial y^2} = \cos(2\theta)\left(\frac{\partial^2}{\partial r^2} - \frac{1}{r}\frac{\partial}{\partial r} - \frac{1}{r^2}\frac{\partial^2}{\partial \theta^2}\right) + \sin(2\theta)\left(\frac{1}{r^2} - \frac{1}{r}\frac{\partial}{\partial r}\right)\frac{\partial}{\partial \theta}$.

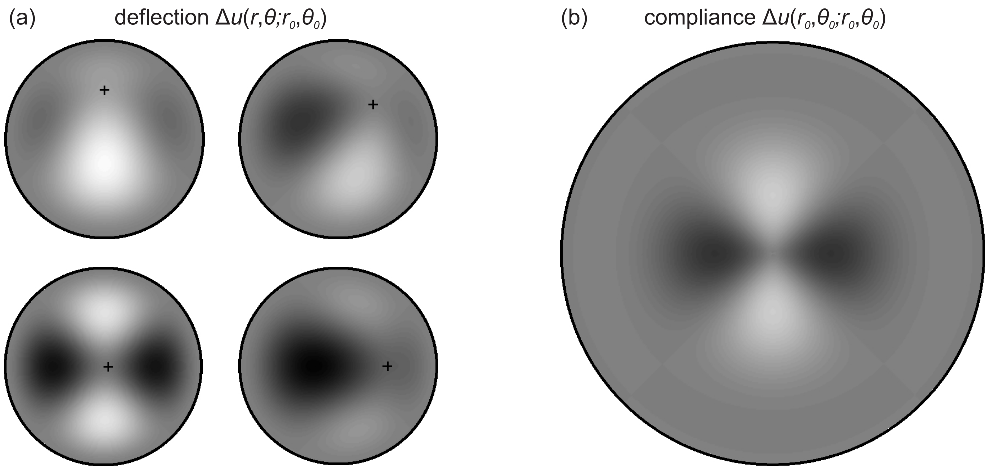

FIGURE 3.10: (a) Colormaps of the calculated change in the deflection profile Δu due to a non-isotropic tension (Eq. 3.59) for $\lambda = 1$. The force is applied at the location of the cross (b) The change in compliance $\Delta(k_f^{-1}) = \Delta u(r_0,\theta_0;r_0,\theta_0)$ for $\lambda = 1$. The color scale is identical in all panels: white corresponds to a larger deflection ($\Delta u > 0$) and black to a smaller deflection $\Delta u < 0$.

This shows that Δu is determined by the same differential equation as the original solution u, but instead of the applied force F_{tip}, now u appears via $\Phi[u]$ on the right hand side. The solution to Eq. 3.59 is found by noting that $g(r,\theta;r_0,\theta_0) \equiv u/F_{\text{tip}}$ is the Green's function of the left hand side of Eqs. 3.54 and 3.59, so that the correction is given by:

$$\Delta u(r,\theta;r_0,\theta_0) = \Delta T \iint_A g(r,\theta;r',\theta')\Phi(r',\theta';r_0,\theta_0)r'\,\mathrm{d}\theta'\,\mathrm{d}r'. \tag{3.60}$$

The angular part of the convolution is solved analytically; the radial part is solved numerically. Figure 3.10a shows some of the resulting deflection profiles, whereas Fig. 3.10b shows the calculated correction to the compliance. Along the x-axis the drum the nanodrum is more stiff, as the tension is stronger there ($T_{xx} > T > T_{yy}$ for $\Delta T > 0$) and in the y-direction the spring constant is reduced.

This concludes the analysis of the different nanomechanical systems that are studied in the following five Chapters of this Thesis. From continuum mechanics, the equations of motion of the devices are obtained. Their behavior is accurately described by sets of harmonic oscillators, systems that ware extensively discussed in Ch. 2. We have also shown that for nano-scale devices, tension is an important factor and that the carbon-based materials have extraordinary useful properties to build NEMS with.

REFERENCES

[1] T. J. Chung, *Applied Continuum Mechanics* (Cambridge University Press, 1996).

[2] A. Cleland, *Foundations of Nanomechanics* (Springer, 2003).

[3] R. E. Newnham, *Properties of materials: anisotropy, symmetry, structure* (Oxford University Press, 2005).

[4] L. D. Landau and E. M. Lifshitz, *Theory of elasticity* (Butterworth-Heineman, 1986).

[5] J. Turley and G. Sines, *The anisotropy of Young's modulus, shear modulus and Poisson's ratio in cubic materials*, J. Phys. D **4**, 264 (1971).

[6] D. R. Lide, ed., *Handbook of Chemistry and Physics* (GRC press, 1974).

[7] A. H. Nayfeh, W. Kreider, and T. J. Anderson, *Investigation of natural frequencies and mode shapes of bukcled beams*, AIAA Journal **33**, 1121 (1995).

[8] H. W. Kroto, J. R. Heath, S. C. O'Brien, R. F. Curl, and R. E. Smalley, *C60: Buckminsterfullerene*, Nature **318**, 162 (1985).

[9] S. Iijima, *Helical microtubules of graphitic carbon*, Nature **354**, 56 (1991).

[10] K. S. Novoselov, A. K. Geim, S. V. Morozov, D. Jiang, Y. Zhang, S. V. Dubonos, I. V. Grigorieva, and A. A. Firsov, *Electric Field Effect in Atomically Thin Carbon Films*, Science **306**, 666 (2004).

[11] K. S. Novoselov, D. Jiang, F. Schedin, T. J. Booth, V. V. Khotkevich, S. V. Morozov, and A. K. Geim, *Two-dimensional atomic crystals*, Proc. Natl. Acad. Sci. U. S. A. **102**, 10451 (2005).

[12] A. K. Geim, *Graphene: Status and Prospects*, Science **324**, 1530 (2009).

[13] L. D. Landau and E. M. Lifshitz, *Statistical Physics, Part I* (Pergamon Press, Oxford, 1980).

[14] J. C. Meyer, A. K. Geim, M. I. Katsnelson, K. S. Novoselov, T. J. Booth, and S. Roth, *The structure of suspended graphene sheets*, Nature **446**, 60 (2007).

[15] A. Fasolino, J. H. Los, and M. I. Katsnelson, *Intrinsic ripples in graphene*, Nat Mater **6**, 858 (2007).

[16] P. Liu and Y. W. Zhang, *Temperature-dependent bending rigidity of graphene*, Appl. Phys. Lett. **94**, 231912 (pages 3) (2009).

[17] D. Gazit, *Theory of the spontaneous buckling of doped graphene*, Phys. Rev. B **79**, 113411 (pages 4) (2009).

[18] L. Sekaric, J. M. Parpia, H. G. Craighead, T. Feygelson, B. H. Houston, and J. E. Butler, *Nanomechanical resonant structures in nanocrystalline diamond*, Appl. Phys. Lett. **81**, 4455 (2002).

[19] A. Gaidarzhy, M. Imboden, P. Mohanty, J. Rankin, and B. W. Sheldon, *High quality factor gigahertz frequencies in nanomechanical diamond resonators*, Appl. Phys. Lett. **91**, 203503 (pages 3) (2007).

[20] O. L. Blakslee, D. G. Proctor, E. J. Seldin, G. B. Spence, and T. Weng, *Elastic Constants of Compression-Annealed Pyrolytic Graphite*, J. Appl. Phys. **41**, 3373 (1970).

[21] K. H. Michel and B. Verberck, *Theory of the elastic constants of graphite and graphene*, Phys. Stat. Sol. (b) **245**, 2177 (2008).

[22] B. I. Yakobson, C. J. Brabec, and J. Bernholc, *Nanomechanics of Carbon Tubes: Instabilities beyond Linear Response*, Phys. Rev. Lett. **76**, 2511 (1996).

[23] A. H. Castro Neto, F. Guinea, N. M. R. Peres, K. S. Novoselov, and A. K. Geim, *The electronic properties of graphene*, Rev. Mod. Phys. **81**, 109 (pages 54) (2009).

[24] M. Dequesnes, S. V. Rotkin, and N. R. Aluru, *Calculation of pull-in voltages for carbon-nanotube-based nanoelectromechanical switches*, Nanotechnology **13**, 120 (2002).

[25] J. Atalaya, A. Isacsson, and J. M. Kinaret, *Continuum Elastic Modeling of Graphene Resonators*, Nano Lett. **8**, 4196 (2008).

[26] W. H. Duan and C. M. Wang, *Nonlinear bending and stretching of a circular graphene sheet under a central point load*, Nanotechnology **20**, 075702 (2009).

[27] R. Faccio, P. A. Denis, H. Pardo, C. Goyenola, and A. W. Mombru, *Mechanical properties of graphene nanoribbons*, J. Phys.: Condens. Matter **21**, 285304 (2009).

[28] P. Poncharal, Z. L. Wang, D. Ugarte, and W. A. de Heer, *Electrostatic Deflections and Electromechanical Resonances of Carbon Nanotubes*, Science **283**, 1513 (1999).

[29] S. Sapmaz, Y. M. Blanter, L. Gurevich, and H. S. J. van der Zant, *Carbon nanotubes as nanoelectromechanical systems*, Phys. Rev. B **67**, 235414 (2003).

[30] K. Flensberg, *Electron-vibron coupling in suspended nanotubes*, New J. Phys. **8**, 5 (2006).

[31] D. J. Griffiths, *Introduction to Electrodynamics* (Prentice Hall, Upper Saddle River, 1999).

[32] Y. K. Kwok, *Applied complex variables for scientists and engineers* (Cambridge University Press, Cambridge, 2002).

[33] R. Lefèvre, M. F. Goffman, V. Derycke, C. Miko, L. Forró, J. P. Bourgoin, and P. Hesto, *Scaling Law in Carbon Nanotube Electromechanical Devices*, Phys. Rev. Lett. **95**, 185504 (pages 4) (2005).

[34] I. Kozinsky, H. W. C. Postma, I. Bargatin, and M. L. Roukes, *Tuning nonlinearity, dynamic range, and frequency of nanomechanical resonators*, Appl. Phys. Lett. **88**, 253101 (pages 3) (2006).

[35] M. Poot, *Driven, doubly clamped nanotubes*, TU Delft (2008).

[36] B. Witkamp, *High-frequency Nanotube Resonators*, Ph.D. thesis, Delft University of Technology (2009), URL `http://resolver.tudelft.nl/uuid:3814f598-488b-4cca-96d2-302d814a10f8`.

[37] D. Chang and N. Popplewell, *A non-uniform, axially loaded euler-bernoulli beam having complex ends*, Q. J. Mech. Appl. Math. **49**, 353 (1996).

[38] A. N. Cleland and M. L. Roukes, *Noise processes in nanomechanical resonators*, J. Appl. Phys. **92**, 2758 (2002).

[39] H. W. C. Postma, I. Kozinsky, A. Husain, and M. L. Roukes, *Dynamic range of nanotube- and nanowire-based electromechanical systems*, Appl. Phys. Lett. **86**, 223105 (pages 3) (2005).

[40] D. A. Walters, L. M. Ericson, M. J. Casavant, J. Liu, D. T. Colbert, K. A. Smith, and R. E. Smalley, *Elastic strain of freely suspended single-wall carbon nanotube ropes*, Appl. Phys. Lett. **74**, 3803 (1999).

[41] D. Bozovic, M. Bockrath, J. H. Hafner, C. M. Lieber, H. Park, and M. Tinkham, *Plastic deformations in mechanically strained single-walled carbon nanotubes*, Phys. Rev. B **67**, 033407 (2003).

[42] Q. Zhao, M. B. Nardelli, and J. Bernholc, *Ultimate strength of carbon nanotubes: A theoretical study*, Phys. Rev. B **65**, 144105 (2002).

[43] J. S. Bunch, S. S. Verbridge, J. S. Alden, A. M. van der Zande, J. M. Parpia, H. G. Craighead, and P. L. McEuen, *Impermeable Atomic Membranes from Graphene Sheets*, Nano Lett. **8**, 2458 (2008).

[44] D. Norouzi, M. M. Mueller, and M. Deserno, *How to determine local elastic properties of lipid bilayer membranes from atomic-force-microscope measurements: A theoretical analysis*, Phys. Rev. E **74**, 061914 (2006).

4

NANOMECHANICAL PROPERTIES OF FEW-LAYER GRAPHENE MEMBRANES

M. Poot and H. S. J. van der Zant

We have measured the mechanical properties of few-layer graphene and graphite flakes that are suspended over circular holes. The spatial profile of the flake's spring constant is measured with an atomic force microscope. The bending rigidity of and the tension in the membranes are extracted by fitting a continuum model to the data. For flakes down to eight graphene layers, both parameters show a strong thickness-dependence. We predict fundamental resonance frequencies of these nanodrums in the GHz range and zero-point motions of the order of a pm, based on the measured bending rigidity and tension.

Parts of this Chapter have been published in Appl. Phys. Lett., **92**, 063111 (2008)

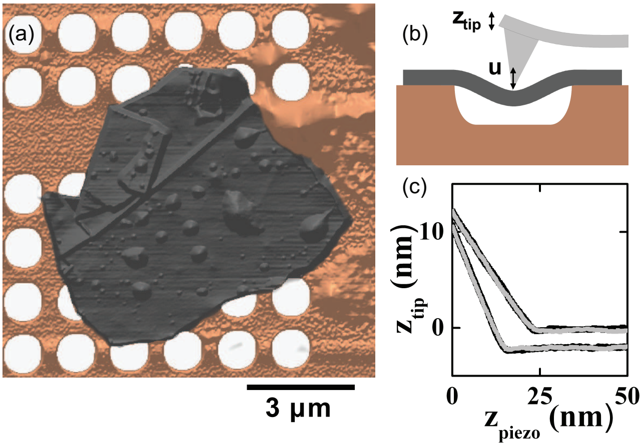

FIGURE 4.1: (a) An AFM height image of a suspended flake (~69 layers). (b) Schematic overview of the method used to determine the local compliance of the flake. (c) Two linear force-distance curves (offset for clarity) taken on the flake shown in (a). The approaching (gray) and retracting (black) parts of the curves lie on top of each other. The bottom curve is taken on an unsuspended part of the flake, while the top curve is taken on a suspended part.

Graphene, a single layer of graphite, has recently been contacted with electrodes [1] and its unique electronic properties are being measured [2–5]. By suspending graphene, membranes of only one atom thick are obtained [6, 7], which may have interesting applications, such as pressure sensors [8] or gas detectors [9]. They are also used to build mechanical resonators [10]. For recent reviews on the research on graphene see Refs. [11] and [12].

In this Chapter, we present a method to obtain the bending rigidity of and the tension in ultra-thin membranes by fitting the spatial profile of the compliance. We applied this method to suspended multi-layer graphene. Over almost four decades, the bending rigidity closely follows the thickness-dependence for graphite, calculated using continuum mechanics.

4.1 NANOMECHANICAL MEASUREMENTS

Samples are made from doped silicon wafers with 285 nm silicon oxide on top, in which circular holes are etched with buffered hydrofluoric acid using resist masks [13]. Graphite grains are put on adhesive tape, cleaved and the tape is pressed against the substrate [1]. This way, graphitic flakes with varying dimensions are left on the surface. Some of the holes are covered completely as Fig. 4.1a shows, thus forming nanodrums.

The elastic properties of more than 50 flakes with thicknesses varying from 2.4 nm to 33 nm (8 to 100 layers) are extracted from ensembles of force-distance curves, measured with an atomic force microscope (AFM) under ambient conditions: The deflection of the AFM tip, z_{tip}, is measured while lowering the tip onto the sample over a distance z_{piezo}, as illustrated in Fig. 4.1b and c. The deflection of the flake u is due to the applied force $F_{\text{tip}} = k_{\text{tip}} z_{\text{tip}}$, where k_{tip} is the spring constant of the AFM tip[1]. The (negative) slope of the force-distance curve $s = -\mathrm{d}z_{\text{tip}}/\mathrm{d}z_{\text{piezo}}$, is used to extract the local compliance of the flake $k_{\text{f}}^{-1} = \mathrm{d}u/\mathrm{d}F_{\text{tip}} = k_{\text{tip}}^{-1}(s^{-1} - 1)$. Knowing the compliance at a single point is, however, not enough to extract all mechanical properties of a membrane [15]. Therefore, multiple force-distance curves are recorded while scanning in a rectangular grid over the sample to construct a map of the local compliance. This is the so-called force-volume method [16].

Fig. 4.1c shows two individual force-distance curves out of a set of 64 × 64 curves. The lower curve was taken on an unsuspended part of the flake, while the other was taken on a suspended part. The deflection of the flake results in a lower slope in the latter case. The curves are linear (apart from the small region where the tip is almost touching the flake) for deflections up to a quarter of the thickness, i.e. the deflection of the flake is proportional to the applied force. Whenever a non-linear force-distance curve was observed, the applied force was reduced significantly to ensure that the measurements were done in the linear regime. Note that with the force modulation technique [17], this check is not possible, as only the slope s is measured. Another advantage of the force-volume method is the absence of lateral forces on the flake while scanning, which might strain or even damage the flakes.

Fig. 4.2a shows a map of the local compliances extracted from a force-volume measurement. In this plot, different regions can be distinguished: In the upper left corner, the tip presses against the hard silicon oxide and the compliance vanishes. The edge of the flake appears as a line of high compliance, because the tip slides along the edge when pressing. The dark gray color indicates that a supported part of the flake has a small, but non-zero compliance, i.e., it is indentable. This is not surprising when the low Young's modulus $E_{\perp} = 33\,\text{GPa}$ of graphite (Sec. 3.4) for stress perpendicular to the graphene planes is considered. We found no clear correlation between the indentability and the thickness of the flake, probably due to the differences in tip geometry in the different measurements. Although not visible in the height image, the hole appears as a circular region with high compliance. At the center of the hole, the flake is more easily deflected than at the edge, as expected.

4.2 EXTRACTING THE BENDING RIGIDITY AND TENSION

To find the bending rigidity of and tension in the membranes, compliance profiles, calculated with the continuum model[2] for the induced deflection described in detail in Sec. 3.6,

[1] Commercially available AFM tips with nominal spring constants $k_{\text{tip}} = 2$ or $42\ \text{N/m}$ are used. The spring constant is calibrated using the thermal noise method and the deflection sensitivity is obtained by taking an ensemble of force-distance curves on the silicon oxide substrate [14].

[2] Even when the continuum approximation fails along the z-direction, it can still be valid in the horizontal direction, as long as the z-dependence of the induced deformations is not considered. Therefore, the bending

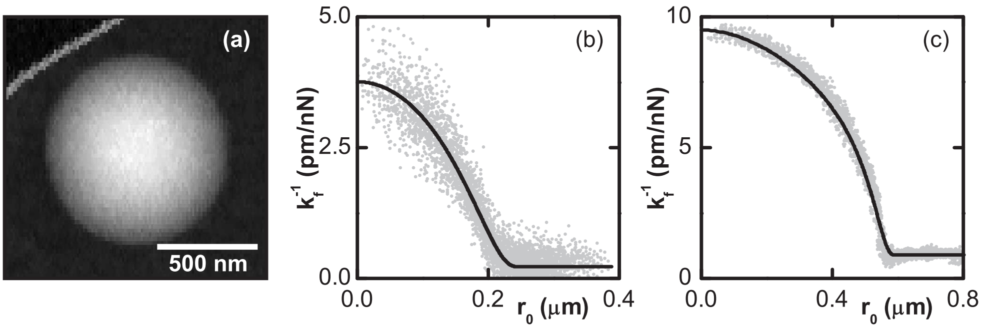

FIGURE 4.2: (a) Colormap of the compliance of a flake with $h = 23$ nm, extracted from a force-volume measurement (64 × 64 force-distance curves) . The compliance ranges from 0 (black) to $9.7 \cdot 10^{-3}$ m/N (white). (b) The measured radial profile of the compliance (symbols) of a 15 nm thick flake and the fit by the model (solid line). (c) The radial profile of the data shown in (a).

are fitted to the experimental data. The AFM tip is modelled as a point force, as its radius of curvature (of the order of 10 nm) is much smaller than the radius of the hole R. This differs from studies on lipid bilayer membranes, where the hole diameter is of the same order as the radius of the tip [18]. The force applied at (r_0, θ_0) is opposed by the bending rigidity D and by the tension T which we assume to be isotropic[3], i.e. the flake is equally stretched in both horizontal directions. The deflection profile for deflections that are small compared to the thickness h is given by [15, 19] (Cf. Eq. 3.54):

$$\left(D\nabla^4 - T\nabla^2\right)u(r,\theta;r_0,\theta_0) = \frac{F_{\text{tip}}}{r}\delta(r-r_0,\theta-\theta_0), \tag{4.1}$$

which was solved in Sec. 3.6 for a flake that is suspended over a circular hole, resulting in deflection profiles as the one in Fig. 3.9b. In the linear regime terms proportional to u^3 [19] are not present in Eq. 4.1 and the compliance is the ratio between the deflection at the point where the force is applied, $u(r_0,\theta_0;r_0,\theta_0)$, and the force F_{tip}. The compliance is independent of θ_0 for a circular hole and isotropic tension. By varying the location of the applied force, a compliance profile $k_f^{-1}(r_0)$ is calculated. It depends on three fitting parameters: the bending rigidity D, the tension T and the radius of the hole R.

As shown in Fig. 4.2, good fits (solid lines) are obtained with this model. When the measurement is repeated on the same hole, the fit parameters differ less than a few percent. The hole radius from the fit is in agreement with height profiles of uncovered holes

rigidity is not expressed in the elastic constants, but it is treated as a fit parameter.

[3] In Sec. 3.6, the first order correction to the compliance for non-isotropic tension was calculated and is shown in Fig. 3.10b. The flake is stiffer than average along the principal direction with the largest tension and weaker along the other. The lines of constant compliance are ellipsoidal instead of circular. As this has not been observed in the measurements, the assumption of isotropic tension is allowed.

and scanning electron microscopy. Fig. 4.2b shows a profile that is rounded at the edge of the hole. This is reproduced by a fit, where the compliance is primarily due to the bending rigidity. The profile in Fig. 4.2c is sharper at the edge, which can be fitted well with a large tension. The question whether a flake is tension or rigidity dominated can only be answered with mechanical measurements, as the height maps do not show any difference. The extracted bending rigidity of every flake is plotted in Fig. 4.3a against its thickness h. The bending rigidity increases strongly with the thickness, while at the same time the spread increases. Measurements on a flake suspended over holes with different diameters confirm that the bending rigidity does not depend on the hole size, but that it is an intrinsic property of the flake.

4.3 THICKNESS-DEPENDENCE

The bending rigidity of bulk graphite can be calculated using continuum mechanics. Graphite is highly anisotropic, but the in-plane mechanical properties are isotropic and are described by the in-plane Young's modulus $E_\square = 0.92\,\mathrm{TPa}$ and the in-plane Poisson's ratio $\nu_\square = 0.16$ as explained in Sec. 3.4. The bending rigidity for deflections perpendicular to the graphene planes is given by Eq. 3.29. The black line in Fig. 4.3a shows this relation; Over the entire range, most values for the bending rigidity are close to this curve. Only flakes thicker than about 10 nm may have a smaller bending rigidity. A possible explanation for this deviation is the presence of stacking defects in the flakes: the bending rigidity is no longer proportional to h^3, but in a first approximation to the sum of the cubes of the thickness of each part separated by the defects, resulting in a smaller bending rigidity. This is also consistent with the fact that the spread in the obtained values grows with increasing thickness. For flakes with $h < 10$ nm, the data points are close to the drawn line in Fig. 4.3a, which would imply the absence of stacking faults in thin flakes.

The tension varies from flake to flake and its thickness-dependence is shown in Fig. 4.3b. The tension is larger for thicker flakes, possibly saturating at 20 N/m, but more measurements are needed to confirm this. Measurements on different holes underneath the same flake give similar values for the tension, so the tension is uniform throughout the flake. Most likely, the tension is induced during the deposition process [10].

4.4 FEW-LAYER GRAPHENE NANODRUMS AS RESONATORS

With the experimentally determined values of the bending rigidity and tension, other mechanical properties of the nanodrum can be calculated. As an example, Fig. 4.3c shows the expected eigenfrequencies [20] of the fundamental mode of the nanodrums, calculated with the measured values of the bending rigidity and tension. The frequency increases with increasing thickness. For holes with $R = 0.55\mu\mathrm{m}$, the frequencies are slightly below 1 GHz, while for smaller holes ($R = 84\,\mathrm{nm}$), the frequency can be over 10 GHz. Moreover, the zero-point motion u_0 of these drums is calculated as shown in Fig. 4.3d. These quantum fluctuations can be as large as a picometer, which is a great improvement over the

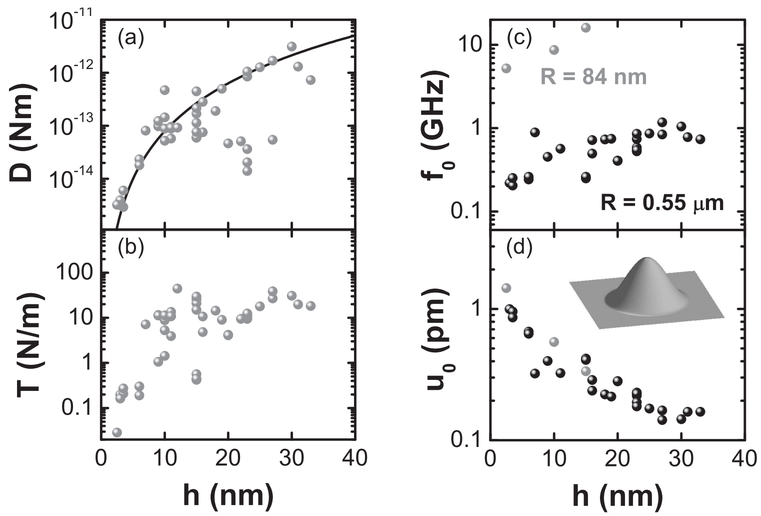

FIGURE 4.3: Thickness-dependence of the mechanical properties extracted from the fits. (a) The bending rigidity D (symbols) and the continuum relation (gray line). (b) The tension in the flake T. The frequency f_R (c) and the zero-point motion u_0 (d) of the fundamental mode calculated with the measured values for D and T for two different hole sizes. The inset in (d) shows the displacement profile of this mode.

femtometer-scale u_0 in the top-down fabricated micro- or nanomechanical devices that are shown in Table 2.1. So both the high resonance frequencies and large zero-point fluctuations make our nanodrums ideal components to study quantum effects in nanomechanical devices.

4.5 SINGLE-LAYER GRAPHENE

Finally, we address the question whether the bending rigidity of single-layer graphene can be measured with this technique. As graphene consists of only a single sheet of atoms, one might expect that its bending rigidity vanishes. However, molecular dynamics calculations indicate that the bending rigidity of graphene is finite. The predicted value $D \sim 1.4 \cdot 10^{-19}$ Nm [21, 22] is four orders of magnitude smaller than the lowest value that we have measured up to now, making the measurement challenging: A single layer will have a high compliance and only small forces can be applied before the force-distance curves become nonlinear. By using a soft tip (AFM tips with spring constants as low as a few mN/m are commercially available), it should still be possible to obtain a sufficiently large tip deflection. Another problem that might arise when the bending rigidity is very small, is that the tension or even the deflection-induced pressure completely determine the compliance and fits can only give a lower bound for the bending rigidity. Fortunately, our data (Fig. 4.3b) shows that the tension decreases with decreasing thickness. The role of tension and pressure can be reduced further by making smaller holes, as can be seen from the scaling behaviour of Eq. 3.53. Taking all these consideration into account, we expect that the when the hole diameter is smaller than 80 nm, it is possible to measure the bending rigidity of single-layer graphene.

4.6 CONCLUSIONS

We have shown that an AFM measurement of the compliance profile of a suspended membrane yields important information on its mechanical properties. This technique is not limited to multi-layer graphene flakes, but can be applied to membranes of any kind.

The bending rigidity of flakes as thin as 8 graphene layers still follows from the bulk properties of graphite. Their small mass and high stiffness make these few-layer graphene nanodrums ideal devices for studying quantum effect in mechanical systems.

ACKNOWLEDGEMENT

We thank Jörgen Konings and Abdulaziz Karimkhodjaev for their help with the measurements and Alberto Morpurgo, Jeroen Oostinga, Samir Etaki, Jari Kinaret and Andreas Isacsson for discussions. Financial support is obtained from the Dutch organizations FOM, NWO (VICI-grant) and NanoNed.

REFERENCES

[1] K. S. Novoselov, A. K. Geim, S. V. Morozov, D. Jiang, Y. Zhang, S. V. Dubonos, I. V. Grigorieva, and A. A. Firsov, *Electric Field Effect in Atomically Thin Carbon Films*, Science **306**, 666 (2004).

[2] K. Novoselov, A. Geim, S. Morozov, D. Jiang, M. Katsnelson, I. Grigorieva, S. Dubonos, and A. Firsov, *Two-dimensional gas of massless Dirac fermions in graphene*, Nature **438**, 197 (2005).

[3] Y. Zhang, Y.-W. Tan, H. L. Stormer, and P. Kim, *Experimental observation of the quantum Hall effect and Berry's phase in graphene*, Nature **438**, 201 (2005).

[4] K. S. Novoselov, Z. Jiang, Y. Zhang, S. V. Morozov, H. L. Stormer, U. Zeitler, J. C. Maan, G. S. Boebinger, P. Kim, and A. K. Geim, *Room-temperature quantum hall effect in graphene*, Science **315**, 1379 (2007).

[5] H. B. Heersche, P. Jarillo-Herrero, J. B. Oostinga, L. M. K. Vandersypen, and A. F. Morpurgo, *Bipolar supercurrent in graphene*, Nature **446**, 56 (2007).

[6] K. S. Novoselov, D. Jiang, F. Schedin, T. J. Booth, V. V. Khotkevich, S. V. Morozov, and A. K. Geim, *Two-dimensional atomic crystals*, Proc. Natl. Acad. Sci. U. S. A. **102**, 10451 (2005).

[7] J. C. Meyer, A. K. Geim, M. I. Katsnelson, K. S. Novoselov, T. J. Booth, and S. Roth, *The structure of suspended graphene sheets*, Nature **446**, 60 (2007).

[8] J. S. Bunch, S. S. Verbridge, J. S. Alden, A. M. van der Zande, J. M. Parpia, H. G. Craighead, and P. L. McEuen, *Impermeable Atomic Membranes from Graphene Sheets*, Nano Lett. **8**, 2458 (2008).

[9] F. Schedin, A. K. Geim, S. V. Morozov, E. W. Hill, P. Blake, M. I. Katsnelson, and K. S. Novoselov, *Detection of individual gas molecules adsorbed on graphene*, Nat Mater **6**, 652 (2007).

[10] J. S. Bunch, A. M. van der Zande, S. S. Verbridge, I. W. Frank, D. M. Tanenbaum, J. M. Parpia, H. G. Craighead, and P. L. McEuen, *Electromechanical resonators from graphene sheets*, Science **315**, 490 (2007).

[11] A. K. Geim, *Graphene: Status and Prospects*, Science **324**, 1530 (2009).

[12] A. H. Castro Neto, F. Guinea, N. M. R. Peres, K. S. Novoselov, and A. K. Geim, *The electronic properties of graphene*, Rev. Mod. Phys. **81**, 109 (pages 54) (2009).

[13] B. Witkamp, M. Poot, and H. S. J. van der Zant, *Bending-mode vibration of a suspended nanotube resonator*, Nano Lett. **6**, 2904 (2006).

[14] H.-J. Butt, B. Cappella, and M. Kappl, *Force measurements with the atomic force microscope: Technique, interpretation and applications*, Surf. Sci. Rep. **59**, 1 (2005).

[15] D. Norouzi, M. M. Mueller, and M. Deserno, *How to determine local elastic properties of lipid bilayer membranes from atomic-force-microscope measurements: A theoretical analysis*, Phys. Rev. E **74**, 061914 (2006).

[16] M. Radmacher, M. Fritz, J. P. Cleveland, D. A. Walters, and P. K. Hansma, *Imaging adhesion forces and elasticity of lysozyme adsorbed on mica with the atomic force microscope*, Langmuir **10**, 3809 (1994).

[17] P. Maivald, H. J. Butt, S. A. C. Gould, C. B. Prater, B. Drake, J. A. Gurley, V. B. Elings, and P. K. Hansma, *Using force modulation to image surface elasticities with the atomic force microscope*, Nanotechnology **2**, 103 (1991).

[18] S. Steltenkamp, M. M. Mueller, M. Deserno, C. Hennesthal, C. Steinem, and A. Janshoff, *Mechanical properties of pore-spanning lipid bilayers probed by atomic force microscopy*, Biophys. J. **91**, 217 (2006).

[19] L. D. Landau and E. M. Lifshitz, *Theory of elasticity* (Butterworth-Heineman, 1986).

[20] T. Wah, *Vibration of Circular Plates*, J. Ac. Soc. Am. **34**, 275 (1962).

[21] B. I. Yakobson, C. J. Brabec, and J. Bernholc, *Nanomechanics of Carbon Tubes: Instabilities beyond Linear Response*, Phys. Rev. Lett. **76**, 2511 (1996).

[22] P. Liu and Y. W. Zhang, *Temperature-dependent bending rigidity of graphene*, Appl. Phys. Lett. **94**, 231912 (pages 3) (2009).

5

THE BENDING-MODE VIBRATION OF A SUSPENDED NANOTUBE RESONATOR

B. Witkamp, M. Poot and H. S. J. van der Zant

We have used a suspended carbon nanotube as a frequency mixer to detect its own mechanical motion. A single gate-dependent resonance is observed, which we attribute to the fundamental bending mode vibration of the suspended carbon nanotubes. A continuum model is used to fit the gate dependence of the resonance frequency, from which we obtain values for the fundamental frequency, the residual and gate-induced tension in the nanotube. This analysis shows that the nanotubes in our devices have no slack and that, by applying a gate voltage, the nanotube can be tuned from a regime without strain to a regime where it behaves as a vibrating string under tension. Finally, the possibility of improving the sensitivity by using the mixing technique in the Coulomb-blockade regime is explored.

Parts of this Chapter have been published in Nano Lett. **6**, 2904–2908 (2006) and New J. Phys. **10**, 095003 (2008)

In nano-electromechanical systems (NEMS), mechanical motion of a nanoscale object induces changes in the object's electrical properties and vice versa [1]. Compared to micro-electromechanical systems, NEMS promise improvements in terms of speed and power consumption. NEMS are also interesting from a fundamental point of view; they can be used to study the fundamental limit of mechanical motion [2]. This regime should be reached with high-frequency resonators (> 1 GHz) at low temperatures (< 50 mK). Single-walled carbon nanotubes (SWNTs) are ideal building blocks for NEMS, because they have a low mass, their resonance frequencies are easily scalable through their length and they have a high Young's modulus of ~ 1 TPa [3], which is almost an order of magnitude higher than that of silicon. At low temperatures, suspended SWNTs have been used to study acoustic vibrations [4], radial breathing modes [5] and phonon assisted tunnelling, mediated by longitudinal vibration modes [6]. At room temperature, thermally excited bending modes of both singly-and doubly clamped suspended nanotubes have been observed [3, 7] and SWNTs have been used in paddle resonators, where the nanotube undergoes torsional vibrations [8]. Previous work also shows that suspended semiconducting nanotubes can be used as frequency mixers to detect mechanical motion of the suspended devices [9].

In this Chapter, we report on the identification and the characterization of bending mode (flexural) vibrations of suspended semiconducting SWNT resonators at room temperature, by using them as frequency mixers. We observe a single gate-dependent resonance in multiple devices with Q-factors between 6 and 300, and frequencies ranging from 20 to 100 MHz. The resonances have frequencies that are close to the estimated bending-mode frequencies of the nanotubes. The resonances fit well to a continuum model from which we can extract quantitative information about the fundamental frequency (the resonance frequency without tension) and the gate-induced and residual tension in the nanotube. From the current noise and transduction factor the sensitivity of the detection technique is calculated. The sensitivity can be improved by using the mixing technique at low temperatures where the nanotube is in the Coulomb-blockade regime.

5.1 DEVICE FABRICATION

Our suspended nanotube devices are fabricated on highly p^{++}-doped silicon substrates with a 500 nm SiO_2 layer. The doped silicon is used as a gate electrode to tune and drive the nanotube resonator into motion. On the substrate, carbon nanotubes are grown in a chemical vapor deposition (CVD) setup [10] which is optimized to produce single-walled carbon nanotubes [11]. After the growth, nanotubes are located using atomic force microscopy (AFM), and subsequently Au/Cr electrodes (typically 50 and 5 nm thick, respectively) are deposited by e-beam lithography. These electrodes are used as source and drain contacts. The SWNT is then suspended, by etching away the SiO_2 under the nanotube with a buffered hydrofluoric acid (B-HF) wet-etch. Two routes have been followed as illustrated in Fig. 5.1: the first method uses the source and drain electrodes as etch masks [12, 13], while in the second method, a trench is defined in a layer of poly(methyl methacrylate)

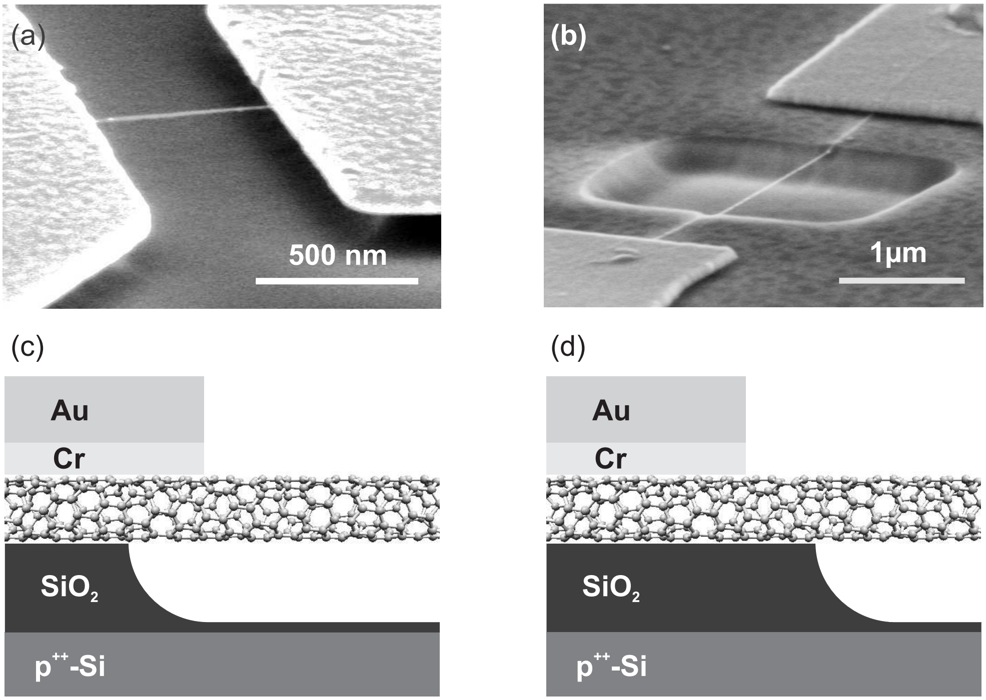

FIGURE 5.1: Scanning electron micrographs of suspended nanotube devices made without (a) and with (b) PMMA etch-masks. (c) and (d) show a schematic side-view. When no etch-mask is employed, the tube hangs underneath the Au/Cr electrodes (c), whereas with etch-masks the tube remains supported by the silicon oxide of the substrate (d).

(PMMA) which serves as an etch mask. The latter method results in a suspended nanotube with clamping points that are defined between the nanotube and the underlying SiO_2 layer. In the scanning electron micrographs (Fig. 5.1a and b) of devices made with these two methods, no slack is visible.

5.2 ELECTROSTATIC ACTUATION AND SELF-DETECTION

The suspended nanotube is actuated by applying an ac voltage $V_{\rm g}^{\rm ac}$ with frequency f to the gate, which induces a driving force on the tube due to the displacement-dependent gate-capacitance $C_{\rm g}$. When the driving frequency approaches a mechanical eigenfrequency, the oscillations of the suspended nanotube increase dramatically. In this case, the displacement amplitude averaged along the tube, $\bar{u}$, can be non-zero and the gate capacitance changes in time. This in turn modulates the gate-induced charge, $Q_g = C_{\rm g} V_{\rm g}$, as $Q_{\rm g}^{\rm mech}(t) = C_{\rm g}^{\rm ac}(t) V_{\rm g}^{\rm dc}$. Here, $V_{\rm g}^{\rm dc}$ is the dc voltage on the back gate electrode. In a semiconducting nanotube, this leads to a modulation of the conductance. In addition to this mechanical contribution, there is also a direct contribution to the conductance change, which is induced by the ac gate voltage: $Q_{\mathrm{g}}^{\mathrm{direct}}(t) = C_{\mathrm{g}} V_{\mathrm{g}}^{\mathrm{ac}}(t)$. This term is always present, even off-resonance. Combining these two contributions[1], the conductance change $G^{\mathrm{ac}}(t)$ can be written as [9]:

$$G^{\mathrm{ac}}(t) = \frac{\partial G}{\partial V_{\mathrm{g}}} \left(V_{\mathrm{g}}^{\mathrm{ac}}(t) + V_{\mathrm{g}}^{\mathrm{dc}} \frac{C_{\mathrm{g}}^{\mathrm{ac}}(t)}{C_{\mathrm{g}}} \right). \tag{5.1}$$

Here $\partial G/\partial V_g$ is the transconductance of the semiconducting nanotube (which is gate voltage dependent and it is typically $0.1 - 10\,\mu$S/V in our devices). By measuring the conductance of the nanotube, its motion can be detected. Note that the conductance oscillates at the driving frequency f.

Conductance changes at high frequencies (typically beyond a few MHz) cannot easily be measured, because of parasitic capacitances and small signal levels. However, if an ac bias voltage with a frequency offset Δf is applied to the source electrode (in our case a bias-voltage with two spectral components: at $f + \Delta f$ and $f - \Delta f$), then a current flows through the nanotube, which is the product of the conductance times the ac bias voltage. The corresponding current is effectively a mixed signal, containing frequencies Δf, $2f + \Delta f$ and $2f - \Delta f$. The first spectral component of the current is located at the offset frequency, which can be chosen conveniently (10 kHz in our experiments). This term is measured with a lock-in amplifier, while the latter two are attenuated by the high output impedance of the nanotube in combination with the parasitic capacitance.

5.3 MEASUREMENT SETUP AND DETECTION SCHEME

Our suspended nanotube devices are measured at a pressure of typically 10^{-5} mbar. Ac and dc voltages are applied to the back gate electrode via a custom-made sample carrier with an on-chip bias-T (a schematic of the measurement setup is shown in Figure 5.2). Since the input impedances of both the nanotube and the back gate are much larger than 50Ω and frequency dependent, 50Ω feed-through terminators are used to minimize circuit resonances. To generate the ac bias voltage, we use a commercially available frequency mixer to mix the ac gate voltage at frequency f with the reference output of a lock-in amplifier. The output of the mixer has spectral components at frequencies $f + \Delta f$ and $f - \Delta f$. A high pass filter is used in the bias voltage path to filter out any leakage of the lock-in reference output through the mixer. The current (at the offset frequency) flowing through the nanotube is converted into a voltage with a gain of 10^6 V/A and is measured with the lock-in amplifier (Stanford Research SR830, time constant 100 ms).

[1] In this equation piezo-resistive and gate-coupling effects are neglected. For a discussion, see the analysis presented in Chapter 7 of Ref. [14].

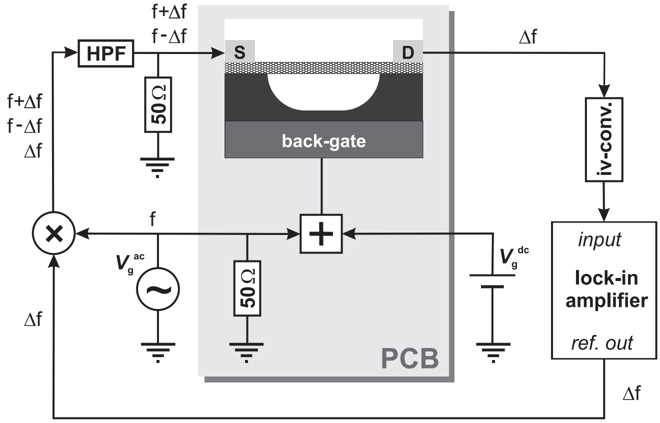

FIGURE 5.2: Schematic overview of the measurement setup. A radio frequency (RF) generator applies an ac voltage to the back-gate electrode to drive the suspended nanotube. A dc gate voltage is added via a bias-T (indicated by the "+"). The same generator is used to generate the ac bias voltage by mixing its output with the reference output of the lock-in amplifier. At the source electrode the voltage has spectral components at $f+\Delta f$ and $f-\Delta f$, whereas the gate voltage is oscillating at frequency f. The nanotube mixes both signals, which results in an output current at the drain electrode with spectral components at Δf, $f+\Delta f$, $f-\Delta f$, $2f+\Delta f$ and $2f-\Delta f$. The Δf part of the current flowing through the nanotube is converted into a voltage and is measured with the lock-in amplifier. The printed circuit board (PCB) with the sample, bias-T and 50Ω terminator is located inside the vacuum chamber of a probe station.

5.4 GATE-TUNABLE RESONANCES

In five devices (two with and three without an etch-mask) we have observed gate-dependent resonances in the current flowing through the semiconducting nanotubes, when we sweep the driving frequency f. The suspended length of the devices ranges between 1.1μm and 1.5μm, and they have nanotube diameters from 1 to 3 nm as determined from AFM measurements. Four of these devices show only a single gate-dependent resonance. In the fifth sample no resonances were observed at low driving amplitudes. However, we observed multiple equidistant resonances at high driving voltages (500 mV), where the system is expected to be strongly non-linear, which could give rise to resonances at harmonics of the eigenfrequency. The experimental and theoretical work presented in this Chapter focuses on the linear vibration of the resonators.

The gate-tunable resonance measured in a typical device (labelled device A) with a length of $\ell = 1.25\,\mu$m and radius $r = 1.4$ nm is highlighted in this Chapter. PMMA etch masks have been used to suspend this device. The normalized lock-in current plotted against the dc gate voltage and the driving frequency is shown in Fig. 5.3. Apart from two (gate-independent) electrical resonances around 30 and 60 MHz, a single gate-dependent resonance can be clearly seen. No other tunable resonances are observed, when measur-

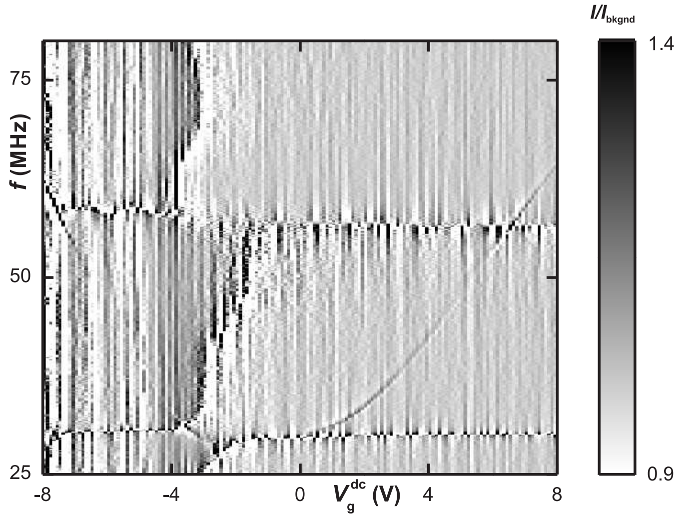

FIGURE 5.3: Color plot of the normalized lock-in current of device A as a function of dc gate voltage and driving frequency with $V_g^{ac} = 20\,\text{mV}$. A single gate-dependent resonance can clearly be seen.

ing up to 250 MHz. The right branch (with respect to $V_g^{dc} = 0\,\text{V}$) appears to be shifted to a higher frequency compared to the left side. This shift is reproduced when the measurement is repeated. The gate voltage tunes the frequency from 30 to 63 MHz, initially with a parabolic form, but for gate voltages larger than about 4 V the increase is less steep. This behavior is in agreement with the calculations in Ch. 3 and Ref. [15] which show that the nanotube can be tuned from the weak to strong bending regime with the gate voltage (see the discussion below).

5.5 PEAK SHAPES AND Q-FACTORS

We also find that the shape of the resonance depends on the dc gate voltage. Two examples are shown in Figures 5.4a and b. The difference in peak shape is caused by changes in the phase difference φ between the RF signals on the gate and the source electrode[2], which are accounted for when calculating the current:

$$I = I_{\text{direct}} \cos(\varphi) + I_{\text{mech}} \big(\cos(\varphi)\text{Re}[H] - \sin(\varphi)\text{Im}[H]\big). \tag{5.2}$$

[2]The ac bias voltage can be written as: $V_{sd}^{ac}(t) = V_{sd}^{ac} \cos(2\pi f t + \varphi) \cos(2\pi \Delta f t)$. The phase difference φ between the gate and source electrode depends on the frequency of the RF signals, on the (gate dependent) conductance of the nanotube and its derivative with respect to V_g^{dc}. Note also that the lock-in detected phase does not contain information about φ.

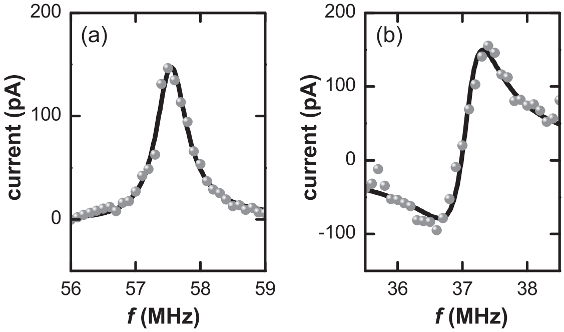

FIGURE 5.4: Linetraces of the down-mixed current of Fig. 5.3 at $V_g^{dc} = -7.5$V (a) and $V_g^{dc} = 2.9$V (b) with the background subtracted. The solid lines are fits of Eq. 5.2 to the data. The resonance of (a) has a quality factor $Q = 100$ and phase difference $\varphi = 0.54\,\pi$; resonance (b) has $Q = 58$ and a phase difference $\varphi = 0.89\,\pi$. For a complete list of the fit parameters, see Table 5.1.

Here, $H = f_R^2/Q \cdot 1/(f_R^2 - f^2 + \mathrm{i} f f_R/Q)$ is the (normalized) response function of a harmonic oscillator with resonance frequency f_R and quality factor Q, driven at frequency f. The solid lines in Fig. 5.4a and b are fits to Eq. 5.2, which reproduce the data well. The resonance on the left has a quality factor $Q = 100$ and phase difference $\varphi = 0.54\pi$; for the resonance on the right we find $Q = 58$ and $\varphi = 0.89\pi$. For other gate voltages we find Q-factors in the range from 40 to 160. It is interesting to note that for the three devices without PMMA etch masks, fits yield smaller Q-values of the order of 10. Their lower Q-factor may be due to a difference in the clamping points but a more systematic study has to be done to confirm this. From the fits, the amplitude of oscillation can be estimated using Eqs. 3.32, 5.1 and 5.2:

$$\frac{I_{\text{mech}}}{I_{\text{direct}}} = \frac{\overline{u}(f_R)}{\sqrt{h_g^2 - r^2} \cdot \operatorname{arccosh}(h_g/r)} \frac{V_g^{dc}}{V_g^{ac}}. \tag{5.3}$$

where h_g and r are the distance of the nanotube to the back-gate electrode (500 nm) and the radius of the nanotube respectively. For the peaks in Fig. 5.4a and b, the amplitudes are: $\overline{u} = 5.0$ nm and 5.5 nm respectively.

5.6 ANALYSIS OF THE GATE-TUNABILITY

To explain the dc gate voltage dependence of the resonance, we use the continuum model for the bending mode of a cylindrical beam of Ch. 3 to describe our nanotube resonator:

$$\rho A \frac{\partial^2 u}{\partial t^2} + \eta \frac{\partial u}{\partial t} + D \frac{\partial^4 u}{\partial x^4} - T \frac{\partial^2 u}{\partial x^2} = F(x,t). \tag{5.4}$$

The first term contains the linear mass density ρA and represents the acceleration of the displacement $u(x,t)$. The next term includes the damping, which is proportional to the velocity of the tube (η is a constant). D is the bending rigidity of the tube, and T is the tension in the tube [15–18]. With a dc and a small ac gate voltage, the external force is given by [15]:

$$F \approx \frac{1}{2}\frac{\partial c_{\mathrm{g}}}{\partial u}\left((V_{\mathrm{g}}^{\mathrm{dc}})^2 + 2V_{\mathrm{g}}^{\mathrm{dc}}V_{\mathrm{g}}^{\mathrm{ac}}\cos(\omega t)\right), \tag{5.5}$$

where $\omega = 2\pi f$ and $c_{\mathrm{g}} = 2\pi\epsilon_0/\mathrm{arccosh}\left(h_{\mathrm{g}}/r - u/r\right)$ is the capacitance per unit length.

The displacement amplitude increases considerably when the tube is driven at an eigenfrequency of the system. However, antisymmetric modes cannot be detected by our detection technique, as the displacement averaged along the tube, $\overline{u}$, is zero: see the discussion of Eq. 3.46. Moreover, higher even modes ($n = 2, 4, \ldots$) have a much smaller average displacement compared to the fundamental mode; the fundamental mode will therefore be the most dominant one in the experiments described in the Chapter.

As explained in Sec. 3.5, two different regimes [15] can be distinguished: when the bending rigidity term is much larger than the tension term, the tube behaves as a beam and the resonance frequency of the fundamental mode is given by [1]: $f_0 = 22.4/2\pi\ell^2 \cdot \sqrt{EI/\rho A}$. In the opposite case, the tube is under large tension and behaves as a rubber band with a resonance frequencies $f_{T_{DC},n} = (n+1)/2\ell \cdot \sqrt{T_{\mathrm{dc}}/\rho A} \cdot [1 + 6a_n^2/\pi^2(n+1)^2]^{1/2}$ (Cf. Eq. 3.52). The static displacement u_{dc} and tension T_{dc} are found by solving Eqs. 3.38 and 3.39 self-consistently [15, 17] with the cross-over voltage V_{g}^* and residual tension T_0 as free parameters. With these results and the value of the frequency scale $\Omega = (D/\rho A)^{1/2}/\ell^2$, the tuning curve of the resonance frequency $f_R(V_{\mathrm{g}}^{\mathrm{dc}})$ can be fitted. The three fit parameters are thus:

- the resonance frequency in the absence of tension f_0,
- the gate voltage V_{g}^* at which the cross-over between the bending and the tension dominated regime occurs,
- the (dimensionless) residual tension at zero gate voltage, $T_0' = T_0\ell^2/D$.

The result of the fit procedure[3] for two different devices (A and B) is shown in Fig. 5.5a. The frequency dependence of the resonance of device A is fitted well with $f_0 = 40\,\mathrm{MHz}$, $V_{\mathrm{g}}^* = 2.5\,\mathrm{V}$ and $T_0\ell^2/D = -18$. The fit parameters can be compared to the values calculated from the dimensions of the device (see Table 3.3). The fundamental frequency of a nanotube with measured dimensions $\ell = 1.25\,\mu\mathrm{m}$ and $r = 1.4\,\mathrm{nm}$ is $f_0 = 56\,\mathrm{MHz}$, which is in reasonable agreement with the fit, considering the uncertainty in the tube radius. Fitting[4]

[3] In this fit, the ac tension has not been taken into account. For a discussion on the differences between the so-called extended and standard model see Ref. [14].

[4] The minimum of the resonance frequency of device B was located at $V_{\mathrm{g}}^{\mathrm{dc}} = -1.7\,\mathrm{V}$. The curves of device B in Fig. 5.5a and b are shifted accordingly. This shift may be explained by a nonzero dc potential on the nanotube due to work function differences between the tube and the metallic electrodes. More research is required to confirm this.

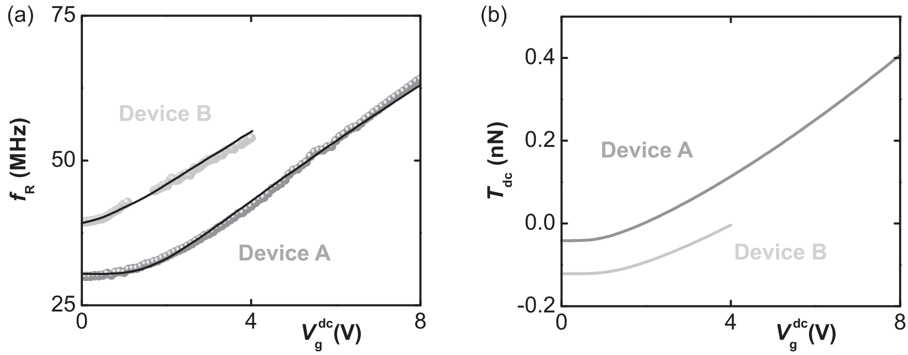

FIGURE 5.5: (a) Resonance frequency f_R extracted from Fig. 5.3 (device A) and from a second device (device B). At some gate voltages, the resonance could not be resolved, due to a low signal-to-noise ratio. The continuum model described in the text (solid lines) fits the gate dependence of the resonance frequency well. (b) The calculated tension in the nanotubes.

the frequency-dependent resonance of device B (upper curve in Fig. 5.5a), yields for the fit parameters: $f_0 = 62\,\text{MHz}$, $V_g^* = 4.8\,\text{V}$ and $T_0\ell^2/D = -26$. Device B consists of a shorter ($\ell = 1.15\,\mu\text{m}$) and thicker nanotube ($r = 1.6\,\text{nm}$), so the predicted fundamental frequency is higher than that of device A: $f_0 = 81\,\text{MHz}$, which is again in reasonable agreement with the frequency obtained from the fit.

We can also estimate the cross-over voltage V_g^* with the model, which yields 1.2 V and 1.9 V for device A and B respectively as indicated in Table 3.3. In both cases, the calculated value is lower than the values obtained from the fits but of the same order. The higher values from the fit may be explained by a screening of the gate by the source and drain electrode, resulting in effectively lower pulling forces. As the cross-over voltage V_g^* in our devices is experimentally accessible, we can tune the nanotube from the beam-like ($V_g^{dc} < V_g^*$) to the string-like ($V_g^{dc} > V_g^*$) regime.

The extracted values for the residual tension T_0 are negative, but still above the critical tension value ($T_c = -4\pi^2 \cdot D/\ell^2$) where *Euler-buckling* occurs (see Sec. 3.3), indicating that the tubes in our devices do not exhibit slack, as confirmed by SEM images (see Fig. 5.1). This has to be contrasted to the work by Sazonova *et al.* [9], where slack is present, which makes the tubes act as hanging chains. When slack is present, the nanotube can oscillate with several modes [9, 18], making the identification of the observed modes difficult.

5.7 MOTION AMPLITUDE AND SENSITIVITY

The consistency of the model can further be checked by estimating the oscillation amplitude. From the fitted gate-dependence we obtain the tension needed to calculate the motion amplitude from the electrostatic driving force. With the Q-factors from the fits shown in Fig. 5.4a and b, the (length-averaged) amplitudes for device A are $\bar{u} = 7.9\,\text{nm}$ and $4.0\,\text{nm}$

TABLE 5.1: Fit parameters extracted from frequency traces of the data displayed in Fig. 5.3 at different gate voltages V_g^{dc}. With the current noise PSD $S_{II}^{1/2}$ and transduction factor $\partial I/\partial \bar{u}$ the displacement sensitivity is calculated.

$\mathbf{V_g^{dc}}$	-7.5	1.0	2.9	3.7	8.0	V
$\mathbf{f_R}$	57.53 ± 0.04	31.42 ± 0.06	37.09 ± 0.04	40.85 ± 0.08	64.29 ± 0.04	MHz
Q	100 ± 11	43 ± 5	58 ± 8	51 ± 12	134 ± 17	
φ	1.69 ± 0.10	2.03 ± 0.20	-3.46 ± 0.11	2.89 ± 0.21	1.49 ± 0.11	rad
$\mathbf{I_{bkgnd}}$	31 ± 2	252 ± 9	850 ± 4	1004 ± 12	593 ± 3	pA
$\mathbf{I_{direct}}$	263 ± 30	569 ± 104	895 ± 31	1037 ± 56	7347 ± 806	pA
$\mathbf{I_{mech}}$	148 ± 19	233 ± 37	228 ± 44	167 ± 60	98 ± 14	pA
$\partial I/\partial \bar{u}$	30	8.6	39	58	-	pA/nm
$\mathbf{S_{II}^{1/2}}$	3.18	3.97	4.50	4.17	4.67	pA/Hz$^{1/2}$
$\mathbf{S_{u_n u_n}^{1/2}}$	0.11	0.46	0.11	0.07	-	nm/Hz$^{1/2}$

at $V_g^{dc} = -7.5$ V and $V_g^{dc} = 2.9$ V respectively. These values are close to the values obtained from the peak height. Thus, the model, together with the fit parameters obtained from the data can be used to estimate $\bar{u}$ and T at any gate voltage. For example, at the highest gate voltage ($V_g^{dc} = 8$ V), the nanotube is under a tension of $T = 0.40$ nN due to a static displacement of $u_{dc}(\ell/2) = 6$ nm. This corresponds to a strain of $6 \cdot 10^{-5}$. Figure 5.5b shows the reconstructed tension $T(V_g^{dc})$ for the two devices discussed in the previous Section.

The model also explains why higher modes were not detected: The mechanical contribution to the current (Eq. 5.3)of the $n = 2$ mode is almost 30 times smaller than for the fundamental mode: $\bar{u}$ is of the order of 0.2 nm. For the data shown in Fig. 5.4a this would result in a resonance of 5 pA, which is of the same order as the background fluctuations. For higher mode numbers this contribution is increasingly smaller; only the fundamental mode can therefore be resolved in our measurements.

We now focus on the sensitivity of the mixing-technique, which is the product of the transduction factor and the current sensitivity. By combining Eq. 5.2 with Eq. 5.3 the transduction factor is obtained:

$$\frac{\partial I}{\partial \bar{u}} = \frac{\partial I_{\mathrm{mech}}}{\partial \bar{u}(f_R)} \frac{\cos(\varphi)\mathrm{Re}[H] + \sin(\varphi)\mathrm{Im}[H]}{|H|} \approx \frac{I_{\mathrm{direct}}}{\sqrt{h_g^2 - r^2} \cdot \mathrm{arccosh}(h_g/r)} \frac{V_g^{dc}}{V_g^{ac}}. \tag{5.6}$$

Together with the parameters extracted from some of the traces of Fig. 5.3 the sensitivity of the mixing technique is found (see Table 5.1). The sensitivity depends gate voltage and is of the order of 0.1 nm/Hz$^{1/2}$. This number can be improved by either increasing the transduction factor or by decreasing the current noise level.

5.8 THE MIXING TECHNIQUE IN COULOMB BLOCKADE

It is often advantageous to do experiments at low temperatures, because this tends to reduce the noise present. When the nanotube is used as a frequency-mixer to detect is own motion, the noise that determines the position resolution is current noise. When this noise is reduced, the displacement sensitivity $S_{u_n u_n}$ improves. In this Section we explore the features of the mixing technique at low temperatures by extend our model of the mixing scheme (Sections 5.3 and 5.5) to the Coulomb blockade regime.

When nanotube devices are cooled down to cryogenic temperatures, tunnel barriers between the metallic leads and the nanotube form. This may lead to the formation of a quantum dot within the nanotube [19, 20]. The gate dependence of the conductance can display different behaviors, depending on the coupling between the nanotube and the leads [21]. For large couplings Γ, Fabry-Perot behavior with a slowly varying conductance is expected [22], while for small Γ, Coulomb blockade is observed [19, 20, 23, 24]. In the latter case the conductance consists of a series of sharp peaks with a width depending on Γ and the electron temperature. Coulomb blockade therefore greatly enhances the transconductance $\partial G/\partial V_{\mathrm{g}}^{\mathrm{dc}}$ of the device [25] and thereby improves the sensitivity.

MIXING

Due to the sharpness of the Coulomb peaks ($\ll V_{\mathrm{g}}^{\mathrm{ac}}$), the usual derivation of the mixing current breaks down, and one may ask whether it is possible to measure the driven vibrations of the nanotube at all with the frequency mixing technique. To answer this question, a simple model is used, where tunnelling between the nanotube and the leads takes place through a single quantum level [26]. The current in the blocked regions is zero, while in the conducting regions it assumes a constant value $\pm I_0$. This can be written as $I = I_0 \cdot \left[\Theta(V_{\mathrm{g}} + V_{\mathrm{sd}}/2) - \Theta(V_{\mathrm{g}} - V_{\mathrm{sd}}/2)\right]$, where Θ is the Heaviside step function; such a dependence of the current on V_{g} and V_{sd} is depicted in Fig. 5.6a, sketching the stability diagram of the quantum dot.

When using the mixing technique, the bias and gate voltage V and V_{g} are the sum of ac and dc components. In other words, while time elapses, the bias and gate voltages trace trajectories through the stability diagram, as illustrated in Fig. 5.6a. The trajectories are ellipsoidal since $V_{\mathrm{g}}^{\mathrm{ac}}$ and $V_{\mathrm{sd}}^{\mathrm{ac}}$ vary as $\cos(\omega t + \varphi)$ and $\cos(\omega t)$ respectively, and their shape depends on the phase φ between $V_{\mathrm{g}}^{\mathrm{ac}}$ and $V_{\mathrm{sd}}^{\mathrm{ac}}$. Well inside the Coulomb blockade region the current remains zero at all times. However, when a trajectory crosses the edge of the Coulomb blockade region, fast current oscillations will occur, since the quantum dot is switching rapidly into and out of blockade. In the experiment, only the low-frequency components of the current are measured. Thus, we calculate the corresponding time-averaged signal:

$$\langle I \rangle = I_0 \cdot A(V_-^{\mathrm{dc}}/V_-^{\mathrm{ac}}) - I_0 \cdot A(V_+^{\mathrm{dc}}/V_+^{\mathrm{ac}}), \tag{5.7}$$

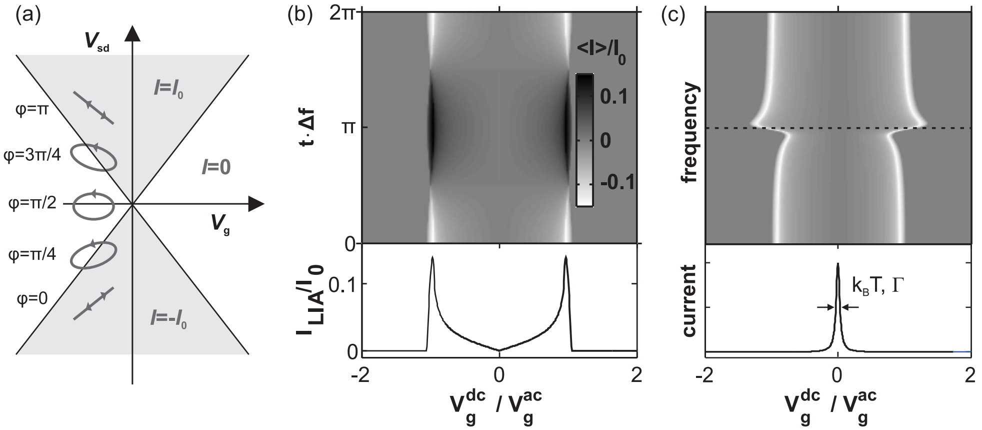

FIGURE 5.6: (a) Schematic of the effect of ac gate and bias voltages in the stability diagram of a quantum dot, where in the SET regime a single transport channel carries a current $\pm I_0$. Ellipsoidal trajectories through the diagram are traced, with a shape depending on the phase difference φ between the two ac voltages. (b) Calculated time dependence (top) of the average current $\langle I\rangle$ for $V_{\rm sd}^{\rm dc} = 0$ and $\varphi = 0$, when modulating the source-drain voltage with $V_{\rm sd}^{\rm ac}/V_{\rm g}^{\rm ac} = 0.1\cdot\cos(2\pi\Delta f\, t)$. The bottom panel shows the component of $\langle I\rangle$ at the lock-in frequency Δf, $I_{\rm LIA}$. (c) Simulated down-mixed nanotube current $I_{\rm LIA}$ (top panel) when sweeping the driving frequency around the mechanical eigenfrequency (dashed line) for the same conditions as (b). The sharpness of the edge of the signal determines how easily the resonance can be observed; this is thus limited by the width of the Coulomb peak on which the signal is mixed (bottom panel), i.e. by temperature $k_{\rm B}T$ or coupling Γ.

where the function A is defined as:

$$A(x) = \begin{cases} 0 & x \geq 1 \\ \arccos(x)/\pi & -1 \leq x \leq 1 \\ 1 & x \leq -1 \end{cases} \tag{5.8}$$

and

$$V_{\pm}^{\rm ac} = \left((V_{\rm g}^{\rm ac})^2 + (V_{\rm g}^{\rm ac}/2)^2 \pm V_{\rm g}^{\rm ac} V_{\rm sd}^{\rm ac}\cos(\varphi)\right)^{1/2}, \tag{5.9}$$

$$V_{\pm}^{\rm dc} = V_{\rm g}^{\rm dc} \pm V_{\rm sd}^{\rm dc}/2. \tag{5.10}$$

The signal depends on the position in the stability diagram through $V_{\rm g}^{\rm dc}$ and $V_{\rm sd}^{\rm dc}$, on the magnitudes of the ac gate and source–drain voltages $V_{\rm g}^{\rm ac}$ and $V_{\rm sd}^{\rm ac}$, and on the phase difference φ between them.

In all experimental realizations, the frequencies of the two ac signals differ by $\Delta f = \Delta\omega/2\pi$. The details depend, however, on the type of mixing setup employed: With the two-generator technique [9] the phase difference is effectively time dependent, i.e. $\varphi = \varphi_0 + \Delta\omega t$, while in our one-generator setup (Fig. 5.2) the ac source–drain voltage is amplitude-modulated, i.e. $V_{\rm sd}^{\rm ac} \to V_{\rm sd}^{\rm ac}\cos(\Delta\omega t)$ and a third technique amplitude-modulates both $V_{\rm g}^{\rm ac}$

and $V_{\mathrm{sd}}^{\mathrm{ac}}$ [27]. In all cases, the time-averaged current contains low-frequency oscillations at the offset frequency Δf that can be measured using a lock-in amplifier. In the following analysis we focus on the single generator setup. The results are qualitatively identical for the other cases.

The time-averaged current $\langle I \rangle$ is calculated numerically while modulating $V_{\mathrm{sd}}^{\mathrm{ac}}$ at a frequency Δf. Then the component of $\langle I \rangle$ at Δf is extracted, as would be measured using a lock-in amplifier. This results in the signal plotted in the lower panel of Fig. 5.6b. The original Coulomb peak is widened due to the ac voltages, but there is still a sharp transition between the regions with and without current.

MOTION DETECTION

The signal that was calculated above is always present, even without any displacement of the nanotube as it only uses the mixing properties of the nanotube [28], similar to the direct contribution that is present in room-temperature mixing. The effect of nanotube vibrations is an apparent change in the magnitude and phase of the ac gate voltage when $C_{\mathrm{g}}^{\mathrm{ac}} \neq 0$, as can be seen from Eq. 5.1. The effects of this becomes clear when the down-mixed current is calculated for different driving frequencies (Fig. 5.6c, top panel). Off-resonance, the original background signal from the bottom panel of Fig. 5.6b is obtained. When approaching the mechanical eigenfrequency, a clear resonance can be seen, which is best visible in the *shape* of the signal. This stands in contrast to the usual mixing signal (i.e. Eq. 5.2) where the resonance appears in the *magnitude* of the current. The sharp edges of the widened Coulomb peak (see the lower panel of Fig. 5.6b) will enable sensitive detection of vibrational motion of the nanotube. Its finite outer slope (i.e. towards higher absolute values of $V_{\mathrm{g}}^{\mathrm{dc}}/V_{\mathrm{g}}^{\mathrm{ac}}$) is due to the non-zero value of $V_{\mathrm{sd}}^{\mathrm{ac}}$. A reduction of this voltage gives an even sharper peak and therefore a higher sensitivity. However, at some point, the broadening of the original Coulomb peak (lower panel of Fig. 5.6c) due to the finite electron temperature or to coupling to the leads starts to dominate this slope and the sensitivity can no longer be increased by reducing $V_{\mathrm{sd}}^{\mathrm{ac}}$.

5.9 CONCLUSIONS

In conclusion, we have measured a single gate-dependent resonance due to mechanical motion of suspended nanotubes. By fitting the gate-dependence to a continuum model, we have identified the resonance as the fundamental flexural bending mode of the nanotube. With the model, we extracted the fundamental frequency, the gate-induced and residual tension in the nanotube, which are in agreement with their predicted values. The good agreement between experiment and model is a starting point for a further study of the flexural bending mode in suspended carbon nanotubes that includes the non-linear and quantum regime of operation and of damping mechanisms such as the one associated with the coupling to the clamping points. The sensitivity of the mixing technique can be improved when using nanotubes that are in the Coulomb blockaded regime.

ACKNOWLEDGEMENT

We thank Raymond Schouten for discussions and technical support. Financial support is obtained from the Dutch organization for Fundamental Research on Matter (FOM), by the "Nederlandse Organisatie voor Wetenschappelijk Onderzoek" (VICI-grant), and from EC FP6 funding (contract no. FP6-2004-IST-003673). This publication reflects the views of the authors and not necessarily those of the EC. The Community is not liable for any use that may be made of the information contained herein.

REFERENCES

[1] A. Cleland, *Foundations of Nanomechanics* (Springer, 2003).

[2] R. G. Knobel and A. N. Cleland, *Nanometre-scale displacement sensing using a single electron transistor*, Nature **424**, 291 (2003).

[3] A. Krishnan, E. Dujardin, T. W. Ebbesen, P. N. Yianilos, and M. M. J. Treacy, *Young's modulus of single-walled nanotubes*, Phys. Rev. B **58**, 14013 (1998).

[4] B. Reulet, A. Y. Kasumov, M. Kociak, R. Deblock, I. I. Khodos, Y. B. Gorbatov, V. T. Volkov, C. Journet, and H. Bouchiat, *Acoustoelectric Effects in Carbon Nanotubes*, Phys. Rev. Lett. **85**, 2829 (2000).

[5] B. J. LeRoy, S. G. Lemay, J. Kong, and C. Dekker, *Electrical generation and absorption of phonons in carbon nanotubes*, Nature **432**, 371 (2004).

[6] S. Sapmaz, P. Jarillo-Herrero, Y. M. Blanter, C. Dekker, and H. S. J. van der Zant, *Tunneling in Suspended Carbon Nanotubes Assisted by Longitudinal Phonons*, Phys. Rev. Lett. **96**, 026801 (pages 4) (2006).

[7] B. Babić, J. Furer, S. Sahoo, S. Farhangfar, and C. Schönenberger, *Intrinsic Thermal Vibrations of Suspended Doubly Clamped Single-Wall Carbon Nanotubes*, Nano Lett. **3**, 1577 (2003).

[8] J. C. Meyer, M. Paillet, and S. Roth, *Single-Molecule Torsional Pendulum*, Science **309**, 1539 (2005).

[9] V. Sazonova, Y. Yaish, H. Üstünel, D. Roundy, T. A. Arias, and P. L. McEuen, *A tunable carbon nanotube electromechanical oscillator*, Nature **431**, 284 (2004).

[10] B. Babić, M. Iqbal, and C. Schönenberger, *Ambipolar field-effect transistor on as-grown single-wall carbon nanotubes*, Nanotechnology **14**, 327 (2003).

[11] J. Kong, H. T. Soh, A. M. Cassell, C. F. Quate, and H. Dai, *Synthesis of individual single-walled carbon nanotubes on patterned silicon wafers*, Nature **395**, 878 (1998).

[12] D. A. Walters, L. M. Ericson, M. J. Casavant, J. Liu, D. T. Colbert, K. A. Smith, and R. E. Smalley, *Elastic strain of freely suspended single-wall carbon nanotube ropes*, Appl. Phys. Lett. **74**, 3803 (1999).

[13] J. Nygard and D. H. Cobden, *Quantum dots in suspended single-wall carbon nanotubes*, Appl. Phys. Lett. **79**, 4216 (2001).

[14] B. Witkamp, *High-frequency Nanotube Resonators*, Ph.D. thesis, Delft University of Technology (2009), URL `http://resolver.tudelft.nl/uuid:3814f598-488b-4cca-96d2-302d814a10f8`.

[15] S. Sapmaz, Y. M. Blanter, L. Gurevich, and H. S. J. van der Zant, *Carbon nanotubes as nanoelectromechanical systems*, Phys. Rev. B **67**, 235414 (2003).

[16] H. W. C. Postma, I. Kozinsky, A. Husain, and M. L. Roukes, *Dynamic range of nanotube- and nanowire-based electromechanical systems,* Appl. Phys. Lett. **86**, 223105 (pages 3) (2005).

[17] R. Lefèvre, M. F. Goffman, V. Derycke, C. Miko, L. Forró, J. P. Bourgoin, and P. Hesto, *Scaling Law in Carbon Nanotube Electromechanical Devices,* Phys. Rev. Lett. **95**, 185504 (pages 4) (2005).

[18] H. Üstünel, D. Roundy, and T. Arias, *Modeling a Suspended Nanotube Oscillator*, Nano Lett. **5**, 523 (2005).

[19] M. Bockrath, D. H. Cobden, P. L. McEuen, N. G. Chopra, A. Zettl, A. Thess, and R. E. Smalley, *Single-Electron Transport in Ropes of Carbon Nanotubes,* Science **275**, 1922 (1997).

[20] S. J. Tans, M. H. Devoret, H. Dai, A. Thess, R. E. Smalley, L. J. Geerligs, and C. Dekker, *Individual single-wall carbon nanotubes as quantum wires*, Nature **386**, 474 (1997).

[21] W. Liang, M. Bockrath, and H. Park, *TRANSPORT SPECTROSCOPY OF CHEMICAL NANOSTRUCTURES: The Case of Metallic Single-Walled Carbon Nanotubes*, Annu. Rev. Phys. Chem. **56**, 475 (2005).

[22] W. Liang, M. Bockrath, D. Bozovic, J. H. Hafner, M. Tinkham, and H. Park, *Fabry - Perot interference in a nanotube electron waveguide*, Nature **411**, 665 (2001).

[23] I. O. Kulik and R. I. Shekhter, *Kinetic phenomena and charge discreteness effects in granulated media*, Soviet Physics - JETP **41**, 308 (1975).

[24] D. V. Averin and K. K. Likharev, *Coulomb blockade of single-electron tunneling, and coherent oscillations in small tunnel junctions*, Journal of Low Temperature Physics **62**, 345 (1986).

[25] H.-Y. Chiu, P. Hung, H. W. C. Postma, and M. Bockrath, *Atomic-Scale Mass Sensing Using Carbon Nanotube Resonators*, Nano Lett. **8**, 4342 (2008).

[26] S. Datta, *Electronic Transport in Mesoscopic Systems* (Cambridge University Press, 1995).

[27] B. Witkamp, M. Poot, H. Pathangi, A. K. Hüttel, and H. S. J. van der Zant, *Self-detecting gate-tunable nanotube paddle resonators*, Appl. Phys. Lett. **93**, 111909 (pages 3) (2008).

[28] S. Rosenblatt, H. Lin, V. Sazonova, S. Tiwari, and P. L. McEuen, *Mixing at 50 GHz using a single-walled carbon nanotube transistor*, Appl. Phys. Lett. **87**, 153111 (pages 3) (2005).

6

Carbon nanotubes as strongly-coupled, ultra-high quality factor mechanical resonators

A. K. Hüttel, G. A. Steele, B. Witkamp, M. Poot, H. B. Meerwaldt, L. P. Kouwenhoven, and H. S. J. van der Zant

We have observed the transversal vibration mode of suspended carbon nanotubes at millikelvin temperatures by measuring the single-electron tunnelling current. The suspended nanotubes are actuated contact-free by the radio-frequency electric field of a nearby antenna; the mechanical resonance is detected in the time-averaged current through the nanotube. Sharp, gate-tuneable resonances due to the bending mode of the nanotube are observed, combining resonance frequencies of up to $f_R = 350\,\mathrm{MHz}$ *with quality factors above* $Q = 10^5$*, much higher than previously reported results on suspended carbon nanotube resonators. The measured magnitude and temperature dependence of the Q-factor shows a remarkable agreement with the intrinsic damping predicted for a suspended carbon nanotube. By adjusting the RF power on the antenna, we find that the nanotube resonator can easily be driven into the non-linear regime. The resonance frequency is tuned by a single electron and backaction due to single electron tunnelling is observed. The mechanical motion and the dynamics of the electrons are strongly correlated.*

Parts of this Chapter have been published in Nano Lett. **9**, 2547–2552 (2009) and Science **325**, 1103–1107 (2009)

High-quality resonating systems, providing high frequency resolution and long energy storage time, play an important role in many fields of physics. In particular, in the field of nanoelectromechanical systems [1, 2] recent research has led to the development of high-frequency top-down fabricated mechanical resonators with high quality factors [3–6]. However, when miniaturizing mechanical resonators to make them lighter and to increase their resonance frequency [1], the quality factor tends to decreases significantly due to surface effects [2]. High Q-values combined with high resonance frequencies are an important prerequisite for applications such as single-atom mass sensing [7–9] and fundamental studies of the quantum limit of mechanical motion [10]. Single-wall carbon nanotubes present a potentially defect-free nanomechanical system with extraordinary mechanical properties: in particular the high Young's modulus ($E = 1.2\,\mathrm{TPa}$) in combination with a very low mass density ($\rho = 1350\,\mathrm{kg/m^3}$, see Ch. 3) [8, 11, 12]. While these favorable properties should result in quality factors of the order of 2×10^5 [13], the observed Q-factors of nanotube resonators both at room temperature (Chapter 5 and Refs. [11, 14, 15]) and in low temperature experiments [7, 8] have not exceeded $Q \sim 2000$.

In this Chapter, we report on the observation of mechanical resonances of a driven suspended carbon nanotube at low temperatures with quality factors above 10^5 and resonance frequencies ranging from 120 MHz to 360 MHz. The resonances are detected with a novel detection scheme which uses the nonlinear gate-dependence of the current through the suspended nanotube quantum dot. In addition, we show that the nanotube resonator can easily be tuned to the non-linear regime, and that the operating temperature affects the non-linearity and the quality factor of the resonator. Finally, we explore the backaction due to the strong coupling of the resonator to the dynamics of the electrons tunnelling on and off the nanotubes.

6.1 DEVICE FABRICATION AND MEASUREMENT SETUP

Suspended carbon nanotube devices are made by growing nanotubes between platinum electrodes over an 800 nm wide pre-defined trench. The device geometry is shown in Fig. 6.1a. The fabrication method is discussed in detail by Steele *et al.* [16]. There, the device includes three local gates for tuning the confinement: here, however, we apply the same voltage to all three gates, so that they act together as one single gate. Since no device processing takes place after nanotube growth and the entire device is suspended, the nanotubes are highly defect-free and do not suffer from potential irregularities induced by the surface of the substrate [16, 17]. The fabrication method also offers the advantage that the resonator is not contaminated with resist residues.

After fabrication, the suspended nanotube devices are mounted in a dilution refrigerator with filtered twisted pair cabling attached to source, drain, and gate contacts (see Fig. 6.1a). This configuration allows us to apply dc gate and bias voltages to the suspended nanotube, and measure the current flowing through it. To minimize heating, we drive the nanotube resonator with the electric field radiated from a radio frequency (RF) antenna positioned near the sample (~ 1 cm) instead of connecting high-frequency cables directly

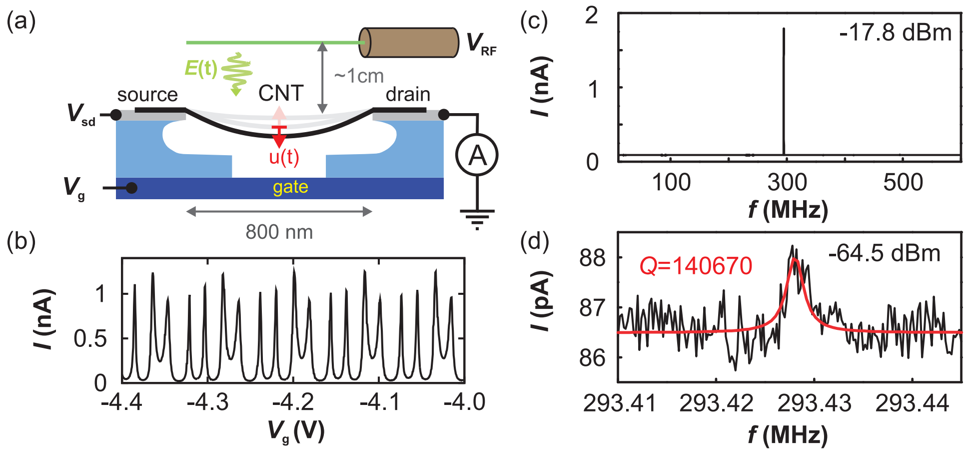

FIGURE 6.1: (a) Schematic drawing of the chip geometry, antenna, and measurement electronics. The nanotube acts as a doubly clamped beam resonator, driven by an electric field $E(t)$. The displacement of the nanotube is $u(t)$. (b) Example trace of the dc current at $V_{sd} = 50\,\mu$V as a function of gate voltage, demonstrating the regularity of the Coulomb peaks. It shows the four-fold degeneracy typical for clean single-wall carbon nanotubes. (c) When the frequency f of an RF signal on the antenna is swept with fixed V_g and V_{sd}, a resonant peak emerges in $I(f)$. An example of such a resonance is shown for a driving power of -17.8 dBm at a temperature of 20 mK. (d) Zoom of the resonance of (c) at low power (-64.5 dBm). The red line is a fit of a squared damped driven harmonic oscillator response to the resonance peak. For both (c) and (d) $V_g = -5.16$ V and $V_{sd} = 0.35$ mV.

to the sample. Measurements are performed at temperatures down to the base temperature of the mixing chamber of the dilution refrigerator, $T \simeq 20$ mK.

6.2 DETECTING FLEXURAL VIBRATIONS

Figure 6.1b shows the Coulomb oscillations of a semiconducting carbon nanotube with a suspended length of 800 nm (device C). A highly regular addition spectrum with clear four-fold degeneracy is visible, characteristic for a defect-free single-wall carbon nanotube [18, 19]. From the magnetic field dependence of the position of the Coulomb oscillations close to the semiconducting gap [20], we find the radius of the nanotube, r, to be between 1 and 1.5 nm. The value of the semiconducting gap ≈ 0.3 eV is estimated from the gate range between electron and hole conduction in the device at low temperatures, which is in agreement with the estimate of r.

When an ac voltage V_{RF} with frequency f is applied to the antenna, we observe a resonant feature at a well-defined frequency in the dc current flowing through the nanotube. Figure 6.1c shows an example of such a measurement at a large radio frequency (RF) voltage, or equivalently a high generator power. A sharp resonant feature is clearly visible at $f = 293$ MHz. Zooming in on this feature at a lower power (Fig. 6.1d) reveals a resonance peak with a narrow lineshape. A numerical fit of this data yields a quality factor $Q = 140670$

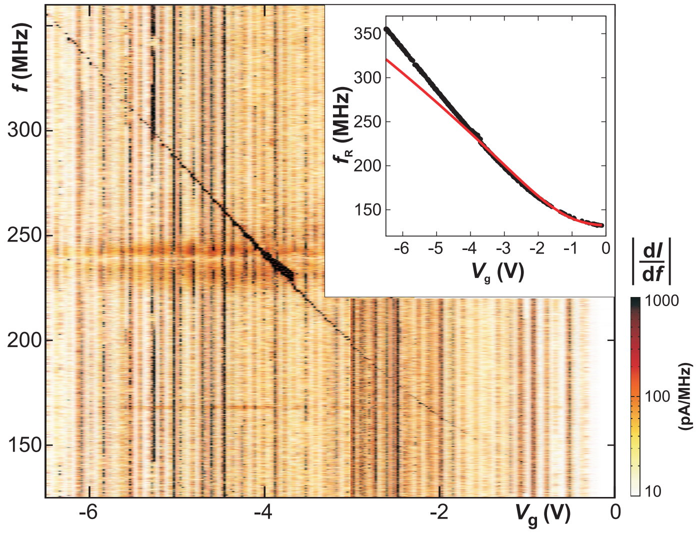

FIGURE 6.2: $|\mathrm{d}I/\mathrm{d}f|$ as a function of frequency f of the ac voltage on the antenna and the dc gate voltage V_g on the back-gate electrode. Horizontal lines are caused by electrical (cable) resonances (see [11] and Ch. 5); the narrow vertical stripe pattern is related to the Coulomb blockade oscillations. In addition, a gate-dependent resonant feature is clearly visible. Inset: Comparison of the extracted resonance frequency to the continuum model for the bending mode with $f_0 = 132.0\,\mathrm{MHz}$, $V_g^* = 2.26\,\mathrm{V}$, $T_0 = 0$, and a shift of 0.775 V in gate voltage to account for an offset in the charge neutrality point of the nanotube from $V_g = 0\,\mathrm{V}$ and the band gap region. The parameters are discussed in the text. An apparent shift of the mechanical resonance frequency at $f_R \simeq 230\,\mathrm{MHz}$ is caused by an electrical (cable) transmission resonance, leading to a strong increase in transmitted RF power and distorted peak shapes.

(see below for a discussion of the expected lineshape). We have also performed measurements on a second device (device D) displaying similar resonant peaks with Q-factors up to 20000; the results on that device are shown in the Supplement.

The resonance observed in Fig. 6.1c and d can be attributed to the flexural vibration mode of the suspended nanotube [7, 8, 11] and Ch. 5. To verify this, we electrostatically induce tension in the nanotube by applying a dc gate voltage V_g to the back-gate electrode. The dc gate voltage dependence is shown in Fig. 6.2. When decreasing the gate voltage from zero to more and more negative values, the resonance is tuned to higher frequencies by almost a factor of three: from less than $f_R = 140\,\mathrm{MHz}$ at $V_g = -1\,\mathrm{V}$ to $f_R = 355.5\,\mathrm{MHz}$ at $V_g = -6.5\,\mathrm{V}$. For the latter resonance frequency, the thermal occupation [10] $\bar{n} = [\exp(hf_R/k_B T) - 1]^{-1}$ would be 0.7 at 20 mK, suggesting that the resonator would be close to its quantum ground state in the absence of the driving fields required for our detection scheme.

We have extracted the resonance peak positions from the data in Fig. 6.2 and plotted them in the inset. The red line shows the gate dependence of the resonance frequency calculated with our continuum model for the fundamental flexural bending mode that is described in Chapters 3 and 5. The parameters are $f_0 = 132.0\,\mathrm{MHz}$, $V_\mathrm{g}^* = -2.26\,\mathrm{V}$, and $T_0 = 0$, where f_0 is the resonance frequency in absence of residual tension T_0 and V_g^* marks the cross over between the weak and strong bending regime. At high gate-voltage the model calculation deviates slightly from the experimental values. This is so far not fully understood and may be related to large static displacements of the nanotube in a complex electrostatic environment [21]. The value $f_0 = 22.4/2\pi\ell^2 \cdot r\sqrt{E/\rho} = 132.0\,\mathrm{MHz}$, assuming a tube length $\ell = 800\,\mathrm{nm}$, yields a nanotube radius of 1.6 nm, in good agreement with the band-gap and magnetic field estimates.

6.3 DETECTION MECHANISM

Depending on the gate voltage, the resonance either appears as a dip (Fig. 6.3a) or as a peak (Fig. 6.3b). Dips are found around the maxima of the Coulomb oscillations; away from these maxima, peaks are observed. This indicates that the detection of the mechanical modes is due to electrostatic interactions as we will now show. We model the effect of a small change in gate voltage δV_g on the current flowing through the nanotube by a Taylor expansion of $I(V_\mathrm{g} + \delta V_\mathrm{g})$ around $\delta V_\mathrm{g} = 0$. A crucial point in this expansion is that the second (and third) order term cannot be neglected, since the current flowing through the nanotube is strongly non-linear in the vicinity of the Coulomb oscillations. This is in contrast to the mixing technique at room temperature (Ch. 5 and Ref. [11]), where only the linear term in the expansion is needed.

The motion of the nanotube enters the measured current as follows: On resonance, the nanotube position $\bar{u}(t) = \bar{u}\cos\left(2\pi f_R t\right)$ oscillates with a finite amplitude $\bar{u}$, which periodically modulates the gate capacitance C_g by an amount $C_\mathrm{g}^\mathrm{ac} = \partial C_\mathrm{g}/\partial u \cdot \bar{u}$. The current flowing through the nanotube does not just depend on the gate voltage itself; more specifically, it depends on the product of the gate voltage and the gate capacitance; the so-called gate-induced charge [11, 22] defined in Chapter 5. A modulation of the capacitance due to the motion of the nanotube therefore has the same effect on the current as if an effective ac gate voltage $V_\mathrm{g,\,eff}^\mathrm{ac} = V_\mathrm{g} C_\mathrm{g}^\mathrm{ac}/C_\mathrm{g}$ were applied to the gate-electrode. The time-dependent current can then be calculated by inserting $\delta V_\mathrm{g} = V_\mathrm{g,\,eff}^\mathrm{ac}\cos(2\pi f t)$ into the Taylor expansion of $I(V_\mathrm{g} + \delta V_\mathrm{g})$.

Since the mechanical resonance frequency is much larger than the measurement bandwidth, time-averaged currents are detected in our setup. We find that the time-averaged mechanically-induced current equals:

$$\langle I\rangle(\bar{u}, V_\mathrm{g}) = I(V_\mathrm{g}) + \frac{\overline{u}^2}{4}\left(\frac{V_\mathrm{g}}{C_\mathrm{g}}\frac{\partial C_\mathrm{g}}{\partial u}\right)^2 \frac{\partial^2 I}{\partial V_\mathrm{g}^2} + \mathcal{O}\left(\bar{u}^4\right), \tag{6.1}$$

where only even powers of $\bar{u}$ enter the low-frequency current due to averaging. The change in dc current on mechanical resonance $\Delta I = \langle I\rangle - I$ is thus proportional to the local curvature $\partial^2 I/\partial V_\mathrm{g}^2$ of the Coulomb blockade oscillations $I(V_\mathrm{g})$.

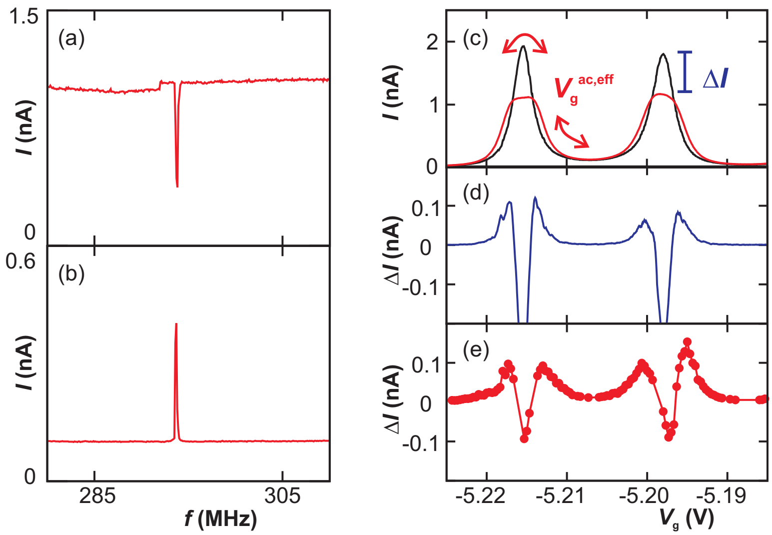

FIGURE 6.3: Averaging model for the current at resonance. (a), (b) Measured frequency sweeps demonstrating the sign change of the resonance amplitude depending on the gate voltage (RF power −13 dBm, $V_{sd} = 0.1\,\text{mV}$, $V_g = -5.17\,\text{V}$ (a) and $V_g = -5.16\,\text{V}$ (b)). (c) The black line shows the measured dc current as function of gate voltage $I(V_g)$ for $V_{sd} = 0.1\,\text{mV}$ (no RF). The red line, shows the effect of an (effective) ac gate voltage on the dc current. This average current (Eq. 6.1) is calculated using the measured data and $V^{ac}_{g,\,eff} = 2\,\text{mV}$. (d) Predicted resonance signal amplitude ΔI calculated by subtracting the dc current from the current averaged over an effective gate voltage $V^{ac}_{g,\,eff} = 1\,\text{mV}$. For a small $V^{ac}_{g,\,eff}$, the signal is proportional to the second derivative $\partial^2 I/\partial V_g^2$ of the black trace shown in (c), as expressed by Eq. 6.1. At the top of the Coulomb peak, ΔI is negative, whereas on the flanks of the Coulomb peak, it is positive. Note that in (c) a larger value of $V^{ac}_{g,\,eff}$ was used to exaggerate the difference between the black and red curves for illustrative purposes. (e) The measured resonance peak amplitudes obtained from $I(f)$ traces similar to Fig. 6.1d, for $V_{sd} = 0.1\,\text{mV}$ and a RF power of −48 dBm.

Using measured Coulomb oscillation traces where no driving signal was applied (black line in Fig. 6.3c), we have numerically calculated the behavior of a current time-averaged over $V^{ac}_{g,\,eff}$. The result is shown as a red line in Fig. 6.3c. Figure 6.3d shows the difference ΔI between the time-averaged and the static current of Fig. 6.3c. On top of a Coulomb oscillation, the curvature is negative and the averaged current (red) is smaller than the static current (black), resulting in a dip in the current on resonance, when the nanotube moves. On the other hand, ΔI is positive on the flanks of the Coulomb oscillations as the curvature is positive there. This can be compared with the traces $I(f)$ shown in Fig. 6.3a and b, and with the measurements of ΔI shown in Fig. 6.3e. Here we plot the amplitude $\Delta I(f_R)$ of the mechanical response in the dc current $I(f)$ for different gate voltages. The gate voltage dependence of the extracted amplitude values in dc current is in good qualitative agreement with the predictions of the model as shown in Fig. 6.3d.

6.4 MASS- AND DISPLACEMENT SENSITIVITY

The model also allows for a quantitative analysis of the peak shape and for an estimate of the displacement amplitude $\bar{u}$ in the case of resonant driving, by evaluating the change in dc current ΔI. We first use the result of Chapter 3 that $\bar{u}$ can be described by the response of a damped driven harmonic oscillator. From Eq. 6.1, we see that $\Delta I \propto \bar{u}^2$ so that the measured mechanical response (dip or peak) in the current is given by the *square* of the harmonic oscillator response function. For the resonance presented in Fig. 6.1d, we find $f_R = 293.428\,\mathrm{MHz}$ and $Q = 140670$. This Q-value is nearly two orders of magnitude higher than previous reported values of the flexural vibration modes in nanotubes [7, 8, 11]. Such high Q-values make this type of device very suitable for mass detection. From the measured response in Fig. 6.4e we estimate (see Supplement) a mass sensitivity of $7\,\mathrm{yg}/\sqrt{\mathrm{Hz}}$, i.e., in one second it should be possible to determine if, for example, a He atom has adsorbed onto the nanotube.

The displacement amplitude $\bar{u}$ in the case of resonant driving is estimated by modelling the capacitance between the nanotube and the back gate as an infinite wire and an infinite conducting plane, see Eq. 3.32. Using a device length of $\ell = 800\,\mathrm{nm}$, a tube radius $r = 1.5\,\mathrm{nm}$ and a gate distance $h_\mathrm{g} = 230\,\mathrm{nm}$, we obtain $C_\mathrm{g} = 7.8\,\mathrm{aF}$ and $\partial C_\mathrm{g}/\partial u = 5.9\,\mathrm{zF/nm}$, see Table 3.3. The calculated capacitance value is consistent with the experimentally determined value of $C_\mathrm{g} = 8.9\,\mathrm{aF}$ as determined from the Coulomb peak spacing. For the resonance in Fig. 6.4b, with $\partial^2 I/\partial V_\mathrm{g}^2 = 4.43\,\mu\mathrm{A/V}^2$ and $\Delta I(f_R) = 1.05\,\mathrm{pA}$, we estimate the oscillation amplitude of the nanotube to be $\bar{u}(f_R) = 0.25\,\mathrm{nm}$ on resonance. This amplitude is two orders of magnitude larger than that of the thermal fluctuations ($\frac{1}{2}k_\mathrm{B}T = \frac{1}{2}m(2\pi f_R)^2 u_\mathrm{th}^2$) of the nanotube [1], which is $\sim 6.5\,\mathrm{pm}$ at $T = 80\,\mathrm{mK}$, and its estimated zero-point motion [10, 23] of $u_0 = 1.9\,\mathrm{pm}$ at this gate voltage.

6.5 NON-LINEAR BEHAVIOR AND TEMPERATURE DEPENDENCE

When driving the nanotube resonator with large antenna voltages, we consistently observe hysteretic peak shapes and a strong frequency pulling of the resonance peaks (i.e. the frequency decreases for a larger motion amplitude [24, 25]). Figure 6.4a-d shows examples of the shape of the resonance peak at $V_\mathrm{g} = -5.16\,\mathrm{V}$ and $V_\mathrm{sd} = 0.35\,\mathrm{mV}$ for four different driving powers. Black lines indicate the sweep direction with increasing frequency; gray lines the one with decreasing frequency. At the lowest power, the mechanical resonance peak is not visible in the noise. With increasing driving power the resonance peak first shows a linear response with its characteristic squared-harmonic-oscillator-response shape (Fig. 6.4b). At higher powers hysteresis sets in, which becomes more pronounced with increasing RF power. This bistability is consistent with what is expected for a nonlinear mechanical (Duffing) resonator [1, 24].

We have studied the dynamic range[1] [2, 21, 26] in more detail and found that the driv-

[1] The lower boundary of the dynamic range is the power at which the resonance is no longer visible in the noise. The current noise in our experiments is caused by fluctuations in the electrostatic environment of the nanotube

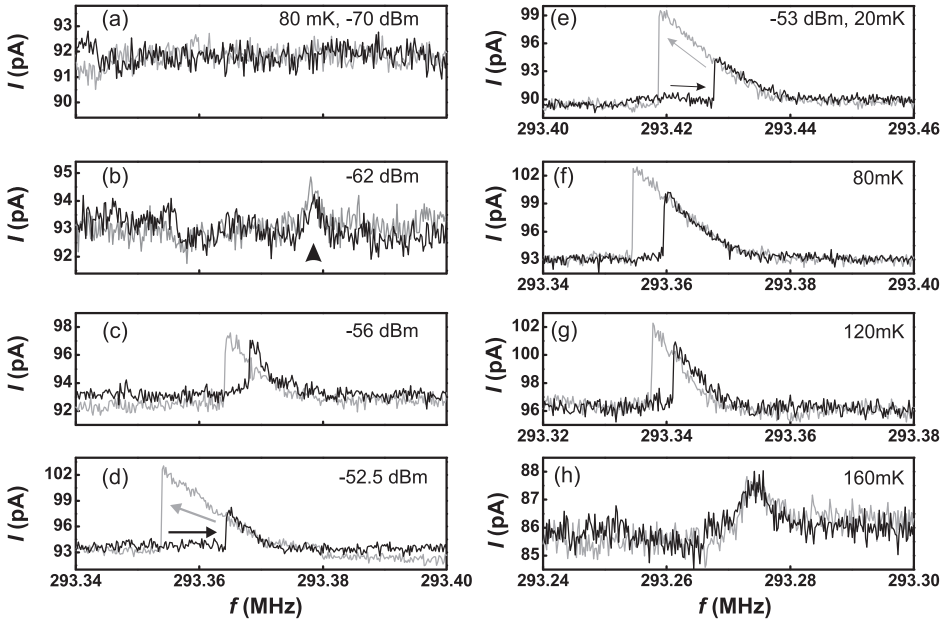

FIGURE 6.4: Evolution of the resonance peak with increasing driving power (a)-(d) and temperature (e)-(h). Black (gray) traces are upward (downward) frequency sweeps. (a) At low powers, the peak is not visible. (b) Upon increasing power, a resonance peak with $Q = 1.3 \cdot 10^5$ appears. (c) and (d) As the power is increased further, the lineshape of the resonance takes on a non-linear oscillator form, with a long high frequency tail and a sharp edge at lower frequencies. It also exhibits hysteresis between the upward and downward sweep that increases with driving power, characteristic of a non-linear oscillator. The traces (a)-(d) are taken at 80 mK. (e)-(h) Forward (black) and reverse (gray) frequency sweeps at a fixed driving power as a function of temperature. At low temperatures, the peak shape is non-linear and strongly hysteretic. At the same power, but higher temperature, the amount of hysteresis decreases significantly. At a temperature of 160 mK, hysteresis and asymmetry are no longer apparent; at the same time, the signal amplitude (and with it, also the signal to noise ratio) is decreased, suggesting a decrease in the Q-factor with increasing temperature. The working point of traces (a)-(h) is at $V_g = -5.16$V and $V_{sd} = 0.35$ mV.

ing powers where the (linear) peak disappears in the noise and where nonlinearity sets in depend on the temperature. An example of this effect is shown in Fig. 6.4e-h. These panels show that for a fixed gate voltage and driving power, the nanotube resonator response changes from non-linear to linear when the operating temperature is increased from 20 mK to 160 mK. This temperature-dependent behavior hints at a decrease in Q-factor as the temperature is increased.

To study the temperature dependence of the quality factor in more detail, we have

and not by to the thermal motion of the nanotube.

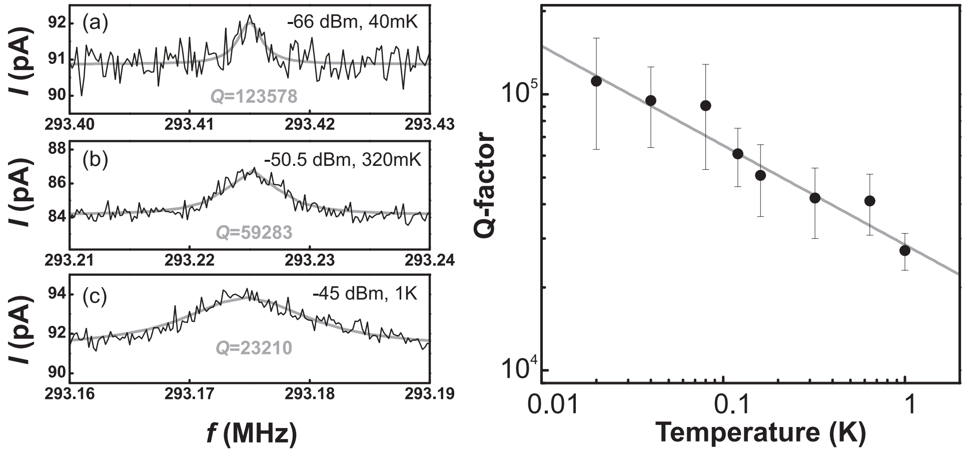

FIGURE 6.5: Temperature dependence of the Q-factor. (a)-(c) Fits of a squared harmonic oscillator response to the resonance in the linear regime at low powers for different temperatures at $V_g = -5.16$V and $V_{sd} = 0.35$mV. (d) A plot of the Q-factor vs. temperature obtained from linear response traces. Q decreases with increasing temperature. The gray line shows a $T^{-0.36}$ power law dependence (see text).

determined Q at different temperatures. For a gate voltage of −5.16V, three examples of resonance traces are depicted in Fig. 6.5a-c. Note that because the dynamic range is temperature dependent, the RF power is adjusted at every temperature to ensure a linear response. In Fig. 6.5d, we plot the Q-factor extracted in the linear regime for eight different temperatures in the range $20\,\text{mK} < T < 1\,\text{K}$. The error margins are estimated from ensembles of responses at the same temperature. The Q-factor changes by a factor four in this temperature range. At the lowest temperatures, the Q-factor reproducibly reaches values above 10^5. These lowest temperature values are close to the intrinsic Q-values calculated with molecular dynamics simulations on single-walled carbon nanotube oscillators [13]. Interestingly, these calculations predict a $T^{-0.36}$ power law dependence of the Q-factor with temperature. The gray line in Fig. 6.5d shows this dependence; the data is consistent with this prediction. This $T^{-0.36}$ dependence has also been observed in top-down fabricated devices at low temperatures [6, 27]. Note that the Q-values of our nanotube resonator are much higher than the ones following the trend of the volume surface ratio in top-down fabricated devices [2].

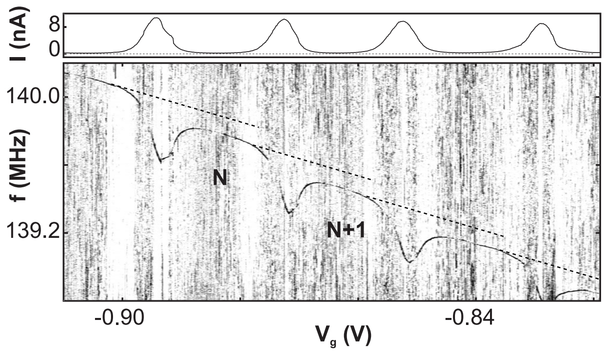

FIGURE 6.6: Nanotube current vs. gate voltage showing single electron tunnelling at the peaks and Coulomb blockade in the valleys (top). Normalized resonance signal (bottom) $|\Delta I/\Delta I(f_R)|$ vs. RF frequency and gate voltage at $V_{\mathrm{sd}} = 1.5\,\mathrm{mV}$. The tuned mechanical resonance shows up as the darker curve with dips at the Coulomb peaks. The offsets between dashed lines indicate the frequency shift due to the addition of a *single* electron to the nanotube. The resonance frequency also shows dips caused by a softening of the spring constant due to single electron charge fluctuations.

6.6 SINGLE-ELECTRON TUNING AND BACKACTION

The narrow linewidth of the resonance peak due to the high Q-factor provides an unprecedented sensitive probe for studying nanomechanical motion. We first show the influence of a single electron on the resonance frequency, f_R. The Coulomb oscillations in Fig. 6.6 are due to single electron tunnelling, giving rise to current peaks and valleys, where Coulomb blockade fixes the electron number N. From valley to valley, the electron number changes by one. The bottom panel of Fig. 6.6 shows the mechanical resonance signal recorded at the same time. Overall, a more negative gate voltage (right to left) increases the total charge on the nanotube, increasing the tension. This is the tuning that is shown in Fig. 6.2. The tension stiffens the mechanical spring constant and increases the resonance frequency. Linear stiffening occurs in the Coulomb valleys (indicated with dashed lines), whereas at Coulomb peaks, a peculiar softening occurs, visible as dips in f_R.

We first focus on the change in resonance frequency due to the addition of one electron, which is measured as offsets of about 0.1 MHz between the dashed lines. This shift due to *single electron tuning*, predicted in Ref. [28], is about 20 times our linewidth and thus resolvable for the first time in a nanomechanical system. Since we compare valleys with a fixed electron number, this single electron tuning comes from a change in a static force on the nanotube. The (electro-) static force is proportional to the square of the charge on the nanotube and thus adding one electron charge results, here, in a detectable shift in the mechanical resonance [28]. The shifts from single electron tuning can be as large as 0.5 MHz, more than 100 times the line width.

Next we focus on the dips in resonance frequency that occur at the Coulomb peaks.

The current at the Coulomb peaks is carried by single electron tunnelling, meaning that one electron tunnels off the nanotube before the next electron can enter the tube. The charge on the nanotube thus fluctuates by exactly one electron charge, e, with a time dynamics understood in detail by the theory of Coulomb blockade [29]. The average rate, Γ, at which an electron moves across the tube can be read off from the current $I = e\Gamma$ (i.e. 1.6 pA corresponds to a 10 MHz rate). Moving the gate voltage off or on a Coulomb peak, we can tune the rate from the regime $\Gamma \sim f_R$ to $\Gamma \gg f_R$ and explore the different effects on the mechanical resonance.

In Fig. 6.6 the Coulomb peak values of $\sim$ 8 nA yield $\Gamma \sim 300 f_R$, the regime of many single electron tunnelling events per mechanical oscillation. In addition to the static force and the oscillating RF driving force, single electron tunnelling now exerts a time-fluctuating, dynamic force on the mechanical resonator. We observe that this dynamic force causes softening, giving dips in the resonance frequency. The single electron charge fluctuations do not simply smooth the stepwise transition from the static single electron tuning shifts. Strikingly, we find that fluctuations instead cause dips in the resonant frequency up to an order of magnitude larger than the single electron tuning shifts. As shown in [30] and discussed in detail in [31], the dynamic force modifies the nanotube's spring constant, k_R, resulting in a softening of the mechanical resonance. The shape of the frequency dip can be altered by applying a finite bias, V_{sd}, across the nanotube as shown in Fig. 6.7. Starting from deep and narrow at small $V_{sd} = 0.5$ mV, the dip becomes shallower and broader on increasing V_{sd}. This dip-shape largely resembles the broadening of Coulomb blockade peaks when increasing V_{sd}. We thus conclude from Figs. 6.6 and 6.7 that the *single electron tuning oscillations* are a mechanical effect that is a direct consequence of single electron tunnelling oscillations.

Besides softening, the charge fluctuations also provide a channel for dissipation of mechanical energy. Fig. 6.8 shows the resonance dip for small RF power with line cuts in Fig. 6.8b. In the Coulomb valleys, tunnelling is suppressed ($\Gamma \sim f_0$), damping of the mechanical motion is minimized, and we observe the highest quality-factors. On a Coulomb peak, charge fluctuations are maximal ($\Gamma \gg f_0$), and the quality-factor decreases to a few thousand. These results explicitly show that detector backaction can cause significant mechanical damping. The underlying mechanism for the damping is an energy transfer occasionally occurring when a current-carrying electron is pushed up to a higher (electrochemical) energy by the nanotube motion before tunnelling out of the dot. This gain in potential energy of the electron is provided by the resonator and is later dissipated in the drain contact.

6.7 STRONG COUPLING

If we drive the system at higher RF powers (Fig. 6.8c and d) we observe an asymmetric resonance peak, along with distinct hysteresis between upward and downward frequency sweeps. Theoretically this marks the onset of non-linear terms in the equation of motion, such as in the well-studied Duffing oscillator [1, 32]. The spring constant, k_R, is modified,

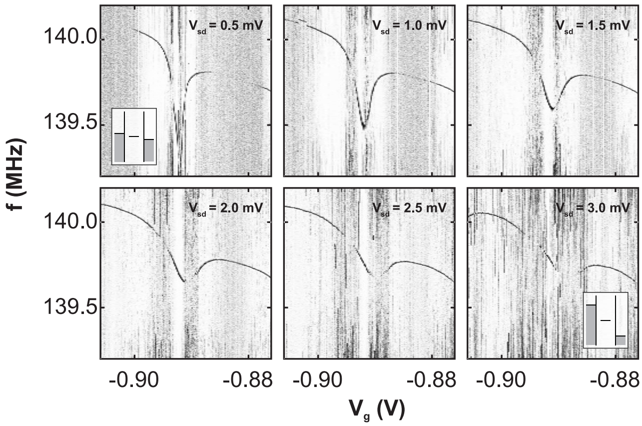

FIGURE 6.7: Zoom on one frequency dip for various source-drain voltages, V_{sd}, showing dip broadening for increasing V_{sd}. The two insets illustrate the energy diagrams for small and large V_{sd}.

due to a large oscillation amplitude, u, which is accounted for by replacing k_R with $(k_R + \alpha u^2)$. The constant increases if $\alpha > 0$, which is accompanied by a sharp edge at the high frequency side of the peak; vice versa for $\alpha < 0$. In addition to the overall softening of k_R yielding the frequency dips of Fig. 6.6, the fluctuating charge on the dot also changes α, giving a softening spring ($\alpha < 0$) outside of the frequency dip (Coulomb valleys), and a hardening spring ($\alpha > 0$) inside the frequency dip (Coulomb peaks), shown in Fig. 6.8. The sign of α follows the curvature of $f_R(V_g)$ induced by the fluctuating electron force, giving a change in sign at the inflection point of the frequency dip. Interestingly, non-linearity from the single electron force in our device dominates, and is much stronger than that from the mechanical deformation [31].

Figs. 6.8e and f show the regime of further enhanced RF driving. The non-linearity is now no longer a perturbation of the spring constant, but instead gives sharp peaks in the lineshape and switching between several different metastable modes (see further data in Ref. [31]). At this strong driving, we observe very rich nonlinear mechanical behavior due to the coupling of the resonator motion to the quantum dot.

The question whether the mechanical resonator can be excited by the fluctuating driving force from electron tunnelling alone, is addressed in Fig. 6.9 with a standard Coulomb blockade measurement shown in a. Mechanical effects in Coulomb diamonds of carbon nanotubes have been studied before via phonon sidebands of electronic transitions [33–35]. New in the data of Fig. 6.9 are reproducible ridges of positive and negative spikes in the differential conductance. This instability has been seen in all 12 measured devices with clean suspended nanotubes and never in non-suspended devices. Fig. 6.9b shows such ridges in a second device (device E), visible as discrete jumps in the current. The barriers in device E were highly tunable: we find that the switch-ridge can be suppressed by

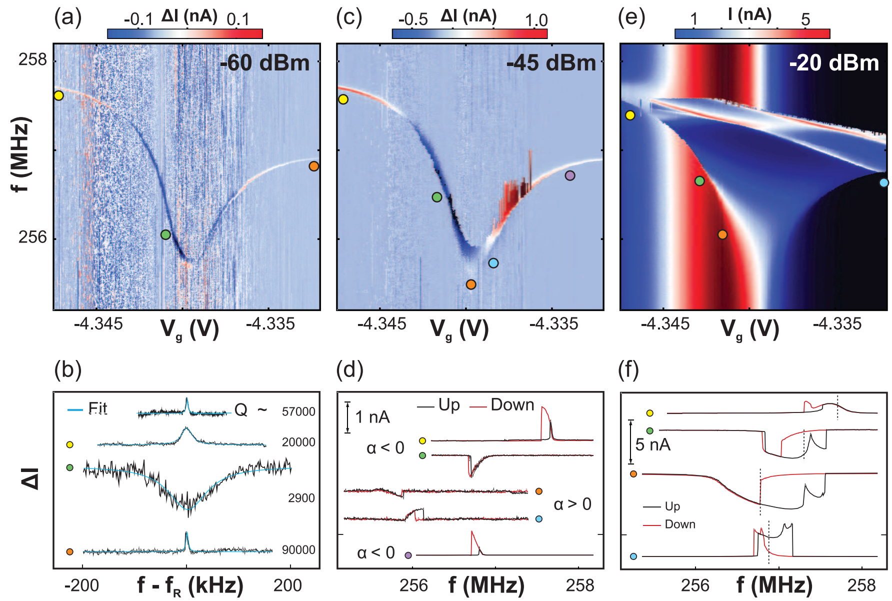

FIGURE 6.8: Lineshapes of the mechanical resonance from linear to non-linear driving regimes. (a) Detector current, ΔI, vs. frequency and gate-voltage at RF excitation power of -60 dBm as the gate voltage is swept through one Coulomb peak. (b) Fits of the resonance to a squared harmonic oscillator lineshape at different gate voltages. The RF power for each trace is adjusted to stay in the linear driving regime (-75, -64, -52, and -77 dBm top to bottom). Traces are taken at the positions indicated by colored circles (aside from the top trace which is taken at V_g = -4.350 V). (c) At -45 dBm, the resonance has an asymmetric lineshape with one sharp edge, see the linecuts in (d), typical for a non-linear oscillator [1, 32]. (e) and (f) At even higher driving powers (-20 dBm), the mechanical resonator displays sharp sub-peaks and several jumps in amplitude when switching between different stable modes. The dashed lines in (f) indicate the resonance frequency f_R at low powers. (c) and (e) are taken in the upwards sweep direction.

reducing the tunnel rate to the source-drain contacts, thereby decreasing the current. The instability disappears roughly when the tunnel rate is decreased below the mechanical resonance frequency [31].

In a model predicting such instabilities [36], positive feedback from single electron tunnelling excites the mechanical resonator into a large amplitude oscillation. The theory predicts a characteristic shape of the switch-ridges and the suppression of the ridges for $\Gamma \sim f_R$, in striking agreement with our observations. If the required positive feedback is present, however, it should also have a mechanical signature: such a signature is indeed observed in Fig. 6.9e. The RF-driven mechanical resonance experiences a dramatic perturbation triggered by the switch-ridge discontinuities in the Coulomb peak current shown in Fig. 6.9d. At the position of the switch, the resonance peak shows a sudden de-

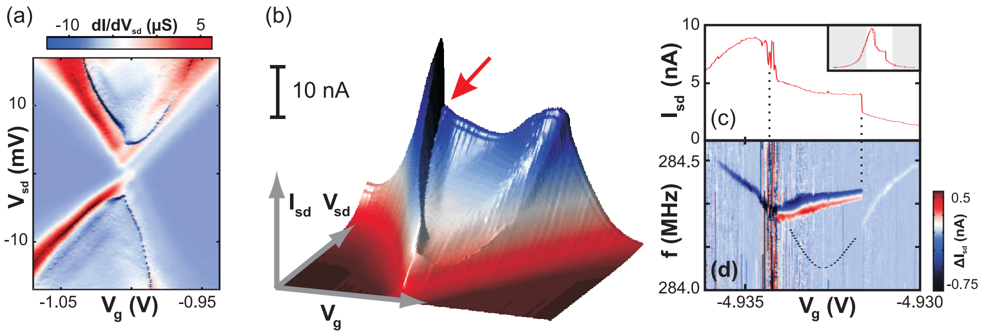

FIGURE 6.9: Spontaneous driving of the mechanical resonance by single-electron tunnelling. (a) Differential conductance, $\partial I/\partial V_{sd}$, showing ridges of sharp negative spikes (deep blue) measured on device E (trench width = 430 nm) in the few-hole regime (4-hole to 3-hole transition). (b) shows the data from the upper half of (a), but now as a 3D current plot. Note that the ridges, that appear as steps in the current, are entirely reproducible. (c) Ridges in device C. Inset: Coulomb peak at V_{sd} = 0.5 mV showing large switching-steps. Main plot: zoom-in on data from inset. (d) RF-driven mechanical resonance measured for the same Coulomb peak in (c) at a driving power of -50 dBm. Outside the "switch-region", the resonance has a narrow lineshape and follows the softening-dip from Figs. 6.6 and 6.7. At the first switch, the resonance position departs from the expected position (indicated by dashed line). The mechanical signal is strongly enhanced in amplitude and displays a broad asymmetric lineshape. At the second switch, the resonance returns to the frequency and narrow lineshape expected at these powers.

parture from the expected frequency dip (dashed line), and becomes strongly asymmetric and broad, as if driven by a much higher RF power. This is indeed the case, but the driving power is now provided by an internal source: due to strong feedback, the fluctuating force from single electron tunnelling becomes a driving force synchronized with the mechanical oscillation. Remarkably, the dc current through the quantum dot can be used both to detect the high-frequency resonance and, in the case of strong feedback, to directly excite resonant mechanical mechanical motion.

6.8 CONCLUSIONS

Using a novel detection mechanism, we have measured the bending mode resonance of suspended carbon nanotubes in the single-electron tunnelling regime. Sharp gate-tunable resonances are found with high Q-values ($Q > 10^5$), which can easily be driven into the nonlinear regime by increasing the driving power on the RF antenna. The motion of the nanotube is strongly coupled to the tunnelling of electrons. By inducing tension with a gate voltage the frequency can be tuned above 350 MHz, so that the thermal occupation of the resonator approaches 1. Shorter devices should have even higher resonance frequencies corresponding to temperatures above the mixing chamber temperature of the dilution refrigerator. These resonators are therefore in their quantum mechanical ground state, which opens up the way to new exciting experiments on the quantum aspects of mechanical motion. The motion of the nanotube is strongly coupled to the dynamics of electrons tunnelling on and off the nanotube. This gives rise to novel effects, such as single-electron tuning, gate-tunable nonlinearity and the recently predicted strong-feedback effects where tunnelling of electrons and mechanical motion synchronize.

ACKNOWLEDGEMENT

The authors thank Yaroslav Blanter, Giorgi Labadze and Yuli Nazarov for discussions and Raymond Schouten for experimental help. This research was carried out with financial support from the Dutch Foundation for Fundamental Research on Matter (FOM), The Netherlands Organisation for Scientific Research (NWO), NanoNed, and the Japan Science and Technology Agency International Cooperative Research Project (JST-ICORP).

SUPPLEMENT

MASS SENSITIVITY

The mass sensitivity is estimated from the data plotted in Fig. 6.4e. In the experiments, the mass sensitivity is limited by the current noise, which has a spectral density $S_I^{1/2} = 0.12\,\mathrm{pA}/\sqrt{\mathrm{Hz}}$ at the particular working point. The mass sensitivity $S_m^{1/2}$ can be calculated as follows: an added mass δm on the nanotube changes the resonance frequency by:

$$\delta f_R = \frac{\partial f_R}{\partial m}\delta m = \frac{f_R}{2m}\delta m, \tag{6.2}$$

where $m = 5.1 \times 10^{-21}$ kg is the mass of an 800 nm long single-walled nanotube with a 1.5 nm radius. When the resonance frequency shifts, the current through the nanotube is modified by:

$$\delta I = \frac{\partial I}{\partial f_R}\delta f_R \simeq -\frac{\partial I}{\partial f}\delta f_R. \tag{6.3}$$

The latter approximation, which is valid for a high Q resonator, allows us to relate the change in current to the measured slope of the response function. For the data in Fig. 6.4e the slope of the red line, just right of the jump is $\partial I/\partial f = 6.0 \times 10^{-16}\,\mathrm{A/Hz}$. The mass sensitivity is calculated using $S_m^{1/2} = \left|\frac{\partial f_R}{\partial m}\frac{\partial I}{\partial f}\right|^{-1} S_I^{1/2}$, which yields $S_m^{1/2} = 7.0\,\mathrm{yg}/\sqrt{\mathrm{Hz}} = 4.2\,\mathrm{u}/\sqrt{\mathrm{Hz}}$. Here, u is the (unified) atomic mass unit, so it is possible to detect a mass change as small as a single helium atom within one second.

DEVICE D

Figure 6.10 shows measurements on a second device. This device also has a suspended length of 800 nm. From room temperature measurements it is inferred that device D is a large ($E_g/k_\mathrm{B} > 300\,\mathrm{K}$) bandgap nanotube as well.

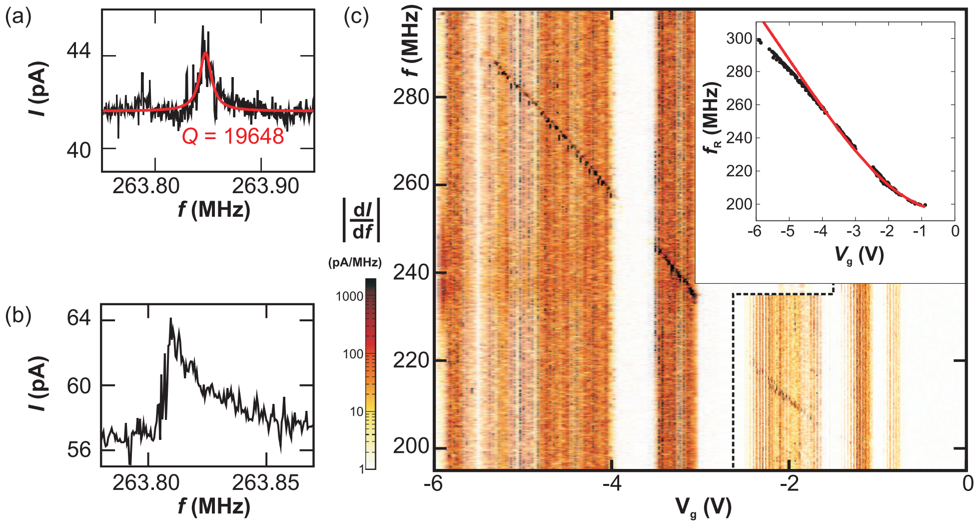

FIGURE 6.10: (a)-(b) Examples of measured resonances in device D in the linear (a) and non-linear regime (b) at 20 mK. Settings: $V_g = -4.241$ V, $V_{sd} = 2.0$ mV, RF power -47 dBm in (a) and $V_g = -4.241$ V, $V_{sd} = 1.5$ mV, RF power -44.5 dBm in (b). (c) $|dI/df|$ in color scale as a function of frequency f of the ac voltage on the antenna and the dc gate voltage V_g on the back-gate electrode for device D. Left of the dashed line a source-drain voltage of 4 mV was used; on the right side $V_{sd} = 10$ mV. The RF power was -13 dBm everywhere. Inset: Comparison of the extracted resonance frequency to the continuum model for the bending mode with $f_0 = 193.7$ MHz, $V_g^* = 4.14$ V, $T_0 = 0$ and a horizontal offset of 1.65 V to account for a shift in the charge neutrality point and the band gap region.

REFERENCES

[1] A. Cleland, *Foundations of Nanomechanics* (Springer, 2003).

[2] K. L. Ekinci and M. L. Roukes, *Nanoelectromechanical systems*, Rev. Sci. Instrum. **76**, 061101 (pages 12) (2005).

[3] A. Naik, O. Buu, M. D. LaHaye, A. D. Armour, A. A. Clerk, M. P. Blencowe, and K. C. Schwab, *Cooling a nanomechanical resonator with quantum back-action*, Nature **443**, 193 (2006).

[4] N. E. Flowers-Jacobs, D. R. Schmidt, and K. W. Lehnert, *Intrinsic Noise Properties of Atomic Point Contact Displacement Detectors*, Phys. Rev. Lett. **98**, 096804 (pages 4) (2007).

[5] X. L. Feng, C. J. White, A. Hajimiri, and M. L. Roukes, *A self-sustaining ultrahigh-frequency nanoelectromechanical oscillator*, Nat Nano **3**, 342 (2008).

[6] G. Zolfagharkhani, A. Gaidarzhy, S.-B. Shim, R. L. Badzey, and P. Mohanty, *Quantum friction in nanomechanical oscillators at millikelvin temperatures*, Phys. Rev. B **72**, 224101 (pages 5) (2005).

[7] B. Lassagne, D. Garcia-Sanchez, A. Aguasca, and A. Bachtold, *Ultrasensitive Mass Sensing with a Nanotube Electromechanical Resonator*, Nano Lett. **8**, 3735 (2008).

[8] H.-Y. Chiu, P. Hung, H. W. C. Postma, and M. Bockrath, *Atomic-Scale Mass Sensing Using Carbon Nanotube Resonators*, Nano Lett. **8**, 4342 (2008).

[9] K. Jensen, K. Kim, and A. Zettl, *An atomic-resolution nanomechanical mass sensor*, Nat Nano **3**, 533 (2008).

[10] K. C. Schwab and M. L. Roukes, *Putting Mechanics into Quantum Mechanics*, Phys. Today **58**, 36 (2005).

[11] V. Sazonova, Y. Yaish, H. Üstünel, D. Roundy, T. A. Arias, and P. L. McEuen, *A tunable carbon nanotube electromechanical oscillator*, Nature **431**, 284 (2004).

[12] B. Witkamp, M. Poot, H. Pathangi, A. K. Hüttel, and H. S. J. van der Zant, *Self-detecting gate-tunable nanotube paddle resonators*, Appl. Phys. Lett. **93**, 111909 (pages 3) (2008).

[13] H. Jiang, M.-F. Yu, B. Liu, and Y. Huang, *Intrinsic Energy Loss Mechanisms in a Cantilevered Carbon Nanotube Beam Oscillator*, Phys. Rev. Lett. **93**, 185501 (2004).

[14] K. Jensen, J. Weldon, H. Garcia, and A. Zettl, *Nanotube Radio*, Nano Lett. **7**, 3508 (2007).

[15] A. Eriksson, S. Lee, A. A. Sourab, A. Isacsson, R. Kaunisto, J. M. Kinaret, and E. E. B. Campbell, *Direct Transmission Detection of Tunable Mechanical Resonance in an Individual Carbon Nanofiber Relay*, Nano Lett. **8**, 1224 (2008).

[16] G. A. Steele, G. Gotz, and L. P. Kouwenhoven, *Tunable few-electron double quantum dots and Klein tunnelling in ultraclean carbon nanotubes*, Nat Nano **4**, 363 (2009).

[17] J. Cao, Q. Wang, and H. Dai, *Electron transport in very clean, as-grown suspended carbon nanotubes*, Nat Mater **4**, 745 (2005).

[18] Y. Oreg, K. Byczuk, and B. I. Halperin, *Spin Configurations of a Carbon Nanotube in a Nonuniform External Potential*, Phys. Rev. Lett. **85**, 365 (2000).

[19] W. Liang, M. Bockrath, and H. Park, *Shell Filling and Exchange Coupling in Metallic Single-Walled Carbon Nanotubes*, Phys. Rev. Lett. **88**, 126801 (2002).

[20] E. D. Minot, Y. Yaish, V. Sazonova, and P. L. McEuen, *Determination of electron orbital magnetic moments in carbon nanotubes*, Nature **428**, 536 (2004).

[21] I. Kozinsky, H. W. C. Postma, I. Bargatin, and M. L. Roukes, *Tuning nonlinearity, dynamic range, and frequency of nanomechanical resonators*, Appl. Phys. Lett. **88**, 253101 (pages 3) (2006).

[22] L. P. Kouwenhoven, C. M. Marcus, P. L. McEuen, S. Tarucha, R. M. Westervelt, and N. S. Wingreen, *Electron transport in quantum dots*, NATO ASI conference proceedings (Kluwer, 1997), edited by L. L. Sohn and L. P. Kouwenhoven and G. Schön.

[23] M. D. LaHaye, O. Buu, B. Camarota, and K. C. Schwab, *Approaching the Quantum Limit of a Nanomechanical Resonator*, Science **304**, 74 (2004).

[24] R. Lifshitz and M. C. Cross, *Reviews of Nonlinear Dynamics and Complexity: Volume 1 (Annual Reviews of Nonlinear Dynamics and Complexity)* (Wiley-VCH, 2008), chap. 1, ISBN 3527407294.

[25] M. C. Cross, A. Zumdieck, R. Lifshitz, and J. L. Rogers, *Synchronization by Nonlinear Frequency Pulling*, Phys. Rev. Lett. **93**, 224101 (pages 4) (2004).

[26] H. W. C. Postma, I. Kozinsky, A. Husain, and M. L. Roukes, *Dynamic range of nanotube- and nanowire-based electromechanical systems*, Appl. Phys. Lett. **86**, 223105 (pages 3) (2005).

[27] S. B. Shim, J. S. Chun, S. W. Kang, S. W. Cho, S. W. Cho, Y. D. Park, P. Mohanty, N. Kim, and J. Kim, *Micromechanical resonators fabricated from lattice-matched and etch-selective GaAs/InGaP/GaAs heterostructures*, Appl. Phys. Lett. **91**, 133505 (pages 3) (2007).

[28] S. Sapmaz, Y. M. Blanter, L. Gurevich, and H. S. J. van der Zant, *Carbon nanotubes as nanoelectromechanical systems*, Phys. Rev. B **67**, 235414 (2003).

[29] C. W. J. Beenakker, *Theory of Coulomb-blockade oscillations in the conductance of a quantum dot*, Phys. Rev. B **44**, 1646 (1991).

[30] M. T. Woodside and P. L. McEuen, *Scanned Probe Imaging of Single-Electron Charge States in Nanotube Quantum Dots*, Science **296**, 1098 (2002).

[31] G. A. Steele, A. K. Huttel, B. Witkamp, M. Poot, H. B. Meerwaldt, L. P. Kouwenhoven, and H. S. J. van der Zant, *Strong Coupling Between Single-Electron Tunneling and Nanomechanical Motion*, Science **325**, 1103 (2009), supplementary information accompanying the article.

[32] A. H. Nayfeh and D. T. Mook, *Nonlinear Oscillations* (Wiley, 1979).

[33] B. J. LeRoy, S. G. Lemay, J. Kong, and C. Dekker, *Electrical generation and absorption of phonons in carbon nanotubes*, Nature **432**, 371 (2004).

[34] S. Sapmaz, P. Jarillo-Herrero, Y. M. Blanter, C. Dekker, and H. S. J. van der Zant, *Tunneling in Suspended Carbon Nanotubes Assisted by Longitudinal Phonons*, Phys. Rev. Lett. **96**, 026801 (pages 4) (2006).

[35] R. Leturcq, C. Stampfer, K. Inderbitzin, L. Durrer, C. Hierold, E. Mariani, M. G. Schultz, F. von Oppen, and K. Ensslin, *Franck-Condon blockade in suspended carbon nanotube quantum dots*, Nat Phys **5**, 327 (2009).

[36] O. Usmani, Y. M. Blanter, and Y. V. Nazarov, *Strong feedback and current noise in nanoelectromechanical systems*, Phys. Rev. B **75**, 195312 (2007).

7

Motion detection of a micromechanical resonator embedded in a dc SQUID

S. Etaki, M. Poot, I. Mahboob*, K. Onomitsu*, H. Yamaguchi*, H. S. J. van der Zant

Superconducting Quantum Interference Devices (SQUIDs) are the most sensitive detectors of magnetic flux [1] and are also used as quantum two-level systems (qubits) [2]. Recent proposals have explored a novel class of devices which incorporate micromechanical resonators into SQUIDs in order to achieve controlled entanglement of the resonator ground state and a qubit [3] as well as permitting cooling and squeezing of the resonator modes and enabling quantum limited position detection [4–10]. In spite of these intriguing possibilities, no experimental realization of an on-chip, coupled mechanical resonator-SQUID system has yet been achieved. Here, we demonstrate sensitive detection of the position of a 2 MHz flexural resonator which is embedded into the loop of a dc SQUID. We measure the resonator's thermal motion at millikelvin temperatures, achieving an amplifier-limited displacement sensitivity of 10 fm/$\sqrt{\mathrm{Hz}}$ and a position resolution that is 36 times the quantum limit.

Parts of this Chapter have been published in Nat. Phys., **4**, 785–788 (2008)
* NTT Basic Research Laboratories, NTT Corporation, Japan

Dc SQUIDs consist of a superconducting loop with two Josephson junctions [1]. The voltage across the dc SQUID does not only depend on the current through it, but also on the magnetic flux piercing through the loop, allowing tiny changes in the magnetic field to be detected. Besides this more common application, the dc SQUID should also be able to detect small variations in the *area* of its loop due to the motion of an integrated flexural resonator in the presence of a static magnetic field. Our Nb-based dc SQUID displacement detector is based on this principle and is shown in Fig. 7.1a and b and is described in more detail in "Methods". Its potential displacement sensitivity can be estimated as follows: The resonator has a length of $\ell = 50\ \mu$m and the loop is placed in a magnetic field of $B = 0.1$ T oriented as described in Fig. 7.1d. A deflection $u = 1$ fm of the resonator will then result in a change in flux through the loop on the order of $B\ell u = 2.5\ \mu\Phi_0$, where $\Phi_0 = h/2e = 2.07\,\mathrm{fTm}^2$ is the flux quantum. Low-temperature dc SQUIDs have a typical flux sensitivity of $10^{-6}\,\Phi_0/\sqrt{\mathrm{Hz}}$ [11], which is sufficient to reach a displacement sensitivity of $0.4\ \mathrm{fm}/\sqrt{\mathrm{Hz}}$. This places the dc SQUID detector in the same league as other highly sensitive on-chip position detectors [12–15].

7.1 DC SQUID CHARACTERIZATION

Before using the dc SQUID as a displacement detector, its characteristics are determined in order to find a proper bias point. Fig. 7.1d shows a schematic of the measurement setup, which is described in detail in Methods. A bias current I_B is applied to the dc SQUID and its output voltage V is measured. The dc SQUID produces a non-zero output voltage once I_B exceeds the dc SQUID's critical current I_C, which depends on the magnetic flux bias Φ through the dc SQUID loop and on the critical current of the individual junctions, I_0. Figure 7.2a shows that at $B = 0\,$T the dc SQUID's V-I_B relationship exhibits hysteresis, indicating that the dc SQUID is underdamped [1]. This hysteresis must be suppressed in order to operate the dc SQUID as a sensitive linear flux detector. This is achieved by increasing B, which decreases the critical current of the junctions [16]. We find that for $B \geq 0.1\,$T the dc SQUID is sufficiently damped such that no hysteresis is observed (Fig. 7.2a). Note that in our detection scheme the dc SQUID is biased above the critical current. It can in principle also be used as a position detector when it is biased below the critical current, where the dc SQUID acts as a tunable inductor [4].

The dc SQUID is most sensitive to changes in the magnetic flux when it is tuned to a working point with a steep slope of $V(\Phi)$. Figure 7.2b shows the relation between V and the applied stripline current I_F which changes Φ. For a dc SQUID, both I_C and V depend periodically on Φ with a period of Φ_0. The steepest slope occurs approximately half-way between the minimum and maximum of the voltage swing. The difference between these two voltages is the peak-to-peak voltage swing V_{PP}. Figure 7.2c shows V_{PP} as a function of I_B, where $V_{PP}^{\max}$ is the maximum voltage swing. Numerical simulations (see Appendix A) show that this maximum occurs at $I_B = 2I_0$.

In our experiment there is a slow flux drift, which makes it difficult to maintain a constant flux bias by just applying a constant stripline current. Therefore a feedback loop is

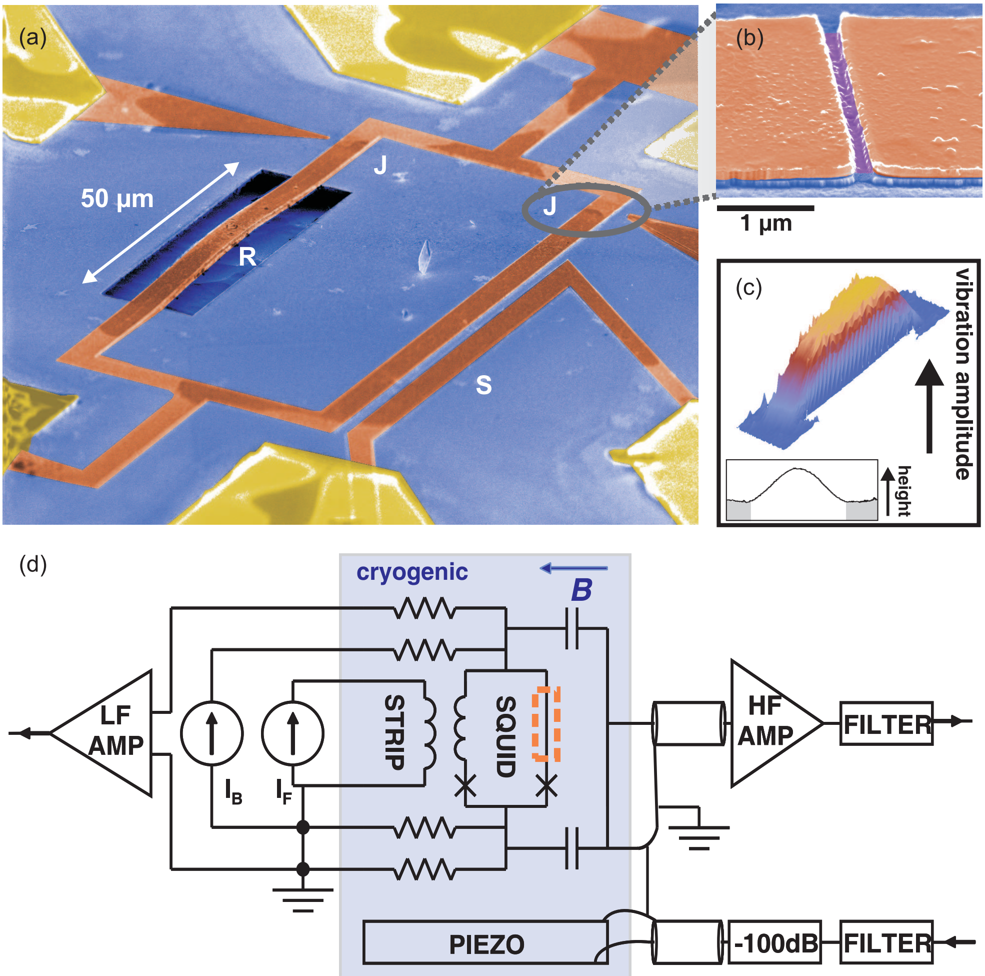

FIGURE 7.1: (a) Colorized scanning electron micrograph of a device at 80° inclination. The beam resonator ('R') is buckled away from the substrate due to compressive strain (see Methods). The stripline ('S') is used to change the flux bias through the dc SQUID. The Nb-InAs weak links ('J') are located adjacent to unused Nb side gates. (b) Colorized scanning electron micrograph of one of the 200 nm long Nb-InAs-Nb junctions. (c) A 3-dimensional image of the vibration amplitude of the driven beam resonance at 2 MHz, acquired at room temperature using dynamic force microscopy. The inset shows the static buckling profile of the beam with a maximum deflection of 1.5 μm measured using atomic force microscopy. (d) Schematic overview of the measurement circuit. A coupling field B is applied parallel to the dc SQUID-plane and perpendicular to the length direction of the resonator (marked by the red box). The sample is glued onto a piezo actuator, which is connected to a filtered voltage source for the driven measurements.

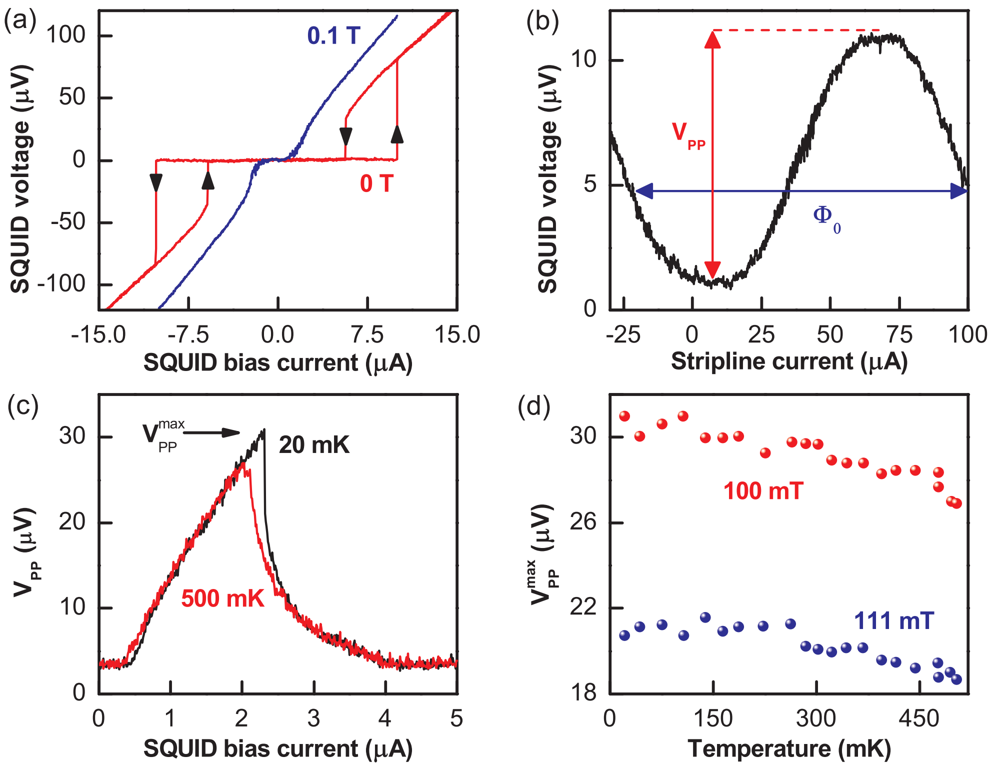

FIGURE 7.2: (a) dc SQUID voltage as a function of the bias current I_B at 20 mK. At zero magnetic field the dc SQUID exhibits hysteretic behavior (red curves). The blue curve shows the voltage-current response at 100 mT, which is the lowest of two fields used for position detection. The increased magnetic field has suppressed the hysteresis due to a reduction of the critical current. (b) Average dc SQUID voltage as a function of the applied stripline current at 100 mT and $I_B = 2.5\ \mu$A. The peak-to-peak voltage swing is V_{PP}. (c) Measurements of V_{PP} as a function of I_B at $B = 100$ mT. The parameters I_0 and V_{PP}^{max} obtained from this measurement are used to tune the dc SQUID to a sensitive bias point. (d) V_{PP}^{max} as a function of refrigerator temperature at two different magnetic fields.

used that maintains a constant average setpoint voltage $\langle V \rangle = V_{SP}$ by adjusting I_F for a given value of I_B. An added advantage of using the feedback loop is that it compensates external low-frequency (< 1 kHz) flux noise.

Numerical analysis (see Appendix A) reveals that the ratios I_B/I_0 and V_{SP}/V_{PP}^{max}, needed to achieve the maximum value of the flux responsivity $\partial V/\partial\Phi$, are approximately constant. This allows us to apply a bias that gives maximum $\partial V/\partial\Phi$ even if I_0 and V_{PP}^{max} are changing due to temperature variations as shown in Fig. 7.2d. In practice, values for V_{SP} and I_B must be chosen that allow stable operation of the feedback loop in addition to maximizing $\partial V/\partial\Phi$. The values $I_B = 2I_0$ and $V_{SP} = V_{PP}^{max}/2$ are found to provide a good balance between these requirements.

7.2 DETECTION OF THE DRIVEN MOTION

As the resonator is integrated into the dc SQUID, the flux through the loop depends on the position u of the fundamental out-of-plane mode of the beam according to $\Phi = \Phi_a + aB\ell u$, where Φ_a is the applied flux when the resonator is in its equilibrium position and a is the geometrical factor that depends on the mode shape[1], as defined by Eq. 3.46. The displacement u is defined such that the effective spring constant of the mode is $k_R = m(2\pi f_R)^2$, where m is the *total* mass of the beam and f_R is the resonance frequency of the mode as shown in Sec. 3.5. Atomic force microscopy shows that the resonator is buckled upwards with a shape belonging to $n = 1$ with a maximal displacement $u_{\max} = 1.5\,\mu$m and we use the continuum model from Sections 3.3 and 3.5 to estimate $a = 0.91$. Furthermore, we find that that the beam was under a compressive residual strain $\epsilon_0 = T_0/EA = -2.5 \cdot 10^{-3}$.

In our configuration, the dc SQUID functions in the small signal limit $aB\ell u \ll \Phi_0$ as a linear displacement detector with a displacement responsivity $\partial V/\partial u = \partial V/\partial\Phi \cdot \partial\Phi/\partial u$. The resonance frequency f_R is located by driving the resonator with a piezo actuator (Fig. 7.1d) and monitoring the resulting output voltage of the dc SQUID. The resonance is located at $f_R = 2.0018\,$MHz and shows a harmonic oscillator amplitude response (Fig. 7.3a). Room-temperature dynamic force microscopy [17] confirms that this is indeed the fundamental mode (Fig. 7.1c) and the resonance frequency is also in good agreement with our continuum model. From a least-squares harmonic oscillator response fit we extract a quality factor $Q = 1.8 \cdot 10^4$ at $B = 100\,$mT and refrigerator temperature $T = 20\,$mK. For all measurements, the peak voltage amplitude is much smaller than $V_{PP}^{\max}$ (Fig. 7.2d), which means that the flux oscillations due to the resonator are indeed within the small signal limit.

7.3 THERMAL NOISE AND SENSITIVITY

Thermomechanical noise thermometry is used to calibrate the deflection responsivity [13–15]. Without actively driving the resonator, the noise power spectral density of the output voltage is acquired around the mechanical resonance frequency. The spectra in Fig. 7.3b show a constant background upon which a harmonic oscillator response peak is superimposed. This peak is caused by the Brownian motion of the beam. The quality factor and resonance frequency are identical to those of the driven response (Fig. 7.3a). The voltage noise power due to the resonator $\langle V_R^2 \rangle$, i.e. the area underneath the peak, is extracted from the fitted response function.

The noise spectrum is measured in the temperature range $20\,\text{mK} \le T \le 500\,\text{mK}$. To compare the noise power at different temperatures, $\langle V_R^2 \rangle$ must be corrected for differences in $\partial V/\partial\Phi$. The flux responsivity is proportional to $V_{PP}^{\max}$ and thus has the same temperature dependence (Fig. 7.2d). This enables the introduction of the corrected voltage noise

[1] In this Chapter we use the short-hand notation u and a for the symbols $u_{\text{ac}}^{(0)}$ and a_0 respectively

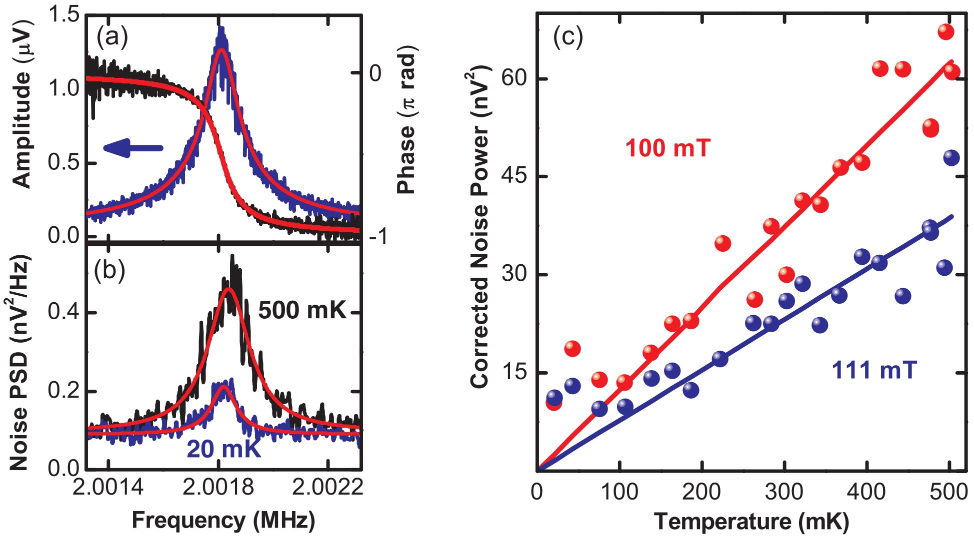

FIGURE 7.3: (a) The driven resonator response at $T = 20\,\mathrm{mK}$ and $B = 100\,\mathrm{mT}$. The amplitude and phase are shown in blue and black, respectively. The amplitude and phase data are well fitted by a harmonic oscillator response (red). The peak amplitude corresponds to approximately 40 pm deflection. (b) Noise power spectral density around the beam's resonance frequency at 100 mT for two different temperatures (black, blue). The peak in the noise spectra is due to the Brownian motion of the resonator. (c) The corrected voltage noise power $\langle V_R'^2\rangle$ extracted from the thermal spectra at 100 mT (red) and 111 mT (blue). The solid lines indicate a linear least mean squares fit to the noise powers for temperatures above 100 mK. The linear relationship is predicted by the equipartition theorem and its slope is used to calibrate the deflection responsivity of the flux-based transducer. The steeper line for the 100 mT data indicates a higher responsivity than at 111 mT. The lowest achieved resonator temperature is 84 mK at a refrigerator temperature of 20 mK. This difference implies that the resonator does not thermalize at the lowest temperatures (see Methods).

power $\langle V_R'^2\rangle = \langle V_R^2\rangle \cdot [V_{PP}^{\max}(20\,\mathrm{mK})/V_{PP}^{\max}(T)]^2$. The corrected noise powers in Fig. 7.3c show a linear decrease with temperature down to 100 mK. The slope $S(B)$ from a linear fit to this data, combined with the equipartition theorem (Eq. 2.10) gives the deflection responsivity $\partial V/\partial u = V_{PP}^{\max}(T)/V_{PP}^{\max}(20\,\mathrm{mK}) \cdot [S(B)k_R/k_\mathrm{B}]^{1/2}$, where k_B is the Boltzmann constant and using $m = 6.1 \cdot 10^{-13}\,\mathrm{kg}$ we find $k_R = 97\,\mathrm{N/m}$. The resulting displacement responsivities at 20 mK are $3.0 \cdot 10^{-2}\,\mathrm{nV/fm}$ and $2.3 \cdot 10^{-2}\,\mathrm{nV/fm}$ for $B = 100$ mT and 111 mT respectively. The fact that the displacement responsivity at 111 mT is lower than at 100 mT might appear counterintuitive, but the larger flux change for the same displacement is compensated by a stronger reduction of $V_{PP}^{\max}$, as shown Fig. 7.2d. The best displacement sensitivity coincides with the highest responsivity because the flux-based position detector is limited by the noise floor of the room temperature voltage amplifier $\bar{S}_{VV}^{1/2}$. The best observed sensitivity is $\overline{S}_{u_n u_n}^{1/2} = (\partial V/\partial u)^{-1}\overline{S}_{VV}^{1/2} = 10\,\mathrm{fm}/\sqrt{\mathrm{Hz}}$ and occurs at 20 mK and 100 mT.

7.4 TOWARDS THE QUANTUM LIMIT

It is interesting to calculate the position resolution of the detector and compare it to the fundamental limit imposed by quantum mechanics [18]. The position resolution due to the detector noise floor (cf. Eq. 2.37) is $\Delta u_n = \left(\overline{S}_{u_n u_n}\Delta f\right)^{1/2}$, where $\Delta f = \pi f_R/2Q$ is the effective noise bandwidth of the resonator. This yields $\Delta u_n = 133\,\mathrm{fm}$ for the highest observed sensitivity of the detector. The quantum limit for the position resolution of a continuous linear detector is $\Delta u_{QL} = \sqrt{\hbar/m(2\pi f_R)} = 4$ fm for our resonator [19], so that the detector resolution is a factor $\Delta u_n/\Delta u_{QL} = 36$ from the quantum limit. The resonator enters the quantum regime once it has a thermal occupation factor $\bar{n} < 1$, as explained in Sec. 2.2. The resonator temperature is found from the voltage noise power using $T_R = \langle V_R^2\rangle k_R/k_\mathrm{B}\langle\partial V/\partial u\rangle^2$. From the data in Fig. 7.3c, the lowest observed resonator temperature is $T_R = 84\,\mathrm{mK}$, which yields $\bar{n} = 878$.

There are two major challenges for observing quantum behavior in a macroscopic mechanical resonator [20]: a quantum limited position detector [18, 19, 21] with resolution $\Delta u = \Delta u_{QL}$ and a resonator with $\bar{n} < 1$ (See Ch. 2). These requirements can be *simultaneously* met by our device configuration: The quantum mechanical ground state for a 1 GHz resonator is reached at temperatures below 70 mK, which can be achieved in a dilution refrigerator. The dc SQUID is known to be a near quantum-limited flux detector and flux sensitivities of $\overline{S}_{\Phi\Phi}^{1/2} = 0.01\ \mu\Phi_0/\sqrt{\mathrm{Hz}}$ should be possible [22]. For the current device $\overline{S}_{\Phi\Phi}^{1/2} \sim 10\mu\Phi_0/\sqrt{\mathrm{Hz}}$ is limited by the room temperature amplifier. Thus, by reducing the amplifier noise floor, for example by using a second dc SQUID as an amplifier, and by increasing the flux responsivity of the first dc SQUID, the sensitivity may ultimately be improved by three orders of magnitude. Under these conditions, an 1 GHz resonator made of a 300 nm long InAs beam with $Q = 1000$ will require a magnetic field of 1 T for the detector to reach quantum limited sensitivity. Note that InAs is very suitable for such a resonator, as beams that are only tens of nanometers wide can still carry a substantial supercurrent [23]. Dc SQUID operation in the required high magnetic field may be possible by utilizing narrow and thin Nb lines [24]. With these improvements, our flux-based measurement method can potentially be extended to detect the resonator's ground state.

METHODS

DEVICE DETAILS

The Nb of the dc SQUID loop and the stripline is evaporated (thickness 100 nm) onto a thin heterostructure that has been grown epitaxially on a GaAs(111)A substrate [25] as illustrated in Fig. 7.4. First an insulating layer of $Al_{0.5}Ga_{0.5}Sb$ is grown on the substrate using molecular beam epitaxy, followed by a layer of InAs. The GaAs substrate is used to grow a high-crystalline-quality InAs/$Al_{0.5}Ga_{0.5}Sb$

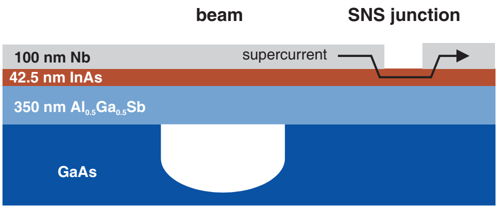

FIGURE 7.4: Schematic overview of the different layers of the beam (left) and the Josephson junctions (right). A part of the GaAs substrate is etched to suspend the beam. An SNS-type Josephson junction is made by omitting a part of the superconductor (Nb), forcing the supercurrent through the InAs surface layer.

film despite the large lattice mismatch of 7% between the substrate and InAs [26]. Finally, a layer of evaporated niobium serves as the superconductor for the dc SQUID. At two positions in the loop, the Nb is interrupted and the supercurrent has to flow through the InAs surface layer, thereby forming two SNS-type Josephson junctions [27] (see Figs. 7.1b and 7.4). The InAs surface layer has a mobility of $8 \cdot 10^3$ cm^2/Vs and an electron density of $1.3 \cdot 10^{12}$ cm^{-2} at 77 K. The inner area of the dc SQUID loop is $40\,\mu$m × $80\,\mu$m and the line width is 4 μm. The stripline is placed 1.5 μm from the dc SQUID and runs 70 μm parallel to the dc SQUID loop. A dry-etch is used to remove the conducting InAs layer everywhere except underneath the metallized parts and at the junctions. Electrical contact to the Nb is made by evaporating 20 nm Ti and 200 nm Au.

The flexural resonator is made by removing the GaAs substrate underneath part of the loop with a wet-etch. The resulting beam is buckled away from the substrate due to compressive strain (Fig. 7.1c). To analyze the flexural modes of the multi-layer beam it is convenient to replace it by an effective beam which has the same mechanical properties and which has a rectangular cross-section $A = wh$. These requirements give four equations from which the values for the thickness h, width w, mass density ρ and Young's modulus E of the effective beam are calculated. Table 7.1 shows the dimensions and mechanical properties of the different layers in the heterostructure and that of the effective single-layer beam. The bending rigidity of the beam is $D = 3.20 \cdot 10^{-15}\,\mathrm{N\,m}^2$. The calculated eigenfrequency of 1.93 MHz of the fundamental mode for the measured static buckling of $u_{max} = 1.5\,\mu$m (See the analysis in Sec. 3.3 and the result in Fig. 3.3) matches the frequency of 2.0018 MHz observed in the experiments well, considering the uncertainty in the tabulated values for the mechanical properties of $Al_{0.5}Ga_{0.5}Sb$.

DC SQUID PARAMETERS

This paragraph gives the dc SQUID parameters at $B = 111$ mT that are needed for the simulations described in appendix A. The relevant parameters are the critical current I_0, the normal state resistance R and capacitance C of a single Josephson junction and the inductance L of the dc SQUID.

In the simulations, identical parameters for the two junctions in the dc SQUID are used. We find good agreement between the measurements and the simulations, which indicates that this assumption is reasonable as asymmetries in the parameters would have caused deviations in the measured $V(I_B, \Phi)$ characteristics [32].

TABLE 7.1: Dimensions and physical properties of the different layers of the SQUID loop (at room temperature, compiled from Refs. [28–31]). The values for $Al_{0.5}Ga_{0.5}Sb$ are estimates based on the properties of GaSb and the similarity between AlAs and GaAs. The properties of the effective beam are obtained by requiring that its mechanical properties beam are identical to those of the original beam.

material	h (nm)	w (μm)	ρ (kg/m^3)	E (GPa)
Nb	100	4.0	$8.57 \cdot 10^3$	104.9
InAs	42.5	4.5	$5.68 \cdot 10^3$	51.4
$Al_{0.5}Ga_{0.5}Sb$	350	4.5	$5.0 \cdot 10^3$	~ 60
effective	512	4.2	$5.72 \cdot 10^3$	67.5

The critical currents of $I_0 = 1.2$ μA and 0.7 μA at 100 mT and 111 mT respectively are obtained from the location of V_{PP}^{max} as indicated in Fig. 7.2c. In Appendix A it is shown that $V_{PP}^{max} \approx I_0 R$, which allows the determination of the normal state resistance R of the individual Josephson junctions from the data in Fig. 7.2c and d. At 111 mT a temperature-independent value $R(111\text{ mT}) = 30\ \Omega$ is obtained.

The capacitance of the Josephson junctions is calculated from the hysteresis of the V-I_B curves at zero magnetic field (Fig. 7.2a) by using the Stewart-McCumber parameter β_C. This number indicates whether the dc SQUID is over- or underdamped, i.e. whether it is hysteretic or not. The restively and capacitively shunted junction (RCSJ) model relates the ratio i_r of the return current and critical current to the Stewart-McCumber parameter $\beta_C = (2-(\pi-2)i_r)/i_r^2$ [1]. For a critical current of 10.1 μA and a return current of 5.7 μA this gives $\beta_C = 4.3$ at $B = 0$ T. The Stewart-McCumber parameter is related to the physical parameters of the dc SQUID according to $\beta_C = 2\pi I_C R_{SQ}^2 C_{SQ}/\Phi_0$, where C_{SQ} and R_{SQ} are the capacitance and the resistance of the two junctions in parallel, respectively. The slope of the V-I_B curve (Fig. 7.2a) at high currents yields $R_{SQ}(0\text{ T}) = 8.7\ \Omega$. With the values for β_C and I_C that are mentioned above, $C_{SQ} = 1.8$ pF and thus $C = C_{SQ}/2 = 0.9$ pF is found. It is assumed that this value is valid at all temperatures and magnetic fields in the experiments. Note that this value is higher than expected from the geometry of the junction, which is most likely caused by the presence of an additional conductive layer in the heterostructure.

The inductance of the dc SQUID is estimated by finite element simulations of the electrodynamics of the superconducting loop using FastHenry [33], giving a value of $L = 175$ pH.

MEASUREMENT SETUP

The device is mounted in a dilution refrigerator and the coarse magnetic field B is applied using a superconducting solenoid magnet. The low frequency (LF) circuit is used to set the dc SQUID to a working point by applying a bias current I_B through the dc SQUID and a current I_F through the stripline. The battery-powered current sources and LF voltage amplifier are optically isolated from mains operated equipment. The high frequency (HF) dc SQUID output voltage at the resonator frequency is measured using a two-stage room temperature amplifier with 80 dB gain, 10 kΩ input impedance and equivalent input voltage noise $\overline{S}_{VV}^{1/2} = 0.3\text{ nV}/\sqrt{\text{Hz}}$. The HF and LF circuits are separated by 1 kΩ resistors and 10 nF capacitors at the cryogenic stage (Fig. 7.1d).

NOISE POWER SATURATION

At temperatures below 100 mK the noise power of the resonator is no longer proportional to the refrigerator temperature and saturates, as shown in Fig 7.3c. This implies that below 100 mK, the temperature of the resonator T_R is higher than the refrigerator temperature T. Similar behavior has been observed in other studies where it was attributed to local heating of the substrate [13, 15] or excessive force noise coming from the position detector [14, 34]. A way to experimentally discriminate between these two effects is to change the coupling between the resonator and the detector, but in our case the coupling field cannot be varied sufficiently to distinguish between the two sources. Instead we shows that the backaction noise is not sufficiently large to cause the rise in resonator temperature. The backaction of the dc SQUID on the resonator is analyzed in detail in Ch. 8 and the backaction temperature is calculated in Appendix A. For typical parameters (see Appendix A) we find that at the setpoint $I_B = 2.0 \cdot I_0$ and $\Phi = 0.25 \cdot \Phi_0$ the backaction of the dc SQUID raises the resonator temperature by ~ 0.6 mK. This temperature increase is much smaller than the difference between the lowest observed resonator temperature, $T_R = 84$ mK, and the base temperature of the dilution refrigerator, $T = 20$ mK, which means that the difference between T_R and T is not caused by backaction.

A more likely possibility is that the substrate temperature is higher than that of the refrigerator. Note that resistive heating of the junctions is not the main cause of this effect; Compared to the measurements at 100 mT, the current through the junctions was 1.7 times less at 111 mT, because of the lower critical current. The data in Fig. 7.3c does not show a lower saturation temperature in the latter case, even though the dissipation in the junction has decreased by a factor 3. The most likely cause of the increased substrate temperature is local heating due to heat transfer through the wires. This effect can be reduced by improving the thermal anchoring of the wires to the refrigerator.

ACKNOWLEDGEMENT

We thank Y. Blanter for discussions, T. Akazaki, H. Okamoto and K. Yamazaki for help with fabrication, R. Schouten for the measurement electronics and A. Bachtold and D. Sanchez-Garcia for advice on the DFM measurement. This work was supported in part by JSPS KAKENHI (20246064 and 18201018), FOM, a Dutch NWO VICI grant and NanoNed.

REFERENCES

[1] J. Clarke and A. Braginski, *The SQUID Handbook volume 1* (Wiley-VCH Verlag, GmbH and Co. KGaA, Weinheim, 2004).

[2] Y. Makhlin, G. Schön, and A. Shnirman, *Quantum-state engineering with Josephson-junction devices*, Rev. Mod. Phys. **73**, 357 (2001).

[3] F. Xue, Y. D. Wang, C. P. Sun, H. Okamoto, H. Yamaguchi, and K. Semba, *Controllable coupling between flux qubit and nanomechanical resonator by magnetic field*, New J. Phys. **9**, 35 (2007).

[4] M. P. Blencowe and E. Buks, *Quantum analysis of a linear dc SQUID mechanical displacement detector*, Phys. Rev. B **76**, 014511 (pages 16) (2007).

[5] X. Zhou and A. Mizel, *Nonlinear Coupling of Nanomechanical Resonators to Josephson Quantum Circuits*, Phys. Rev. Lett. **97**, 267201 (pages 4) (2006).

[6] E. Buks, E. Segev, S. Zaitsev, B. Abdo, and M. P. Blencowe, *Quantum nondemolition measurement of discrete Fock states of a nanomechanical resonator*, EPL **81**, 10001 (2008).

[7] E. Buks and M. P. Blencowe, *Decoherence and recoherence in a vibrating rf SQUID*, Phys. Rev. B **74**, 174504 (pages 8) (2006).

[8] Y.-D. Wang, K. Semba, and H. Yamaguchi, *Cooling of a micro-mechanical resonator by the back-action of Lorentz force*, New J. Phys. **10**, 043015 (15pp) (2008).

[9] W. Y. Huo and G. L. Long, *Generation of squeezed states of nanomechanical resonator using three-wave mixing*, Appl. Phys. Lett. **92**, 133102 (pages 3) (2008).

[10] F. Xue, Y. xi Liu, C. P. Sun, and F. Nori, *Two-mode squeezed states and entangled states of two mechanical resonators*, Phys. Rev. B **76**, 064305 (pages 9) (2007).

[11] M. Mück, J. B. Kycia, and J. Clarke, *Superconducting quantum interference device as a near-quantum-limited amplifier at 0.5 GHz.*, Appl. Phys. Lett. **78**, 967 (2001).

[12] R. G. Knobel and A. N. Cleland, *Nanometre-scale displacement sensing using a single electron transistor*, Nature **424**, 291 (2003).

[13] M. D. LaHaye, O. Buu, B. Camarota, and K. C. Schwab, *Approaching the Quantum Limit of a Nanomechanical Resonator*, Science **304**, 74 (2004).

[14] N. E. Flowers-Jacobs, D. R. Schmidt, and K. W. Lehnert, *Intrinsic Noise Properties of Atomic Point Contact Displacement Detectors*, Phys. Rev. Lett. **98**, 096804 (pages 4) (2007).

[15] C. A. Regal, J. D. Teufel, and K. W. Lehnert, *Measuring nanomechanical motion with a microwave cavity interferometer*, Nat Phys **4**, 555 (2008).

[16] J. C. Cuevas and F. S. Bergeret, *Magnetic Interference Patterns and Vortices in Diffusive SNS Junctions*, Phys. Rev. Lett. **99**, 217002 (pages 4) (2007).

[17] D. Garcia-Sanchez, A. S. Paulo, M. J. Esplandiu, F. Perez-Murano, L. Forró, A. Aguasca, and A. Bachtold, *Mechanical Detection of Carbon Nanotube Resonator Vibrations*, Phys. Rev. Lett. **99**, 085501 (pages 4) (2007).

[18] C. M. Caves, K. S. Thorne, R. W. P. Drever, V. D. Sandberg, and M. Zimmermann, *On the measurement of a weak classical force coupled to a quantum-mechanical oscillator. I. Issues of principle*, Rev. Mod. Phys. **52**, 341 (1980).

[19] C. M. Caves, *Quantum limits on noise in linear amplifiers*, Phys. Rev. D **26**, 1817 (1982).

[20] K. C. Schwab and M. L. Roukes, *Putting Mechanics into Quantum Mechanics*, Phys. Today **58**, 36 (2005).

[21] A. A. Clerk, *Quantum-limited position detection and amplification: A linear response perspective*, Phys. Rev. B **70**, 245306 (2004).

[22] R. H. Koch, D. J. V. Harlingen, and J. Clarke, *Quantum noise theory for the dc SQUID*, Appl. Phys. Lett. **38**, 380 (1981).

[23] Y.-J. Doh, J. A. van Dam, A. L. Roest, E. P. A. M. Bakkers, L. P. Kouwenhoven, and S. De Franceschi, *Tunable Supercurrent Through Semiconductor Nanowires*, Science **309**, 272 (2005).

[24] G. Stan, S. B. Field, and J. M. Martinis, *Critical Field for Complete Vortex Expulsion from Narrow Superconducting Strips*, Phys. Rev. Lett. **92**, 097003 (2004).

[25] H. Yamaguchi, S. Miyashita, and Y. Hirayama, *Microelectromechanical displacement sensing using InAs/AlGaSb heterostructures*, Appl. Phys. Lett. **82**, 394 (2003).

[26] H. Yamaguchi, J. G. Belk, X. M. Zhang, J. L. Sudijono, M. R. Fahy, T. S. Jones, D. W. Pashley, and B. A. Joyce, *Atomic-scale imaging of strain relaxation via misfit dislocations in highly mismatched semiconductor heteroepitaxy: InAs/GaAs(111)A*, Phys. Rev. B **55**, 1337 (1997).

[27] H. Takayanagi and T. Kawakami, *Superconducting Proximity Effect in the Native Inversion Layer on InAs*, Phys. Rev. Lett. **54**, 2449 (1985).

[28] W. F. Gale and T. C. Totemeier, *Smithells metals reference book* (Elsevier Butterworth-Heinemann, 2004).

[29] D. R. Lide, ed., *Handbook of Chemistry and Physics* (GRC press, 1974).

[30] M. Levinshtein, S. Rumyantsev, and M. Shur, *Handbook Series on Semiconductor Parameters Vol.1 and 2* (World Scientific, 1996).

[31] S. Adachi, *Properties of Group-IV, III-IV and II-VI Semiconductors* (John Wiley and Sons, 2005).

[32] C. D. Tesche and J. Clarke, *dc SQUID: Noise and optimization*, J. Low Temp. Phys. **29**, 301 (1977).

[33] Software available from
`http://www.ece.rochester.edu/~sde/research/software/fasthenry/index.html`.

[34] A. Naik, O. Buu, M. D. LaHaye, A. D. Armour, A. A. Clerk, M. P. Blencowe, and K. C. Schwab, *Cooling a nanomechanical resonator with quantum back-action*, Nature **443**, 193 (2006).

8

TUNABLE BACKACTION OF A DC SQUID ON AN INTEGRATED MICROMECHANICAL RESONATOR

M. Poot, S. Etaki, I. Mahboob*, K. Onomitsu*, H. Yamaguchi*, Ya. M. Blanter, H. S. J. van der Zant

We have measured the backaction of a dc superconducting quantum interference device (SQUID) position detector on an integrated 2 MHz flexural resonator. The frequency and quality factor of the micromechanical resonator can be tuned independently with bias current and applied magnetic flux. The backaction is caused by the Lorentz force due to the change in circulating current when the resonator displaces, and the measurements are in qualitative agreement with numerical simulations. Backaction can enable cooling, squeezing of the mechanical resonator and synchronization of multiple embedded resonators.

Parts of this Chapter have been submitted to Phys. Rev. Lett.
* NTT Basic Research Laboratories, NTT Corporation, Japan

Recent experiments with mechanical resonators are rapidly approaching the quantum limit on position detection, as shown in Ch. 2. This limit implies that the position of the resonator cannot be measured with arbitrary accuracy, as the detector itself affects the resonator position [1]. This is an example of backaction, i.e. the influence of a measurement device on an object. Moreover, backaction does not just impose limits, it can also be used to one's advantage: Backaction can be used to cool the resonator, to squeeze its motion, and to couple and synchronize multiple resonators. In experiments with micro- or nanomechanical resonators, different backaction mechanisms have been identified: In optical interferometers [2–5] and in electronic resonant circuits [6, 7] the backaction is due to photon pressure. When using single electron transistors [8] or atomic point contacts [9] as position detectors, it results from the tunneling of electrons. These examples stress the need for a good understanding of backaction to achieve quantum limited position detection.

We have shown in Ch. 7 that a dc SQUID can be used as a sensitive detector of the position of an integrated mechanical resonator. This embedded resonator-SQUID geometry enables the experimental realization of a growing number of theoretical proposals [10–16]. In this Chapter, we present measurements that show that the dc SQUID detector exerts backaction on the resonator with a different origin than in the experiments mentioned above. By varying the bias conditions of the dc SQUID, the damping and frequency of the resonator can be tuned independently. The backaction is due to the Lorentz force generated by the circulating current in the dc SQUID. We find qualitative agreement between the observed effects and calculations with the resistively and capacitively shunted junction (RCSJ) model for the dc SQUID [17].

8.1 DEVICE DESCRIPTION AND FABRICATION

Our device (Fig. 8.1a) consists of a dc SQUID in which a part of one arm is underetched, forming a flexural resonator with length $\ell = 50\,\mu$m [18]. Before studying the backaction of the dc SQUID position detector on the resonator, first the dc SQUID is characterized by measuring its current-voltage characteristics. The measured VI-curves in Fig. 8.1b are fitted using the widely-used RCSJ model [17]. The details and results of this procedure are discussed in the Supplement: At a magnetic field of $B = 115\,$mT, the critical current of a single junction is $I_0 = 1.22\,\mu$A. After increasing the magnetic field to 130 mT to reduce the critical current, the fit gives $I_0 = 0.51\,\mu$A. This reduction of the critical current decreases the backaction strength as we will show in the next Sections.

Our flux-based position detector works as follows: The output voltage of the dc SQUID does not only depend on the bias current, but also on the amount of magnetic flux through the loop. An in-plane magnetic field B transduces a displacement of the beam u into a flux change $\sim \ell B u$, which in turn leads to a change in the SQUID voltage. This way, the flux dependence of the SQUID voltage is used to detect the position of the resonator. During all position-detection measurements, the dc SQUID is operated at a given setpoint voltage V_{SP} by a feedback loop (see Fig. 8.1a) that adjusts the flux via the stripline current [17–

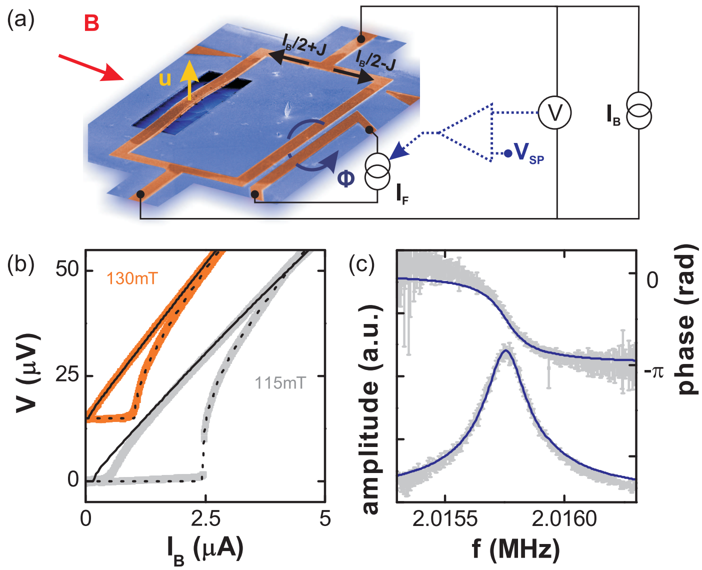

FIGURE 8.1: (a) Schematic overview of the dc SQUID and measurement setup. The scanning electron micrograph shows the dc SQUID with the suspended resonator. The magnetic field B transduces a displacement of the beam u into a change in flux. A bias current I_B is sent through the SQUID and its output voltage is measured. The flux Φ is fine-tuned with a stripline current I_F that is controlled by a feedback circuit (dashed) that keeps the output voltage V at V_{SP}. (b) The bias-current dependence of the measured V_{min} and V_{max} at two different magnetic fields (see Supplement). The lines show the calculated VI-curves at integer (dashed) and half-integer (solid) number of flux quanta. The plots for $B = 130\,\text{mT}$ are vertically offset for clarity. (c) The amplitude (bottom) and phase (top) response of the resonator (mean value and standard deviation of five frequency sweeps), with a fitted harmonic oscillator response (lines). The fit gives the resonance frequency $f_R = 2015755.0\,\text{Hz}$ and quality factor $Q = 12.5 \times 10^3$.

19]. The feedback loop is used to reduce low-frequency flux noise and flux drift and has a bandwidth of $\sim 2\,\text{kHz}$. The fundamental mode of the beam is excited with a piezo element underneath the sample and the output voltage is recorded. Figure 8.1c shows that both the amplitude and phase response are reproduced well by a harmonic oscillator response.

8.2 BACKACTION MEASUREMENTS

To observe backaction of the dc SQUID detector on the resonator, the frequency response is measured for different bias conditions of the dc SQUID. Figure 8.2 shows that the resonance frequency f_R and quality factor Q depend on the bias current. (For clarity, the difference between the resonator frequency and a fixed reference frequency $f_{\text{ref}} = 2015800$ Hz is plotted). When decreasing the bias current, the resonance frequency shifts by almost 300

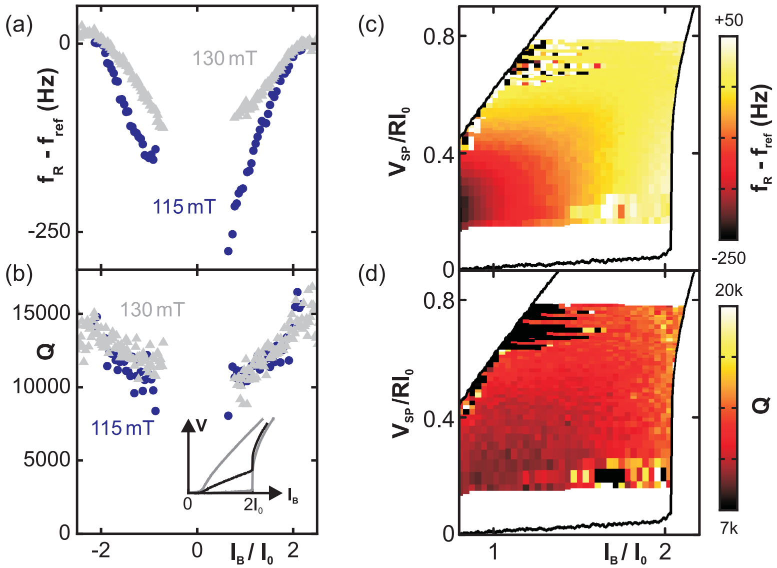

FIGURE 8.2: (a) Frequency shift and (b) quality factor plotted versus the normalized bias current at $B = 115\,\mathrm{mT}$ (circles) and $B = 130\,\mathrm{m}T$ (triangles). The inset depicts the voltage setpoint for these measurements w.r.t. V_{min} and V_{max}. Bias current and setpoint dependence of the frequency shift (c) and damping (d) at $B = 115$ mT. The solid lines indicate the measured V_{min} and V_{max}.

Hz for $B = 115\,\mathrm{mT}$, which is about twice the linewidth $\gamma_R = f_R/Q$ of the resonance shown in Fig. 8.1c. After increasing the magnetic field to $B = 130\,\mathrm{mT}$ the frequency shift shows a similar bias-current dependence, but its magnitude is reduced. Figure 8.2b shows that the quality factor changes more than a factor two. The changes are nearly identical at the two different magnetic fields[1]. At low bias currents ($|I_B| \lesssim 0.5 \cdot I_0$), the response is no longer resolved because the voltage-to-flux transduction becomes too small. Figures 8.2c and d show that the frequency and damping can also be changed by adjusting V_{SP}. The shifts are largest for low setpoints and low bias currents (dark regions). Measurements at setpoints below 0.1 RI_0 are challenging as stable operation of the feedback loop is difficult.

Figures 8.3a and b show the temperature dependence of the frequency shift and damping. Apart from some scatter in the data, the frequency shift is independent of temperature, whereas the quality factor decreases with increasing temperature. An increased damping at higher temperatures is seen more often when using micro- or nanomechanical resonators (See Ch. 6 and Refs. [20–22]). This rules out that the observed frequency shift and Q-factor change are caused by heating of the resonator due to Joule heating in

[1] The small asymmetry between the data at positive and negative bias current in Fig. 8.2a and b is caused by differences in the regions where the feedback loop locks and drift in the amplifier offset.

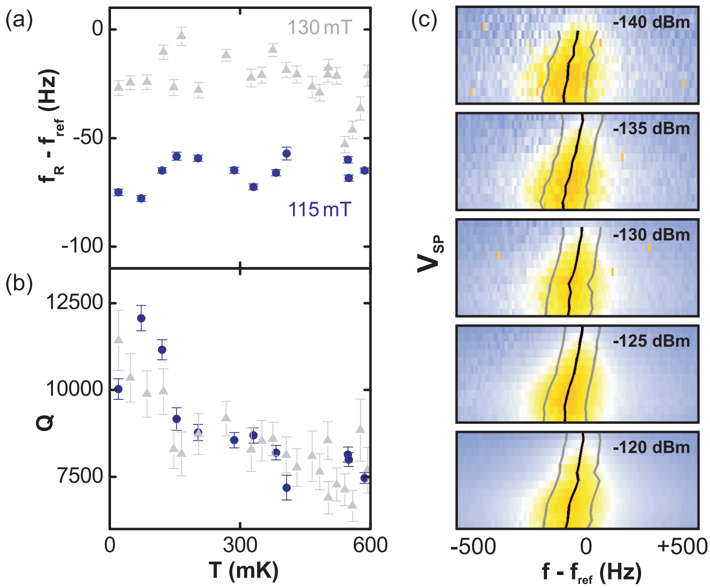

FIGURE 8.3: Temperature dependence of the frequency shift (a) and quality factor (b) at $I_B = 1.5\ I_0$ for $B = 115\,\mathrm{mT}$ (blue circles, $V_{SP} = 0.3\ RI_0$) and $B = 130\,\mathrm{mT}$ (gray triangles, $V_{SP} = 0.65\ RI_0$). (c) Colorscale plot of the oscillator response at $I_B = 2.0\mu\mathrm{A}$ and $B = 115\,\mathrm{mT}$ for $V_{SP} = 0.05$ to $0.66\ RI_0$ at different driving powers. The resonance frequency (black) and the full-with-at-half-maximum $\gamma_R = f_R/Q$ of the peak (gray) obtained from fits are indicated. At the highest power ($-120\,\mathrm{dBm}$), the motion amplitude of the piezo element is of the order of 1 fm.

the junctions: We observe an *increase* in quality factor with increasing bias current and voltage setpoint (i.e. dissipated power), but a *decrease* in quality factor with increasing temperature.

The driving-power dependence of the frequency shift and damping is shown in Fig. 8.3c. The signal-to-noise ratio becomes better when increasing the driving power, but the shifts remain the same even although the power is varied over two orders of magnitude. This indicates that the changes in frequency and damping are not caused by non-linearities in the resonator.

Finally, after reversing the direction of the magnetic field or when operating the dc SQUID at a setpoint with a different sign of $\partial V/\partial\Phi$, the sign of the change in f_R and Q remains the same.

8.3 MODELLING THE BACKACTION

The backaction of a generic linear detector was discussed in detail in Sec. 2.4. In our dc SQUID position detector, the backward coupling between the dc SQUID and beam is the Lorentz force F_L due to the current through the resonator [11, 14]. As shown in Sec. 2.4 the backaction force has a random and a deterministic component. The former is important when determining the backaction temperature as shown in Appendix A. In this Chapter we focus on the deterministic term that responds linearly to the displacement. The reason for such a response is as follows: A displacement of the beam u changes the flux, which in turn changes the circulating current in the loop J. In the presence of the magnetic field, this results in a change in the force on the beam. In addition, a time-varying flux through the loop induces an electro-motive force which also generates currents that change the Lorentz force [23]. The backaction-force transfer function λ_F (see Fig. 2.10) of the dc SQUID position detector thus contains a constant term and a term that is proportional to $\partial/\partial t$.

The displacement of the fundamental out-of-plane flexural mode of the beam u is given by the equation of motion of a damped harmonic oscillator [24]:

$$m\ddot{u} + m\omega_0\dot{u}/Q_0 + m\omega_0^2 u = F_d(t) + F_L(t). \tag{8.1}$$

The resonator has a mass m, (intrinsic) frequency $f_0 = \omega_0/2\pi$ and quality factor Q_0. F_d is the driving force and $F_L = aB\ell(I_B/2 + J)$ is the Lorentz force. Here, a is the geometrical factor, defined by Eq. 3.46, that relates the average of the spatial profile of the mode $u(x)$ to the coordinate u: $a = (u\ell)^{-1}\int_0^\ell u(x)\,\mathrm{d}x \approx 0.91$, so that also $\partial\Phi/\partial u = aB\ell$ [18, 24]. For small amplitudes and low resonator frequencies (much smaller than the characteristic SQUID frequency $\omega_c = 2\pi RI_0/\Phi_0 \sim 10^2\,\mathrm{GHz}$), the average circulating current can be expanded in the displacement and velocity $\dot{u}$:

$$J(u,\dot{u}) = J_0 + \frac{\partial J}{\partial u}u + \frac{\partial J}{\partial \dot{u}}\dot{u} = J_0 + aB\ell(J_\Phi u + J_{\dot{\Phi}}\dot{u}). \tag{8.2}$$

The transfer functions [17] $J_\Phi = \partial J/\partial\Phi$ and $J_{\dot{\Phi}} = \partial J/\partial\dot{\Phi}$ are intrinsic properties of the dc SQUID (i.e., they do not depend on the properties of the resonator). The first function indicates how much the circulating current changes when the flux through the ring is altered, whereas the second quantifies the effect of a time-dependent flux on the circulating current. The transfer functions are calculated numerically, as analytical results are only available in certain limits [25]. Our method is based on the commonly-used RCSJ model as discussed in more detail in Appendix A.

Inserting Eq. 8.2 into Eq. 8.1 shows that the $\partial J/\partial u$ term affects the spring constant $m\omega_R^2$ of the resonator, whereas the $\partial J/\partial\dot{u}$ term renormalizes the damping. The shifted resonance frequency and quality factor become:

$$f_R = f_0\left(1-\Delta_f J_\phi\right)^{1/2}, \text{ with } \Delta_f = \frac{a^2B^2\ell^2}{m\omega_0^2}\frac{I_0}{\Phi_0}, \tag{8.3}$$

$$Q = Q_0\frac{f_R}{f_0}\frac{1}{1-\Delta_Q J_{\dot\phi}}, \text{ with } \Delta_Q = \frac{a^2B^2\ell^2}{m\omega_0 R}\frac{Q_0}{2\pi}. \tag{8.4}$$

Here $J_\phi = J_\Phi\Phi_0/I_0$ and $J_{\dot\phi} = \omega_c J_{\dot\Phi}\Phi_0/I_0$ are the scaled transfer functions. The dimensionless parameters Δ_f [13] and Δ_Q characterize the strength of the backaction. Both parameters scale as A^2, where A is the coupling strength between the detector and the resonator that was used in Ch. 2. At 115 mT their values are: $\Delta_f = 1.7\times10^{-4}$ and $\Delta_Q = 3.2\times10^{-4}$, while at 130 mT they are: $\Delta_f = 0.9\times10^{-4}$ and $\Delta_Q = 3.5\times10^{-4}$ for $Q_0 = 14000$, which is its high-bias-current value. By reducing the critical current, Δ_f is reduced by a factor 2, whereas Δ_Q hardly changes. This in agreement with the reduced frequency shift but equal change in damping that were shown in Fig. 8.2a and b. By a careful design of resonators and dc SQUIDs, the backaction strengths can be tuned over a large range. Eqs. 8.3 and 8.4 show that the largest backaction occurs for large flux changes $aB\ell$, low spring constants $m\omega_0^2$ and large circulating currents, i.e. large I_0 and low R.

The dependence of the numerically-calculated circulating current transfer functions on the bias conditions is shown in Fig. 8.4. The transfer functions do not depend on the direction of the bias current, nor on the sign of the slope of $V(\Phi)$, in agreement with the experimental results. In the region where $V=0$, the circulating current distributes the bias current over the two junctions in such a way that no voltage develops. Here, the circulating current is of the order of I_0, which gives $J_\phi \sim -1$ (blue). In the dissipative region ($V\neq 0$), the circulating current is suppressed, leading to a small J_ϕ (light yellow and light blue) that scales to a good approximation as β_L for the experimental conditions. At the onset of the dissipative region, J increases rapidly ($J_\phi \gg 1$).

We now switch to the velocity transfer function which affects the damping. For high bias currents, $J_{\dot\phi} \approx -\pi$ (light blue). This is the current induced by a time-varying flux: $\dot\Phi/2R$ [25]. When approaching the edge from the dissipative region, $J_{\dot\phi}$ goes through zero and rises to more than 1000. This reduces the damping and might even lead to instability ($Q<0$) when Δ_Q is large enough. Further towards to the edge, $J_{\dot\phi}$ jumps to large *negative* values, leading to an enhanced dissipation. This is a manifestation of Lenz' law which states that nature tries to undo changes in flux, in this case by reducing the velocity of the beam. Well inside the non-dissipative region $J_{\dot\phi}\approx -\pi$ is found again. Note, that although Δ_Q is small, the SQUID response $J_{\dot\phi}$ can be so large that their product is of the order 1.

With these transfer functions, the frequency shift and damping are calculated. Figure 8.5a shows the results for the experimental conditions at 115 mT. A comparison of this with Fig. 8.3 shows a good qualitative agreement with the experiments: The largest changes in f_R and Q are found in the region of low bias current and low voltage setpoint, whereas the backaction becomes smaller at higher setpoints. The order of magnitude of the calculated

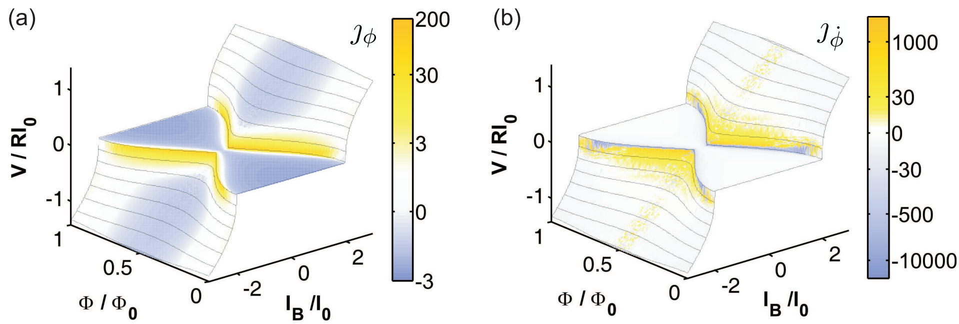

FIGURE 8.4: Bias dependence of the calculated circulating-current transfer functions for $B = 115\,\mathrm{mT}$. The (logarithmic) color-scale of the surface plots represents the transfer functions J_ϕ (a) and $J_{\dot\phi}$ (b); the height of the surface is the dc SQUID voltage.

frequency shift is similar to that of the observed frequency shift for $V_{SP}/RI_0 > 0.1$. The exact values of the calculated shift in frequency are, however, larger than observed experimentally. In contrast, the calculated Q changes less than observed, but for low setpoints (lower than measured), large changes are visible, which are of the same order as observed experimentally. The difference between the calculated and measured values may be due the flux noise which is present in the experiments, but which is not included in the calculations. A full quantitative analysis of the backaction in the presence of flux noise is, however, beyond the scope of this Chapter.

8.4 OUTLOOK

Backaction opens the way to the observation of various interesting effects when the couplings Δ_Q and Δ_f are large. In the current experiments, these couplings are relatively small. Couplings of the order of unity can be obtained with realistic device parameters: For example, $B = 1\,\mathrm{T}$, $R = 1\,\Omega$, $I_0 = 10\,\mu\mathrm{A}$ and a four times smaller width of the resonator result in $\Delta_Q = 3$ and $\Delta_f = 0.5$. When the resonator and dc SQUID are so strongly coupled, the resonator temperature is determined by the effective bath temperature [8, 9] of the dc SQUID, which might lead to cooling of the resonator. Furthermore, the dependence of the resonator frequency and quality factor on the bias conditions, allows parametric excitation of the mechanical resonator by either modulating the flux or the bias current. This enables squeezing of the thermomechanical noise of the resonator [13, 26]. Finally, if the dc SQUID contains multiple, nearly identical mechanical resonators, these are coupled to each other by the backaction. This, in turn, can synchronize their motion and might lead to frequency entrainment if higher order terms in Eq. 8.2 become significant [27]. These examples are only a few intriguing possibilities of the rich physics connected to the backaction that we have described in this Chapter.

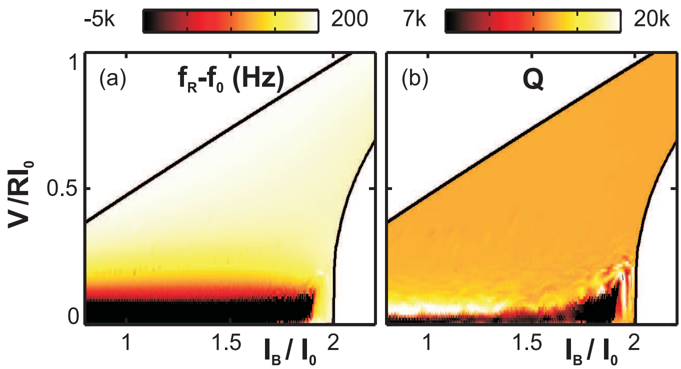

FIGURE 8.5: Color plots of the calculated frequency shift (a) and quality factor (b) with the experimental parameters $\Delta_f = 1.7\times10^{-4}$, $\Delta_Q = 3.2\times10^{-4}$, $f_0 = 2.0158\,\text{MHz}$ and $Q_0 = 14000$ (orange). The largest frequency shift occurs in the black region and is $f_R - f_0 = 34\,\text{kHz}$. The quality factor varies between 1500 and 24000.

SUPPLEMENT

DC SQUID CHARACTERIZATION

To characterize the dc SQUID, we measure the minimum and maximum voltage (V_{min} and V_{max}) by sweeping the magnetic flux Φ over a few flux quanta, $\Phi_0 = h/2e$, using the stripline. The feedback loop is switched off during these experiments. The minimum and maximum voltages are determined for different bias currents, yielding the current-voltage curves at an integer and half-integer number of flux-quanta[2]. VI-curves that are calculated with the restively and capacitively shunted junction (RCSJ) model [17], are fitted to the V_{min} and V_{max} data. This procedure[3] yields values for the critical current I_0 and the normal state resistance R of the individual junctions. Moreover, this gives the inductive screening parameter $\beta_L = 2I_0L/\Phi_0$ and the Stewart-McCumber number $\beta_C = 2\pi I_0 R^2 C/\Phi_0$ [17]. The former indicates how much a change in flux is screened by the circulating current J flowing through the self-inductance of the loop L, whereas the latter indicates the importance of the junction capacitance C. The results from the fits are summarized in Table 8.1. For more details about the parameters, the RCSJ model and the fitting procedure, we refer to Appendix A.

By combining the values of the fit parameters, the self-inductance of the dc SQUID and the junction capacitance are obtained, as shown in Table 8.1. The self-inductance of the dc SQUID loop is in agreement with the value $L = 175\,\text{pH}$, that is calculated with finite element simulations of the electrodynamics of the superconducting loop using FastHenry [29]. Also the junction capacitance can be estimated via an independent method, using the hysteretic VI-curves of the dc SQUID at

[2] The current-voltage curve at a (half) integer flux cannot be measured directly due to the presence of intrinsic flux noise and drift.

[3] In the simulations, identical parameters for the two junctions in the dc SQUID are assumed. We find good agreement between the measurements and the simulations, which indicates that this assumption is reasonable as asymmetries in the parameters would have caused deviations in the $V(I_B,\Phi)$ characteristics [28].

zero magnetic field (similar to the one in Fig. 7.2a). The RCSJ model relates the ratio i_r of the return current I_r and the critical current I_c of a dc SQUID to the Stewart-McCumber parameter: $\beta_c = (2-(\pi-2)i_r)/i_r^2$ [17]. Using this method, a value $C = 0.34\,\mathrm{pF}$ is obtained, which is in agreement with the values obtained from the fits.

ACKNOWLEDGEMENT

We thank T. Akazaki, H. Okamoto and K. Yamazaki for help with fabrication and R. Schouten for the measurement electronics. This work was supported in part by JSPS KAKENHI (20246064 and 18201018), FOM, NWO (VICI grant), and NanoNed.

TABLE 8.1: Parameters of the dc SQUID at two different magnetic fields. The critical current I_0 and normal-state resistance R of a single junction, the Stewart-McCumber number β_C, and the screening parameter β_L are used to fit the calculated VI-curves to the measured V_{min} and V_{max} characteristics. The other quantities are derived from these four fit parameters.

	$B = 115\,\mathrm{mT}$	$B = 130\,\mathrm{mT}$
R (Ω)	25.32	29.84
I_0 (μA)	1.22	0.51
RI_0 (μV)	30.94	15.13
$\omega_c/2\pi$ (GHz)	15.1	7.4
T_c (K)	0.36	0.18
β_C	0.76	0.31
β_L	0.16	0.10
C (pF)	0.32	0.23
L (nH)	0.14	0.20

REFERENCES

[1] C. M. Caves, K. S. Thorne, R. W. P. Drever, V. D. Sandberg, and M. Zimmermann, *On the measurement of a weak classical force coupled to a quantum-mechanical oscillator. I. Issues of principle*, Rev. Mod. Phys. **52**, 341 (1980).

[2] S. Gigan, H. R. Bohm, M. Paternostro, F. Blaser, G. Langer, J. B. Hertzberg, K. C. Schwab, D. Bauerle, M. Aspelmeyer, and A. Zeilinger, *Self-cooling of a micromirror by radiation pressure*, Nature **444**, 67 (2006).

[3] O. Arcizet, P.-F. Cohadon, T. Briant, M. Pinard, and A. Heidmann, *Radiation-pressure cooling and optomechanical instability of a micromirror*, Nature **444**, 71 (2006).

[4] A. Schliesser, P. Del'Haye, N. Nooshi, K. J. Vahala, and T. J. Kippenberg, *Radiation Pressure Cooling of a Micromechanical Oscillator Using Dynamical Backaction*, Phys. Rev. Lett. **97**, 243905 (pages 4) (2006).

[5] J. D. Thompson, B. M. Zwickl, A. M. Jayich, F. Marquardt, S. M. Girvin, and J. G. E. Harris, *Strong dispersive coupling of a high-finesse cavity to a micromechanical membrane*, Nature **452**, 72 (2008).

[6] J. D. Teufel, J. W. Harlow, C. A. Regal, and K. W. Lehnert, *Dynamical Backaction of Microwave Fields on a Nanomechanical Oscillator*, Phys. Rev. Lett. **101**, 197203 (pages 4) (2008).

[7] K. R. Brown, J. Britton, R. J. Epstein, J. Chiaverini, D. Leibfried, and D. J. Wineland, *Passive Cooling of a Micromechanical Oscillator with a Resonant Electric Circuit*, Phys. Rev. Lett. **99**, 137205 (pages 4) (2007).

[8] A. Naik, O. Buu, M. D. LaHaye, A. D. Armour, A. A. Clerk, M. P. Blencowe, and K. C. Schwab, *Cooling a nanomechanical resonator with quantum back-action*, Nature **443**, 193 (2006).

[9] N. E. Flowers-Jacobs, D. R. Schmidt, and K. W. Lehnert, *Intrinsic Noise Properties of Atomic Point Contact Displacement Detectors*, Phys. Rev. Lett. **98**, 096804 (pages 4) (2007).

[10] X. Zhou and A. Mizel, *Nonlinear Coupling of Nanomechanical Resonators to Josephson Quantum Circuits*, Phys. Rev. Lett. **97**, 267201 (pages 4) (2006).

[11] M. P. Blencowe and E. Buks, *Quantum analysis of a linear dc SQUID mechanical displacement detector*, Phys. Rev. B **76**, 014511 (pages 16) (2007).

[12] F. Xue, Y. xi Liu, C. P. Sun, and F. Nori, *Two-mode squeezed states and entangled states of two mechanical resonators*, Phys. Rev. B **76**, 064305 (pages 9) (2007).

[13] W. Y. Huo and G. L. Long, *Generation of squeezed states of nanomechanical resonator using three-wave mixing*, Appl. Phys. Lett. **92**, 133102 (pages 3) (2008).

[14] P. D. Nation, M. P. Blencowe, and E. Buks, *Quantum analysis of a nonlinear microwave cavity-embedded dc SQUID displacement detector*, Phys. Rev. B **78**, 104516 (pages 17) (2008).

[15] E. Buks and M. P. Blencowe, *Decoherence and recoherence in a vibrating rf SQUID*, Phys. Rev. B **74**, 174504 (pages 8) (2006).

[16] F. Xue, Y. D. Wang, C. P. Sun, H. Okamoto, H. Yamaguchi, and K. Semba, *Controllable coupling between flux qubit and nanomechanical resonator by magnetic field*, New J. Phys. **9**, 35 (2007).

[17] J. Clarke and A. Braginski, *The SQUID Handbook volume 1* (Wiley-VCH Verlag, GmbH and Co. KGaA, Weinheim, 2004).

[18] S. Etaki, M. Poot, I. Mahboob, K. Onomitsu, H. Yamaguchi, and H. S. J. van der Zant, *Motion detection of a micromechanical resonator embedded in a d.c. SQUID*, Nat Phys **4**, 785 (2008).

[19] M. Matsuda, T. Kataishi, and S. Kuriki, *SQUID Operation at a Constant Voltage*, IEEE Trans. Appl. Supercond. **17**, 695 (2007).

[20] H. Yamaguchi, S. Miyashita, and Y. Hirayama, *Mechanical and piezoresistive properties of InAs/AlGaSb cantilevers*, Appl. Surf. Sci. **237**, 645 (2004), proceedings of the Seventh International Symposium on Atomically Controlled Surfaces, Interfaces and Nanostructures.

[21] M. D. LaHaye, O. Buu, B. Camarota, and K. C. Schwab, *Approaching the Quantum Limit of a Nanomechanical Resonator*, Science **304**, 74 (2004).

[22] G. Zolfagharkhani, A. Gaidarzhy, S.-B. Shim, R. L. Badzey, and P. Mohanty, *Quantum friction in nanomechanical oscillators at millikelvin temperatures*, Phys. Rev. B **72**, 224101 (pages 5) (2005).

[23] A. N. Cleland and M. L. Roukes, *External control of dissipation in a nanometer-scale radiofrequency mechanical resonator*, Sens. Act. A **72**, 256 (1999).

[24] A. N. Cleland and M. L. Roukes, *Noise processes in nanomechanical resonators*, J. Appl. Phys. **92**, 2758 (2002).

[25] Ya. M. Blanter, in preparation.

[26] D. Rugar and P. Grütter, *Mechanical parametric amplification and thermomechanical noise squeezing*, Phys. Rev. Lett. **67**, 699 (1991).

[27] S.-B. Shim, M. Imboden, and P. Mohanty, *Synchronized Oscillation in Coupled Nanomechanical Oscillators*, Science **316**, 95 (2007).

[28] C. D. Tesche and J. Clarke, *dc SQUID: Noise and optimization*, J. Low Temp. Phys. **29**, 301 (1977).

[29] Software available from `http://www.ece.rochester.edu/~sde/research/software/fasthenry/index.html`.

A

A MODEL FOR THE DC SQUID

A.1 RCSJ MODEL

The dc SQUID is modelled using the RCSJ model (for a review, see Ref. [1]). The two junctions of the dc SQUID are modelled as a resistor (R), capacitor (C) and an "ideal" Josephson junction in parallel, as illustrated in Fig. A.1a. Current conservation yields two second order differential equations, governing the time dependence of the phase differences $\delta_{1,2}$ of the junctions (each with a critical current I_0) in the dc SQUID. The voltage V is related to the time derivative of the phase differences: $V = \Phi_0(\partial\delta_1/\partial t + \partial\delta_1/\partial t)/4\pi$. For a symmetric, noiseless dc SQUID the differential equations are:

$$\frac{\Phi_0}{2\pi}C\ddot{\delta}_1 + \frac{\Phi_0}{2\pi}\frac{1}{R}\dot{\delta}_1 + I_0\sin\delta_1 = \frac{1}{2}I_B + J, \tag{A.1}$$

$$\frac{\Phi_0}{2\pi}C\ddot{\delta}_2 + \frac{\Phi_0}{2\pi}\frac{1}{R}\dot{\delta}_2 + I_0\sin\delta_1 = \frac{1}{2}I_B - J. \tag{A.2}$$

These equations are coupled to each other by the amount of flux piercing the loop:

$$\delta_2 - \delta_1 = 2\pi\cdot\Phi_{\mathrm{tot}}/\Phi_0. \tag{A.3}$$

The total flux Φ_{tot} has two contributions: the externally applied flux Φ and the flux LJ due to the circulating current J flowing through the inductance of the loop L, so $\Phi_{\mathrm{tot}} = \Phi + LJ$.

First, the equations are scaled to simplify their numerical integration. This yields:

$$\beta_C\ddot{\delta}_1 + \dot{\delta}_1 + \sin\delta_1 = \imath/2 + \jmath, \tag{A.4}$$

$$\beta_C\ddot{\delta}_2 + \dot{\delta}_2 + \sin\delta_2 = \imath/2 - \jmath, \tag{A.5}$$

$$2\pi(\phi + \beta_L\jmath/2) = \delta_2 - \delta_1, \tag{A.6}$$

when the bias current and circulating current are normalized as $\imath = I_b/I_0$ and $\jmath = J/I_0$. Furthermore, time is scaled using the characteristic frequency $\omega_c = 2\pi I_0 R/\Phi_0$, flux using the flux quantum: $\phi = \Phi/\Phi_0$, and voltage by RI_0 so that $\upsilon = V/RI_0 = (\dot{\delta}_1 + \dot{\delta}_2)/2$.

Parts of this Appendix have been published in Nat. Phys. **4**, 785–788 (2008)

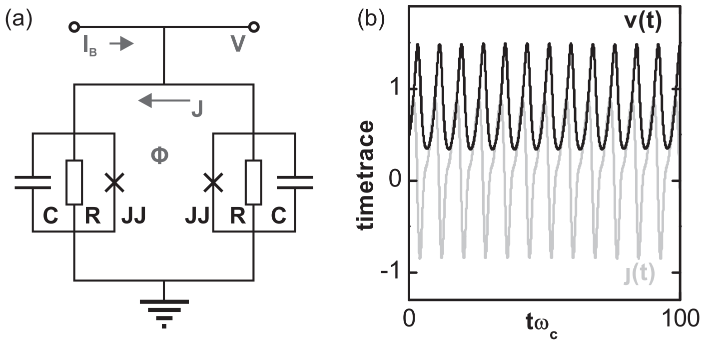

FIGURE A.1: (a) Schematic view of the dc SQUID. Each arm of the loop contains a Josephson junction (JJ) that is shunted by the normal state resistance of the junction (R) and the junction capacitance (C). A bias current I_B is sent into the dc SQUID. When the current through the two junction is unequal, a circulating current J flows. The output voltage V depends on the amount of flux throught the loop. (b) Calculated timetrace of the circulating current $\jmath(t)$ and voltage $v(t)$ in the absence of noise with $\imath = 2$, $\phi = 0.25$, $\beta_C = 0.78$ and $\beta_L = 0.16$.

The scaled model contains two parameters that completely describe the behavior of dc SQUIDs with different physical parameters, geometries and dimensions. The first is the Stewart-McCumber number, $\beta_C = 2\pi I_0 R^2 C/\Phi_0$, which indicates the importance of dissipation in the resistances. A dc SQUID with $\beta_C \lesssim 1$ is overdamped, whereas an underdamped dc SQUID has $\beta_C \gtrsim 1$. In the first case, the current-voltage characteristics are hysteretic. The other parameter is the screening parameter, $\beta_L = 2LI_0/\Phi_0$, which indicates how much a change in flux is screened by the circulating current flowing through the self-inductance of the loop L.

Figure A.1b shows a typical example of calculated time-traces of the circulating current $\jmath$ and voltage v. Both are rapidly oscillating at a frequency $\omega = 0.71 \cdot \omega_c$, which is the Josephson frequency that determines the average value of the voltage $\overline{v}$ [1].

A.2 FLUX RESPONSIVITY

In this Section, the flux responsivity of the dc SQUID is calculated using numerical simulations for the experimental conditions of Ch. 8 at a field $B = 115\,\mathrm{mT}$. The Stewart-McCumber number and the screening parameter were $\beta_C = 0.78$ and $\beta_L = 0.16$ respectively in this case. With these values, the scaled differential equations are integrated for different values of the bias current and the flux through the dc SQUID. The output voltage of the dc SQUID is calculated from the resulting time traces $\delta_{1,2}(t)$ using $V = RI_0(\dot{\delta}_1 + \dot{\delta}_2)/2$. This voltage has high frequency components (at the Josephson frequency) and an average value, as shown in Fig. A.1b. The latter of the two is the voltage that is measured. Figure A.2a shows a colorplot of the SQUID voltage as a function of the bias current and flux. From the average voltage at different amounts of flux penetrating the dc SQUID,

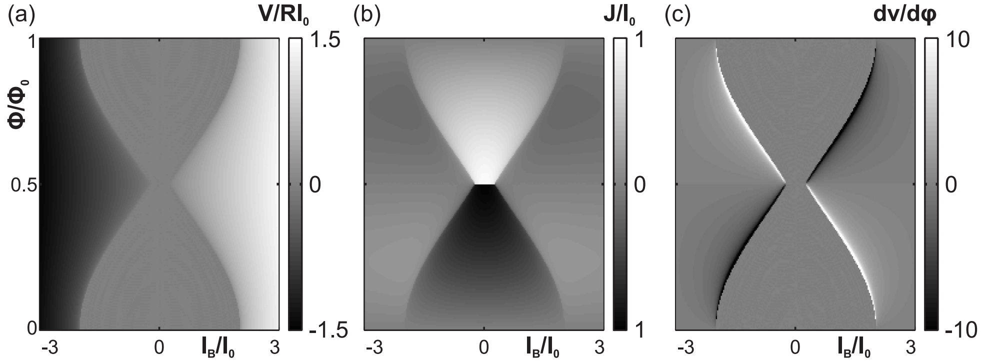

FIGURE A.2: Colormaps of the average voltage (a), circulating current (b) and flux responsivity (c) for different bias currents and fluxes of a dc SQUID with $\beta_C = 0.78$ and $\beta_L = 0.16$.

the peak-to-peak voltage swing V_{PP} is obtained. V_{PP} is bias-current dependent and the maximum voltage swing $V_{PP}^{\max}$ equals RI_0 and occurs at $I_B = 2I_0$. The dimensionless flux responsivity v_ϕ is obtained by numerically differentiating the scaled voltage with respect to the applied flux. To obtain the real flux responsivity, the dimensionless version is multiplied with RI_0 (or equivalently with $V_{PP}^{\max}$) and divided by Φ_0, i.e. $\partial V/\partial\Phi = RI_0/\Phi_0 \cdot v_\phi$. Fig. A.2c shows that the highest responsivity is obtained when the dc SQUID is biased just inside the dissipative region, where $V \neq 0$.

A.3 CALCULATION OF THE TRANSFER FUNCTIONS

In this Section, our method for calculating the transfer functions j_ϕ and $j_{\dot\phi}$ of the dc SQUID is discussed. As Eqs. 8.3 and 8.4 show, these transfer functions are the key quantities that determine the backaction of the dc SQUID detector on the resonator. A displacement u changes the flux through the dc SQUID, which alters the voltage V and the circulating current J. The former effect is the basis of position detection scheme (Ch. 7) and the latter changes the Lorentz force on the resonator causing backaction (Ch. 8). How the circulating current reacts to a change in displacement or flux is quantified by the transfer functions J_Φ and $J_{\dot\Phi}$ (cf. Eq. 8.2). These transfer functions are intrinsic properties of the dc SQUID (i.e. they do not depend on the properties of the resonator), so that a model of the dc SQUID with a time-varying flux suffices to find them.

To obtain the transfer functions, a small modulation is added to the flux: $\phi \to \phi + \phi_{\text{mod}} \cos(\omega_{\text{mod}} t)$. Figure A.3a shows that this amplitude-modulates the circulating current. Thereby it broadens the peaks at the harmonics of the Josephson frequency in the Fourier spectrum shown in Fig. A.3b. More importantly, in the spectrum of j a peak appears at the *modulation* frequency. The real part of the peak corresponds to the derivative

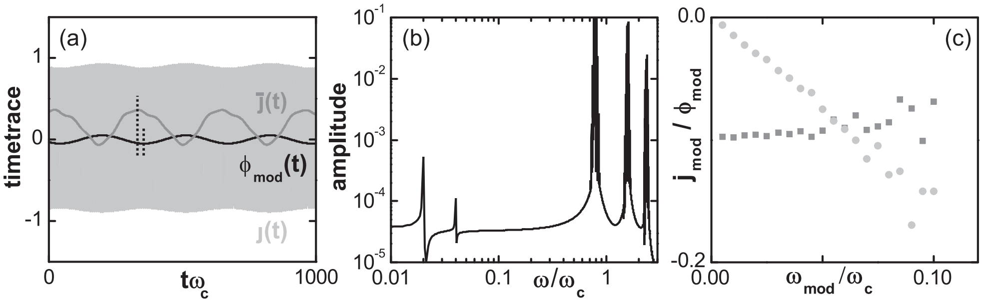

FIGURE A.3: (a) Circulating current for a small ($\phi_{\text{mod}} = 0.01$) modulation of the flux with $\omega_{\text{mod}}/\omega_c = 0.02$. The time-averaged value of the circulating current $\bar{\jmath}(t)$ has a phase shift with respect to the modulation $\phi(t)$ as indicated by the dashed lines. (b) Magnitude of the Fourier transform of the time trace of the circulating current that was shown in (a). (c) The modulation-frequency dependence of the real (squares) and imaginary (circles) parts of the circulating-current modulation. These simulations were done with $\imath = 2.0$, $\phi = 0.25$, $\beta_C = 0.78$ and $\beta_L = 0.16$.

$\jmath_\phi = \text{Re}[\jmath_{\text{mod}}/\phi_{\text{mod}}]$, while $\text{Im}[\jmath_{\text{mod}}/\phi_{\text{mod}}] = -\omega_{\text{mod}}\jmath_{\dot{\phi}}$. The frequency dependence of the modulation of the circulating current is shown in Fig A.3c. The real part $\text{Re}[\jmath_{\text{mod}}]$ is constant and the imaginary part $\text{Im}[\jmath_{\text{mod}}]$ increases linearly with the modulation frequency. Note that higher order time derivatives in Eq. 8.2 show up as deviations from the straight lines in Fig. A.3c. For low frequencies (in the experiments $\omega_R/\omega_c \sim 10^{-4}$) the higher order terms can thus safely be neglected.

A.4 BACKACTION TEMPERATURE

Coupling a resonator strongly to a detector can greatly modify the resonator temperature. This has been used to cool micromechanical resonators well below their environmental temperature as discussed in Ch. 2. The resonator temperature T_R is the weighted average of the environmental temperature T and the backaction temperature T_{BA} of the detector as indicated by Eq. 2.26. For the dc SQUID, the detector-induced damping rate is $\gamma_{BA} = -\gamma_0 \Delta_Q \jmath_{\dot{\phi}}$. The backaction temperature is found using the fluctuation-dissipation theorem (Eq. 2.10) that relates temperatures to force noise. The force noise has two contributions[1]: the first is the intrinsic contribution with PSD $\overline{S}_{F_nF_n} = m\omega_0 k_B T/Q_0$ and is due to the environment at temperature T. The second contribution comes from the backaction of the dc SQUID and is the Lorentz force due to the noise in the current $I_R = I_B/2 + J$, flowing through the resonator, which gives $\overline{S}_{F_{BA,n}F_{BA,n}} = (aB\ell)^2 \overline{S}_{I_RI_R}$. The resonator current-noise PSD, $\overline{S}_{I_RI_R}$, is caused by Johnson noise in the junction resistances ($I_{1,n}$ and $I_{2,n}$), and by fluctuations in the bias current $I_{B,n}$ [3]. Both contribution are included in the RCSJ model (see the previous Sections) by adding $\frac{1}{2}I_{B,n} + I_{1,n}$ and $\frac{1}{2}I_{B,n} + I_{2,n}$ to the right hand side of Eqs. A.1 and A.2 respectively. These equations can be integrated numerically to

[1] In the present analysis, quantum fluctuation [2] are not taken into account.

calculate the current noise flowing through the resonator. From this, the backaction temperature is obtained.

If the noise is not too large, the backaction temperature can also be expressed via the changes in the circulating current due to changes in the bias current $\partial J/\partial I_B$, and due to currents generated in the resistances $\partial J/\partial I_{1,2}$:

$$\overline{S}_{I_R I_R} \approx \frac{4k_\mathrm{B}T}{R}\left\{\left(\frac{\partial J}{\partial I_1}\right)^2 + \left(\frac{\partial J}{\partial I_2}\right)^2\right\} + \overline{S}_{I_B I_B}\left(\frac{1}{2} + \frac{\partial J}{\partial I_B}\right)^2. \tag{A.7}$$

By combining Eqs. 2.26 and A.7 with the results for the backaction (Eq. 8.3 and 8.4), the backaction temperature is found:

$$T_{BA} = \overline{S}_{I_R I_R}\frac{2R}{4k_\mathrm{B}}\frac{\pi}{(-J_{\dot\phi})} = 2\left\{\left(\frac{\partial J}{\partial I_1}\right)^2 + \left(\frac{\partial J}{\partial I_2}\right)^2\right\}\frac{\pi}{(-J_{\dot\phi})}T + \left(\frac{1}{2} + \frac{\partial J}{\partial I_B}\right)^2\frac{\pi}{(-J_{\dot\phi})}\mathscr{F}\imath T_c, \tag{A.8}$$

where we have introduced the Fano-factor $\mathscr{F} = \overline{S}_{I_B I_B}/2eI_B$ and the characteristic temperature of the dc SQUID $T_c = eRI_0/k_\mathrm{B} = 0.3\,\mathrm{K}$ at 115 mT (see Table 8.1). Note, that the force noise contribution due to the bias current can be made vanishingly small by operating the dc SQUID at a setpoint where $\partial J/\partial I_B = -1/2$, i.e. where the noise in the bias current does not flow through the arm with the resonator, but through the other arm instead. Furthermore, note that both terms in A.8 have the same structure: they are the product of an enhancement of the noise due to the dc SQUID dynamics, the cooling power of the dc SQUID $\pi/(-J_{\dot\phi})$ and a temperature.

The difference in resonator temperature due to the backaction, $\Delta T_R = T_R - T$, is given by:

$$\Delta T_R = \frac{\gamma_{BA}}{\gamma_0 + \gamma_{BA}}(T_{BA} - T) = \frac{\Delta_Q J_{\dot\phi}}{1 - \Delta_Q J_{\dot\phi}}(T - T_{BA}). \tag{A.9}$$

By using the parameters for the measurements at 115 mT (Ch. 8), we find that at $\imath = 2$ and $\phi = 0.25$, the transfer functions that are needed to calculate the backaction temperature using Eq. A.8 are: $\partial J/\partial I_1 = 0.49$, $\partial J/\partial I_2 = -0.51$, $\partial J/\partial I_B = 0.00$ and $\partial \jmath/\partial\dot\phi = 1.24$. For these values, the noise generated in the junction resistances is negligible as $T \ll T_c$. Shot noise contributes $0.9\,\mathrm{pA}/\sqrt{\mathrm{Hz}}$ to the noise in the bias current and the $10\,\mathrm{k\Omega}$ input resistance of the room-temperature high-frequency amplifier contributes $1.3\,\mathrm{pA}/\sqrt{\mathrm{Hz}}$. This gives $\mathscr{F} = 3.1$. The backaction temperature of the dc SQUID at this particular bias point is $T_{BA} = -1.47\,\mathrm{K}$ and this raises the resonator temperature by 0.6 mK. Note, that the resonator is not cooled by the backaction because $\partial \jmath/\partial\dot\phi$ is positive, reducing the damping. The negative backaction temperature means that when the resonator would be strongly coupled to the detector, the resonator response becomes unstable (the damping becomes negative), an effect that can be used to make a narrow-linewidth oscillator with good frequency stability [4].

REFERENCES

[1] J. Clarke and A. Braginski, *The SQUID Handbook volume 1* (Wiley-VCH Verlag, GmbH and Co. KGaA, Weinheim, 2004).

[2] R. H. Koch, D. J. V. Harlingen, and J. Clarke, *Quantum noise theory for the dc SQUID*, Appl. Phys. Lett. **38**, 380 (1981).

[3] J. Clarke, C. D. Tesche, and R. P. Giffard, *Optimization of dc SQUID voltmeter and magnetometer circuits*, J. Low Temp. Phys. **37**, 405 (1979).

[4] X. L. Feng, C. J. White, A. Hajimiri, and M. L. Roukes, *A self-sustaining ultrahigh-frequency nanoelectromechanical oscillator*, Nat Nano **3**, 342 (2008).

SUMMARY

MECHANICAL SYSTEMS AT THE NANOSCALE

Mechanics has been studied for millennia. First only at the human scale, but the rapidly developing microfabrication techniques of the last decades, made it possible to build smaller and smaller systems. Nowadays, mechanical systems can be made at the nanoscale. These devices are interesting from both an application and a scientific point of view. Compared to micromechanical devices, nano(electro)mechanical systems (NEMS) are faster as they have higher resonance frequencies, are lighter, making them sensitive to the addition of only a single atom, and consume less energy. Currently, NEMS are being used as sensors and high-frequency filters. NEMS can also be used to study the foundations of quantum mechanics: Preparing a man-made object in a quantum state might answer the question whether a clear separation exists between quantum and classical mechanics. To do this, the nanomechanical resonator has to be cooled to its ground state and its position has to be observed with a high resolution.

Many different techniques can be used to cool a resonator, but two different routes can be distinguished. The first is to use an ultra-high-frequency mechanical resonator (> 1 GHz), so that its thermal occupation is less than one when the device is cooled in a dilution refrigerator. The second approach is to use the detector to damp the resonator's Brownian motion, thus cooling it. This requires very good detectors. Quantum mechanics, however, puts constraints on the detector: One can either measure the position very accurately at the expense of severely disturbing the resonator, or measure an undisturbed resonator with a very bad signal-to-noise ratio. The optimal trade-off between these two limits is discussed.

In Chapter 2 an overview of the key experiments done so far in the field of quantum-(electro)mechanical systems is given. A wide range of different resonators, detectors and cooling mechanisms that are currently being employed to reach the ultimate goal: A resonator in the ground state combined with quantum-limited position detection.

In this Thesis measurements on a variety of different micro- and nanomechanical systems are presented; these can all be modelled using continuum mechanics, although some modifications have to be made when the device dimensions are of the order of a nanometer. The elasticity relations of isotropic materials and of highly anisotropic graphite are discussed. The latter is ideal for building devices to study mechanics in the quantum regime as they have a large zero-point motion and yet high resonance frequencies.

The first system that is studied in this Thesis is the graphene nanodrum. These devices consist of few-layer graphene flakes that are suspended over circular holes. Their mechanical properties are studied by measuring their compliance profile using an atomic force microscope. By fitting a continuum model to the data, the bending rigidity of and the tension in the graphitic flakes can be determined simultaneously. From this, the fundamental resonance frequencies and zero-point motion are estimated. This novel method of measuring the bending rigidity and tension is applicable to thin membranes of any kind.

Suspended carbon nanotubes form another important class of nanomechanical systems. Their bending-mode vibrations are detected at room temperature using a frequency mixing technique that converts fast conductance oscillations to more easily measurable low-frequency current changes. The resonance frequency of these atomically thin devices can be varied over a large range using the gate electrode: When a static gate voltage is applied, a force is exerted on the nanotube, thereby straining it. This tension tunes the nanotube resonator in a similar way as the tuning of a guitar string. The tuning curves are accurately reproduced by the continuum model discussed in this Thesis. An analysis of the resonance peak shape gives information about the quality factor and the phase differences between the radio-frequency signals on the gate and source electrode. High-quality carbon nanotubes are defect-free, covalently-bound structures, which should in principle have low dissipation. However, the Q-factors that are found are low. This holds for all bottom-up carbon-based resonators made so far. Using a novel detection scheme that uses current rectification at sharp Coulomb peaks, combined with a driving force exerted by a nearby antenna, nanotubes resonators are studied at millikelvin temperatures. Here, ultra-high quality factors were observed, redeeming the promise of low dissipation in high-quality nanotubes. These devices are expected to be close to their ground state when they are not being driven. They might also be able to detect changes in mass as small as a that of a single He atom. The motion of the nanotube is strongly coupled to the tunnelling of electrons through the nanotube quantum dot, giving rise to a range of interesting effects. This includes single electron tuning, strong backaction and feedback-induced instabilities.

Finally, a 2 MHz flexural resonator that is embedded in the loop of a dc SQUID, is studied. The dc SQUID is frequently used as a near quantum-limited detector of magnetic fields, but here it is used in a different way: As a position detector for the mechanical resonator. Using the Brownian motion of the resonator, the detector can be calibrated and its sensitivity is found to be in the $\mathrm{fm}/\sqrt{\mathrm{Hz}}$ range. This sensitive detection scheme makes it possible to study the backaction of the dc SQUID on the resonator. By measuring the driven response of the resonator while varying the bias conditions of the dc SQUID, shifts in resonance frequency and changes in quality factor are observed. These effects, caused by the Lorentz' force on the resonator due to the circulating current in the dc SQUID, are in semi-quantitative agreement with numerical simulations of the RCSJ model for the SQUID.

Menno Poot
Delft, October 2009

SAMENVATTING

MECHANISCHE SYSTEMEN OP DE NANOSCHAAL

Mechanica wordt al millennia lang bestudeerd. Eerst alleen op de menselijke schaal, maar de snelle ontwikkelingen in microfabricage-technieken tijdens de laatste decennia hebben het mogelijk gemaakt om systemen met steeds kleinere afmetingen te maken. Vandaag de dag kunnen mechanische systemen met nanometer afmetingen worden gemaakt. Deze systemen zijn zowel voor toepassingen als voor wetenschappelijk onderzoek interessant. In vergelijking met micromechanische systemen, zijn nano(elektro)mechanische systemen (NEMS) sneller vanwege hun hoge resonantiefrequenties, zijn zij lichter wat hen gevoelig maakt voor de toevoeging van een enkel atoom en verbruiken zij minder energie. Momenteel worden NEMS gebruikt als sensoren en hoogfrequente filters. NEMS kunnen ook worden gebruikt om de grondslagen van de quantummechanica te bestuderen: Het creëren van een door mensen gemaakt object dat zich in een quantumtoestand bevindt, zou de vraag of er een duidelijke scheidslijn bestaat tussen klassieke- en quantummechanica kunnen beantwoorden. Om dit voor elkaar te krijgen dient de nanomechanische resonator tot de grondtoestand gekoeld te worden en dient zijn positie met hoge gevoeligheid te kunnen worden bepaald.

Er bestaan verschillende koeltechnieken, maar er kunnen twee verschillende richtingen worden onderscheiden. In de eerste wordt een ultrahoogfrequente mechanische resonator gebruikt, die, wanneer hij afgekoeld wordt in een mengkoeler, een thermische bezetting van minder dan één zal hebben. Bij de tweede manier wordt de detector gebruikt om de Brownse beweging van de resonator te dempen en hem hiermee dus te koelen. Hiervoor zijn zeer goede detectoren nodig. De quantummechanica legt echter beperkingen op aan de detector: De positie van de resonator kan slechts met hoge precisie worden bepaald als de resonatorbeweging sterk verstoord wordt en een meting waarbij de resonator nauwelijks verstoord wordt, zal resulteren in een onnauwkeurige positiebepaling. In dit proefschrift wordt de balans tussen deze twee limieten besproken.

In hoofdstuk 2 wordt een overzicht van de belangrijkste experimenten die tot nu toe gedaan zijn in het veld van quantum(elektro)mechanische systemen gegeven. Een va riëteit aan resonatoren, detectoren en koeltechnieken wordt op dit moment gebruikt om het ultieme doel te realiseren: Een mechanische resonator in zijn grondtoestand, gecombineerd met een detector die op de door quantummechanica bepaalde limiet werkt.

Dit proefschrift beschrijft verschillende micro- en nanomechanische systemen; zij kunnen allemaal worden gemodelleerd binnen het raamwerk van de continuümmechanica, hoewel er verfijningen nodig zijn wanneer de afmetingen van het systeem de nanometer benaderen. De relatie tussen de spanning en rek in een isotroop materiaal en die van het sterk anisotrope grafiet worden besproken. Dit laatste materiaal is ideaal voor het maken van beweegbare apparaatjes om mechanische systemen in het quantumregime te kunnen bestuderen, omdat zij een grote nulpuntsbeweging hebben, gecombineerd met hoge resonantiefrequenties.

Het eerste systeem dat wordt bestudeerd is een grafeen nanotrommel. Deze trommels bestaan uit grafeenflinters die vrijhangen boven cirkelvormige gaten. Hun mechanische eigenschappen worden bestudeerd door het profiel van de veerconstante te meten met een atomaire-krachtmicroscoop. Door deze gemeten data met een continuümmodel te vergelijken, worden rekspanning in en de buigstijfheid van de flinters bepaald. Hiermee worden de resonantiefrequentie en de nulpuntbeweging geschat. Deze methode kan gebruikt worden om de rekspanning en buigstijfheid van ieder dun membraan te bepalen.

Vrijhangende koolstof nanobuisjes vormen een andere belangrijke klasse van nanoelektromechanische systemen. Hun transversale trillingen worden bij kamertemperatuur door middel van een frequentie-mix techniek waargenomen. Hierbij worden hoogfrequente geleidingsoscillaties omgezet in stroomveranderingen met een lagere frequentie. De resonantiefrequentie van deze buisjes kan over een groot bereik gestemd worden met een gate-elektrode. Door hierop een gelijkspanning aan brengen, wordt een kracht op de nanobuis uitgeoefend en wordt deze uitgerekt. Net zoals bij het stemmen van een gitaarsnaar gaat de frequentie hierdoor omhoog. Een analyse van de vorm van de resonantiepiek geeft informatie over de kwaliteitsfactor en het faseverschil tussen de radiofrequente signalen op de source- en de gate-elektrode. Koolstof nanobuisjes van hoge kwaliteit zijn in principe vrij van defecten, wat in een lage dissipatie zou moeten resulteren. De gemeten Q-factoren zijn echter teleurstellend laag. Dit gold tot nu toe voor alle NEMS die gemaakt zijn van kleine, op koolstof gebaseerde structuren. Met een nieuwe detectietechniek die gelijkrichting op een Coulombpiek gebruik, in combinatie met aandrijving via een nabije antenne hebben wij nanobuisresonatoren bij millikelvin temperaturen kunnen bestuderen. Hierbij werden ultra hoge Q-factoren gevonden en kon de belofte van lage dissipatie in dit soort systemen eindelijk worden ingelost. De nanobuis zou dicht bij zijn grondtoestand moeten zijn als hij niet wordt aangedreven. Hij zou ook in staat moeten zijn om een massaverandering ter grootte van een enkel heliumatoom te detecteren. De beweging van de nanobuis is sterk gekoppeld aan die van de elektronen die door de nanobuis heen stromen. Dit leidt o.a. tot afstemming door een enkel elektron, sterke terugwerking en terugkoppelinggeïnduceerde instabiliteit.

Tot slot wordt een 2 MHz resonator die in de lus van een dc SQUID geïntegreerd is, behandeld. De dc SQUID wordt vaak gebruikt als een magneetvelddetector die de quantumlimiet benadert. Hier wordt hij echter op een andere manier gebruikt, namelijk als detector van de verplaatsing van een balkresonator. Middels de Brownse beweging van de resonator is de detector gekalibreerd en zijn gevoeligheid ligt in het $\mathrm{fm}/\sqrt{\mathrm{Hz}}$ gebied. Dit gevoelige detectieschema maakt het mogelijk om de terugwerking van de dc SQUID op de resonator te bestuderen. Door de respons van de resonator op een aangelegde kracht te meten bij verschillende instellingen van de dc SQUID, worden verandering in de frequentie en demping van de resonator waargenomen. Deze effecten, veroorzaakt door de Lorentzkracht vanwege de circulerende stroom in de dc SQUID, zijn in semikwantitative overeenkomst met de uitkomst van numerieke simulaties van het RCSJ model voor de dc SQUID.

Menno Poot
Delft, oktober 2009

CURRICULUM VITAE

MENNO POOT

03–03–1982	Born in Maassluis, the Netherlands.
1994–2000	Secondary education, W.V.O. at "Christelijke scholengemeenschap Aquamarijn" in Vlaardingen.
2000–2003	B.Sc. Applied Physics (*cum laude*), Technische Universiteit Delft.
2003–2005	M.Sc. Applied Physics (*cum laude*), Technische Universiteit Delft. Supervisor: Prof. dr. ir. H. S. J. van der Zant.
2005–2009	Ph.D. research at Delft University of Technology Promotor: Prof. dr. ir. H. S. J. van der Zant.

LIST OF PUBLICATIONS

14. M. Poot, S. Etaki, I. Mahboob, K. Onomitsu, H. Yamaguchi, Ya. M. Blanter and H. S. J. van der Zant
    Tunable backaction of a dc SQUID on an integrated micromechanical resonator
    Submitted to Phys. Rev. Lett. (2009)

13. G. A. Steele, A. K. Hüttel, B. Witkamp, M. Poot, H. B. Meerwaldt, L. P. Kouwenhoven and H. S. J. van der Zant
    Strong coupling between single-electron tunneling and nano-mechanical motion
    Science **325**, 1103–1107 (2009)

12. S. Etaki, M. Poot, W. Venstra and H. S. J. van der Zant
    Elektromechanische systemen op de nanoschaal (in Dutch)
    Ned. Tijds. v. Nat. **75**, 272–276 (2009)

11. W. Venstra, S. Etaki, K. Babaei Gavan, M. Poot and H. S. J. van der Zant
    Nanoelektromechanische systemen (in Dutch)
    NEVAC blad **47**, 5–8 (2009)

10. A. K. Hüttel, G. A. Steele, B. Witkamp, M. Poot, L. P. Kouwenhoven and H. S. J. van der Zant
    Carbon nanotubes as ultra-high quality factor mechanical resonators
    Nano Lett. **9**, 2547–2552, (2009)

9. B. Witkamp, M. Poot, H. Pathangi, A. K. Hüttel and H. S. J. van der Zant
   Self-detecting gate-tunable nanotube paddle resonators
   Appl. Phys. Lett. **93**, 111909 (2008)

8. S. Etaki, M. Poot, I. Mahboob, K. Onomitsu, H. Yamaguchi and H. S. J. van der Zant
   Motion detection of a micromechanical resonator embedded in a d.c. SQUID
   Nature Phys. **4**, 785–788 (2008)

7. A. K. Hüttel, M. Poot, B. Witkamp and H. S. J. van der Zant
   Nano-electromechanics of suspended carbon nanotubes
   New J. Phys. **10**, 095003 (2008)
   Selected in “the NJP Best of 2008”

6. M. Poot and H. S. J. van der Zant
   Nanomechanical properties of few-layer graphene membranes
   Appl. Phys. Lett. **92**, 063111 (2008)

5. M. Poot, B. Witkamp, M. A. Otte and H. S. J. van der Zant
   Modelling suspended carbon nanotube resonators
   Phys. Stat. Sol. (b) **244**, 4252–4256 (2007)

4. H. S. J. van der Zant, Y.-V. Kervennic, M. Poot, K. O'Neill, Z. de Groot, J. M. Thijssen, H. B. Heersche, N. Stuhr-Hansen, T. Bjornholm, D. Vanmaekelbergh, C. A. van Walree and L. W. Jenneskens,
   Molecular three-terminal devices: fabrication and measurements
   Faraday Discuss. **131**, 347–356 (2006)

3. B. Witkamp, M. Poot and H. S. J. van der Zant
   The bending mode vibration of a suspended nanotube oscillator
   Nano Lett. **6**, 2904–2908 (2006)

2. H. S. J. van der Zant, E. A. Osorio, M. Poot and K. O'Neill
   Electromigrated molecular junctions
   Phys. Stat. Sol. (b) **243**, 3408–3412 (2006)

1. M. Poot, E. A. Osorio, K. O'Neill, J. M. Thijssen, D. Vanmaekelbergh, C. A. van Walree, L. W. Jenneskens and H. S. J. van der Zant
   Temperature dependence of three-terminal molecular junctions with sulfur end-functionalized tercyclohexylidenes
   Nano Lett. **6**, 1031–1035 (2006)

ACKNOWLEDGEMENTS

This last part of the Thesis is, in my opinion, the most important one. Although a Thesis has only one name on the cover, the work described in it is hardly ever possible without the help of others. The last words of this Thesis I will use to thank everyone that I had the pleasure to work with during the last four years.

Without doubt, the first person to thank is Herre. He has been my supervisor since my BEP on charge-density waves. When that project ended, he asked me if I was interested in doing a master project with him as well. So I did, and for about one year I worked on transport through single molecules. At that time the group “Molecular Electronics and Devices” was founded and we moved to the other side of the physics building. Because of the good atmosphere in the group, I decided to do my PhD in MED as well. During all this time, I learned many things from Herre, ranging from how to write papers, how to pragmatically work focussed in parallel, and, most importantly, that tickmarks should be on the inside!

When I started my PhD (and a bit before that), I had the pleasure to share room F388 with Kevin and Iulian, the first MED postdocs. Kevin, my colleague in CDWs and single molecules, I wish you, Saskia, Liam and Fiona all the best. Iulian, I greatly enjoyed the fun we had with your Ali G/Borat movies and to see the interaction between you and your supervisor (“Did you submit already?”).

Speaking of supervisors, when MED started we had tree staff members. Soon Peter Hadley got a nice position in Graz, taking Piet with him, and three years after the “birth” of MED, Alberto Morpurgo became professor in Geneva. Alberto, are you coming over for the borrel? Lets also not forget all the people that worked together with (for?) Alberto: Anna, Monica & Saverio (still entangled), Helena, and those who also moved to Geneva: Hangxing, Ignacio and Jeroen. Good luck over there.

When I started to work in nanomechanics, I had no experience with working in a clean-room. Fortunately, Benoit was there to help me to fabricate my own samples. He also introduced me to his magic mixing-setup and to the wonderful world of “korte en lange tubes”. Benoit, I think that we formed the perfect team! I should also thank all the other nanotube guys: Sami, Bert, André, Andreas, Hari and mr. everlasting smile Harold. Also I should not forget Gary. Although Herre claims that you can write an APL in one afternoon, Gary showed that with a good team you can make it into Science in just a few weeks. Andreas has been my officemate for many years. He has introduced us to the world of svn, gnuplot and wiki and is always available as computer guru. In the beginning the transition from top-down quantum dots to nanotubes was difficult, but in the end it worked out fine. Shine on you crazy diamond!

Another important theme is graphene. I like to thank Dominique, Samira and especially Jeroen and Alberto for the good discussions we had on this amazing material. I hope that the results in Geneva will be as nice as those in Delft. In MED, Abdulaziz is the person who will continue the graphene-NEMS work. Perhaps with a slow start at the begin, but now full of ideas. I am sure that we will get a few papers out in the coming year. The AFM experiments with the nanodrums have resulted in several good BEP reports though the years, by Jörgen, Sjoerd and Bob.

Within MED there is certainly more nanomechanics than just the nanotube team: Gijs, soon dr. Gavan, I am sure that a lot of people will appreciate your optical setup alias "the sample terminator". For his master thesis, Hidde worked with me on a theoretical project on nanotubes, but then decided that an experimental PhD on NEMS would be much more fun. Warner, the last but certainly not the least postdoc-roommate and Joop and Joris the SQUID bachelor students.

In MED every now and then we have movie nights, where somebody picks a movie, and a beamer and beer do the rest. In all these years we had very good and also very bad movies. On two occasions we organized a poker night and that brings me to the next person that I am greatly indebted to: Samir, the man with the wild/great ideas. You are the one who got me interested in the SQUID business. I always like the discussions with you on electric circuits, feedback loops, transfer function and Labview "programming". Sometimes you are right, sometimes I am, but we always learn a lot. Another thing that I will never forget is the week-long road trip that we had al the way from Ventura, via LA, Joshua Tree NP and grand canyon to the poker tournament in Vegas!

The SQUID experiments in Chapters 7 and 8 of this Thesis would not have been possible without the expertise and facilities from our collaborators from NTT Japan: Hiroshi Yamaguchi, Koji Onomitsu, Kenji Yamazaki, Tatsushi Akazaki, Hajime Okamoto and Imran Mahboob. I hope that this collaboration will lead to many more nice results.

The single molecules form the other part of MED. Its most notorious member is super-postdoc II. Well Edgar, where shall I start... remember the Greek dance, the Menno-hours, being zwarte Piet for sint Rami, and the stolen wuppies? I think that I should have written a Chapter 9 about everything that happened or that you made happen in the last 5 years. I'm sure that MED would have been very different without you and your jokes. Jos, thank you for making the nanotube movies and the Thesis templates. Christian, it was a pleasure go with you to the March meeting and to walk through German town. Ferry, I am really sorry that I asked you to take over the CRUM meetings, but someone had to do it... Of course this list is not complete without Anne, Hubert, Bo, Jay, Alexander, Diana and all the students: Dapeng, Constant, Bertold, Johan and Arjan.

One of the best thing of doing physics here in Delft, is that the theory group is so nearby. I had the pleasure to work together with Yaroslav Blanter and his students, Omar, Rachid, Georgi and Stefano. Just a few doors away is Jos Thijssen, who is always willing to help with any computational challenge. I also had the opportunity to visit Miles Blencowe in Dartmouth College. The discussions I had there opened my eyes for many interesting effects in SQUIDs and NEMS. I enjoyed the daily walks to the coffee place with Paul. And Miles, thank you for your hospitality, the nice dinners at your place and the trip to the Maple farm.

I am also grateful to all the support staff. First of all, to the secretaries of the group, Maria, Monique, Irma and Daphne, who always do their best to shield us from the bureaucracy. To the technicians: Mascha van Oossanen and Jan Toth from MED, the nanofacility staff, Jaap Beekman for keeping the MB AJA in perfect shape, and the helium team. A special thanks to Raymond Schouten, the electronics wizard, and to the people from DEMO for their help with the electronic equipment. Finally, I hope that I did not forget anyone in this Acknowledgement, but I will finish here. It has been decided.

Menno Poot, October 2009